Anthracene-Fused Porphyrins

A thesis submitted to the board of the faculty of Physical Science in partial fulfilment of the requirements for the degree of

Doctor of Philosophy of the University of Oxford

By

Nicola Kathleen Sybille Davis

The Chemistry Research Laboratory and Worcester College, Oxford

Trinity Term 2011

Abstract: Anthracene-Fused Porphyrins

Nicola Kathleen Sybille Davis, Worcester College, University of Oxford.
D. Phil. Thesis, Trinity Term 2011.

This thesis describes the synthesis of a novel family of porphyrins fused to anthracenes, together with investigations into their optical and electrochemical properties, as well as exploring their potential for application in dye-sensitised solar cells.

Chapter 1 gives an overview of the structure-property relationships of large planar π-systems for organic electronic applications. Porphyrins are introduced as suitable building blocks for such systems, and approaches for extending the π-conjugation of these macrocycles are presented.

A literature review of porphyrins fused to aromatic units is presented in *Chapter 2*, with a focus on the influence of structure on the optoelectronic properties of such systems. The chapter concludes with a summary of my previous work on the synthesis of anthracene-fused porphyrins, and the aims of this project are stated.

Chapter 3 describes the syntheses of fully and partially fused bis-anthracene porphyrin monomers and dimers. By varying peripheral substituents, it was possible to solve problems of aggregation encountered for these systems. Fusion of anthracene units to a porphyrin core was found to result in systems displaying strong absorption in the near-IR, small HOMO-LUMO gaps, and low oxidation potentials.

Chapter 4 explores the synthesis, crystal structure and optoelectronic properties of a porphyrin fused to four anthracenes, revealing this system to exhibit the longest wavelength absorption of any porphyrin monomer. The synthesis of a liquid crystalline tetra-anthracene fused porphyrin was proposed, and attempts to synthesise the necessary anthracene precursors were undertaken.

Chapter 5 describes the molecular design and synthetic pathway to a mono-anthracene fused porphyrin, and its unfused analogue, for use in liquid electrolyte dye-sensitised solar cells. By varying the metal oxide layer or lithium ion concentration of the device, it was possible to achieve incident photon to current conversion efficiency (IPCE) responses at wavelengths beyond 1050 nm.

Chapter 6 details the experimental synthetic procedures and characterisation data for all the compounds synthesised during this project.

Publications

Papers:

'Towards a Porphyrin-Based Panchromatic Sensitizer for Dye-Sensitized Solar Cells'
James M. Ball, Nicola K. S. Davis, James Wilkinson, Joël Teuscher, James Kirkpatrick, Robert Gunning, Harry L. Anderson, Henry J. Snaith
Pending submission to *Journal of Materials Chemistry*

'A Porphyrin Fused to Four Anthracenes'
Nicola K. S. Davis, Amber L. Thompson, Harry L. Anderson
Journal of the American Chemical Society **2011**, *133*, 30-31.
Highlighted in C&EN December 20th, 2010 — 'Long-proposed porphyrin is finally made'

'Bis-Anthracene Fused Porphyrins: Synthesis, Crystal Structure, and Near-IR Absorption'
Nicola K. S. Davis, Amber L. Thompson, Harry L. Anderson
Organic Letters **2010**, *12*, 2124-2127.

Lectures:

'Anthracene-Porphyrins for Photovoltaics'
Nicola K. S. Davis, James M. Ball, Harry L. Anderson, Henry J. Snaith
Japan — UK Dye-Sensitised & Organic Photovoltaic Workshop 2011 (JUDO PV), University of Oxford UK, July 2011.

Posters:

'Towards Molecular Graphenes: Fusing Anthracenes to Porphyrins'
Nicola K. S. Davis, Amber L. Thompson, Harry L. Anderson
RSC 10th International Conference on Materials Chemistry (MC10), University of Manchester, July 2011.

'Towards Larger π-Conjugated Sheets: Fusing Anthracenes to Porphyrins'
Nicola K. S. Davis, Amber L. Thompson, Harry L. Anderson
Pfizer Organic Chemistry Poster Symposium, University of Oxford, October 2010.

'Towards Larger π-Conjugated Sheets: Fusing Anthracenes to Porphyrins'
Nicola K. S. Davis, Amber L. Thompson, Harry L. Anderson
3rd EuCheMS Chemistry Congress: 'Chemistry, the Creative Force', Nürnberg, Germany, August 2010.

'Towards Larger π-Conjugated Sheets: Fusing Anthracenes to Porphyrins'
Nicola K. S. Davis, Miłosz Pawlicki, Harry L. Anderson
RSC Supramolecular and Macrocycles Meeting, University of Cambridge, December 2009.

Prizes:

Winner of the 'Advanced Technologies and Nanomaterials' poster prize at the RSC 10th International Conference on Materials Chemistry (MC10), University of Manchester, July 2011.

First prize winner of the Pfizer Organic Chemistry Poster Symposium at the University of Oxford, October 2010.

Winner of the *ChemComm* poster prize at the RSC Supramolecular and Macrocycles Meeting, University of Cambridge, December 2009.

Acknowledgements

He did not say 'You shall not be tempest-tossed, you shall not be work-weary, you shall not be discomforted'. But he did say, 'You shall not be overcome.' — Julian of Norwich.

First of all, I would like to thank Harry for the opportunity to work on such a great project, and the freedom to explore new areas — particularly in photovoltaics. Many thanks to Harry also for all the help and advice over the last three years, for support and encouragement when things weren't working so well, and for celebrating the successes!

Many thanks must go to DSTL for funding my DPhil and allowing me to investigate such interesting compounds, and to Ken McEwan for the informative discussions.

Thanks to Dr Barbara Odell for help and advice with NMR experiments, and for squeezing my samples into the NMR queue at short notice. A big thank you to Dr Amber Thompson who has done some wonderful work on my porphyrin crystals, and who has fed me with tea and cake on many an occasion. Thanks to Dr James Ball for his hard work on the photovoltaic part of the project, and for the interesting discussions and debates we have had over how improve IPCE responses! Thanks also to James for patiently answering all my questions about the many aspects of solar cells, and for letting me into the clean room to make some of my own. Thanks to Dr Joël Teuscher for transient absorption experiments, James Wilkinson for the data regarding porphyrin **205**, and Dr James Kirkpatrick for DFT calculations and images (and for many helpful hints about the world of science journalism).

Many thanks and hugs to the Anderson group past and present who have been wonderful friends and colleagues, cheering me up when chemistry wasn't going so well, reassuring me when I lost confidence, and laughing at me for being 'such a girl'. Thanks to all those who proof read my thesis, and who answered my endless questions. Particularly I would like to mention: Miłosz Pawlicki who got me into this fusion lark in the first place, Louisa Esdaile, who has been a constant support (even across the pond) and who is so much fun to be around; Sébastien Ulrich, who always had time for me and my stresses; Steve Karlen for the lively debates; Johannes Sprafke who has always been incredibly supportive and helpful, and who is frankly the best chemist I have ever known; Guzmán Gil-Ramírez, who will never forget *that* conference where he spent most of the time looking after me in hospital (and for which I will be eternally grateful) — thanks for all the chats and laughs; Mitsuhiko Morisue for not killing me with potassium permanganate; Jon Matichak and Georg Fischer who have always been happy to answer the silliest of questions; Christiane Knappke for getting me through the last few weeks; Ismael López-Duarte who has been so supportive during my write up and who has been a well of information about photovoltaic devices, and

finally Dima Kondratuk who always tells me I am beautiful (and is never afraid to tell me when I am wrong).

I would like to thank Rev Dr Jonathan Arnold for his tremendous support during the writing of this thesis, and for the Galaxy cake bars. Thanks also to Prof Tim Softley and Dr Grant Ritchie who have been so helpful over the years and helped me see the wood for the trees. Thanks also to David Reay and David Adam who have given me some wonderful opportunities to write for national newspapers and magazines, and have helped me to realise my dreams.

Thanks must go to all my friends who have been a constant support throughout my DPhil, ready to celebrate or commiserate depending on the occasion. Special thanks to: Alex V Barnard who is the greatest vegan punk activist I have ever known (one word: Falafel…); Christoph Wegener for all the balance; Hannah Hogben who has been a rock of support and oodles of fun (as well as a great housemate) over the last four years; Amy Taylor who has learnt more about chemistry than I am sure she ever wanted to know, and who is always around when there are japes to be had; Sam Roots for all the London larks and general frivolity; Andrew Seel for *always* making me laugh; Kelly-Anne Ferguson and Alice Bowen for good soup conversation; Ishmael Roslan for being a wonderful, understanding friend over so many years; Yang for, well, *everything*, especially the martinis, Bach and Zuleika moments; James Lamming for all the good times, and for commiserating over the first year blues; Jonathan Griffiths and the TUBAsoc boys for the Cotswold hikes; Nick Coyle for sarcasm over the years, and for letting me crash his home; David Longworth for hugs mainly; Leila Battison for all the work on the best science magazine Oxford has ever seen; Tim Funnell for being plain entertaining; Laura Best (ooops, Richards) and Catherine Mather who have been there for me since I was four years old and who I hope will be there for many, many years to come; the Worcester MCR gang (Filip Rindler, John Pearson, Jason Lee, Emily Parker and the others) who made me feel so welcome; everyone at Merton for making me feel like I never left, and *finally* a big thank you to all those other chaps who have made life sparkle.

Finally, I couldn't have done any of this without my family who have always been there for me. Sybilla and Chris (mum and dad) THANK YOU, especially for helping me through the tough times, as well as celebrating the good. Abi, Andrew and baby Amara — thanks for helping me to keep life in perspective. Gram — thanks so much for the chats, the laughs and for making things seem OK even when I haven't a clue if they are. Uncle Povl — thanks for helping me deal with the stresses and strains of a doctorate. Finally, thank you to Nan and Pop who aren't here anymore to read this, but who gave me so much love and support, and who I miss so much.

Contents

Abbreviations

A	Absorbance
α	Twist angle
Ac	Acetyl
acac	Acetylacetonate
aq	Aqueous
ALD	Atomic layer deposition
AM	Air mass
Ar	Aryl
ATR	Attenuated total reflectance
BAHA	Tris(4-bromophenyl)aminium hexachloroantimonate
bipy	4,4'-Bipyridine
B3LYP	Becke, three parameter, Lee-Yang-Parr
BODIPY	Boron-dipyrromethene
br	Broad
BuLi	n-Butyllithium
CDCA	Chenodeoxycholic acid
CEP	Compact effective potential
χ^n	n^{th} order macroscopic susceptibility
CSD	Cambridge structural database
d	Doublet
1D	One dimensional
2D	Two dimensional
dba	Dibenzylideneacetone
DCE	1,2-Dichloroethane
DCM	Dichloromethane
DDQ	2,3-Dichloro-5,6-dicyano-*p*-benzoquinone
DEPT	Distortionless enhancement by polarisation transfer
DFT	Density functional theory
DMF	Dimethylformamide
DMPU	1,3-Dimethyl-3,4,5,6-tetrahydro-2(1H)-pyrimidinone
DOSY	Diffusion-ordered spectroscopy
dppf	1,1'-Bis(diphenylphosphino) ferrocene
DSSC	Dye-sensitised solar cell
E	Electrode potential
E_0	External electric field
E_{CB}	Conduction band potential
E_{g}	Energy gap (as defined in text)
E_1^{ox}	First oxidation potential
E_1^{red}	First reduction potential
ε	Extinction coefficient
ε_0	Vacuum permittivity
η	Overall solar-to-electrical energy conversion efficiency
η_c	Efficiency of charge collection
ESA	Excited state absorption
ESI	Electrospray ionisation
Et	Ethyl
Fc	Ferrocene
FET	Field effect transistor
FF	Fill factor
FTO	Fluorine doped tin oxide
fwhm	Full width at half maximum

ΔG^0	Standard Gibbs free energy change
$\Delta G^{\#}$	Gibbs energy of activation
h	Planck's constant
HAT	Hexaazatriphenylene
HBC	Hexabenzocoronene
HMBC	Heteronuclear multiple bond coherence
HMPA	Hexamethylphosphoramide
HOMO	Highest occupied molecular orbital
IC	Internal conversion
I_{in}	Intensity of incident light
INDO	Intermediate neglect of differential overlap
IPCE	Incident photon to current conversion efficiency
IR	Infrared
ISC	Inter-system crossing
J_{mp}	Current at maximum power output
J_{SC}	Short circuit current
k_B	Boltzmann constant
k_{et}	Rate of electron transfer
λ	Wavelength in the context of light, reorganisation energy in the context of electron transfer
λ_i	Inner reorganisation energy
λ_s	Outer reorganisation energy
LED	Light-emitting diode
LHE	Light harvesting efficiency
LiHMDS	Lithium hexamethyldisilazide
LUMO	Lowest unoccupied molecular orbital
μ	Charge carrier mobility
m-	Meta
m	Multiplet in the context of NMR spectroscopy, medium in the context of IR spectroscopy
M	Molarity
MALDI	Matrix-assisted laser desorption ionisation
Me	Methyl
m.p.	Melting point
MPN	2-methoxypropionitrile
MS	Mass spectrometry
MSA	Methane sulfonic acid
N	Number
N_A	Avogadro constant
NBS	*N*-bromosuccinimide
Nd:YAG	Neodymium-doped yttrium aluminium garnet
NHE	Normal hydrogen electrode
NIR	Near infrared
NLO	Nonlinear optical
NMR	Nuclear magnetic resonance
NOESY	Nuclear Overhauser effect spectroscopy
NREL	National renewable energy laboratory
o-	Ortho
OD	Optical density
OPA	One photon absorption
OTFT	Organic thin-film transistor
p-	Para
p-chloroanil	Tetrachloro-1,4-benzoquinone

p-TsOH	*p*-Toluenesulfonic acid
PAH	Polycyclic aromatic hydrocarbon
PDT	Photodynamic therapy
PET	Petroleum ether
φ_{inj}	Quantum yield of electron injection
PIFA	Phenyliodine(III) bis(trifluoroacetate)
PM3	Parametric method 3
$P_{(\omega)}$	Polarisation (at frequency ω)
ppm	Parts per million
PR-TRMC	Pulse-radiolysis time-resolved microwave conductivity
q	Electronic charge
ref	Reference
RSA	Reverse saturable absorption
RT	Room temperature
s	Singlet in context of NMR spectroscopy, strong in the context of IR spectroscopy
σ	Conductivity in the context of electronics, absorption cross section in the context of photochemistry
S_n	Singlet state n
SEC	Size exclusion chromatography
S_N2	Biomolecular nucleophilic substitution
SPhos	2-Dicyclohexylphosphino-2',6'-dimethoxybiphenyl
t	Triplet
t	Intermolecular transfer integral in the context of organic electronics, tertiary in the context of molecular structure
T	Temperature
T	Triphenylene
T_n	Triplet state n
TBAF	Tetrabutylammoniumfluoride
4TBP	4-*Tert*-butyl pyridine
TEG	Triethylene glycol
Tf	Triflate
TFA	Trifluroacetic acid
THF	Tetrahydrofuran
THS	Trihexylsilyl
TIPS	Triisopropylsilyl
TLC	Thin layer chromatography
TOF	Time of flight
TPA	Two photon absorption
UPS	Ultraviolet photoelectron spectroscopy
v_d	Drift speed of charge carriers
UV	Ultra-violet
Vis	Visible
V_{mp}	Voltage at maximum power output
V_{OC}	Open circuit voltage
w	Weak
ΔX	Lateral displacement
ΔZ	Horizontal displacement

Chapter 1: Introduction

This chapter examines the electronic structure of large π-systems and explores the optical and electronic properties which arise from extensive electronic delocalisation. The potential application of such systems for charge transport, near-IR absorption, nonlinear optics and photovoltaic devices is discussed and porphyrins are introduced as versatile building blocks for such expanded aromatic systems.

1.1 Background

In the 21st century we are becoming increasingly interested in a huge range of optoelectronic devices which incorporate organic materials, including light-emitting diodes, dye-sensitised solar cells, and thin film transistors. Compared to inorganic materials, organic systems have many advantages including increased processability, reduced costs and improved speed. As a result, the development of new organic compounds with unusual optoelectronic properties has gained a great deal of interest in recent years.

In order to develop new organic materials for optoelectronic devices, it is important to understand structure-property relationships underlying behaviour such as charge transport and light absorption in an organic material. This introduction aims to explore the origin of optoelectronic properties in large π-systems, focussing on the structure-property relationships which make these systems suitable for applications as near-IR dyes, liquid crystalline semiconductors, dyes for photovoltaic devices and dyes for nonlinear optics. This investigation will provide the basis for the design of a new family of organic compounds with extended π-conjugation which may be expected to display properties suitable for many of the above applications. Exploration of the synthetic routes towards these novel compounds will be the primary focus of this thesis.

1.2 Structure-Property Relationships of Materials for Organic Electronics

1.2.1 Electronic Structure of Organic Materials

Organic molecules may display two types of covalent bonds: σ-bonds and π-bonds. σ-Bonds are formed when s-orbitals, hybridised orbitals, or p-orbitals of two atoms point directly at each other along the inter-atom axis, and overlap. This gives rise to the formation of two molecular orbitals: a bonding orbital which, if filled, experiences a region of maximum electron density between the two atomic nuclei, and an antibonding orbital which, when occupied, experiences an internuclear space largely devoid of electron density (Figure 1.1).

Only when there are a greater number of electrons in the bonding orbital than the antibonding orbital will a bond be formed between the two atoms.

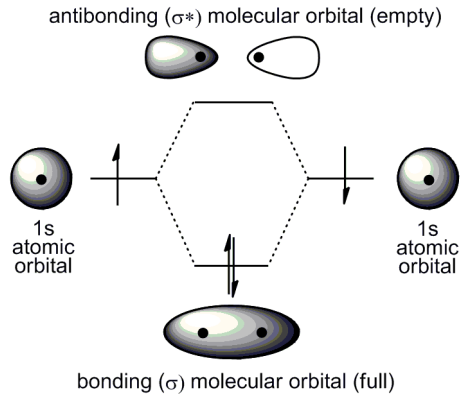

Figure 1.1: Molecular orbital diagram representing the formation of σ-bonding and antibonding molecular orbitals from two 1s atomic orbitals.

The connectivity of the atoms in most carbon-based organic compounds is defined by orbital overlap of adjacent atoms to form relatively stable σ-bonds. The energy required to promote an electron from the bonding to the antibonding levels (and hence cause bond cleavage) is much higher than typical energy fluctuations at ambient conditions e.g. room temperature and daylight (~0.02 — 3 eV).[1,2] For example diamond consists of a giant structure of carbon atoms, each coupled together by four σ-bonds formed from sp^3 orbitals. In such an extended lattice, the large number of bonding molecular orbitals with a distribution of energies form a filled 'band' called the 'valence' band, while the many high energy antibonding molecular orbitals form an unfilled 'conduction' band. In diamond, the energy gap between these two bands is 5.5 eV.[3] This large energy gap means that, at ambient conditions, there is practically no occupation of the σ^* molecular orbitals composing the conduction band, and hence no 'free' electrons or holes available to move through the structure. This results in the observation that organic molecules containing only σ-bonds are usually insulators.[1] In contrast, inorganic silicon crystals have a much smaller energy gap between the valence and conduction bands of just 1.1 eV, which is within the energy range of daylight and ambient room temperature. This means that some electrons are promoted into the σ^* orbitals generating partially filled valence and conduction bands — the key requirement for electron movement, and hence charge conduction, through the lattice. Furthermore, the number of electrons and holes available can be tuned by a process called

doping (see Section 1.2.2) to increase the conductivity of the material. These properties of silicon have led to its widespread use as an inorganic semiconductor in an enormous range of devices.

In contrast to σ-bonds, π-bonds are formed by the overlap of p-orbitals (on adjacent atoms) which lie at 90° to the inter-atom axis. This results in the creation of molecular orbitals which are orthogonal to the sigma framework (Figure 1.2). The overlap between a pair of neighbouring orbitals is weaker for a π-bond than for a σ-bond, hence the energy gap between the bonding and antibonding orbitals is smaller for the π-bond.

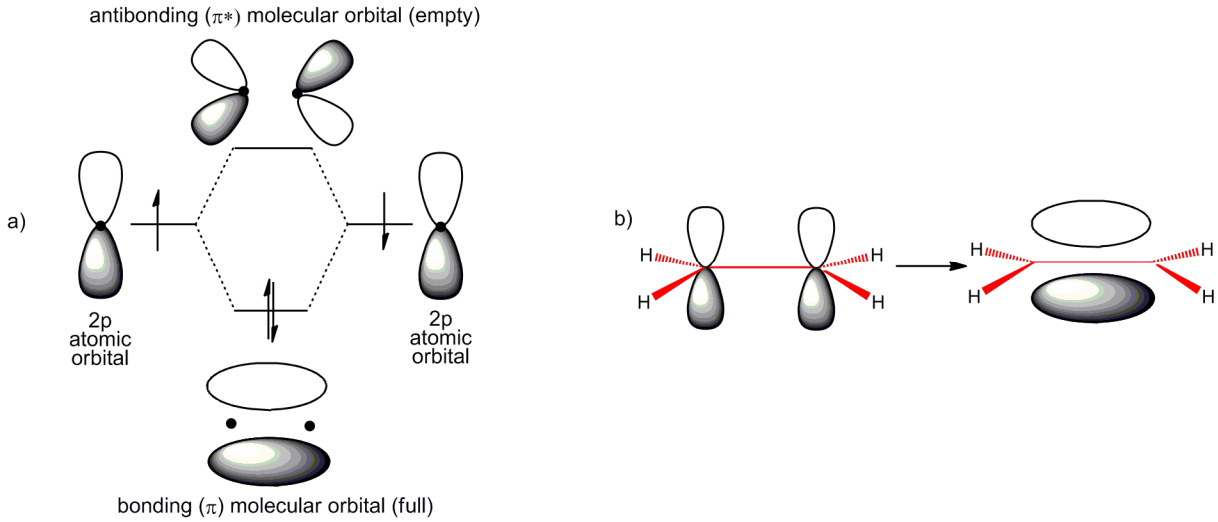

Figure 1.2: a) Molecular orbital diagram representing the formation of π-bonding and antibonding molecular orbitals from two 2p atomic orbitals, b) Diagram showing the formation of a π–bond in ethene, illustrating the orthogonal arrangement of the π-orbital and the sigma bonded framework (shown in red).

If two π-bonds are separated by a single σ-bond, and both exist in the same plane (i.e. the system is not twisted), they are said to be conjugated. This means that all four p-orbitals involved in the two bonds interact with each other, forming one large molecular orbital. This conjugation can only occur if all of the p-orbitals are parallel so that each p-orbital is able to overlap with the p-orbital on the next atom; as a result, planarity of the system greatly facilitates conjugation.

Increasing the number of conjugated double bonds in a polyacetylene system affects the energies of the molecular orbitals, as shown in Figure 1.3. When N atomic orbitals overlap, N molecular orbitals are formed, each of which can accommodate two electrons. In

the case of butadiene, the four p-orbitals interact to form four molecular orbitals. Since butadiene has four electrons in the π-system, only the two lowest energy (bonding) molecular orbitals are filled. Overall, the combined energy of these two bonding molecular orbitals for butadiene is lower than for twice the energy of an ethene bonding orbital, hence a system with conjugated double bonds is more thermodynamically stable than a system with the same number of isolated double bonds.

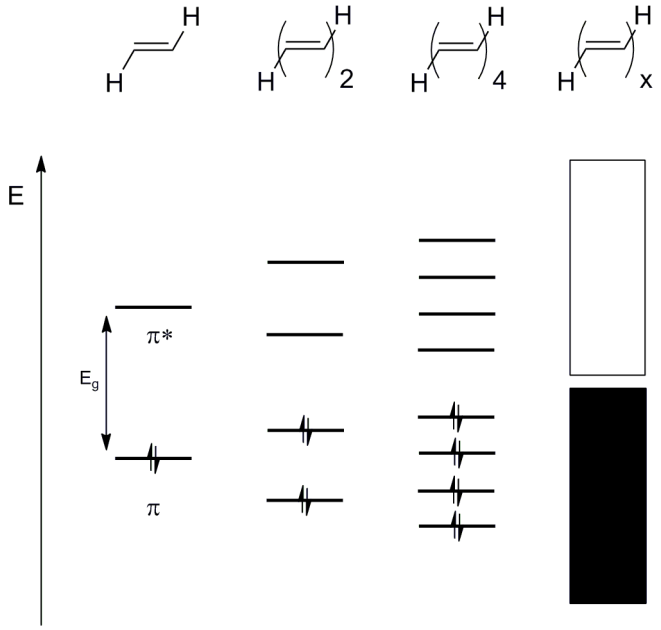

Figure 1.3: A simplified schematic molecular orbital diagram to show the effect of increasing the number of conjugated π-bonds on the molecular orbitals of a linear polyacetylene system.

Furthermore, it can be seen from Figure 1.3 that the HOMO of butadiene is higher than that for ethene, while the LUMO of butadiene is lower than for ethene. The same trend is observed on going from butadiene to octatetraene. This demonstrates that increasing the degree of π-conjugation decreases the HOMO-LUMO gap (E_g) of the system.

As the polyacetylene chain length increases, the number of molecular orbitals gets larger and larger and the energy gap between them decreases such that the bonding molecular orbitals form a valence band, while antibonding orbitals form a conduction band. It may be expected that for a polyacetylene chain of infinite length, the huge number of bonding and antibonding molecular orbitals present would result in overlap of the valence and conduction bands resulting in the formation of one broad π-electron band (E_g = zero),

half filled with electrons.[1] This system would be predicted to behave as a 1D metal, as the minute energy gap between the molecular orbitals would mean that some electrons would always populate the higher energy levels of the band creating 'free' holes and electrons which may travel through the structure. In fact, polyacetylene does not exhibit an E_g of zero, as shown by the small gap between the valence band (black) and the conduction band (white) in Figure 1.3. This energy gap exists because carbon-carbon bond lengths in polyacetylene are not identical for all the carbon-carbon bonds in the conjugated chain; the occurrence of this bond length alternation is called the Peierls Distortion.[4] As a result, polyacetylene behaves not as a metal, but as an organic semiconductor.

1.2.2 Charge Transport in Organic Semiconductors

With the components of integrated circuits becoming smaller all the time, the concept of molecular electronics has become increasingly popular, and is expected to play a key role in future data transportation, processing and storage.[5] Since the first iodine doped, polyacetylene crystalline films were investigated by Nobel laureates Heeger, MacDiarmid and Shirakawa in the 1970s,[6] this new field of organic electronics has led to the development of a large range of conjugated oligomers, polymers and small molecules which exhibit high charge mobilities in the solid state. Such systems combine the electronic properties of semiconductors with the advantages of low cost, structural flexibility and processibility displayed by organic compounds.[7] In addition, the development of individual conjugated oligomers as 'molecular wires' could lead to systems capable of connecting molecular scale (nm) electronic components.[8]

The conductivity of a semiconductor increases upon thermal or optical excitation to give values between that of good conductors ($10^6\ \Omega^{-1}\ cm^{-1}$) and good insulators ($10^{-5}\ \Omega^{-1}\ cm^{-1}$).[2] The conductivity ($\sigma$) of a material is defined as

$$\sigma = qN\mu$$

where q is the electronic charge of the mobile charge carrier, N is the number of charge carriers per unit volume and μ is the charge carrier mobility (in $cm^2/(V\ s)$).[1] The addition of a

small amount of a specific impurity to a semiconductor is called doping, and increases conductivity by increasing the number of charge carriers in the system. Indeed the conductivity of polyacetylene has been seen to increase greatly from 4.4×10^{-5} Ω^{-1} cm^{-1} to 20,000 Ω^{-1} cm^{-1} in stretch-oriented thin films upon doping with iodine.[9,10] Such doping is often necessary as pure semiconductors have very small charge carrier concentrations at ambient temperatures.

Charge carrier mobility is defined as

$$\mu = \frac{v_d}{E_0}$$

where v_d is the drift speed of the charge carriers and E_0 is the external electric field. Charge carrier mobility depends upon many factors including structural ordering of the material, which affects the electronic interactions between adjacent molecules and hence both the mechanism and speed at which the charge carriers move through the material.

While inorganic semiconductors such as silicon are formed from single giant covalent structures, organic semiconductors are usually based upon molecular solids, composed of discrete units which are bound together in the solid state by weak intermolecular forces such as van der Waals interactions.[11] The mechanism of charge transport along individual conjugated polymer chains has been the focus of many studies and has been found to depend upon several parameters including the dopant levels and degree of structural order.[12-14] However since the distances between electrodes in devices such as field effect transistors (FETs) and photovoltaic cells are on the scale of tens to hundreds of nanometres,[14] charge transport between molecules is necessary to achieve good conduction through the organic material. It has been found that the nature of this charge transport depends greatly upon the packing of molecules. Band structure may exist in some carefully grown, highly ordered organic single crystals at low temperature, due to the interaction of the π-systems of adjacent molecules which form new bonding and antibonding molecular orbitals which extend across the whole crystal.[15] However the weakness of such intermolecular interactions, combined with the presence of defects, often results in the formation of very narrow bands, inhibiting charge transport between molecules via charge-carriers in

delocalised states.[1] In addition, the levels of disorder present in solution processed materials such as polymers and liquid crystals means that charge transport through these materials seldom occurs via a band-like mechanism.[14,16,17]

Instead, many organic semiconductors undergo charge transport by a 'hopping' mechanism whereby charge carriers are localised on individual molecules and jump from molecule to molecule.[17] The rate of this charge hopping between adjacent molecules may be estimated from the semiclassical Markus electron transfer equation:

$$k_{et} = \left(\frac{4\pi^2}{h}\right) t^2 (4\pi\lambda k_B T)^{-0.5} \exp^{[(-\Delta G^0 + \lambda^2)/4\lambda k_B T]}$$

where t is the intermolecular transfer integral, λ is the total lattice/nuclei and surrounding media reorganisation energy, and ΔG^0 is the standard Gibbs free energy change from the initial to the final states. In a self-exchange electron transfer process between two molecules, both the initial and final states consist of one charged and one neutral molecule, therefore $\Delta G^0 \approx 0$. However for electron transfer to occur, the system must go through a transition state, where $\Delta G^{\#}$ represents the Gibbs activation energy to reach this state (Figure 1.4).

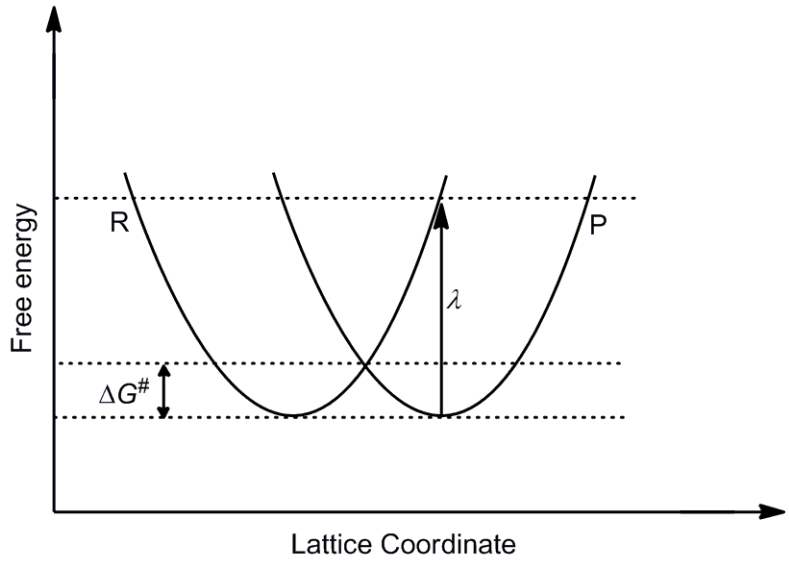

Figure 1.4: Schematic diagram showing potential energy surfaces for a self-exchange electron transfer process between reactants (R) and products (P) ($\Delta G^0 = 0$). The Gibbs activation energy, $\Delta G^{\#}$, required to reach transition state is shown as well as the reorganisation energy, λ.

From the semi-classical Markus equation above it can be deduced that the fastest rates of charge transport occur for systems with small reorganisation energies and large transfer integrals. The reorganisation energy of a system is made up of two terms, the outer reorganisation energy (λ_s) and the inner (intramolecular) reorganisation energy (λ_i). The outer reorganisation energy arises from changes in the electronic polarisation and orientation of surrounding media, such as solvent molecules, upon electron transfer between the organic semiconducting units. This parameter, λ_s, is expected to display little sensitivity to the chemical structure of the molecules involved in charge transfer, hence it will not be considered further here. The inner reorganisation energy arises from the change in equilibrium geometry of the donor and acceptor molecules upon electron transfer and has been shown to vary with $1/N_\pi$ where N_π is the number of atoms involved in the π-system of the molecule.[18,19] The inner reorganisation energy therefore provides a direct link between the geometrical and electronic structure of the molecules and the charge transport observed for the system.[18-20] In order to minimise λ_i, it is desirable that the molecules involved in electron transfer exhibit a rigid geometry, together with highly delocalised frontier molecular orbitals (to the spread of geometrical distortions and changes in charge density over the whole molecule). The importance of these factors has been shown by both theoretical estimates of the internal reorganisation energies and gas-phase ultraviolet photoelectron (UPS) spectra of a series of oligoacenes, whereby a decrease in λ_i (for hole transport) was found on moving from naphthalene (0.187 eV) to anthracene (0.137 eV) to tetracene (0.113 eV) to pentacene (0.97 eV).[7,18,21,22] This decrease in λ_i reflects the greater degree of rigidity in the oligoacenes as size increases, together with a larger area over which to spread the necessary geometrical strain.[7]

The intermolecular transfer integral, t, is a measure of the strength of electronic interaction between two adjacent molecules. A common approximation of this value may be made by considering a dimer composed of two neutral molecules held together by non covalent intermolecular interactions e.g. van der Waals forces or π-stacking. Theoretically, interaction of the HOMO (or LUMO) energy levels of the two molecules would cause these energy levels to split, creating a stabilised level (the dimer HOMO-1 level) and a destabilised

level (the dimer HOMO level). In the case of LUMO interactions to create the LUMO/LUMO+1 levels, a smaller interaction is observed.[23] By halving the magnitude of this calculated energy gap between the HOMO and HOMO-1 levels of the dimer, the value of the intermolecular transfer integral may be estimated for hole transport.[23-26] Using quantum mechanical calculations it is possible to examine the size of this splitting as a function of the relative positions of the interacting units.[23] It has been found that intermolecular transfer integrals depend greatly upon the size of the interacting conjugated systems, their relative orientations and the shape of their frontier electronic wavefunctions which govern the nature of the bonding or antibonding interactions. Hence it may be deduced that the transfer integral of an organic semiconductor depends greatly on the nature of the molecular packing; the greater the level of disorder and the larger the intermolecular distance, the smaller the transfer integral and the lower the rate of electron hopping — these factors are discussed in more detail in Section 1.2.3. In the case of single molecule molecular wires, usually conjugated oligomers, this charge transfer parameter manifests itself in the degree of electronic communication between monomer units in the chain.

The two parameters, reorganisation energy and intermolecular transfer integral, are often interlinked. Anderson and co-workers demonstrated this principle by investigating charge transport along 'molecular wires' consisting of porphyrin oligomers (**1**, Figure 1.5).[26,27] The porphyrin units in these long chains experience π-conjugation through the butadiyne linking groups, however the porphyrin units are free to rotate about the molecular axis. The low energy barrier to this rotation means that there is a broad distribution of dihedral angles between porphyrin units in the molecular wire at room temperature, hence the planarity, and therefore conjugation, of the 'wire' is disrupted. Upon coordination of 4,4′-bipyridine (Bipy), a double-strand ladder complex forms (**2**) in which the porphyrin units are locked in a planar arrangement.

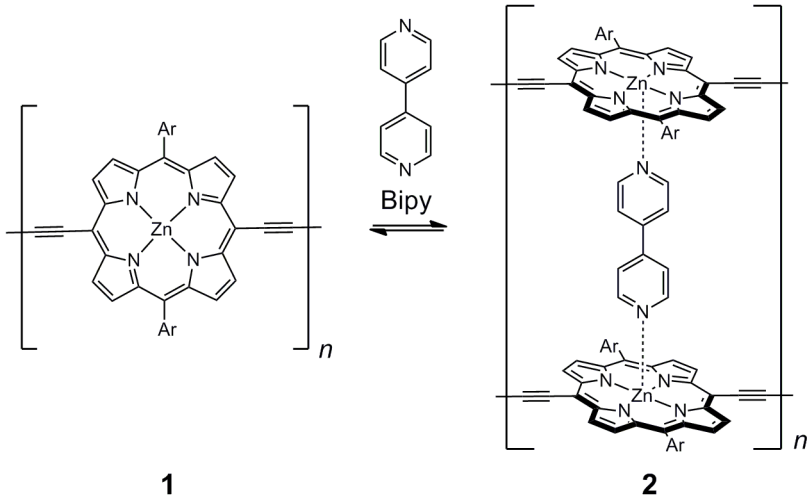

Figure 1.5: Formation of double stranded porphyrin ladders (**2**) upon addition of 4,4′-bipyridine (Bipy) to porphyrin oligomers (**1**). Ar = 3,5-bis(trihexylsilyl)phenyl.[27]

This rigidification has been shown to have a large impact on the charge carrier mobilities of the polymers. Uncomplexed, free single strands of the polymer were found by pulse-radiolysis time-resolved microwave conductivity (PR-TRMC) to have charge carrier mobilities of 0.084 $cm^2/(V\ s)$, however upon formation of the ladder complex, this value increases by an order of magnitude to 0.91 $cm^2/(V\ s)$. Planarisation of the porphyrin units may be expected to increase the transfer integral between adjacent porphyrins due to greater orbital overlap, however calculations show that this effect would result in an increase in charge carrier mobility by only a factor of four. The ten-fold increase in charge mobility observed is therefore likely to be due to a combination of this increased transfer integral, together with a reduction in the number of degrees of freedom experienced by the porphyrin oligomers upon ladder formation which greatly reduces the reorganisation energy of the system.[27]

Conjugated polymers with linear π-systems such as polyacetylene and poly(*p*-phenylene) have long been explored for use as organic semiconductors. The highly regular packing of molecules, together with the low defect concentration, makes single crystals of such organic π-conjugated systems highly attractive materials for charge transport. However, growth of these single crystals can be challenging, expensive and their small, fragile nature can cause difficulties in handling and manipulating the crystals for use in devices such as organic thin film transistors (OTFTs).[16,28] However, the alternative

approach, involving solution processed materials, may suffer setbacks due to the low solubility of the organic polymers. The addition of substituents to the conjugated backbone of the polymer may increase its solubility, however steric interactions between these side groups often lead to distortions from planarity and hence a loss of conjugation along the polymer, leading to charge localisation.[29] In terms of the Markus equation, this can be envisaged as decreasing the transfer integral between units in the chain and raising the reorganisation energy of the system, thereby increasing the activation energy for charge transport. In addition, the packing between molecules in solution processed conjugated polymers is often highly disordered and contains defects, resulting in charge mobilities ranging from just 0.009 to 0.125 $cm^2/(V\ s)$,[30] far lower than the values observed for single crystals (single crystals of rubrene, for example, may show charge carrier mobilities of up to 20 $cm^2/(V\ s)$ at room temperature).[16] Hence there is a strong need for materials which may be solution processed yet still exhibit order in the solid state to provide significant charge carrier mobilities — liquid crystals are one class of such materials which show great promise in this area.

1.2.3 Discotic Liquid Crystals for Charge Transport

The discovery of discotic liquid crystals in 1977 opened up a whole new class of organic semiconductors.[31] These systems, based upon the stacking of discotic molecules, or 'mesogens', with large π-conjugated cores (often aromatic in nature), have shown potential as semiconductors in field effect transistors (FETs),[32] light-emitting diodes (LEDs)[33] and photovoltaic solar cells.[34]

The discotic mesogens which make up these systems bear long alkyl chains attached to the core periphery. These chains convey solubility to the molecules in organic solvents, facilitating processability, and are essential to the formation of liquid crystalline phases. Little energy is required to facilitate conformational disorder, or 'side chain melting', in these substituents, causing disruption in the molecular packing of the crystalline phase. However, the strength of interaction between the aromatic cores is not disrupted at such

temperatures. As a result the system retains partial crystalline nature — a liquid crystalline phase is formed.

The self assembly of conjugated disc-shaped molecules into extended columnar stacks has been shown to enable efficient charge transport along the columnar axis, with the highest charge carrier mobility values ranging from 0.2 — 1.3 $cm^2/(V\ s)$.[30,35,36] Furthermore, columnar liquid crystals exhibit long range order and are able to self-heal structural defects due to the dynamic nature of the system. In addition, thermal annealing of columnar liquid crystalline phases has been shown to increase charge carrier mobility due to improved structural order.[37] These properties, together with simpler purification (due to the low molecular weight of the discotic mesogens) and processibility of the materials, make columnar liquid crystals based on discotic molecules attractive alternatives to single crystal or solution processed conjugated polymers and oligomers for charge transport.

Self assembly of discotic molecules into columnar stacks is driven by π-stacking interactions. Hence large, aromatic cores of discotic, or near-discotic, shape such as triphenylene (**T**), phthalocyanine (**3**) and perylene (**4**), are excellent candidates for forming the basis of columnar liquid crystals due to their rigidity, planarity and large numbers of π-electrons (Figure 1.6).[14,38]

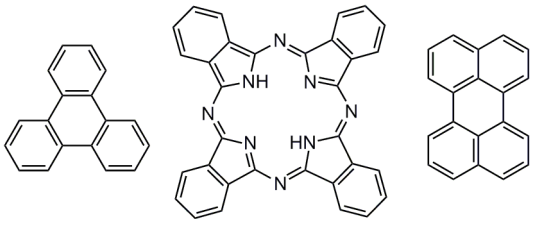

T 3 4

Figure 1.6: Some examples of widely studied core units for columnar liquid crystals.[38]

The mechanism of charge transport along the columnar axis of a discotic liquid crystal depends upon the packing of the discotic mesogens and the degree of structural disorder within the system. However, the magnitude of measured charge mobilities along liquid crystalline stacks implies that charge transport in these systems usually occurs by the hopping mechanism, as discussed in Section 1.2.2.[14,17,24,39] As such, charge carrier mobilities are strongly influenced by the degree of electronic coupling between the π-orbitals of

adjacent molecules in the column, i.e. the intermolecular transfer integral, and the magnitude of the internal reorganisation energy of the system.

The transfer integral of the π-stacked columnar system depends upon the intermolecular distance, the twist angle and the lateral displacement of adjacent mesogens (Figure 1.7).

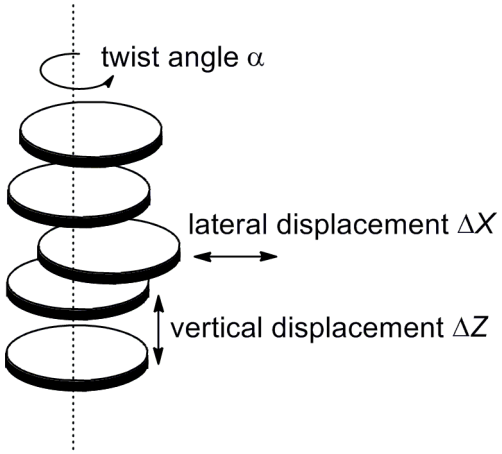

Figure 1.7: Schematic representation of a columnar stack of discotic mesogens, with disorder due to different twist angles (α), vertical displacements (ΔZ) and lateral displacements (ΔX).[25]

The effect of these three parameters on the magnitude of the calculated HOMO and LUMO splittings (and hence intermolecular transfer integrals) in dimers of triphenylene (**T**), hexaazatriphenylene (**HAT**) and hexabenzocoronene (**HBC**) molecules (Figure 1.8), has been investigated using quantum mechanical calculations.[24,25,39]

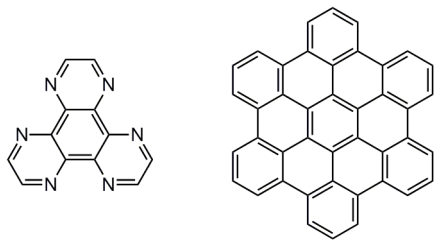

Figure 1.8: Hexaazatriphenylene (**HAT**) and hexabenzocoronene (**HBC**) molecules.

It is seen that, for a dimer comprised of two **T**, **HAT** or **HBC** molecules superimposed directly over each other, the magnitude of the splittings decays exponentially with an increase in vertical displacement, ΔZ, from 3.1 to 4.1 Å.[24] This may be rationalised by a

decrease in transfer integral due to a reduction in π-orbital overlap as two molecules are drawn apart. However for small fluctuations in distance (~0.1 Å), the decrease in HOMO or LUMO splittings is not large (~20%) and the magnitude of the transfer integrals is not greatly affected.[24]

The magnitude of the twist angle, α, of one molecule with respect to another was investigated for **T**, as well as for **HBC**. In contrast to intermolecular distance, it can be seen that fluctuations in this parameter have a large impact on the size of the HOMO and LUMO splittings (Figure 1.9).[24,25,39] For all of these molecules, the magnitude of the electronic splitting was seen to be greatest for cofacial conformations; any twist between the two molecules away from such an arrangement is therefore seen to decrease the transfer integral and hence would be predicted to decrease charge mobility in the system.

Figure 1.9: Change in HOMO splittings in a dimer composed of two triphenylene (**T**) (squares) or hexabenzocoronene (**HBC**) molecules (triangles) as a function of twist angle (α). Measurements were made by two difference quantum mechanical approaches: Blue lines correspond to calculations made using the semiempirical intermediate neglect of differential overlap (INDO) Hamiltonian, while red lines correspond to values based on twice the charge transfer integral calculated at the density functional theory (DFT) level.[24]

It can be seen from Figure 1.9 that the symmetry of the mesogen plays a role in determining the relationship between the magnitude of electronic splitting and the twist angle. In the case of **T**, which has D_{3h} symmetry, one explanation is that rotation of one molecule by 60° corresponds to poor spatial overlap of the π-systems in the dimer, with the external rings of one molecule sitting above the gaps in the other. However, this explanation is far too simplistic and does not correlate well with the twist angle dependence of electronic

splitting observed for **HBC**. Here the D_{6h} symmetry of the **HBC** molecule means that a cofacial conformation in the dimer is regained after rotation of one molecule through a twist angle of 60°, rather than 120° as required for the same effect to be achieved for the **T** system. Hence the oscillations observed for **HBC** in Figure 1.9 occur at twice the frequency of those for **T**. However, the size of the **HBC** π-system indicates that appreciable overlap of the π-orbitals in the dimer may still be expected even when the molecules are twisted with respect to each other by 30°, yet as shown in Figure 1.9, a dramatic decrease in electronic splitting is observed in this case.[24] For a phthalocyanine core (**3**) (Figure 1.10),[40] splitting maxima are observed at both multiples of 90° (corresponding to a cofacial arrangement) *and* at 45° (corresponding to a twisted arrangement) with the splitting slightly larger in the former case. This seems at odds with the angle dependence of splitting energy observed for the large π-system of **HBC**, highlighting that symmetry considerations alone are not sufficient to explain the observed fluctuations in splitting energy.

From these examples it is therefore clear that the magnitude of the electronic splitting, and hence the transfer integral, depends not only on the size of the conjugated π-system involved and the shape of the molecule but also, critically, on the shape of the frontier electronic wavefunctions of the system which can only be determined by quantum mechanical analysis.

Figure 1.10: INDO calculated HOMO (squares) and LUMO (triangles) splittings for a dimer made of two phthalocyanine (**3**) molecules with increasing twist angle α (rotation angle) at a fixed intermolecular distance.[40]

The dependence of electronic splitting on the lateral displacement (ΔX, Figure 1.7) has also been investigated for **T** and its derivatives as well as for **HBC** molecules.[24,25,39] Figure 1.11(a) shows the change in HOMO splittings with lateral displacement for **HBC** and **T** where the twist angle between two molecules in the dimer is 0°, while Figure 1.11(b) shows the correlation of these parameters for a dimer of **T** with a twist angle of 60°.[24]

Figure 1.11: Change in HOMO splittings in a dimer composed of two triphenylene (**T**) (squares) or hexabenzocoronene (**HBC**) molecules (circles) as a function of lateral displacement at a fixed intermolecular distance. a) for **HBC** and **T** dimers in a cofacial conformation (twist angle = 0°), b) for **T** dimer with a twist angle of 60°.[24]

It can be seen that both **HBC** and **T** dimers (where the twist angle between the molecules is 0°) display a decrease in HOMO splitting upon translation of one molecule with respect to the other. This reduction is far more pronounced in the case of **T** than for **HBC**, presumably because the larger π-system of **HBC** means that the *relative* decrease in orbital overlap upon translation is much less than for the smaller, lower symmetry, π-system of **T**. In addition, Figure 1.11(b) shows that lateral displacement does not always lead to a decrease in electronic splitting. In the case where two **T** molecules exhibit a twist angle of

60°, lateral displacement in fact increases the electronic splitting, thereby increasing the intermolecular transfer integral.

As discussed in Section 1.2.2, smaller reorganisation energies favour a faster rate of charge transport through a system. Theoretical estimates for a series of oligoacenes has shown that reorganisation energies are smaller in the case of hole transport than electron transport.[18] This trend has also been observed for calculations performed on a series of aromatic cores which often constitute mesogens which display liquid crystalline phases, namely triphenylene (**T**), hexaazatriphenylene (**HAT**), hexaazatrinaphthylene (**HATNA**, Figure 1.12) and hexabenzocoronene (**HBC**).[24]

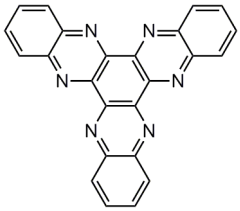

HATNA

Figure 1.12: Hexaazatrinaphthylene (HATNA).

In addition, HOMO splittings are usually larger than LUMO splittings for two interacting π-systems, indicating a larger charge transfer integral in the case of hole transport.[7] Together, these findings imply that charge transport between neighbouring π-systems is often more favourable in the case of hole transport than electron transport. It has also been shown that the larger the aromatic core, the smaller the reorganisation energy, with values decreasing from 0.3 to 0.14 to 0.10 eV for the reorganisation energies of **HAT**, **HATNA** and **HBC** respectively (in the case of hole migration).[24] The correlation between the size of the core π-system and the charge mobility through the columnar stacks has been investigated for a wide range of cores, with van de Craats and Warman proposing the empirical relationship

$$\Sigma\mu_{1D} = 3\exp(-83/n)\ \mathrm{cm}^2/(\mathrm{V\ s})$$

where $\Sigma\mu_{1D}$ is the mobility sum for holes and electrons along the columnar stacks and n is the number of carbon atoms in the aromatic core.[41] The value of 3 $cm^2/(V\ s)$ corresponds to the charge carrier mobility found for graphite (perpendicular to the plane of the graphene sheets) which is considered to be the maximum possible value for an aromatic system of infinite size. While this relationship suggests that increasing the core size will inevitably yield higher values for charge carrier mobilities, large π-systems may suffer from difficulties in synthetic accessibility and purification which limit these values. Müllen and co-workers encountered such problems when exploring the charge carrier mobilities of large π-systems based upon subunits of graphene (Figure 1.13).[42,43] These large liquid crystalline polycyclic aromatic hydrocarbon (PAH) systems show an increase in charge carrier mobility from 0.1 to 0.38 $cm^2/(V\ s)$ on moving from PAH **5** to PAH **6**, as expected due to the increase in the size of the π-system which may be expected to result in smaller reorganisation energies and greater column stability (due to larger van der Waals and π-π interactions). Larger PAHs such as **7** and **8** however, suffered from very poor solubility and hence were not possible to purify — this prevented the measurement of the charge carrier mobility values due to the sensitivity of conductivity towards the presence of trace inorganic impurities.

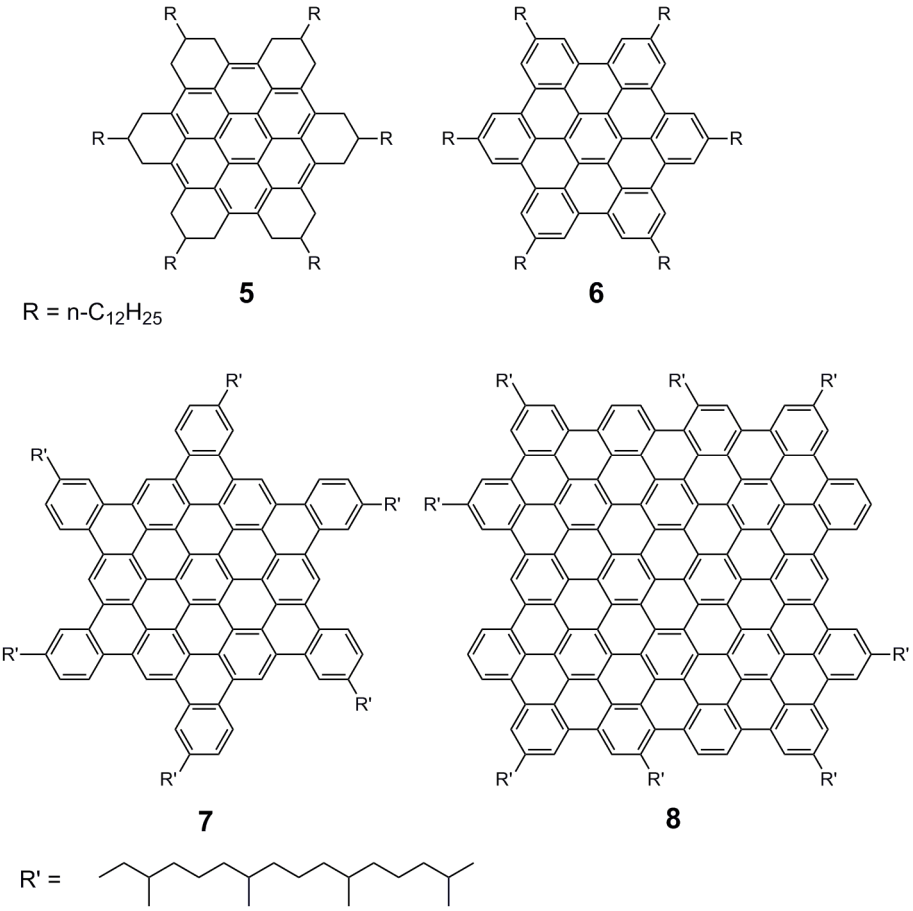

Figure 1.13 Chemical structures of disc-like PAHs synthesised by Müllen and co-workers.[42]

Many reviews have been published exploring the structure-property relationships which exist for columnar liquid crystals based upon discotic molecules.[38,44] It is important to stress that it is not just the aromatic core, but also the nature of peripheral substituents around the aromatic core, that determines the liquid crystalline behaviour of these discotic molecules, and their charge transport properties. In general it has been found that the longer the alkyl chain, the lower the temperature of transition between the crystalline and liquid crystalline phases due to the large degree of disorder conferred on the system by the chains.[45] Very long linear chains however can cause a reverse in this trend,[46,47] probably due to van der Waals interactions between the chains which become appreciable at high chain length. Branched alkyl chains do not exhibit as regular packing as linear chains, and hence they promote the conformational disorder necessary for a transition between crystalline and liquid crystal phases to occur.

The nature of the linking atom or group which separates the alkyl chain from the aromatic core has been demonstrated to have a profound effect upon charge transport in the system. While alkylthio substitutents have been shown to have little impact on charge mobility values, relative to the unsubstituted core, alkoxy chains have been shown to have a far larger effect, significantly reducing charge mobility values. Calculations have shown that this is due to the larger reorganisation energy exhibited by alkoxy substituted compounds, for example this energy increases from 0.18 to 0.33 eV on going from an unsubstituted triphenylene core to an OH substituted triphenylene core.[24] Such large increases in reorganisation energy are thought to be due to changes in packing upon charge transfer.

Stabilisation of the columnar stacks may also be affected by the nature of the peripheral substituents surrounding the mesogen core. For example, the use of substituents capable of undergoing hydrogen bonding interactions has been shown to increase column stability and hence increase charge transport in liquid crystalline systems.[45,48-52] In addition, the use of a phenyl linker instead of a CH_2 group between the core and the side chains, has been shown to increase the thermal stability of the liquid crystalline phase for substituted HBCs such as compound **6** (Figure 1.13).[43,53] In these phenyl substituted HBCs, the steric repulsion of the side groups prevents cofacial stacking, forcing the molecules to stack in a twisted geometry. This reduces the mobility of the mesogens, effectively 'locking' them into a particular position. The reduction in rotational and translational freedom of the discotic molecules, which arises as a consequence of this steric effect, stabilises the column leading to high charge carrier mobilities over a large temperature range, with values of 0.22 $cm^2/(V\ s)$ at 22 °C and 0.46 $cm^2/(V\ s)$ at 192 °C being recorded.[43] While the steric constraints exerted by peripheral substituents may stabilise columnar stacks in some instances, the influence on mesogen packing geometries can have an adverse effect on charge carrier mobilities. As with the phenyl-bearing HBC molecules, many discotic mesogens are forced to stack in a helical arrangement rather than a cofacial arrangement, such that the twist angle α (Figure 1.7) is greater than 0°, in order prevent steric clashes between the substituents.[45,54,55] This enforced twist can affect the magnitude of the charge transfer integrals (Figure 1.9 and 1.10), thereby

influencing charge transport in the system. Careful choice of the peripheral substituents can therefore allow the twist angle to be tuned to facilitate efficient charge transport.

The nature of the peripheral side chains around an aromatic core has also been shown to dictate whether it is electron or hole transport that occurs in the liquid crystalline phase.[56,57] Aida and co-workers have shown a fused metalloporphyrin dimer with semifluoroalkyl side chains on one porphyrin unit and triethylene glyocol (TEG) sides chains on the other, forms a liquid crystalline phase where electron mobility gives rise to a semiconducting character. In contrast, the fused porphyrin dimer with semifluoroalkyl side chains on both porphyrin units acts as a semiconductor due to hole transport.[56] This surprising influence of the side chains is thought to be due to the different twist angles they induce in the columnar stacks. As shown in Figures 1.9 and 1.10, the size of HOMO and LUMO splitting depends upon the twist angle; however the maximum splitting energies do not necessarily occur at the same angle for both HOMO and LUMO interactions. This means that in some cases the LUMO splitting at a given angle is larger than the HOMO splitting, thereby favouring electron rather than hole transport.[58]

The presence of substituents has also been shown to exert an insulating effect on the columnar stacks. Indeed, Müllen and co-workers have reported that the decay time of conductivity in liquid crystals depends exponentially on the effective diameter of the discotic molecules. The 'sheath' of alkyl chains inhibits charge recombination between adjacent columns such that these liquid crystals may be considered as one dimensional 'nanowires'.[59]

In conclusion, the efficiency of charge transport in discotic liquid crystals depends upon both the nature of the core and the choice of peripheral substituents. It has been shown that the intermolecular transfer integral in a columnar discotic liquid crystalline system shows a strong dependence on lateral displacement and twist angles between the π-conjugated cores of discotic mesogens, together with a weaker dependence on small fluctuations in vertical displacements. The magnitudes of these dependencies are based upon the size and symmetry of the core together with the shape of the frontier wavefunctions. Hence these relationships are not simple to predict from the molecular structure. It is notable however that the phthalocyanine core (**3**) exhibits large splitting

values (and hence large transfer integrals) over a wider range of twist angles than may be expected by comparison with calculations based on **HBC**. This suggests that charge transport in discotic liquid crystals based on similar π-systems, besides being expected to show a high efficiency when in a cofacial arrangement, may be predicted to display a low sensitivity towards the level of mesogen disorder. It has also been shown that the larger the π-system, the smaller the reorganisation energy of the mesogen upon charge transfer. In addition the larger the π-system, the greater the magnitude of van der Waals or π-stacking interactions between mesogens, thereby the greater the thermal stability of the column.[41] These factors imply that the fastest rates of charge transport may therefore be expected for mesogens with a core consisting of a large, rigid, circular π-system with near-planar geometry. In addition, the high energy HOMOs of these systems facilitate hole generation in the liquid crystalline material, while the low energy LUMOs are ideal for electron injection. Therefore, it is of great interest to explore the synthesis of new large aromatic π-systems with discotic or near-discotic shape and investigate their optical and electronic properties.

1.2.4 Large π-Systems for Near-IR Dyes

As seen in Section 1.2.1, increasing the degree of conjugation in a molecule reduces the HOMO-LUMO gap. As a result, light of lower energy (and hence longer wavelength) is required to promote an electron from the HOMO to the LUMO. Molecules with large π-conjugated systems are often coloured because the light is absorbed in the visible region. Figure 1.14 shows the structures of organic chromophores β-carotene (**9**) and octaethylporphyrin (**10**), which are orange and purple respectively, together with their pathways of conjugation. The absorption of light by such systems means that UV-vis-NIR spectroscopy can give a measure of the degree of π-conjugation in a system — the more red-shifted the absorption, the lower the energy of the HOMO-LUMO gap and hence the greater the extent of conjugation.

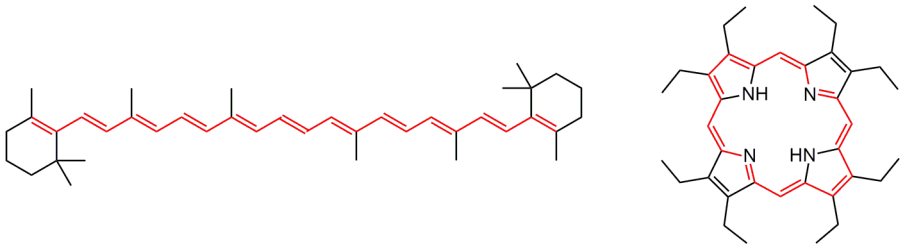

9 **10**

Figure 1.14: Organic chromophores β-carotene (**9**) and octaethylporphyrin (**10**). The pathway of conjugation is shown in red.

The decrease in HOMO-LUMO gap arises as a consequence of the raising of the HOMO energy level and lowering of the LUMO energy level with increased π-conjugation. This means that large π-systems not only require less energy to form an excited state, but are also generally easier to oxidise and reduce than smaller π-systems. Hence in the pursuit of large π-systems for charge transport, both the extent of near-IR absorption and the electrochemical properties of the material may be considered useful figures of merit to determine the suitability of a system for optoelectronic applications.

Chromophores which absorb light in the near-IR region (750 to 2500 nm) have become of increasing interest in recent years owing to their many and varied practical applications including laser printers, thermal writing displays,[60] infrared photography and optical recording devices for data storage.[60,61] In this latter application, the dye is spin-coated onto a plastic substrate and a near-IR laser (operating at 780 nm) is used to form micropits in the layer. In order to 'read' the information a second, low power, near-IR laser beam (at 830-840 nm) is directed at the substrate — the micropits in the dye layer cause variations in the reflection of the beam which are detected by a photodiode.[60]

Plasma display televisions, a common feature in many households, radiate near-IR light in the region of 850 — 1100 nm which can interfere with remote controlled devices. Coating of the television surface with a near-IR dye introduces an optical filter which reduces the transmission of this radiation by absorption.[62]

Biological uses of near-IR dyes include biomedical imaging to allow visualisation of tumours, as well as investigations into organs such as the heart and brain.[63-65] Another application is photodynamic therapy (PDT) where light energy absorbed by chromophores

via one or multiple photon absorption (see Section 1.2.5) is transferred to oxygen molecules in the cell to produce toxic singlet oxygen. Near-IR light can penetrate deeper into tissues and causes less tissue damage than shorter wavelength light, hence dyes which absorb in the near-IR region are attractive candidates for PDT, provided their excited state is of sufficient energy to generate singlet oxygen.[66]

Near-IR dyes are also gaining popularity in the field of photovoltaics (Section 1.2.6). Nearly 50% of solar energy lies in the near-IR, indicating that the development of photovoltaic devices capable of absorbing in this region could lead to great advances in solar energy technology.[67]

From the discussion above, it is clear that the synthesis of novel near-IR absorbing dyes is of interest for a large variety of applications; hence it is worth considering some common structural characteristics for near-IR absorbing dyes.

As shown in Section 1.2.1, an increase in the π-conjugation of an organic molecule results in a decrease in the HOMO-LUMO gap of the system, lowering the energy required for electron excitation. This manifests itself in the UV-vis-NIR absorption spectrum of a molecule by a bathochromic-shift, also known as a red-shift, often with an increase in extinction coefficient. Disruptions to conjugation, which may arise from bond length alternation effects such as the Peierls distortion or from torsional strain, means that increasing the length of the π-system does not always produce longer wavelength absorption. For example chromophores based upon long polyene chains often show convergence of absorption at a particular wavelength with increasing chain length — a typical example of this is *trans*-polyacteylene which demonstrates convergence around 600 nm.[68,69] Furthermore, the low stability and solubility of such polyenes poses many challenges for processability of these dyes.

Many strategies have been developed for the synthesis of organic chromophores with absorption into the near-IR beyond 800 nm, as discussed in review articles by Fabian and, later, Qian.[60,67] These approaches include the introduction of donor and acceptor end groups to a molecule. Such D-A systems exhibit an alternative resonance form, $^{+}D{=}A^{-}$, which gives rise to a reduction in bond length alteration. In addition, the high energy HOMO of the

donor and low energy LUMO of the acceptor act to narrow the HOMO-LUMO gap.[67] Rigidifying the π-system, for example by cyclisation, is another strategy for increasing the wavelength of near-IR absorption.[70] Such rigidification can result in a more planar geometry and hence better orbital overlap between adjacent p-orbitals resulting in a smaller HOMO-LUMO gap. Expansion of the π-system by fusion to large aromatic units is also an effective way to increase electron delocalisation. This method increases in the number of conjugated π-electrons, while avoiding the problems encountered by formation of a long chain in one dimension.

While the large π-systems produced by such synthetic strategies are expected to exhibit strong linear absorption in the near-IR, these chromophores may also exhibit other interesting optical properties such as nonlinear absorption.

1.2.5 Large π-Systems for Nonlinear Optics

In discussing the near-IR absorption of π-conjugated molecules in Section 1.2.4, only linear absorption was considered. In this regime the interaction of light with the material may be described by

$$P(\omega) = \varepsilon_0 \chi^{(1)} E$$

where E is the electric field of the light, ε_0 is the vacuum permittivity, $P(\omega)$ is the polarisation of the material (relating to geometrical and electronic perturbations of the system) and $\chi^{(1)}$ is the first order macroscopic susceptibility.[71] $\chi^{(1)}$ contains both real and imaginary parts, and it is the imaginary part which is proportional to the extinction coefficient of the chromophore. The equation above shows that the polarisation of the material depends linearly upon the light intensity i.e. the material obeys the Beer-Lambert law.[72] At high light intensities, such as those produced by lasers, materials may exhibit deviations from this linear relationship, resulting in the observation of nonlinear optical effects.[71,73]

One such nonlinear optical effect is optical limiting. This occurs when the absorption of light by a material changes with light intensity such that the transmittance of a material decreases as light intensity increases (Figure 1.15).[74] Such materials have military

applications, as both human eyes and delicate technological devices require the means to survive the powerful radiation of laser weapons. The operating spectrum for which optical limiting is required depends upon the nature of the device, with typical night-vision equipment used in military situations have an operating spectrum of 600 — 900 nm, while eye-protection for military or lab use requires optical limiting to occur over the visible spectrum in the range 400 — 700 nm.[75]

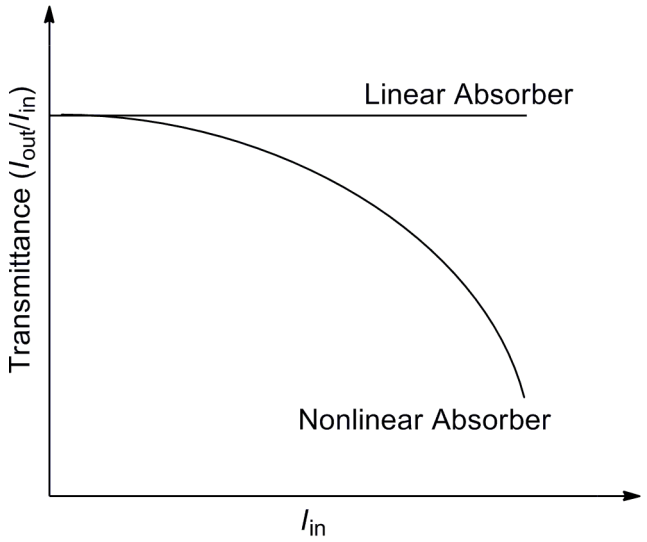

Figure 1.15: Schematic representation of the relationship between transmittance and incident light intensity for a linear and nonlinear absorber.

Optical limiting may occur by two mechanisms: Reverse Saturable Absorption (RSA) and multiphoton absorption, of which Two Photon Absorption (TPA) is the most highly studied.[71,76,77] RSA occurs when absorption by excited states is stronger than absorption by the ground state at a given wavelength. The absorption of excited states is generally quantified by molar absorption cross sections, σ, which are related to extinction coefficients, ε, by

$$\sigma = \varepsilon/(N_A 10^{-3} \log e) = \varepsilon \times 3.82 \times 10^{-21}$$

where N_A is Avogadro's constant.[78] Optical limiting by RSA is a cumulative effect — over time the excited state population increases and hence absorption increases.[77] In order for RSA to occur, it is necessary for there to be some ground state absorption in the optical window of interest to enable the population of excited states. These excited states must be

long lived on the timescale of the laser pulse to ensure a build-up of population; for laser pulses with duration greater than nanoseconds, absorption by excited singlet states is inadequate to provide a strong optical limiting response due to the short lifetimes of these states. Triplet states however, have a lifetime in the region of μs; optical limiting for longer laser pulses therefore occurs by a five-level model (Figure 1.16).[77,79,80] Here ground state (S_0) absorption raises the molecules to the first singlet excited state (S_1) whereupon excited state absorption from the S_1 state to S_n states may occur. Fast intersystem crossing (ISC) competes with this process, allowing population of the triplet state (T_1) and subsequent absorption from this state to excited triplet states (T_n).[79]

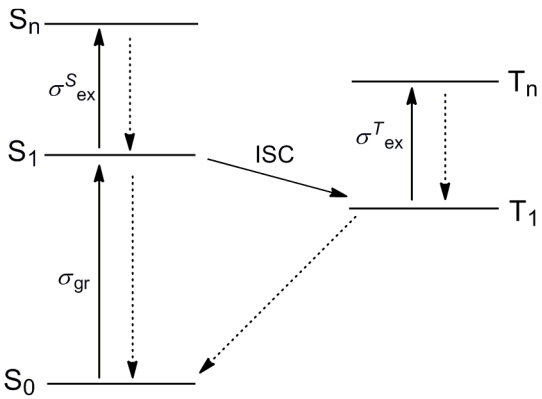

Figure 1.16: Jablonsky diagram showing the five-level model for RSA. Dotted lines correspond to decay processes (e.g. internal conversion (IC), fluorescence and phosphorescence).

In order for efficient optical limiting to occur by the five-level mechanism for RSA, several criteria must be met by the material. First, the ratio of absorption cross sections $\sigma^T_{ex}/\sigma_{gr}$ must be in the region of 10 — 50 over the range of wavelengths within the optical spectrum of interest.[77] The larger this ratio, the greater the excited state absorption (ESA) and hence the greater the optical limiting effect. In addition for the material to exhibit a fast response to increased laser intensity, it must possess a fast rate of ISC with a large triplet quantum yield to ensure both a rapid and high population of the T_1 state upon exposure to the laser radiation.[80] The lifetime of the triplet state is also a key parameter in determining the performance of an optical limiting material;[81] long lived triplet states are necessary to ensure a population build-up, allowing stronger light absorption to occur due to the large absorption cross section of this excited state.

For a material to exhibit RSA it must, obviously, absorb light across the UV-vis-NIR spectrum, hence chromophores including fullerenes, macrocycles such as porphyrins and phthalocyanines, and metal cluster compounds demonstrate RSA.[76] Porphyrins and phthalocyanines are particularly attractive candidates for optical limiting devices because they can exhibit RSA over a wide range of wavelengths within the visible region.[81] Furthermore, their architectural flexibility allows tuning of the intensity, wavelength and spectral shape of this absorption, with an extension of the π-system enabling RSA at lower energies, making them suitable for use in night-vision equipment.[80,82] These macrocyclic systems have also been shown to exhibit high triplet quantum yields and lifetimes. Such parameters may be optimised by coordination of metal ions such as indium or thallium in the central cavity of the macrocycle as it is well known that heavy atoms facilitate the process of ISC.[81]

TPA, unlike RSA, provides an instantaneous method of optical limiting. In this mechanism, two photons of light are absorbed simultaneously; one promotes a molecule to a virtual excited state, while the second photon promotes the molecule to a real excited state (Figure 1.17).[72]

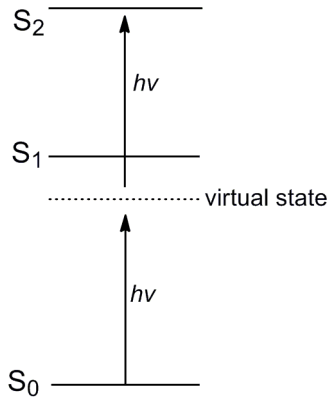

Figure 1.17: TPA from the ground state to the S_2 state for laser light of energy $h\nu$. Arrows represent photon absorption. The dotted line represents a virtual state.

TPA may occur at wavelengths where zero one-photon absorption occurs, hence at low light intensities the material may be totally transparent to light. At high light intensities, TPA is observed and hence the transmittance of light is reduced. It has been found that TPA is enhanced when the virtual state is close enough to a real state to

experience resonance effects (but this can result in competitive one photon absorption).[72] Optical limiting by TPA may occur at longer wavelength than by RSA when the energy of the virtual state exists below that of the S_1 state. In order to understand the structural requirements for a good TPA dye it is necessary to examine how the polarisation of a system changes under high light intensity.

When exposed to a high intensity light source, the polarisation of a material may be described by

$$P(\omega) = \varepsilon_0\chi^{(1)}E + \varepsilon_0\chi^{(2)}E^2 + \varepsilon_0\chi^{(3)}E^3 + \ldots$$

where $\chi^{(2)}$ and $\chi^{(3)}$ are the second and third order macroscopic susceptibilities respectively. In small electric fields, the second and third terms in this expansion are vanishingly small, however in large electric fields, such as in the case of a laser, these terms become significant, giving rise to nonlinear optical effects.[82] The strength of TPA by a molecule depends upon the TPA cross section, σ_2, which is related to the imaginary part of $\chi^{(3)}$ by

$$\sigma_2 = \frac{4\pi^2 \mathrm{Im}\chi^{(3)}\hbar\omega^2}{n^2c^2N}$$

where N is the number density, ω is the excitation frequency, n is the refractive index and c is the speed of light.[83,84] The magnitude of $\chi^{(3)}$ has been shown to depend strongly upon both the size of the π-conjugated system and its dimensionality, with $\chi^{(3)} \propto L^7$ for one-dimensional systems (where L is the delocalisation length) and $\chi^{(3)} \propto L^4$ for two-dimensional systems.[73,85] Hence large, conjugated π-systems may be expect to show strong 3rd order nonlinear optical effects. These effects may be further enhanced if the π-system contains donor and acceptor moieties.[72]

In addition to finding application for optical limiting devices, TPA is potentially useful in the field of photodynamic therapy where photosensitisers absorb light and transfer this energy to oxygen, thereby generating singlet oxygen which causes cell death.[86] TPA has several advantages over one photon absorption (OPA) in this process. First, for TPA, light of a longer wavelength may be used (provided it is still of sufficient energy to raise the molecule to an excited state capable of generating singlet oxygen) which is less damaging to

tissue. Second, TPA absorption occurs within a smaller focal volume than for OPA, enabling it to target specific areas with greater precision. This latter property has led to the development of TPA for two-photon initiated polymerisation, a process which may be used in optical data storage.

From the discussion above, it may be seen that nonlinear optical effects such TPA may be expected to occur for organic compounds composed of large π-systems, as such molecules are predicted to display high $\chi^{(3)}$ values. Such systems have also been shown to exhibit RSA, with an increase in the size of the π-system resulting in red-shifted absorption spectra necessary for optical limiting to occur in the near-IR. Furthermore, RSA may be enhanced if the system is capable of coordinating metal ions, as this can result in high ISC rates necessary to enable efficient optical limiting by ESA from triplet states. Such nonlinear optical effects may be harnessed in a wide range of devices and applications, however linear absorption by large π-systems may also be exploited in optoelectronic devices as the following section reveals.

1.2.6 Large π-Systems as Dyes for Photovoltaic Devices

With conventional fuel sources such as coal, oil and natural gas running out, and the impact of harmful emissions such as carbon dioxide on the environment becoming apparent, there is a growing need for a renewable, clean and stable energy supply. The harnessing of solar energy to efficiently produce electricity through solar cells is one approach towards solving this problem. Currently, silicon based solar cells make up the commercial market due to their high energy efficiencies of over 25%,[87] however these devices are very expensive to produce, limiting their feasibility for large-scale use.[88] One attractive alternative to silicon based solar cells is the liquid dye-sensitised solar cell (DSSC) where molecules of a dye are adsorbed onto the surface a metal oxide semiconductor film (commonly titanium dioxide, TiO_2).[89] Absorption of light by the chromophore generates an excited state which undergoes electron transfer, donating an electron into the conducting band of the metal oxide. The electrons diffuse through this layer to the anode, while the dye is reduced by electron

transfer from a redox active species (such as the I^-/I_3^- redox couple) in the electrolyte — subsequent reduction of this species at the cathode completes the circuit (Figure 1.18).[88,89]

Early liquid DSSC devices produced conversion yields from solar light to electricity of less than 1% due to a combination of low dye stability and poor absorbance of incident light by the dye molecules.[89] Increasing the number of layers of dye present at the semiconductor surface could increase the efficiency of light absorption, however this approach appears to encounter difficulties due to the low level of dye adsorption away from the naked titanium dioxide surface.

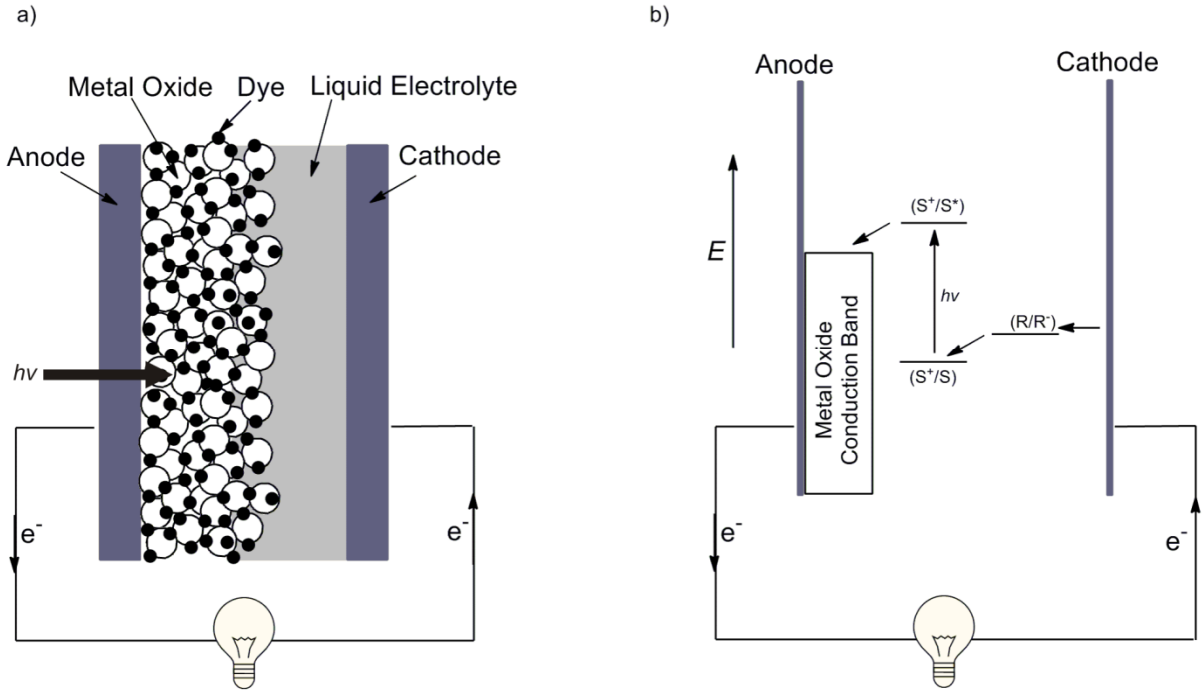

Figure 1.18: a) Schematic representation of a dye-sensitised solar-cell. White circles represent nanoparticles of the semiconducting metal oxide, black circles represent molecules of dye sensitiser adsorbed onto the surface of this metal oxide layer. b) Schematic representation of the key steps and energy levels involved in a DSSC where S is the dye sensitiser and R/R^- is the redox couple which regenerates the oxidised dye.

Grätzel and co-workers have led the field of dye-sensitized solar cells since discovering that the use of rough titanium dioxide surfaces provides a higher surface area than smooth surfaces, allowing more dye molecules to be directly adsorbed for a given area and thereby dramatically increasing the light harvesting capability of the system. Combined with a stable ruthenium based dye which exhibits broad absorption across the UV-vis spectrum, these photovoltaic devices exhibit efficiencies of up to 12% in diffuse daylight.[89-92]

Despite the high efficiencies of these systems, there are several disadvantages which arise from using ruthenium based dyes. First, ruthenium is a rare metal with limited resources indicating future problems with both supply and cost.[93,94] Second, ruthenium complexes are toxic — a setback for production and disposal/recycling of the devices.[95] In addition, ruthenium based dyes exhibit poor absorption in the near-IR — a problem since around 50% of solar energy falls beyond 750 nm. As a result of these drawbacks, efforts have been directed towards the synthesis of organic dyes which are either metal free, or which incorporate a cheap metal, to result in a non-toxic chromophore.[96,97]

The general requirements for a dye sensitiser are that it should be photostable to ensure a long lifetime for the device; absorption must be strong and extend over the UV-vis-NIR spectrum up to around 920 nm (the limit exists due to the need for the LUMO level of the dye to be above the energy level of the metal oxide conduction band);[98,99] the HOMO level of the dye must be of a lower energy than the redox couple which acts to regenerate the dye (R/R^- in Figure 1.18 (b)).[96,100] Furthermore, the positive charge formed on the dye after charge injection should be localised away from the metal oxide surface to prevent charge recombination from occurring.[96,101-103] In addition the dye must be able to be functionalised with an 'anchor' group to enable it to be attached to the metal oxide surface, and should not be prone to aggregation as this results in unfavourable intermolecular energy transfer and 'self-quenching' processes which reduce device efficiency.[96,104] It is also favourable for the dye to be very hydrophobic to prevent its desorption from the metal oxide surface in the presence of traces of water, and to reduce contact between the electrolyte and the anode.[96]

Organic chromophores with large π-systems such as chlorins and bacteriochlorins (partially reduced porphyrinic rings) are used by nature as the key light harvesting compounds which drive photosynthetic pathways in plants and bacteria. Hence many extended π-systems based on, or related to, the porphyrin macrocycle (including phthalocyanines)[105-108] have been explored synthetically for use in dye-sensitised solar cells.[94,109,110] These molecules may be modified at the ring periphery, for example by the addition of electron donating or withdrawing moieties, allowing their optical, electronic, photophysical and physical properties (such as solubility and aggregation) to be tuned.

Furthermore, these compounds are able to bind metal ions, or simply two protons, in their central cavity providing an additional method by which the properties of the system may be tailored to suit the particular components of a photovoltaic device.

Currently many efforts are being directed towards expanding the π-system of such compounds to enable charge generation in photovoltaic devices from absorption of near-IR light.[94,111-114] This provides an attractive opportunity to harvest the large proportion of solar energy which falls beyond 750 nm.

A more detailed review of the use of large π-systems as sensitisers for dye-sensitised solar cells is given in Chapter 5, however the optical properties of the commonly used porphyrin building block are now discussed.

1.3 Porphyrins as Building Blocks for Large π-Systems

Section 1.2 has shown that large, planar π-systems with conjugation in two dimensions, are likely to exhibit absorption in the near-IR, as well as 3rd order nonlinear optical properties. Such molecules may also be expected to possess the necessary structural and electronic properties required for the formation of discotic liquid crystals capable of efficient charge transport behaviour (provided such systems bear suitable side chains). In addition, chromophores incorporating large π-systems may be adapted for use as sensitisers in DSSC devices, offering new approaches to achieving the efficient conversion of solar energy to electricity.

Porphyrins are disc-shaped, aromatic macrocyclic systems which display a high degree of architectural flexibility at their *meso*- and β-positions (Figure 1.19). These properties, together with their planar geometry, make porphyrins extremely suitable building blocks for extended π-systems.

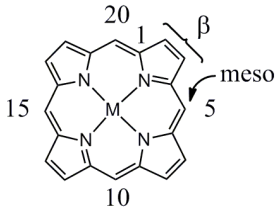

Figure 1.19: Standard IUPAC numbering system for porphyrins. The *meso*-positions are numbered 5, 10, 15 and 20; the β-positions are labelled 2, 3, 7, 8, 12, 13, 17 and 18. M = 2H or metal ion.

With 22 electrons in the ring, of which 18 participate in the delocalisation pathway (Figure 1.14), these large π-systems absorb light in the visible region due to π-π^* transitions.

The absorption spectrum of a porphyrin unconjugated to any substituents, is best explained by the Gouterman four orbital model. A porphyrin core, with a metal ion bound in the central cavity, possesses D_{4h} symmetry and the frontier molecular orbitals consist of two HOMOs and two LUMOs (Figure 1.20 (i)). The two HOMOs are very close in energy, while the two LUMOs are degenerate, resulting in two transitions of very similar energy, namely $a_{1u} \rightarrow e_g$ and $a_{2u} \rightarrow e_g$. These two transitions both give excited states of ^{1}Eu character which mix due to configuration interaction. As a result, one state is raised in energy due to constructive interference (S_2), while the other is lowered in energy due to destructive interference (S_1), as shown in Figure 1.20 (ii). This gives rise to two transitions of very different energy; the weak 'Q-bands' at low energy (around 550 nm) and the intense 'B-band', also known as the Soret band, at high energy (around 400 nm) (Figure 1.20 (iii)).[115,116] A free-base porphyrin has a lower symmetry than a metalloporphyrin (D_{2h} vs D_{4h}) which results in the occurrence of four Q-bands rather than two.

Figure 1.20: i) Molecular orbitals for a metalloporphyrin core of D_{4h} symmetry, ii) corresponding states, iii) UV-vis absorption spectrum.[115]

As described in Section 1.2.5, in addition to highly tunable one photon absorption in the visible region, porphyrins have also been shown to exhibit strong nonlinear optical behaviour when subjected to intense laser radiation which may also be tailored by structural modifications.[80,82]

1.3.1 Tuning the Optical Properties of Porphyrin Systems

The wavelength and intensity of light absorption by a porphyrin system can be tuned by the choice of the central metal ion, coordinating ligands and, most significantly, by modifications to the porphyrin ring periphery. The frontier molecular orbital coefficients are greater for the *meso*-positions of the porphyrin than for the β-positions (Figure 1.20 (i)). As a result, it may be expected that substituents attached to the *meso*-positions will exert a greater perturbation of the electronic structure of the porphyrin than those attached to the β-positions.[82,115]

Direct attachment of phenyl groups to the *meso*-positions of the porphyrin ring has little effect on the electronic system of the porphyrin, because steric interactions between the substituent and the β-hydrogens of the porphyrin force the phenyl group to sit out of the plane of the porphyrin, with a torsional angle of about 70°.[115] However, there are two main approaches by which π-conjugation between the porphyrin core and aromatic substituents may be increased.

The first way to increase π-conjugation involves the use of an alkyne linker group between the porphyrin and aromatic unit. The increase in distance between these moieties due to the presence of the linker enables them to adopt a coplanar arrangement with far less steric strain. The alkyne group is linear with two orthogonal pairs of π-orbitals; one of these pairs is therefore in the correct geometry to overlap with both the π-orbitals of the porphyrin and those of the aromatic unit when these moieties sit in a coplanar conformation, offering excellent electronic communication between the two.

Anderson and co-workers reported the synthesis of a series of porphyrin oligomers, with the porphyrin units linked by alkyne bridges (**11**, Figure 1.21).[117]

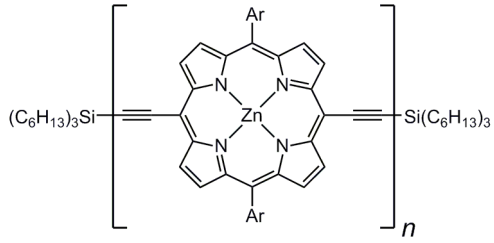

11

Figure 1.21: Acetylene-linked porphyrin oligomers synthesised by Anderson and co-workers, n = 1-6.[117] Ar = 3,5-di(*t*-butyl)phenyl.

As expected, the bis-acetylene substituted porphyrin monomer (**11**, n=1) shows Q-bands which are red-shifted with respect to the analogous unsubstituted diaryl porphyrin, indicating a decreased HOMO-LUMO gap due to increased π-conjugation to the alkyne groups. Increasing the value of n from one to six results in further red-shifting of Q-band absorption, with the Q-band peak moving from 650 nm for the monomer (n = 1) to 858 nm for the hexamer; a significant increase in intensity of absorption was observed for both the Soret and Q-bands upon increasing chain length. However, although the maximum wavelength of absorption increases with increasing chain length, the magnitude of this red-shift decreases.[117]

While the use of alkyne linkers has been shown to facilitate conjugation between porphyrins, the series of oligomers (**11**) shown in Figure 1.21 display a convergence of absorption below 900 nm. Furthermore, the solubility of these systems decreases with increasing chain length, reducing the ease of their synthesis and purification.[117] As a result, this approach to achieving highly conjugated porphyrins for near-IR dyes and charge transport is limited.

A second method to increasing π-conjugation in porphyrin systems is by fusion of aromatic units to the porphyrin periphery across the *meso*- and β-positions. This approach forces co-planarity of the porphyrin and the aromatic group, yielding a rigidified structure with extended π-conjugation. Such planar, highly conjugated systems are therefore ideal candidates not only for near-IR dyes and panchromatic sensitisers for photovoltaic devices, but also as building blocks for columnar liquid crystals due to the near-discotic shape of the fused porphyrin systems.

In the pursuit of near-IR absorbing porphyrins, fusion of aromatic units to a porphyrin ring has several advantages over the synthesis of alkyne-linked systems. First, fusion of even one substituent to the porphyrin ring can greatly perturb the optical and electronic properties of the porphyrin, shifting absorption into the near-IR and hence exhibiting a small HOMO-LUMO gap. Similar properties are only observed for very long alkyne-linked porphyrin oligomers. Fused porphyrin monomers are far simpler to purify than long oligomeric systems, making them attractive alternatives. Second, while alkyne-linked porphyrins show extension of the π-system by red-shifted absorption spectra, the spectral shape of such systems remains similar to that of a porphyrin monomer, with distinct Soret and Q-band regions. Fusion of a porphyrin to an aromatic unit however, may drastically alter this spectral shape, resulting in strong absorption over a much wider range of wavelengths. This is a particularly desirable property in dyes for photovoltaic devices, as it may be expected to lead to more efficient harvesting of solar energy.

Several reviews have been published which explore the various synthetic strategies towards fused porphyrin systems with extended π-conjugation.[118,119] However it is of interest to explore how these modifications, such as the choice of fused aromatic group and the number and position of bonds between it and the porphyrin periphery, affect the optoelectronic properties and conjugation pathway of a porphyrin. Examples of highly conjugated fused porphyrin systems will now be presented and discussed with an emphasis on exploring these structure-property relationships.

1.4 References

(1) Sun, S.; Dalton, L. R. *Introduction to Organic and Optoelectronic Materials and Devices*; 1st ed.; Taylor and Francis Group: Boca Raton, 2008.
(2) Bar-Lev, A. *Semiconductors and Electronic Devices*; 2nd ed.; Prentice-Hall International: Englewood Cliffs, 1984.
(3) Sze, S. M.; Ng, K. K. *Physics of Semiconductor Devices*; 3rd ed.; Wiley Interscience: New York, 2006.
(4) Peierls, R. E. *Quantum Theory of Solids*; Oxford University Press: Oxford, 1955.
(5) Carroll, R. L.; Gorman, C. B. *Angew. Chem. Int. Ed.* **2002**, *41*, 4378-4400.
(6) Chiang, C. K.; Fincher, C. R.; Park, Y. W.; Heeger, A. J.; Shirakawa, H.; Louis, E. J.; Gau, S. C.; MacDiarmid, A. G. *Phys. Rev. Lett.* **1977**, *39*, 1098-1101.
(7) Brédas, J. L.; Beljonne, D.; Coropceanu, V.; Cornil, J. *Chem. Rev.* **2004**, *104*, 4971-5003.
(8) Prins, P.; Grozema, F. C.; Schins, J. M.; Patil, S.; Scherf, U.; Siebbeles, L. D. A. *Phys. Rev. Lett.* **2006**, *96*, 146601.
(9) Chiang, C. K.; Druy, M. A.; Gau, S. C.; Heeger, A. J.; Louis, E. J.; MacDiarmid, A. G.; Park, Y. W.; Shirakawa, H. *J. Am. Chem. Soc.* **1978**, *100*, 1013-1015.
(10) Basescu, N.; Liu, Z. X.; Moses, D.; Heeger, A. J.; Naarmann, H.; Theophilou, N. *Nature* **1987**, *327*, 403-405.
(11) Salaneck, W. R.; Stafström, S.; Brédas, J. L. *Conjugated Polymer Surfaces and Interfaces*; 1st ed.; Cambridge University Press: Cambridge, 1996.
(12) Kivelson, S.; Epstein, A. J. *Phys. Rev. B* **1984**, *29*, 3336-3340.
(13) Kaiser, A. B. *Rep. Prog. Phys.* **2001**, *64*, 1-49.
(14) Grozema, F. C.; Siebbeles, L. D. A. *Int. Rev. Phys. Chem.* **2008**, *27*, 87-138.
(15) Takeya, J.; Kato, J.; Hara, K.; Yamagishi, M.; Hirahara, R.; Yamada, K.; Nakazawa, Y.; Ikehata, S.; Tsukagoshi, K.; Aoyagi, Y.; Takenobu, T.; Iwasa, Y. *Phys. Rev. Lett.* **2007**, *98*, 196804.
(16) Klauk, H. *Organic Electronics*; 1st ed.; Wiley-VCH: Weinheim, 2006.
(17) Bässler, H. *Phys. Status Solidi B* **1993**, *175*, 15-56.
(18) Coropceanu, V.; Malagoli, M.; da Silva Filho, D. A.; Gruhn, N. E.; Bill, T. G.; Brédas, J. L. *Phys. Rev. Lett.* **2002**, *89*, 275503.
(19) Devos, A.; Lannoo, M. *Phys. Rev. B* **1998**, *58*, 8236-8239.
(20) Barbara, P. F.; Meyer, T. J.; Ratner, M. A. *J. Phys. Chem.* **1996**, *100*, 13148-13168.
(21) Klimkāns, A.; Larsson, S. *Chem. Phys.* **1994**, *189*, 25-31.
(22) Kato, T.; Yamabe, T. *J. Chem. Phys.* **2001**, *115*, 8592-8602.
(23) Cornil, J.; Beljonne, D.; Calbert, J. P.; Brédas, J. L. *Adv. Mater.* **2001**, *13*, 1053-1067.
(24) Lemaur, V.; da Silva Filho, D. A.; Coropceanu, V.; Lehmann, M.; Geerts, Y.; Piris, J.; Debije, M. G.; van de Craats, A. M.; Senthilkumar, K.; Siebbeles, L. D. A.; Warman, J. M.; Brédas, J. L.; Cornil, J. *J. Am. Chem. Soc.* **2004**, *126*, 3271-3279.
(25) Senthilkumar, K.; Grozema, F. C.; Bickelhaupt, F. M.; Siebbeles, L. D. A. *J. Chem. Phys.* **2003**, *119*, 9809-9817.

(26) Kocherzhenko, A. A.; Patwardhan, S.; Grozema, F. C.; Anderson, H. L.; Siebbeles, L. D. A. *J. Am. Chem. Soc.* **2009**, *131*, 5522-5529.
(27) Grozema, F. C.; Houarner-Rassin, C.; Prins, P.; Siebbeles, L. D. A.; Anderson, H. L. *J. Am. Chem. Soc.* **2007**, *129*, 13370-13371.
(28) Zhou, Y.; Lei, T.; Wang, L.; Pei, J.; Cao, Y.; Wang, J. *Adv. Mater.* **2010**, *22*, 1484-1487.
(29) Martin, R. E.; Diederich, F. *Angew. Chem. Int. Ed.* **1999**, *38*, 1350-1377.
(30) Warman, J. M.; de Haas, M. P.; Dicker, G.; Grozema, F. C.; Piris, J.; Debije, M. G. *Chem. Mater.* **2004**, *16*, 4600-4609.
(31) Chandrasekhar, S.; Sadashiva, B. K.; Suresh, K. A. *Pramana- J. Phys.* **1977**, *9*, 471-480.
(32) Pisula, W.; Menon, A.; Stepputat, M.; Lieberwirth, I.; Kolb, U.; Tracz, A.; Sirringhaus, H.; Pakula, T.; Müllen, K. *Adv. Mater.* **2005**, *17*, 684-689.
(33) Hassheider, T.; Benning, S. A.; Kitzerow, H. S.; Achard, M. F.; Bock, H. *Angew. Chem. Int. Ed.* **2001**, *40*, 2060-2063.
(34) Schmidt-Mende, L.; Fechtenkötter, A.; Müllen, K.; Moons, E.; Friend, R. H.; MacKenzie, J. D. *Science* **2001**, *293*, 1119-1122.
(35) Adam, D.; Schuhmacher, P.; Simmerer, J.; Häussling, L.; Siemensmeyer, K.; Etzbach, K. H.; Ringsdorf, H.; Haarer, D. *Nature* **1994**, *371*, 141-143.
(36) An, Z. S.; Yu, J. S.; Jones, S. C.; Barlow, S.; Yoo, S.; Domercq, B.; Prins, P.; Siebbeles, L. D. A.; Kippelen, B.; Marder, S. R. *Adv. Mater.* **2005**, *17*, 2580-2583.
(37) Feng, X.; Liu, M.; Pisula, W.; Takase, M.; Li, J.; Müllen, K. *Adv. Mater.* **2008**, *20*, 2684-2689.
(38) Laschat, S.; Baro, A.; Steinke, N.; Giesselmann, F.; Hägele, C.; Scalia, G.; Judele, R.; Kapatsina, E.; Sauer, S.; Schreivogel, A.; Tosoni, M. *Angew. Chem. Int. Ed.* **2007**, *46*, 4832-4887.
(39) Cornil, J.; Lemaur, V.; Calbert, J. P.; Brédas, J. L. *Adv. Mater.* **2002**, *14*, 726-729.
(40) Tant, J.; Geerts, Y. H.; Lehmann, M.; De Cupere, V.; Zucchi, G.; Laursen, B. W.; Bjørnholm, T.; Lemaur, V.; Marcq, V.; Burquel, A.; Hennebicq, E.; Gardebien, F.; Viville, P.; Beljonne, D.; Lazzaroni, R.; Cornil, J. *J. Phys. Chem. B* **2005**, *109*, 20315-20323.
(41) van de Craats, A. M.; Warman, J. M. *Adv. Mater.* **2001**, *13*, 130-133.
(42) Iyer, V. S.; Wehmeier, M.; Brand, J. D.; Keegstra, M. A.; Müllen, K. *Angew. Chem. Int. Ed. Engl.* **1997**, *36*, 1604-1607.
(43) van de Craats, A. M.; Warman, J. M.; Fechtenkötter, A.; Brand, J. D.; Harbison, M. A.; Müllen, K. *Adv. Mater.* **1999**, *11*, 1469-1472.
(44) Sergeyev, S.; Pisula, W.; Geerts, Y. H. *Chem. Soc. Rev* **2007**, *36*, 1902-1929.
(45) Pisula, W.; Feng, X.; Müllen, K. *Adv. Mater.* **2010**, *22*, 3634-3649.
(46) Vanderpol, J. F.; Neeleman, E.; Zwikker, J. W.; Nolte, R. J. M.; Drenth, W.; Aerts, J.; Visser, R.; Picken, S. J. *Liq. Cryst.* **1989**, *6*, 577-592.
(47) Engel, M. K.; Bassoul, P.; Bosio, L.; Lehmann, H.; Hanack, M.; Simon, J. *Liq. Cryst.* **1993**, *15*, 709-722.
(48) Bushey, M. L.; Nguyen, T. Q.; Zhang, W.; Horoszewski, D.; Nuckolls, C. *Angew. Chem. Int. Ed.* **2004**, *43*, 5446-5453.
(49) Malthête, J.; Levelut, A. M.; Liébert, L. *Adv. Mater.* **1992**, *4*, 37-41.

(50) Brunsveld, L.; Zhang, H.; Glasbeek, M.; Vekemans, J. A. J. M.; Meijer, E. W. *J. Am. Chem. Soc.* **2000**, *122*, 6175-6182.
(51) Paraschiv, I.; Giesbers, M.; van Lagen, B.; Grozema, F. C.; Abellon, R. D.; Siebbeles, L. D. A.; Marcelis, A. T. M.; Zuilhof, H.; Sudhölter, E. J. R. *Chem. Mater.* **2006**, *18*, 968-974.
(52) Gearba, R. I.; Lehmann, M.; Levin, J.; Ivanov, D. A.; Koch, M. H. J.; Barberá, J.; Debije, M. G.; Piris, J.; Geerts, Y. H. *Adv. Mater.* **2003**, *15*, 1614-1618.
(53) Fechtenkötter, A.; Saalwächter, K.; Harbison, M. A.; Müllen, K.; Spiess, H. W. *Angew. Chem. Int. Ed.* **1999**, *38*, 3039-3042.
(54) Wu, J.; Fechtenkötter, A.; Gauss, J.; Watson, M. D.; Kastler, M.; Fechtenkötter, C.; Wagner, M.; Müllen, K. *J. Am. Chem. Soc.* **2004**, *126*, 11311-11321.
(55) Feng, X.; Wu, J.; Ai, M.; Pisula, W.; Zhi, L.; Rabe, J. P.; Müllen, K. *Angew. Chem. Int. Ed.* **2007**, *46*, 3033-3036.
(56) Sakurai, T.; Tashiro, K.; Honsho, Y.; Saeki, A.; Seki, S.; Osuka, A.; Muranaka, A.; Uchiyama, M.; Kim, J.; Ha, S.; Kato, K.; Takata, M.; Aida, T. *J. Am. Chem. Soc.* **2011**, *133*, 6537-6540.
(57) Sakurai, T.; Shi, K.; Sato, H.; Tashiro, K.; Osuka, A.; Saeki, A.; Seki, S.; Tagawa, S.; Sasaki, S.; Masunaga, H.; Osaka, K.; Takata, M.; Aida, T. *J. Am. Chem. Soc.* **2008**, *130*, 13812-13813.
(58) Marcon, V.; Breiby, D. W.; Pisula, W.; Dahl, J.; Kirkpatrick, J.; Patwardhan, S.; Grozema, F.; Andrienko, D. *J. Am. Chem. Soc.* **2009**, *131*, 11426-11432.
(59) Warman, J. M.; Piris, J.; Pisula, W.; Kastler, M.; Wasserfallen, D.; Müllen, K. *J. Am. Chem. Soc.* **2005**, *127*, 14257-14262.
(60) Fabian, J.; Nakazumi, H.; Matsuoka, M. *Chem. Rev.* **1992**, *92*, 1197-1226.
(61) Mizuguchi, J.; Rochat, A. C. *J. Imaging Sci.* **1988**, *32*, 135-140.
(62) Song, I. H.; Rhee, C. H.; Park, S. H.; Lee, S. L.; Grudinin, D.; Song, K. H.; Choe, J. *Org. Process Res. Dev.* **2008**, *12*, 1012-1015.
(63) Weissleder, R. *Nat. Biotechnol.* **2001**, *19*, 316-317.
(64) Hilderbrand, S. A.; Weissleder, R. *Curr. Opin. Chem. Biol.* **2010**, *14*, 71-79.
(65) Escobedo, J. O.; Rusin, O.; Lim, S.; Strongin, R. M. *Curr. Opin. Chem. Biol.* **2010**, *14*, 64-70.
(66) Luo, S.; Zhang, E.; Su, Y.; Cheng, T.; Shi, C. *Biomaterials* **2011**, *32*, 7127-7138.
(67) Qian, G.; Wang, Z. Y. *Chem. Asian. J.* **2010**, *5*, 1006-1029.
(68) Fincher, C. R.; Ozaki, M.; Tanaka, M.; Peebles, D.; Lauchlan, L.; Heeger, A. J.; MacDiarmid, A. G. *Phys. Rev. B* **1979**, *20*, 1589-1602.
(69) Christensen, R. L.; Faksh, A.; Meyers, J. A.; Samuel, I. D. W.; Wood, P.; Schrock, R. R.; Hultzsch, K. C. *J. Phys. Chem. A* **2004**, *108*, 8229-8236.
(70) Blattman.Hr; Heilbron.E; Wagniere, G. *J. Am. Chem. Soc.* **1968**, *90*, 4786-4789.
(71) He, G. S.; Tan, L. S.; Zheng, Q.; Prasad, P. N. *Chem. Rev.* **2008**, *108*, 1245-1330.
(72) Pawlicki, M.; Collins, H. A.; Denning, R. G.; Anderson, H. L. *Angew. Chem. Int. Ed.* **2009**, *48*, 3244-3266.
(73) Nalwa, H. S. *Adv. Mater.* **1993**, *5*, 341-358.
(74) Calvete, M.; Yang, G. Y.; Hanack, M. *Synth. Met.* **2004**, *141*, 231-243.

(75) Miller, M. J.; Mott, A. G.; Ketchel, B. P. *Proc. SPIE* **1998**, *3472*, 24-29.
(76) Tutt, L. W.; Boggess, T. F. *Prog. Quant. Electr.* **1993**, *17*, 299-338.
(77) Miles, P. A. *Appl. Opt.* **1994**, *33*, 6965-6979.
(78) Protasenko, V.; Bacinello, D.; Kuno, M. *J. Phys. Chem. B* **2006**, *110*, 25322-25331.
(79) Sutherland, R. L.; Brant, M. C.; Heinrichs, J.; Rogers, J. E.; Slagle, J. E.; McLean, D. G.; Fleitz, P. A. *J. Opt. Soc. Am. B.* **2005**, *22*, 1939-1948.
(80) McEwan, K.; Lewis, K.; Yang, G. Y.; Chng, L. L.; Lee, Y. W.; Lau, W. P.; Lai, K. S. *Adv. Funct. Mater.* **2003**, *13*, 863-867.
(81) Su, W. J.; Cooper, T. M.; Brant, M. C. *Chem. Mater.* **1998**, *10*, 1212-1213.
(82) Senge, M. O.; Fazekas, M.; Notaras, E. G. A.; Blau, W. J.; Zawadzka, M.; Locos, O. B.; Mhuircheartaigh, E. M. N. *Adv. Mater.* **2007**, *19*, 2737-2774.
(83) Terenziani, F.; Katan, C.; Badaeva, E.; Tretiak, S.; Blanchard-Desce, M. *Adv. Mater.* **2008**, *20*, 4641-4678.
(84) Burris, J.; McIlrath, T. J. *J. Opt. Soc. Am. B.* **1985**, *2*, 1313-1317.
(85) Kaino, T.; Tomaru, S. *Adv. Mater.* **1993**, *5*, 172-178.
(86) Collins, H. A.; Khurana, M.; Moriyama, E. H.; Mariampillai, A.; Dahlstedt, E.; Balaz, M.; Kuimova, M. K.; Drobizhev, M.; Yang, V. X. D.; Phillips, D.; Rebane, A.; Wilson, B. C.; Anderson, H. L. *Nat. Photonics* **2008**, *2*, 420-424.
(87) Green, M. A. *Prog. Photovolt: Res. Appl.* **2009**, *17*, 183-189.
(88) Snaith, H. J.; Schmidt-Mende, L. *Adv. Mater.* **2007**, *19*, 3187-3200.
(89) O'Regan, B.; Grätzel, M. *Nature* **1991**, *353*, 737-740.
(90) Gao, F.; Wang, Y.; Shi, D.; Zhang, J.; Wang, M.; Jing, X.; Humphry-Baker, R.; Wang, P.; Zakeeruddin, S. M.; Grätzel, M. *J. Am. Chem. Soc.* **2008**, *130*, 10720-10728.
(91) Nazeeruddin, M. K.; De Angelis, F.; Fantacci, S.; Selloni, A.; Viscardi, G.; Liska, P.; Ito, S.; Bessho, T.; Grätzel, M. *J. Am. Chem. Soc.* **2005**, *127*, 16835-16847.
(92) Nazeeruddin, M. K.; Kay, A.; Rodicio, I.; Humphry-Baker, R.; Müller, E.; Liska, P.; Vlachopoulos, N.; Grätzel, M. *J. Am. Chem. Soc.* **1993**, *115*, 6382-6390.
(93) Tian, H.; Yang, X.; Chen, R.; Hagfeldt, A.; Sun, L. *Energy Environ. Sci.* **2009**, *2*, 674-677.
(94) Imahori, H.; Umeyama, T.; Ito, S. *Acc. Chem. Res.* **2009**, *42*, 1809-1818.
(95) Yasbin, R. E.; Matthews, C. R.; Clarke, M. J. *Chem. Biol. Interact.* **1980**, *31*, 355-365.
(96) Mishra, A.; Fischer, M. K. R.; Bäuerle, P. *Angew. Chem. Int. Ed.* **2009**, *48*, 2474-2499.
(97) Koumura, N.; Wang, Z. S.; Mori, S.; Miyashita, M.; Suzuki, E.; Hara, K. *J. Am. Chem. Soc.* **2006**, *128*, 14256-14257.
(98) Yum, J. H.; Baranoff, E.; Wenger, S.; Nazeeruddin, M. K.; Grätzel, M. *Energy Environ. Sci.* **2011**, *4*, 842-857.
(99) Snaith, H. J. *Adv. Funct. Mater.* **2010**, *20*, 13-19.
(100) Hagberg, D. P.; Yum, J. H.; Lee, H.; De Angelis, F.; Marinado, T.; Karlsson, K. M.; Humphry-Baker, R.; Sun, L.; Hagfeldt, A.; Grätzel, M.; Nazeeruddin, M. K. *J. Am. Chem. Soc.* **2008**, *130*, 6259-6266.
(101) Argazzi, R.; Bignozzi, C. A.; Heimer, T. A.; Castellano, F. N.; Meyer, G. J. *J. Am. Chem. Soc.* **1995**, *117*, 11815-11816.

(102) Clifford, J. N.; Yahioglu, G.; Milgrom, L. R.; Durrant, J. R. *Chem. Commun.* **2002**, 1260-1261.
(103) Hirata, N.; Lagref, J. J.; Palomares, E. J.; Durrant, J. R.; Nazeeruddin, M. K.; Grätzel, M.; Di Censo, D. *Chem. Eur. J.* **2004**, *10*, 595-602.
(104) Hara, K.; Dan-oh, Y.; Kasada, C.; Ohga, Y.; Shinpo, A.; Suga, S.; Sayama, K.; Arakawa, H. *Langmuir* **2004**, *20*, 4205-4210.
(105) Reddy, P. Y.; Giribabu, L.; Lyness, C.; Snaith, H. J.; Vijaykumar, C.; Chandrasekharam, M.; Lakshmikantam, M.; Yum, J. H.; Kalyanasundaram, K.; Grätzel, M.; Nazeeruddin, M. K. *Angew. Chem. Int. Ed.* **2007**, *46*, 373-376.
(106) Cid, J. J.; Yum, J. H.; Jang, S. R.; Nazeeruddin, M. K.; Ferrero, E. M.; Palomares, E.; Ko, J.; Grätzel, M.; Torres, T. *Angew. Chem. Int. Ed.* **2007**, *46*, 8358-8362.
(107) Eu, S.; Katoh, T.; Umeyama, T.; Matano, Y.; Imahori, H. *Dalton Trans.* **2008**, 5476-5483.
(108) Cid, J. J.; García-Iglesias, M.; Yum, J. H.; Forneli, A.; Albero, J.; Martínez-Ferrero, E.; Vázquez, P.; Grätzel, M.; Nazeeruddin, M. K.; Palomares, E.; Torres, T. *Chem. Eur. J.* **2009**, *15*, 5130-5137.
(109) Walter, M. G.; Rudine, A. B.; Wamser, C. C. *J. Porphyrins Phthalocyanines* **2010**, *14*, 759-792.
(110) Campbell, W. M.; Burrell, A. K.; Officer, D. L.; Jolley, K. W. *Coord. Chem. Rev.* **2004**, *248*, 1363-1379.
(111) Jiao, C.; Zu, N.; Huang, K. W.; Wang, P.; Wu, J. *Org. Lett.* **2011**, *13*, 3652-3655.
(112) Mai, C. L.; Huang, W. K.; Lu, H. P.; Lee, C. W.; Chiu, C. L.; Liang, Y. R.; Diau, E. W. G.; Yeh, C. Y. *Chem. Commun.* **2010**, *46*, 809-811.
(113) Tanaka, M.; Hayashi, S.; Eu, S.; Umeyama, T.; Matano, Y.; Imahori, H. *Chem. Commun.* **2007**, 2069-2071.
(114) Hayashi, S.; Tanaka, M.; Hayashi, H.; Eu, S.; Umeyama, T.; Matano, Y.; Araki, Y.; Imahori, H. *J. Phys. Chem. C.* **2008**, *112*, 15576-15585.
(115) Anderson, H. L. *Chem. Commun.* **1999**, 2323-2330.
(116) Gouterman, M. *J. Mol. Spectrosc.* **1961**, *6*, 138-163.
(117) Taylor, P. N.; Huuskonen, J.; Rumbles, G.; Aplin, R. T.; Williams, E.; Anderson, H. L. *Chem. Commun.* **1998**, 909-910.
(118) Fox, S.; Boyle, R. W. *Tetrahedron* **2006**, *62*, 10039-10054.
(119) Aratani, N.; Kim, D.; Osuka, A. *Chem. Asian J.* **2009**, *4*, 1172-1182.

Chapter 2: A Review of Edge-Fused Porphyrin Systems

This chapter presents a literature review of porphyrins fused to aromatic units, focussing on the influence of structural effects, such as the number and location of fusion sites and the nature of the aromatic unit, on the optical and electrochemical properties of the fused systems. My previous work on the synthesis of mono-anthracene fused porphyrins is summarised and the aims for this project are outlined.

2.1 Literature Review of Edge-Fused Porphyrin Systems

There are two main classes of highly conjugated, fused porphyrin systems; those in which two or more porphyrin units are directly fused to each other, and those in which a porphyrin is fused to a different aromatic ring. Both classes of fused porphyrin systems are explored below, together with discussion of optical and electrochemical data where appropriate. All electrochemical potentials are reported relative to the ferrocene/ferrocinium redox couple.

2.1.1 Directly Fused Porphyrin Systems

The formation of rigid porphyrin systems comprised of two or more porphyrin rings, involves the formation of at least two direct bonds between the porphyrin units. These bonds may exist across either the *meso*- or the β-positions to yield highly conjugated systems.

Fusion of two or more porphyrins across their β-positions has been reported by Smith and co-workers.[1,2] Synthesis of the porphyrin dimer (**12**) and trimer (**13**) was achieved in 6 and 5% yields respectively by condensation reaction between a pyrrole **14** and a pyrroloporphyrin **15** (Scheme 2.1), while trimer **16** was prepared by a similar procedure in 18% yield.

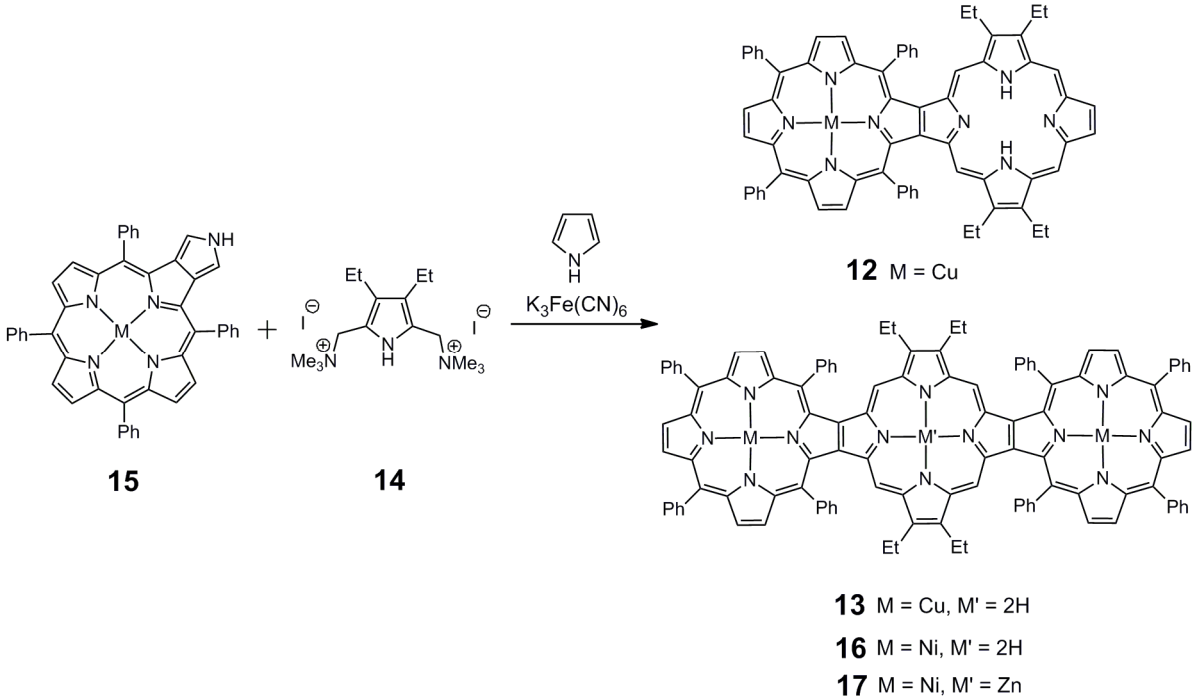

Scheme 2.1: Synthesis of β-fused porphyrin dimer and trimers reported by Smith and co-workers.[2]

These fused oligomers show a red-shift in their absorption spectra, relative to pyrroloporphyrin **15**, with a peak in the Q-band at 652 nm for dimer **12**, 722 nm for trimer **13** and 715 nm for trimer **16**. Insertion of zinc into the vacant cavity of trimer **16** gave the $Ni^{(II)}$-$Zn^{(II)}$-$Ni^{(II)}$ metalated trimer **17**, which displays a greater red-shift in the absorption spectrum with a peak at 742 nm (an additional shift to 752 nm was observed in the presence of pyridine), demonstrating that the metal ion can affect optical absorption properties.

While such porphyrin systems clearly show an increase in π-conjugation as the oligomer length increases, the size of the red-shift is surprisingly small. One reason for this may be deduced from the crystal structure of trimer **16** which shows the fused porphyrin system to be very non-planar; hence conjugation between adjacent porphyrin π-systems is highly disrupted, reducing the extent of electron delocalisation.[2] The non-planarity observed for trimer **16** is likely to be due to large steric interactions between the phenyl and ethyl substituents of the neighbouring porphyrin units. A second reason for the limited degree of π-conjugation between the porphyrin units of trimer **16** may be due to the small frontier orbital coefficients for porphyrin β-positions (Figure 1.20 (i)).[3]

Smith and co-workers have also reported the synthesis of a cruciform pentamer **19**, by tetramerisation of pyrroloporphyrin **18**, followed by oxidation (Scheme 2.2). The absorption spectrum of **19** shows a long wavelength peak at 774 nm, indicating that the porphyrin units are conjugated. The lack of *meso*-substituents on the central porphyrin suggests that the system is likely to be less sterically strained than for trimer **16**, hence the relatively small red-shift observed in the absorption spectrum is probably due weak interporphyrin electronic coupling through the β-positions.[1,3]

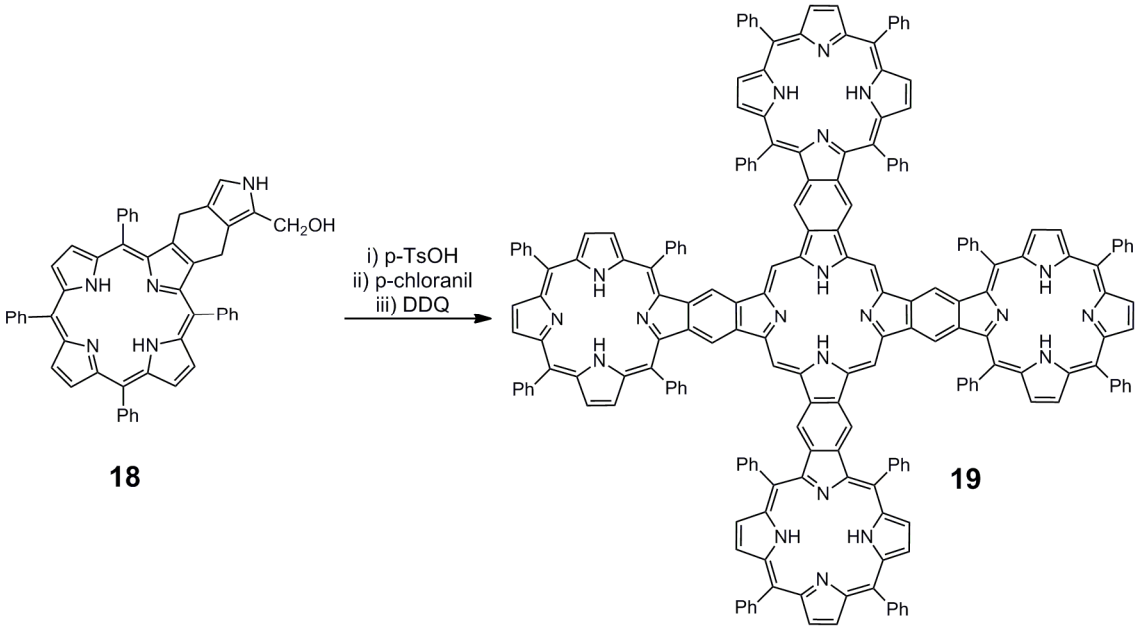

Scheme 2.2: Synthesis of fused cruciform porphyrin pentamer reported by Smith and co-workers.[1]

The larger frontier orbital coefficients at the *meso*-positions of a porphyrin core (Figure 1.20 (i)) suggest directly fused porphyrins with a *meso-meso* bond may be expected to exhibit a greater degree of electronic coupling than those fused through the β-positions. Doubly and triply linked porphyrin dimers, connected through the *meso*-position (Figure 2.1), have been achieved by several synthetic routes including oxidative ring-closure of *meso*-linked precursors, and simultaneous dimerisation and fusion of unlinked porphyrin monomers.[4-9]

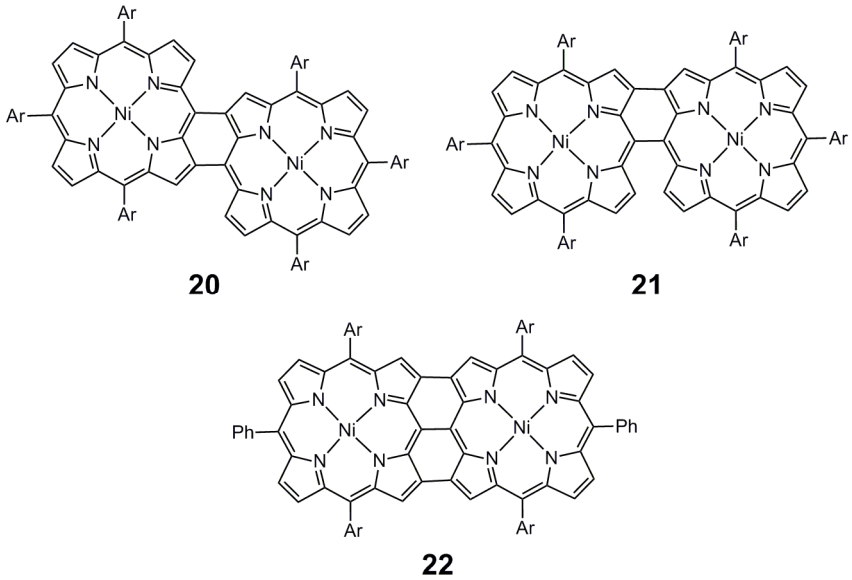

Figure 2.1: Fused porphyrin dimers linked across the *meso*-positions reported by Osuka and co-workers. Ar = 3,5-di(*t*-butyl)phenyl.[9]

In 2001, Osuka and co-workers synthesised the family of doubly and triply linked porphyrin dimers shown in Figure 2.1 and compared their optoelectronic properties.[9] Fused porphyrins **20** and **21**, linked across one *meso*- and one *β*-position, show long wavelength maxima in their absorption spectra at 756 and 735 nm respectively.[9] The differences in the red-shift observed in the absorption spectra may be rationalised by the difference in planarity of the two systems, as seen from their respective crystal structures. The crystal structure of doubly linked **20** reveals that the two porphyrin units are nearly coplanar, while the crystal structure of **21** shows the two porphyrins are slightly twisted with respect to each other due to the steric congestion between the two *β*-hydrogens. The red-shift in the long wavelength maxima of **20** and **21** compared to that of dimer **12** demonstrates the greater degree of electronic coupling between porphyrins linked at the *meso*-position.

The absorption spectrum of triply linked porphyrin **22** displays a peak at 933 nm, which moves to 1068 nm upon substitution of the nickel(II) ions for zinc(II) ions.[9] Fusion of doubly linked **21** to give triply linked **22**, forces an increase in co-planarity of the porphyrin units, however this is unlikely to account for the substantial red-shift, as shown by the small difference in wavelength maxima between planar **20** and twisted **21**. Instead the large red-shift for porphyrin **22** may be explained by an increase in the size of the conjugation pathway with fusion across multiple positions, thereby facilitating a greater degree of electronic communication between the two porphyrins.

Furthermore, electrochemical analysis of these three dimers shows a decrease in the first oxidation potential (E_1^{ox}) upon the increase in the number of porphyrin-porphyrin bonds, with a first oxidation potential (E_1^{ox}) of 0.52 V for doubly linked dimer **20**, 0.48 V for **21** and an E_1^{ox} of 0.46 V for triply linked dimer **22**.[9] This lowering of the first oxidation potential (hence raising the HOMO energy) as the degree of fusion increases, indicates that triply linked dimer **22** experiences a greater degree of *π*-conjugation than the doubly linked dimers.

The synthesis of longer doubly and triply fused porphyrin oligomers has also been achieved,[5,7,10,11] with Osuka and co-workers reporting *meso-meso*, *β-β, β-β* triply linked porphyrin 'tapes' containing up to 24 porphyrin units.[12] These systems display extensive

absorption in the near-IR, with the maximum (λ_{max}) at longest wavelength occurring at 2800 nm for an oligomer comprised of 16 porphyrin units. Further extension of the porphyrin tape to 24 porphyrin units did not result in a red-shift in this absorption, indicating that the effective conjugation length of the system had been reached. Electrochemical analysis shows E_1^{ox} values of -0.28, -0.32 and -0.40 V for the tetramer, hexamer and octamer tapes respectively, and E_1^{red} values of -0.88, -0.75 and -0.65 V for the same series. This clearly shows a trend in increasing HOMO energy and decreasing LUMO energy as the oligomer length increases, resulting in highly extended π-systems with very small HOMO-LUMO gaps (the octamer tape has an E_1^{ox} - E_1^{red} value of just 0.25 V).

Two-dimensional arrays of directly fused porphyrins such as **23** and **24** have also been reported by Osuka and co-workers (Figure 2.2). These systems were synthesised by oxidative ring-closure of their *meso*-linked precursors by scandium(III) triflate and DDQ.[13,14]

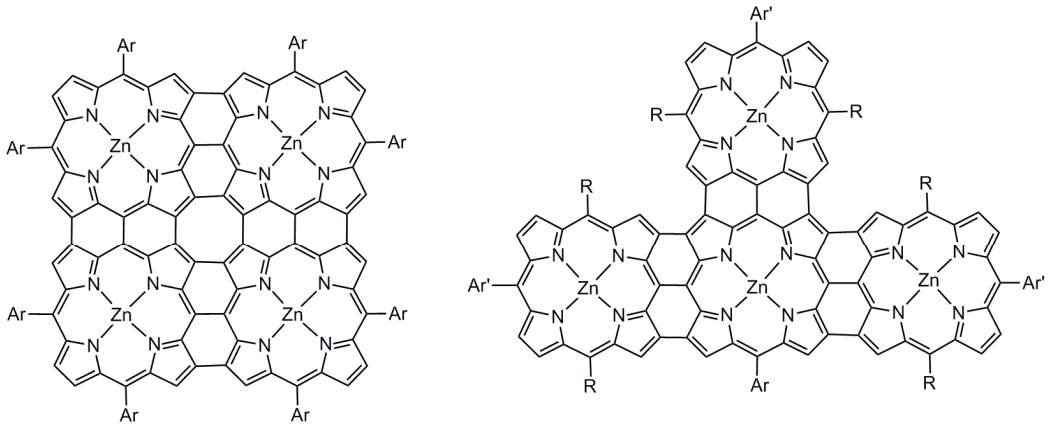

23 **24**

Figure 2.2: Two dimensional fused porphyrin arrays synthesised by Osuka and co-workers. Ar = 3,5-di(*t*-butyl)phenyl, Ar' = 4-dodecyloxyphenyl, R = C_9H_{19}.[13,14]

While these large, fused porphyrin systems exhibit absorption at long wavelengths similar to those at which linear oligomers absorb, the intensity of absorption in the near-IR is far smaller for these two-dimensional structures. Tetrameric porphyrin sheet **23** exhibits strong absorption at 756 nm, however this rapidly decreases at long wavelength, resulting in weak absorption beyond 1000 nm (logε = 3.99 at 1256 nm) and a long tail stretching into the near-IR as far as 1500 nm.[13] The UV-vis-NIR absorption spectrum of tetramer **24** shows a distinct peak in the near-IR at 1805 nm, however this peak is of low intensity (logε = 4.45).[14] This λ_{max} is at a very similar wavelength to that of the analogous linear tetramer (1813 nm).

2.1.2 Porphyrins Fused to Aromatic Groups Other than Porphyrins

While direct fusion of porphyrins has been shown to generate highly conjugated oligomers and arrays, fusion of porphyrin units to other aromatic units has also been an area of great interest in recent years. The large range of aromatic rings available, together with the possibility of their functionalisation, offers a new approach to tuning the optical and electronic properties of porphyrin units and investigating structure-property relations in such large π-systems.

As illustrated in Section 2.1.1, the smaller frontier orbital coefficients at the β-positions can have a significant effect upon the degree of delocalisation observed across a porphyrin system. Crossley and co-workers have explored the synthesis of a series of porphyrin oligomers, fused across the β-positions by 1,4,5,8-tetraazaanthracene moieties, as exemplified by tetramer **25** (Figure 2.3).[15-19]

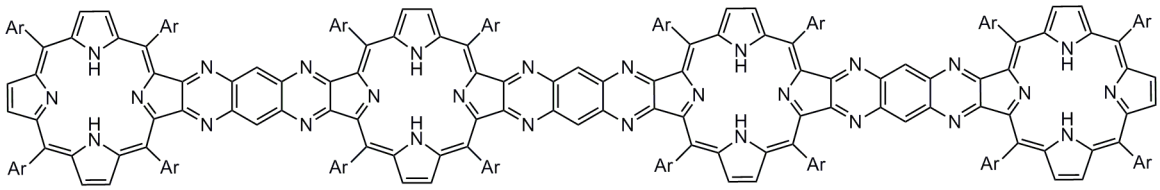

25

Figure 2.3: 1,4,5,8-tetraazaanthracene linked porphyrin tetramer synthesised by Crossley and co-workers. Ar = 3,5-di(*t*-butyl)phenyl.[18]

This long, rigid fused system extends over 56 Å, however it does not behave as a large fully delocalised aromatic network; the absorption spectrum of tetramer **25** in the near-IR exhibits a longest wavelength λ_{max} at 786 nm with very weak absorption (logε at 786 nm is only 2.88). These observations indicate that the fused tetramer is best described as consisting of weakly interacting porphyrin and bridge systems, which act as isolated aromatic units.[16]

Similar quinoxaline-fused porphyrin systems such as **26**, **27** and **28** have been reported by Imahori and co-workers (Figure 2.4).[20,21] The absorption spectra of quinoxaline-fused zinc porphyrins **26**, **27** and **28** do not show extensive absorption in the near-IR, with long wavelength Q-band maxima at just 622, 628 and 642 nm respectively. The greatest perturbation in the absorption spectra of the quinoxaline-fused porphyrins compared to a tetraaryl porphyrin however, is the dramatic broadening of the Soret band, combined with a

drop in intensity. These quinoxaline-fused porphyrins have shown promise as dyes for photovoltaic devices, with **26** exhibiting a solar-to-electricity conversion efficiency of 6.3% (in the presence of co-adsorbed chenodeoxycholic acid).[21]

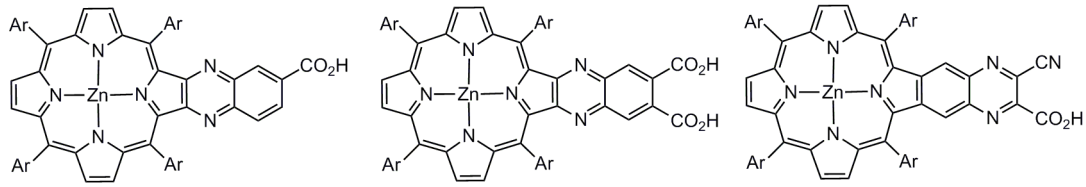

26 **27** **28**

Figure 2.4: Quinoxaline fused porphyrins synthesised by Imahori and co-workers. Ar = 2,4,6-trimethylphenyl.[20,21]

Lash and co-workers have reported the synthesis of porphyrins directly fused across the β-positions to a variety of aromatic ring systems (Figure 2.5). Porphyrins **29**, **30** and **31** exhibit absorption spectra with clearly defined Soret and Q-band regions, together with λ_{max} values at their longest wavelengths of 628, 630 and 658 nm respectively. These values are only slightly red-shifted compared to the longest wavelength λ_{max} value of 622 nm observed for octaethylporphyrin.[22] This emphasises the relatively small effect that fusion to aromatic units at the porphyrin β-positions has on the electronic structure of the porphyrin. Tetraacenaphthoporphyrin porphyrin **32** shows a larger red-shift relative to octaethylporphyrin, with Q-band absorption reaching as far as 790 nm, however, the intensity of these Q-bands is weak ($\log\varepsilon$ = 3.76 at 708 nm).[23]

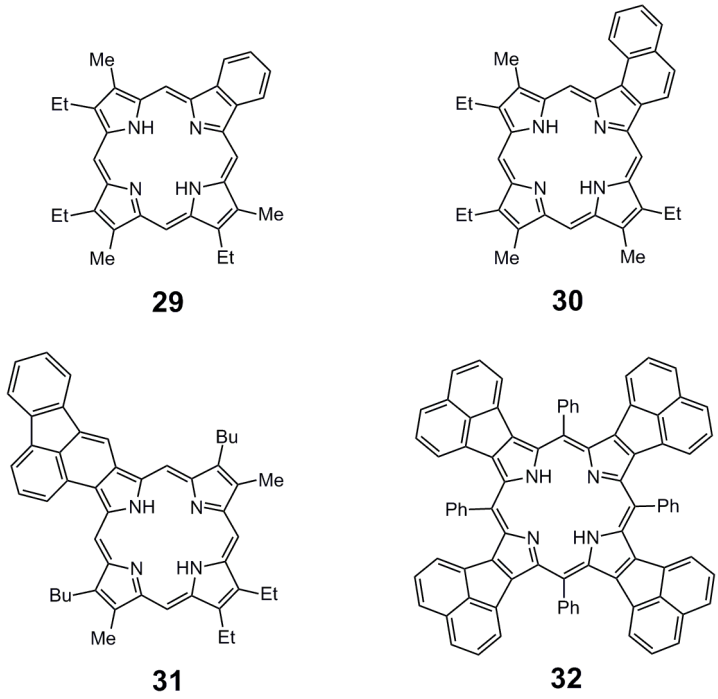

Figure 2.5: A selection of porphyrins fused to exocyclic rings reported by Lash and co-workers.[22,23]

The fusion of aromatic groups across the *meso*-positions of the porphyrin ring periphery has been attempted with many different aromatic units, yielding highly conjugated monomeric species.

Fusion of a *meso*-linked phenyl porphyrin by formation of a bond from the phenyl *ortho*-position to the porphyrin β-position was first reported by Fox and Boyle (Scheme 2.3).[24] Fused porphyrin **34** was synthesised by an intramolecular palladium-catalysed cyclisation reaction of porphyrin **33**. From a comparison of the absorption spectra of porphyrins **33** and **34**, it can be seen that fusion of a phenyl group across the *meso*- and β-positions of a porphyrin perturbs the electronic structure of the system. The absorption spectrum of fused porphyrin **34** is red-shifted with respect to porphyrin **33** and displays broader peaks, with the Soret band exhibiting a λ_{max} at 453 nm for fused porphyrin **34** compared to 406 nm for porphyrin **33**.[24] The Soret band observed for fused porphyrin **34** is more red-shifted than for porphyrin **29**, which displays a λ_{max} at 404 nm, indicating the greater influence of the *meso*-position on facilitating electronic communication between the porphyrin and the fused aromatic substituent (the coordination of copper by free-base porphyrins has little effect on the wavelength of Soret band absorption). The Q-band region of the absorption spectrum of

fused porphyrin **34** displays weak absorption which tails off around 680 nm, compared to around 570 nm for porphyrin **33**, indicating that fusion of a phenyl group results in a modest increase in π-conjugation of the porphyrin system.

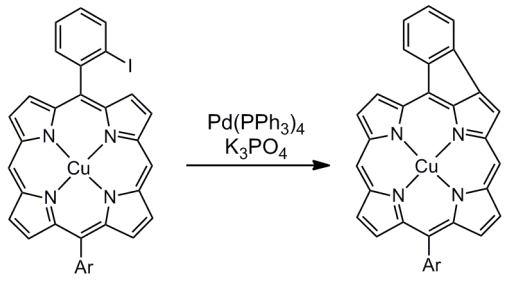

33 **34**

Scheme 2.3: Phenyl-fused porphyrins synthesised by Fox and Boyle. Ar = 3,5-dimethoxyphenyl.[24]

Porphyrins fused to phenyl groups via a carbonyl bridge have been synthesised by Callot and co-workers (Figure 2.6).[25-27] Nickel porphyrin **35** displays an absorption spectrum with a Soret band at 462 nm and a longest wavelength λ_{max} at 686 nm, while the copper analogue displays a longest wavelength λ_{max} at 695 nm. The presence of this absorption peak beyond the limit of absorption by porphyrin **34** demonstrates that the carbonyl bridge influences electron delocalisation across the aromatic system, possibly due to its mesomeric and inductive electron withdrawing effects.[27]

Porphyrins **36** and **37** are both fused to two phenyl groups via carbonyl bridges, however the degree of π-conjugation appears to be higher for porphyrin **36** which displays a longest wavelength Q-band with a λ_{max} at 826 nm compared to 776 nm observed for porphyrin **37** (Figure 2.6).[25] This highlights the sensitivity of the extent of π-electron delocalisation towards the regiochemistry of fused aromatic substituents.

Figure 2.6: Porphyrins fused to *meso*- phenyl groups via carbonyl bridges as synthesised by Callot and co-workers.[25-27] Absorption spectra of **36** (left) and **37** (right) are shown.[25]

In 2004, research led by Scott resulted in the synthesis of porphyrins fused to naphthalene units via cycloheptanone and azulenone bridges. Dispiroporphodimethene **38** was converted into *cis* and *trans* fused porphyrins **40** and **39** respectively upon exposure to light and DDQ (Scheme 2.4).[28] It can be seen from their crystal structures that these porphyrins exhibit non-planar geometries due to the steric clash between naphthyl and β-pyrrolic hydrogens. However the red-shifted absorption spectra of **39** and **40** show that the naphthalene unit is conjugated with the porphyrin ring; porphyrin **40** displays a long wavelength λ_{max} at 681 nm, while porphyrin **39** exhibits a λ_{max} at 705 nm. Fusion of porphyrins **39** and **40** to form bis(naphthoazulenone) fused porphyrin systems **41** and **42** respectively was achieved with iron(III) chloride and DDQ. These porphyrins exhibit a more planar structure and enhanced electron delocalisation than **39** and **40**, as seen by the very large red-shifts in long wavelength absorption; porphyrin **41** exhibits a λ_{max} at 1204 nm while porphyrin **42** shows a peak at 894 nm (Scheme 2.4). The significant difference in these λ_{max} values may be due to the interplay between the delocalisation pathway of the porphyrin

core and the position of the carbonyl bridges. As shown in Figure 1.14, the delocalisation pathway of π-electrons in a porphyrin lies diagonally across the core, hence two carbonyl bridges fused to the porphyrin crosswise to each other will both interact with the same porphyrinic delocalisation pathway, resulting in a larger degree of electronic communication that if the two carbonyl bridges lie opposite each other.

These results highlight the significant effects that fusion of an aromatic group may have on the electronic structure of a porphyrin. In particular it is shown that increasing the number of bonds from the porphyrin to the fused aromatic unit results in an expansion of the conjugation pathway, thereby greatly increasing the degree of electronic communication between the aromatic unit and the porphyrin ring it is fused to.

Scheme 2.4: Bis(naphthoazulenone) fused porphyrin systems synthesised by Scott and co-workers. R = ^{t}Butyl, Ar = 2,4,6-trimethylphenyl. Absorption spectra for porphyrin **41** (solid line) and **42** (dashed line) are shown.[28]

Direct fusion of a naphthalene unit to a porphyrin has been achieved by several synthetic pathways. Cammidge and co-workers demonstrated that such fused porphyrin systems could be synthesised by an intramolecular Heck reaction involving naphthalene-

linked porphyrin precursor **43** bearing a triflate group (Scheme 2.5(a)).[29] An alternative route was followed by Imahori and co-workers, where a family of mono naphthalene-fused porphyrins was synthesised by fusion of naphthalene-linked nickel porphyrin **45**, via an oxidative ring-closure reaction with iron(III) chloride (Scheme 2.5(b)).[30,31]

Scheme 2.5: Two approaches to naphthalene-fused porphyrins.[29-31] Absorption spectra of unfused naphthalene-linked porphyrin **46** (dashed line) and naphthalene-fused porphyrin **48** (solid line, ε×3 for clarity) are shown.[30] R = 2,4,6-trimethylphenyl, Ar = 2,4,6-trimethylphenyl.

The absorption spectra of naphthalene-fused porphyrins display a similar spectral shape to the unfused precursors, with distinct Soret and Q-band regions (Scheme 2.5). The

wavelengths of absorption however, are seen to red-shifted upon fusion, with porphyrin **48** displaying a λ_{max} at 682 nm, compared to the λ_{max} at 551 nm observed for the unfused zinc analogue **46**.[30] Furthermore, the intensity of the long wavelength maxima increases slightly upon fusion ($\log\varepsilon$ = 4.32 at 551 nm for **46**, $\log\varepsilon$ = 4.39 at 682 nm for **48**), although as seen for other fused systems, the intensity of the Soret band decreases upon fusion ($\log\varepsilon$ = 5.64 at 422 nm for **46**, $\log\varepsilon$ = 5.09 at 482 nm for **48**). Electrochemical studies of porphyrin **48** reveal it to possess an E_1^{ox}-E_1^{red} separation of 1.77 V whereas unfused porphyrin **46** has an E_1^{ox}-E_1^{red} separation of 2.15 V.[30] These results confirm that fusion of a naphthalene unit to a porphyrin increases the degree of conjugation in the system, thereby lowering the HOMO-LUMO gap.

Azulene, like its isomer naphthalene, is an aromatic molecule containing ten π-electrons. However, while naphthalene is colourless, azulene is dark blue. An oversimplified way to viewing this chromophore is to consider promotion of an electron from the seven membered ring to the five membered ring, resulting in the formation of two aromatic subunits; the tropylium cation and the cyclopentadienyl anion. The differences between the electronic structure of azulene and naphthalene may be expected to result in the observation of different optoelectronic properties in naphthalene- and azulene-fused porphyrin systems. In 2006 Osuka and co-workers reported the synthesis of a family of azulene-fused porphyrins (Figure 2.7).[32]

Figure 2.7: Azulene-fused porphyrins synthesised by Osuka and co-workers. The absorption spectra show an increase in red-shift upon increasing the number of fused azulene units from one (**49**, solid line) to two (**50**, dashed lined), to four (**51**, dotted line). Ar = 3,5-di(*t*-butyl)phenyl, R = 2,4,6-tri(*t*-butyl)phenyl.[32]

The unfused precursor porphyrins linked to azulene units at the *meso*-positions show absorption typical of tetraaryl porphyrins. However, fusion of the azulene units to the β-positions of the porphyrin periphery with iron(III) chloride, results in a dramatic red-shift in absorption together with a significant distortion of spectral shape (Figure 2.7). The absorption spectrum of mono-azulene fused porphyrin **49** shows a broad Soret band with a λ_{max} at 467 nm, together with a very broad Q-band region which extends into the near-IR. While the intensity of this near-IR absorption is very low, absorption is seen to reach nearly 1000 nm, with a very broad peak 890 nm.[32] This is quite different to the case of mono-naphthalene fused porphyrin **48**, which displays a much sharper peak in the near-IR than mono–azulene fused porphyrin **49** and displays no absorption beyond 780 nm. Furthermore, the intensity of this near-IR absorption is an order of magnitude greater for mono-naphthalene fused porphyrin **48** than mono-azulene fused porphyrin **49**.[30]

Increasing the number of azulene groups fused to the porphyrin ring periphery increases the degree of conjugation in the system, as seen from the absorption spectra of

azulene-fused porphyrins **50** and **51** (Figure 2.7). Bis-azulene fused porphyrin **50** shows a red-shifted absorption spectrum compared to mono-azulene fused porphyrin **49**, with a λ_{max} in the near-IR at 1014 nm, together with an increase in intensity of this near-IR absorption. Fusion of four azulene units to the porphyrin further red-shifts this near-IR absorption and increases its intensity, with a long wavelength λ_{max} at 1136 nm and absorption extending into the near-IR as far as 1250 nm.[32] The spectral shapes of absorption observed for azulene-fused porphyrins **50** and **51** are distorted from those of unfused tetraaryl porphyrins. This highlights the change in symmetries and conjugation pathways for the azulene-fused porphyrins. It is interesting to note that the azulene units of porphyrins **50** and **51** are only seen in an *anti*- arrangement, suggesting that the regiochemistry of the second, and subsequent, oxidative ring-closure reactions is influenced by the first fused azulene unit.[32] Electrochemical studies of azulene-fused porphyrins **49**, **50** and **51** reveal a decrease in the E_1^{ox}-E_1^{red} separation as the number of fused azulene units increases, with **51** exhibiting a separation of just 1.01 V, reflecting the expansion of the π-system.

Porphyrins fused to larger aromatic units such as pyrene have also been reported. Yamane and co-workers have shown that oxidative ring-closure of a pyrene-linked zinc porphyrin **52** with scandium(III) triflate and DDQ, affords pyrene-fused porphyrin **54**, while pyrene-fused nickel porphyrin **55** may be formed from the unfused precursor **53** using $PhI(OTf)_2$ and BF_3 (Scheme 2.6).[33] Furthermore, it was found that fusion only occurs when the pyrene unit bears one or more electron donating alkoxy substituents.

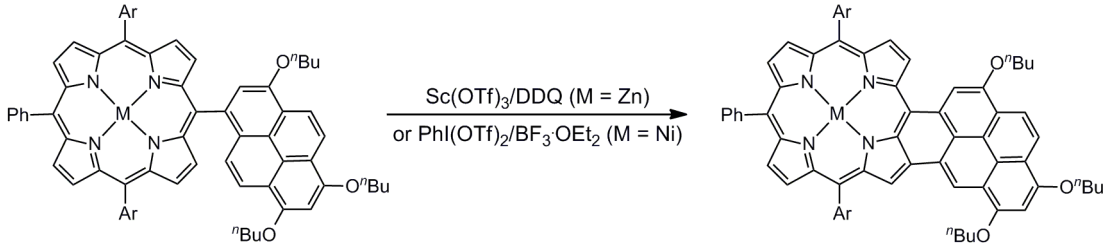

52 M = Zn
53 M = Ni
54 M = Zn
55 M = Ni

Scheme 2.6: Mono-pyrene fused porphyrins synthesised by Yamane and co-workers.[33]

The absorption spectrum of pyrene-fused nickel porphyrin **55** shows a long wavelength λ_{max} at 724 nm reflecting the increase in π-conjugation relative to an unfused

tetra-aryl porphyrin. As observed for naphthalene- and azulene-fused porphyrin systems, the intensity of UV-vis-NIR absorption in the Soret region decreases upon fusion of the aromatic unit (pyrene) to the porphyrin ring, although the intensity increases in the near-IR. This is thought to be due to a lowering of the symmetry of the π-conjugated system.[33] The longer wavelength absorption seen for mono-azulene fused porphyrin **49** compared to pyrene-fused porphyrin **55**, emphasises that increasing the number of π-electrons in the aromatic unit does not necessarily lead to an increase in conjugation across the fused porphyrin system.

Very recently, and stimulated perhaps by the publication of my own work[34] (see Chapter 3), Thompson and co-workers reported the synthesis of bis-pyrene fused porphyrin dimer **58** from monomer **56** via dimer **57** (Scheme 2.7).[35] Dimers **57** and **58** show strong absorption in the near-IR, with longest wavelength maxima at 1141 and 1323 nm respectively. While the λ_{max} value observed for dimer **57** is comparable to those of other triply-linked porphyrin dimers, the value for dimer **58** is nearer to that observed for triply-linked porphyrin trimers, reflecting the expansion of the π-conjugated pathway upon fusion of the pyrene units to the porphyrin dimer.[7] This high degree of conjugation is reflected in the electrochemistry of dimer **58** which exhibits an E_1^{ox} of -0.13 V and an E_1^{red} of -0.97 V leading to a very small E_1^{ox}-E_1^{red} separation of just 0.84 V. Furthermore, the presence of terminal pyrene groups in dimers **57** and **58** appears to enhance the intensity of absorption in the near-IR compared to the analogous unsubstituted fused porphyrin dimer.[35]

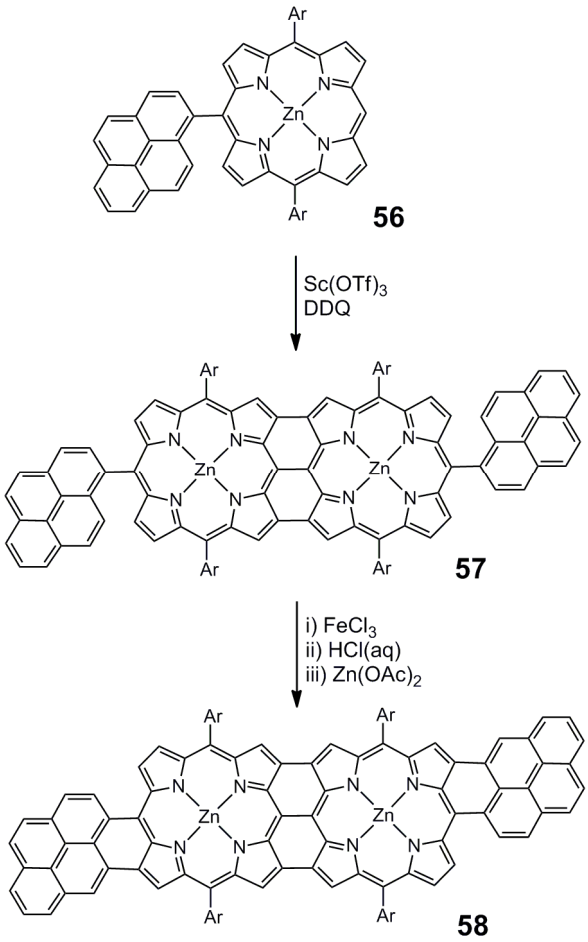

Scheme 2.7: Synthesis of pyrene-fused porphyrin dimers reported by Thompson and co-workers. Ar = 3,5-di(*t*-butyl)phenyl.[35]

After the publication of my work detailed in Chapter 3,[34] Wu and co-workers reported the synthesis of perylene fused porphyrin monomers **59**, **60** and **61** from the *meso*-linked perylene porphyrin precursors by oxidative ring-closure using either iron(III) chloride or scandium(III) triflate and DDQ (Figure 2.8).[36,37] The degree of π-conjugation observed in the system increases with the number of bonds between the porphyrin and perylene units, with doubly-linked perylene-porphyrin **59** exhibiting a longest wavelength λ_{max} at 804 nm, while triply-linked perylene-porphyrin displays a λ_{max} at 897 nm.[36]

Scheme 2.7 and Figure 2.8 illustrate that fusion reactions do not always require electron-donating substituents on the aromatic ring. This is contrary to the findings reported by Yamane and co-workers,[33] however it is likely that the need for such substituents to facilitate oxidative ring-closure depends upon the HOMO energy of the aromatic ring; larger aromatic systems have higher energy HOMO's and hence may more readily undergo

oxidative ring-closure to form bonds to the porphyrin ring, whereas smaller rings may require activation by electron donating substituents.

R

Figure 2.8: Perylene-fused porphyrin monomers reported by Wu and co-workers. Ar = 3,5-di(*t*-butyl)phenyl.[36,37] Absorption spectra are shown for **59** (black line) and **60** (red line).[36]

The push-pull nature of porphyrins **59** and **60** enhances the extent of π-electron delocalisation, compared to perylene-fused porphyrin **61** (which exhibits a longest wavelength λ_{max} at 775 nm).[37] The effect of this push-pull system on the electronic structure of perylene-fused porphyrins may be seen by comparison of the electrochemical data of porphyrin **59** with that of porphyrin **61**. While both porphyrins **59** and **61** have similar E_1^{ox}-E_1^{red} separations of 1.52 and 1.54 V respectively, the first reduction potential of **59** is much less negative than for **61**, with a value of -1.15 V for **59** compared to the value of -1.42 V observed for **61**. While this may in part be due to the coordination of different metal ions, the magnitude of the difference indicates that the electron accepting nature of porphyrin **59**

(which arises due to the presence of the imide group) is also influencing the energies of the HOMO and LUMO.[36]

Wu and co-workers also reported the synthesis of perylene-fused porphyrin dimer **62** from the unfused dimer precursor, via oxidative ring-closure with scandium(III) triflate and DDQ (Figure 2.9).[37] As expected, fused dimer **62** displays absorption into the near-IR with a longest wavelength λ_{max} value at 952 nm. This maximum lies at longer wavelength than the near-IR maximum observed for doubly linked porphyrin **21**, (Figure 2.1) which has a λ_{max} value at 735 nm,[9] illustrating efficient expansion of the π-system upon the incorporation of a fused perylene linking group.

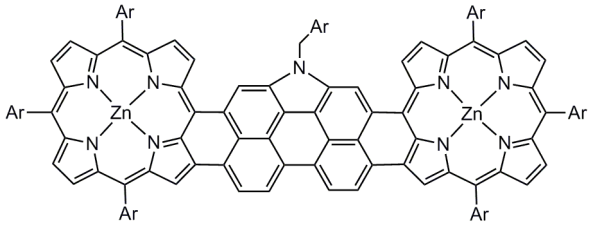

62

Figure 2.9: Perylene-fused porphyrin dimer reported by Wu and co-workers. Ar = 3,5-di(*t*-butyl)phenyl.[37]

Boron dipyrromethene (BODIPY) is a strongly UV-vis absorbing dye and displays an excellent geometry match to that of the porphyrin ring periphery. Following the publication of my work detailed in Chapters 3 and 4,[34,38] Wu and co-workers very recently reported the synthesis of BODIPY-fused porphyrins **63** and **64** from their unfused *meso*-linked precursors by oxidative ring-closure reaction with iron(III) chloride (Figure 2.10).[39]

Figure 2.10: BODIPY-fused porphyrin dyes synthesised by Wu and co-workers. Ar = 3,5-di(*t*-butyl)phenyl. Absorption spectra of **63**, **64** and their unfused precursors are shown.[39]

The highly conjugated nature of the π-system of BODIPY-fused porphyrins is evident from the absorption spectra of **63** and **64**, which display long wavelength maxima at 890 and 1040 nm respectively (Figure 2.10).[39] While the intensity of this near-IR absorption is lower than for the Soret region of the spectra, it is comparable to the intensity of near-IR absorption observed for other fused porphyrin systems.[32] Furthermore, the near-IR λ_{max} of bis-BODIPY fused porphyrin **64** is red-shifted with respect to bis-azulene fused porphyrin **50**, despite the similar molecular size of the BODIPY and azulene units. This may in part be due to the presence of three bonds between each BODIPY unit and the porphyrin, compared to azulene-fused porphyrin **50** where only two such bonds are present.

BODIPY moieties fused across the β-positions of the porphyrin ring have been reported by Smith and co-workers.[40] BODIPY-fused zinc porphyrin **66** was formed by condensation of a copper formylpyrroloporphyrin **65** with 2,4-dimethylpyrrole, followed by

coordination of boron trifluoride and metalation of the porphyrin with zinc(II) acetate (Scheme 2.8).

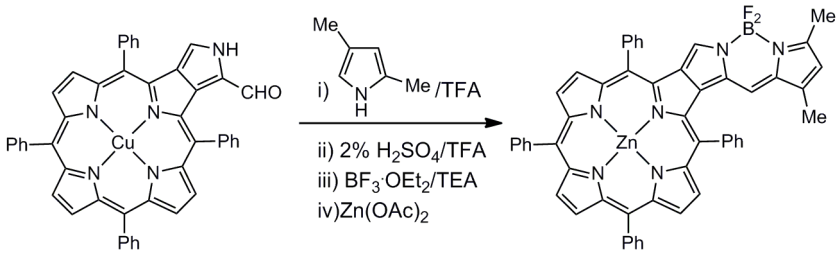

65 **66**

Scheme 2.8: Synthesis of BODIPY-fused porphyrins by Smith and co-workers.[40]

The degree of π-conjugation present in β-fused porphyrin **66** is lower than for *meso*-fused porphyrin **63**, with porphyrin **66** exhibiting an absorption spectrum with a longest wavelength maximum at 676 nm.[40] This λ_{max} value occurs at much shorter wavelength than for the longest wavelength maximum observed for porphyrin **63**, indicating that the degree of conjugation in a fused porphyrin system depends strongly upon site of fusion and the number of bonds formed.

From this review of fused porphyrins with extended π-conjugation, it can be seen that the degree of delocalisation of electron density across a fused porphyrin system depends upon many factors. These include the size of the aromatic unit being fused to the porphyrin, the position at which fusion to the porphyrin ring occurs and the number of bonds formed between the aromatic group and the porphyrin. Furthermore, the electronic properties of the system may be tuned by the presence of electron withdrawing or donating substituents on either the porphyrin or the aromatic unit fused to it.

While many fused porphyrin systems have been discussed above, it is interesting to note that very few exhibit near-IR absorption beyond 800 nm, and of those that do, even fewer display intense absorption at such long wavelengths. It is therefore of interest to synthesise a new class of fused porphyrin systems which display intense absorption in the near-IR beyond 800 nm. Furthermore, the high energy HOMO and low energy LUMO levels expected from such novel systems could result in fused porphyrins capable of efficient exciton formation, as well as facile oxidation and reduction, which would be highly desirable for charge transport materials. In addition, the potential for a fused porphyrin system to

find application as a charge transport material would be greatly enhanced if it possessed a planar structure of discotic or near-discotic shape, due to the possibility of the formation of liquid crystal phases. Combined with intense absorption of light over a large range of wavelengths, the optoelectronic properties of these fused porphyrins could also render such novel dyes suitable for use in photovoltaic cells, where efficient absorption of solar radiation and photogeneration of electrons and holes is crucial.

2.2 Anthracene-Fused Porphyrins

2.2.1 Background and Previous Work

In 1975, Yen proposed the synthesis of fully fused tetra-anthracene porphyrin **68** by dehydrogenation of unfused *meso*-linked tetra-anthracene porphyrin precursor **67** (Scheme 2.9), writing that such a fused system 'may exhibit graphite-like properties such as electrical conduction'.[41]

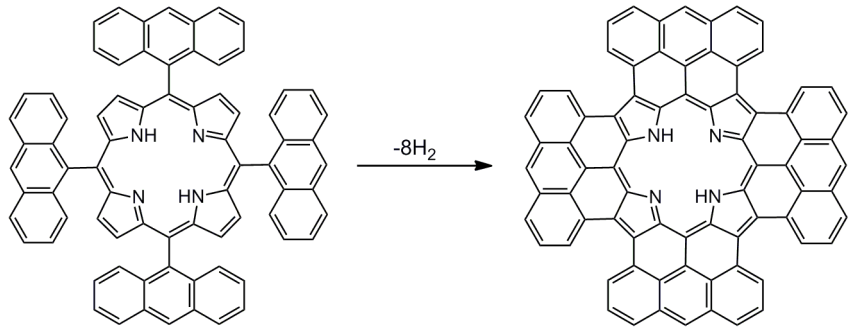

67 **68**

Scheme 2.9: Formation of a tetra-anthracene fused porphyrin by dehydrogenation of an unfused precursor.[41]

Indeed, a porphyrin fused to four anthracenes is an attractive target; the good symmetry match between the anthracene and the porphyrin periphery suggests the system is likely to adopt a near-planar geometry, while the disc-like shape could facilitate the formation of π-stacked aggregates, which may lead to the construction of columnar liquid crystals. Furthermore the large number of π-conjugated electrons in the system, combined with fusion of the anthracene units across all of the porphyrin β-positions, may be expected to facilitate a high degree of electron delocalisation. The high energy HOMO and low energy

LUMO levels which may arise as a consequence of this delocalisation could lead to facile oxidation and reduction, enabling efficient hole or electron injection into the bulk material. In addition, the resultant small HOMO-LUMO gap may allow the photogeneration of excitons which could be exploited in photovoltaic devices. Such a fused porphyrin system, with a high degree of conjugation, may be expected to display an absorption spectrum which extends far into the near-IR. This absorption may be predicted to exhibit sharp maxima due to the high symmetry of the fused tetra-anthracene porphyrin system.

While tetra-anthracene fused porphyrin **68** was proposed over 35 years ago, the synthesis of such a system is challenging; no reports were published concerning the synthesis of anthracene-fused porphyrins in the years which followed Yen's suggestion. However, in 2007 I began my Part II Master's project which led to the first report of anthracene-fused porphyrin systems.[42] My target compounds were mono-anthracene fused porphyrins, as these were expected to be more synthetically accessible than tetra-anthracene fused porphyrin systems. It was hoped that synthetic procedures found to be successful in the synthesis of mono-anthracene fused porphyrins would enable a route to be found to porphyrins fused to multiple anthracene units.

The synthetic pathway to mono-anthracene fused porphyrins, devised during my Part II work, is shown in Scheme 2.10. Suzuki coupling of bromoanthracene **70** to porphyrin boronic ester **69** yielded the corresponding anthracene-linked porphyrin **75**. In order to fuse the anthracene unit to the porphyrin ring of **75**, oxidative ring-closure conditions involving scandium(III) triflate and DDQ were employed, as these have commonly be found to successfully fuse aromatic substituents to the porphyrin periphery.[5,33] When subjected to these conditions however, no reaction of **75** was observed.

The observation that electron rich groups linked to the periphery of an aromatic substituent are necessary for fusion to a porphyrin to occur, has been noted by Yamane and co-workers, regarding the synthesis of mono-pyrene fused porphyrins systems.[33] Hence it was decided to test whether anthracenes substituted with electron donating alkoxy groups would be more amenable to the fusion reaction.

In order to ensure efficient electron donation to the sites of fusion, it was decided to synthesise 1,8-methoxy substituted 10-bromoanthracene. When unsubstituted anthracene is

reacted with bromine, substitution occurs on the central ring of the anthracene unit, i.e. at the 9 and 10 positions (Figure 2.11). However, the presence of methoxy groups at the 1- and 8- positions of an anthracene were found to increase the reactivity of positions *para* to these substituents. As a result, bromination of 1,8-dimethoxyanthracene with bromine or NBS led to an inseparable mixture of bromoanthracenes **71** and **73**. This mixture of anthracenes was subjected to Suzuki coupling conditions with porphyrin **69** to give anthracene-linked porphyrins **74** and **76**, which also proved impossible to separate.

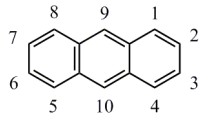

Figure 2.11: IUPAC numbering system for anthracene species.[43]

Fusion of this mixture of isomers with scandium(III) triflate and DDQ, led to complete consumption of the starting material, however only doubly linked porphyrin **78** was isolated. It is thought that porphyrin **80** was formed in the reaction, however its low solubility resulted in it being lost during silica chromatography.

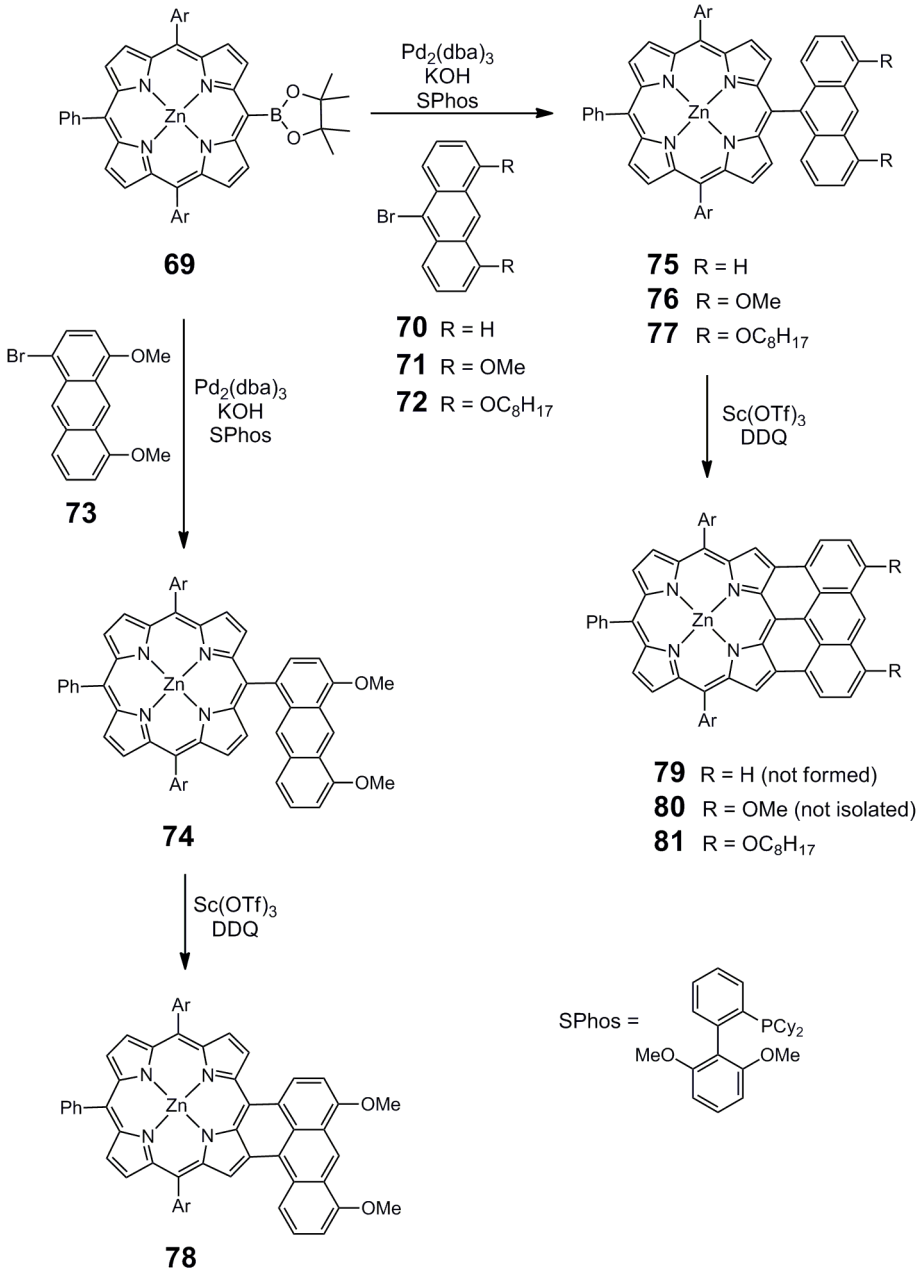

Scheme 2.10: Synthesis of mono-anthracene fused porphyrin systems. Ar = 3,5-di(*t*-butyl)phenyl.[42]

In order to achieve regioselective synthesis of a 10-bromo-1,8-dialkoxyanthracene, it is necessary to protect the electron rich oxygen atoms in the 1- and 8-positions with poorly electron donating groups, thereby creating a system which favours bromination on the central anthracene ring (Scheme 2.11). This procedure was achieved by introducing acetoxy substituents at the 1- and 8-positions which facilitate bromination exclusively at the 10-position of anthracene **84** in 45% yield. Hydrolysis of these acetoxy groups proceeded in a near quantitative yield and subsequent alkylation with octylbromide gave 10-bromo-1,8-

bis(octyloxy)anthracene **72** in 41% yield; the introduction of octyl chains was designed to increase the solubility of the final fused porphyrin.

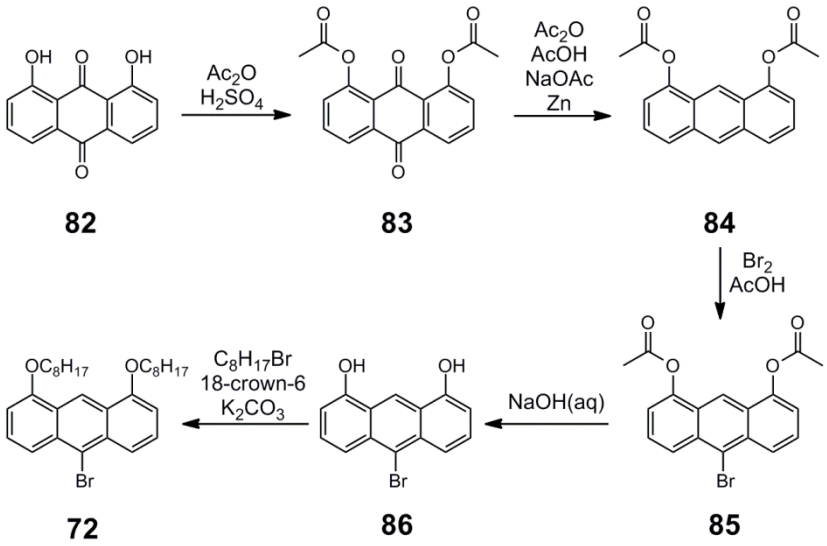

Scheme 2.11: Regioselective synthesis of 10-bromo-1,8-bis(octyloxy)anthracene 72.[42]

Suzuki coupling of bromoanthracene **72** with porphyrin **69** resulted in the formation of anthracene-linked porphyrin **77** in 36% yield, which underwent an oxidative ring-closure reaction in the presence of scandium(III) triflate and DDQ to give triply linked porphyrin **81** in 82% yield (Scheme 2.10).

Expansion of a porphyrin π-system by fusion to an anthracene unit greatly perturbs the electronic structure, as seen from the dramatic differences between the absorption spectra of unfused anthracene-linked porphyrin **77**, and anthracene-fused porphyrins **78** and **81** (Figure 2.12). Anthracene-fused porphyrins **78** and **81** exhibit highly red-shifted absorption, with longest wavelength absorption maxima at 725 and 855 nm respectively, indicating a high degree of electronic communication between the anthracene and porphyrin units. The greater red-shift in absorption observed for **81** compared to **78** reveals that increasing the number of bonds between the porphyrin and the anthracene increases the size of the π-conjugation pathway, lowering the HOMO-LUMO gap. This is reflected by the optical gaps of porphyrins **78** and **81**, measured at their near-IR maxima, which were calculated to be 1.71 and 1.45 eV respectively. Furthermore, the significant distortion of the spectral shape observed for both **81** and **78** arises from the formation of a new π-system upon fusion with reduced symmetry (relative to that of the unfused porphyrin).

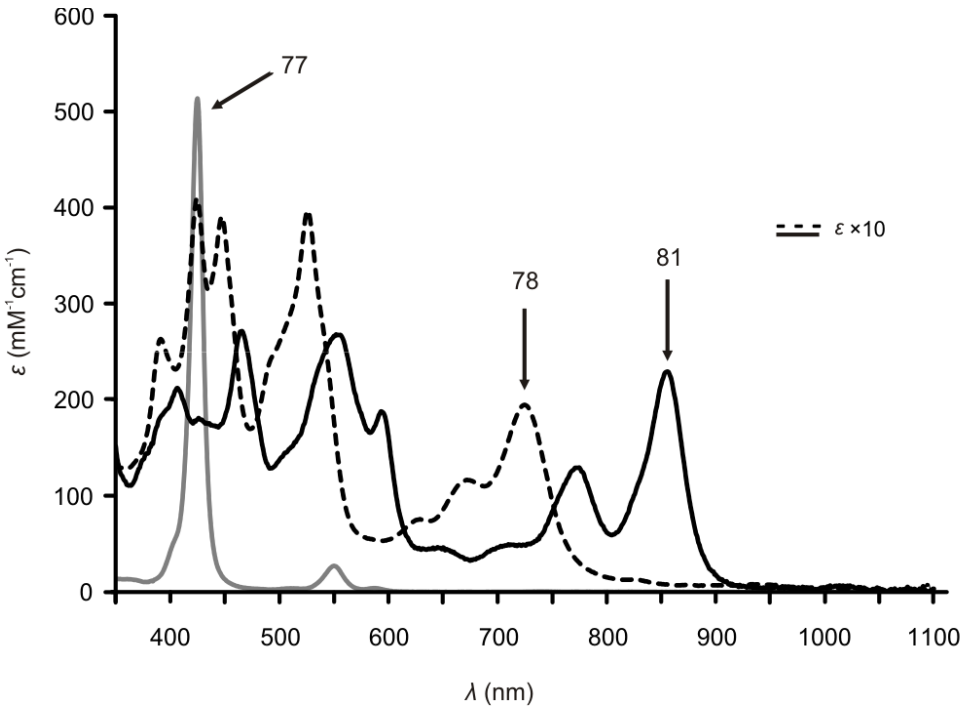

Figure 2.12: UV-vis-NIR absorption spectra in $CHCl_3$ for **77** (grey), **78** (ε × 10 for clarity, black dash) and **81** (ε × 10 for clarity, black solid line).[42]

Compared to the absorption spectra of other fused porphyrin systems, such as mono-naphthalene fused porphyrin **48** and mono-azulene fused porphyrin **49** (Scheme 2.5 and Figure 2.7), anthracene-fused porphyrins **78** and **81** exhibit unusually sharp absorption in the near-IR. This is probably due to the greater symmetry of the anthracene-porphyrin π-system. It may therefore be concluded that a porphyrin fused to multiple anthracene units would be expected to exhibit very sharp bands deep into the near-IR. The absorption by **81** across the whole visible region, combined with the sharp and relatively intense absorption in the near-IR, suggests potential application of **81** as a dye for photovoltaic devices, where efficient absorption of light across the visible and near-IR regions is highly desirable.

The synthesis of mono-anthracene fused porphyrins **78** and **81**, carried out during my Part II project, opens up a new class of near-IR dyes which have never before been reported, and which could show potential in a variety of applications including dye-sensitised solar cells.

2.2.2 Project Aims

From the review of fused porphyrin systems given in this chapter, it may be seen that porphyrins fused to aromatic units across multiple positions on the ring periphery exhibit absorption which extends into the near-IR, together with small HOMO-LUMO gaps. Such properties may allow application of these dyes to a broad range of emerging technologies. The synthesis of mono-anthracene fused porphyrins, carried out during my Part II work, demonstrates that these novel systems also display such desirable characteristics, but have the advantage of higher symmetry than many of the fused systems described in this chapter, facilitating sharper, stronger near-IR absorption. In addition such anthracene-fused porphyrins may be expected to display near-planar geometries. Hence the aim of this project is to synthesise a family of porphyrins fused to multiple anthracene units and explore their optical and electronic properties. In addition the application of anthracene-fused porphyrins as sensitisers for dye-sensitised solar cells will also be explored. Since one of the requirements for a sensitiser is that is absorbs light up to around 920 nm, mono-anthracene fused porphyrins will be investigated for this application.

2.3 References

(1) Vicente, M. G. H.; Cancilla, M. T.; Lebrilla, C. B.; Smith, K. M. *Chem. Commun.* **1998**, 2355-2356.

(2) Jaquinod, L.; Siri, O.; Khoury, R. G.; Smith, K. M. *Chem. Commun.* **1998**, 1261-1262.

(3) Anderson, H. L. *Chem. Commun.* **1999**, 2323-2330.

(4) Sahoo, A. K.; Nakamura, Y.; Aratani, N.; Kim, K. S.; Noh, S. B.; Shinokubo, H.; Kim, D.; Osuka, A. *Org. Lett.* **2006**, *8*, 4141-4144.

(5) Tsuda, A.; Osuka, A. *Science* **2001**, *293*, 79-82.

(6) Tsuda, A.; Furuta, H.; Osuka, A. *Angew. Chem. Int. Ed.* **2000**, *39*, 2549-2552.

(7) Cheng, F.; Zhang, S.; Adronov, A.; Echegoyen, L.; Diederich, F. *Chem. Eur. J.* **2006**, *12*, 6062-6070.

(8) Fendt, L. A.; Fang, H.; Plonska-Brzezinska, M. E.; Zhang, S.; Cheng, F.; Braun, C.; Echegoyen, L.; Diederich, F. *Eur. J. Org. Chem.* **2007**, 4659-4673.

(9) Tsuda, A.; Furuta, H.; Osuka, A. *J. Am. Chem. Soc.* **2001**, *123*, 10304-10321.

(10) Tsuda, A.; Osuka, A. *Adv. Mater.* **2002**, *14*, 75-79.

(11) Tsuda, A.; Nakamura, Y.; Osuka, A. *Chem. Commun.* **2003**, 1096-1097.

(12) Ikeda, T.; Aratani, N.; Osuka, A. *Chem. Asian J.* **2009**, *4*, 1248-1256.

(13) Nakamura, Y.; Aratani, N.; Shinokubo, H.; Takagi, A.; Kawai, T.; Matsumoto, T.; Yoon, Z. S.; Kim, D. Y.; Ahn, T. K.; Kim, D.; Muranaka, A.; Kobayashi, N.; Osuka, A. *J. Am. Chem. Soc.* **2006**, *128*, 4119-4127.

(14) Nakamura, Y.; Jang, S. Y.; Tanaka, T.; Aratani, N.; Lim, J. M.; Kim, K. S.; Kim, D.; Osuka, A. *Chem. Eur. J.* **2008**, *14*, 8279-8289.

(15) Crossley, M. J.; Burn, P. L. *J. Chem. Soc., Chem. Commun.* **1987**, 39-40.

(16) Lü, T. X.; Reimers, J. R.; Crossley, M. J.; Hush, N. S. *J. Phys. Chem.* **1994**, *98*, 11878-11884.

(17) Crossley, M. J.; Burn, P. L.; Langford, S. J.; Prashar, J. K. *J. Chem. Soc., Chem. Commun.* **1995**, 1921-1923.

(18) Crossley, M. J.; Burn, P. L. *J. Chem. Soc., Chem. Commun.* **1991**, 1569-1571.

(19) Crossley, M. J.; Govenlock, L. J.; Prashar, J. K. *J. Chem. Soc., Chem. Commun.* **1995**, 2379-2380.

(20) Eu, S.; Hayashi, S.; Umeyama, T.; Matano, Y.; Araki, Y.; Imahori, H. *J. Phys. Chem. C.* **2008**, *112*, 4396-4405.

(21) Kira, A.; Matsubara, Y.; Iijima, H.; Umeyama, T.; Matano, Y.; Ito, S.; Niemi, M.; Tkachenko, N. V.; Lemmetyinen, H.; Imahori, H. *J. Phys. Chem. C* **2010**, *114*, 11293-11304.

(22) Lash, T. D.; Werner, T. M.; Thompson, M. L.; Manley, J. M. *J. Org. Chem.* **2001**, *66*, 3152-3159.

(23) Spence, J. D.; Lash, T. D. *J. Org. Chem.* **2000**, *65*, 1530-1539.

(24) Fox, S.; Boyle, R. W. *Chem. Commun.* **2004**, 1322-1323.

(25) Richeter, S.; Jeandon, C.; Kyritsakas, N.; Ruppert, R.; Callot, H. J. *J. Org. Chem.* **2003**, *68*, 9200-9208.

(26) Richeter, S.; Jeandon, C.; Ruppert, R.; Callot, H. J. *Tetrahedron Lett.* **2001**, *42*, 2103-2106.

(27) Callot, H. J.; Schaeffer, E.; Cromer, R.; Metz, F. *Tetrahedron* **1990**, *46*, 5253-5262.
(28) Gill, H. S.; Harmjanz, M.; Santamaría, J.; Finger, I.; Scott, M. J. *Angew. Chem. Int. Ed.* **2004**, *43*, 485-490.
(29) Cammidge, A. N.; Scaife, P. J.; Berber, G.; Hughes, D. L. *Org. Lett.* **2005**, *7*, 3413-3416.
(30) Tanaka, M.; Hayashi, S.; Eu, S.; Umeyama, T.; Matano, Y.; Imahori, H. *Chem. Commun.* **2007**, 2069-2071.
(31) Hayashi, S.; Tanaka, M.; Hayashi, H.; Eu, S.; Umeyama, T.; Matano, Y.; Araki, Y.; Imahori, H. *J. Phys. Chem. C.* **2008**, *112*, 15576-15585.
(32) Kurotobi, K.; Kim, K. S.; Noh, S. B.; Kim, D.; Osuka, A. *Angew. Chem. Int. Ed.* **2006**, *45*, 3944-3947.
(33) Yamane, O.; Sugiura, K.; Miyasaka, H.; Nakamura, K.; Fujimoto, T.; Nakamura, K.; Kaneda, T.; Sakata, Y.; Yamashita, M. *Chem. Lett.* **2004**, *33*, 40-41.
(34) Davis, N. K. S.; Thompson, A. L.; Anderson, H. L. *Org. Lett.* **2010**, *12*, 2124-2127.
(35) Diev, V. V.; Hanson, K.; Zimmerman, J. D.; Forrest, S. R.; Thompson, M. E. *Angew. Chem. Int. Ed.* **2010**, *49*, 5523-5526.
(36) Jiao, C.; Huang, K. W.; Chi, C.; Wu, J. *J. Org. Chem.* **2011**, *76*, 661-664.
(37) Jiao, C.; Huang, K. W.; Guan, Z.; Xu, Q. H.; Wu, J. *Org. Lett.* **2010**, *12*, 4046-4049.
(38) Davis, N. K. S.; Thompson, A. L.; Anderson, H. L. *J. Am. Chem. Soc.* **2011**, *133*, 30-31.
(39) Jiao, C.; Zhu, L.; Wu, J. *Chem. Eur. J.* **2011**, *17*, 6610-6614.
(40) Tan, K.; Jaquinod, L.; Paolesse, R.; Nardis, S.; Di Natale, C.; Di Carlo, A.; Prodi, L.; Montalti, M.; Zaccheroni, N.; Smith, K. M. *Tetrahedron* **2004**, *60*, 1099-1106.
(41) Yen, T. F. *The Role of Trace Metals in Petroleum*; Ann Arbor Science Publishers: Ann Arbor, 1975.
(42) Davis, N. K. S.; Pawlicki, M.; Anderson, H. L. *Org. Lett.* **2008**, *10*, 3945-3947.
(43) Moss, G. P. *Pure Appl. Chem.* **1998**, *70*, 143-216.

Chapter 3: Bis-Anthracene Fused Porphyrins[a]

Chapter 3 describes the synthesis and characterisation of bis-anthracene fused porphyrins. The formation of a bis-anthracene fused porphyrin monomer requires a two-step fusion process; while the analogous bis-anthracene fused porphyrin dimer is formed in a one-pot reaction from unfused monomer. These large π-systems suffer from strong aggregation effects, so bulky aryl ether groups on the anthracene moieties are required to limit π-stacking between molecules. The optical and electronic properties of these chromophores are investigated and the extensive absorption they display in the near-IR, together with small HOMO-LUMO gaps, indicates an excellent degree of electronic delocalisation across the fused systems.

[a] Part of this chapter has been published in *'Bis-Anthracene Fused Porphyrins: Synthesis, Crystal Structure, and Near-IR Absorption.'* Nicola K. S. Davis, Amber L. Thompson and Harry L. Anderson, *Organic Letters*, **2010**, *12*, 2124 — 2127.

3.1 Introduction

Synthesis of bis-anthracene fused porphyrin monomers and dimers will enable investigation into the effect that systematic expansion of the π-system along one axis has on the optical and electronic properties of the porphyrin system. Furthermore this project will explore how the properties of fused porphyrin tapes can be tuned by capping with an anthracene unit, as well as elucidating the potential of these anthracene-fused porphyrins as materials for charge transport.

During my previous work in the Anderson group, I showed that a single anthracene unit may be fused to the porphyrin periphery by oxidative ring-closure with scandium(III) triflate and DDQ (Section 2.2.1).[1] These reagents have also been shown by Osuka and co-workers to yield triply linked porphyrin dimers in a one-pot reaction from their unfused monomeric precursors.[2] It is therefore feasible to expect that these reaction conditions would yield the desired bis-anthracene fused porphyrin monomer **87** from the unfused bis-anthracene linked porphyrin monomer **88**, and the bis-anthracene fused porphyrin dimer **89** from the unfused mono-anthracene linked porphyrin monomer **90** (Scheme 3.1).

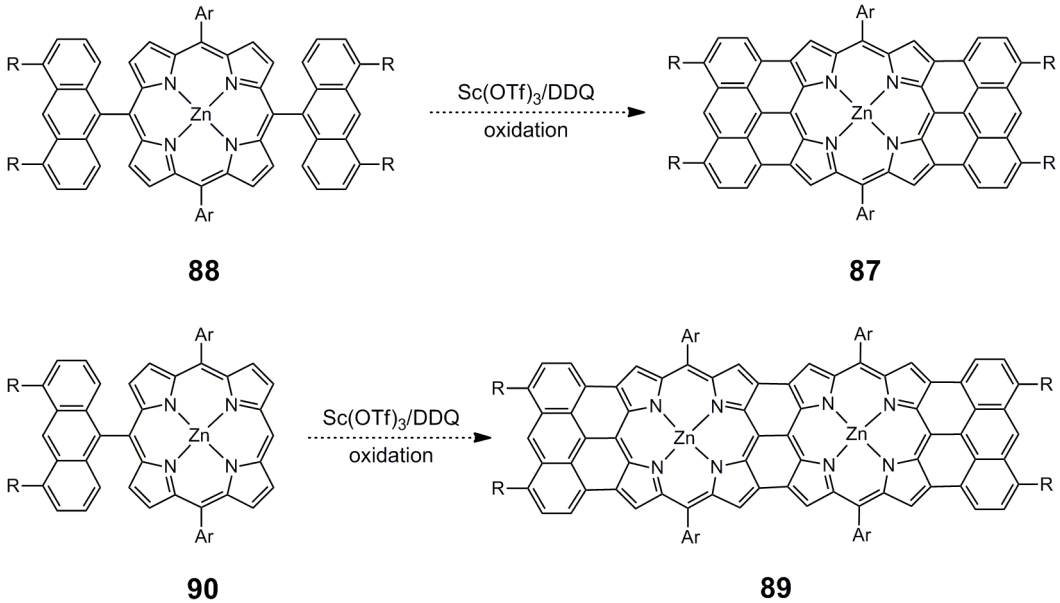

Scheme 3.1. Proposed reaction pathway for the formation of bis-anthracene fused porphyrins from their unfused precursors by oxidative ring-closure reactions. R represents solubilising side chains.

3.2 Bis-Anthracene Fused Porphyrins Bearing Octyloxy Substituents

3.2.1 Molecular Design

The initial synthetic targets were anthracene-fused porphyrins **91** and **92** (Figure 3.1).

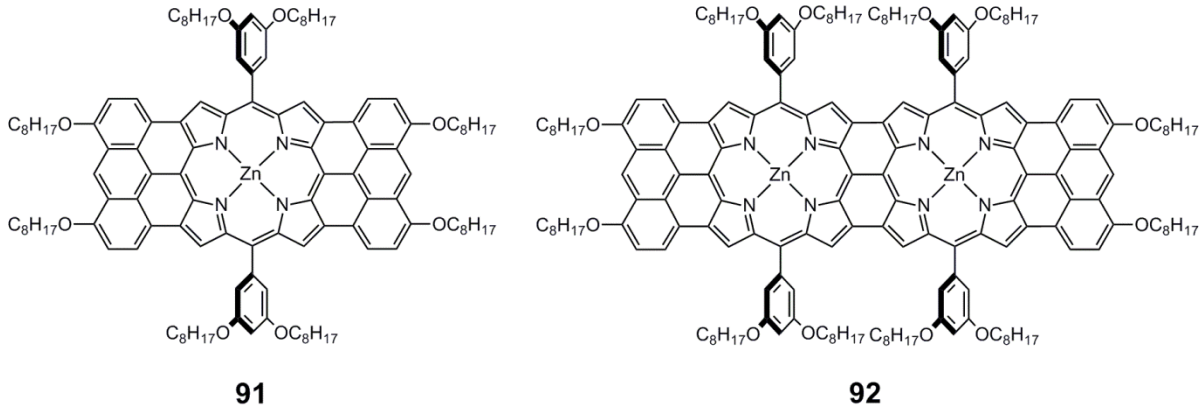

Figure 3.1: Target bis-anthracene fused porphyrin monomer (**91**) and dimer (**92**).

Large π-systems have the potential to suffer from both poor solubility and aggregation effects. Target porphyrins **91** and **92** were therefore designed to bear aryl rings directly attached to the porphyrin periphery at the *meso*-positions. These aryl groups do not sit in a planar arrangement, but are twisted with respect to the porphyrin core due to steric hindrance, limiting the potential for π-stacking between molecules. Octyloxy chains were chosen as substituents, both for these aryl groups and for the anthracene units, because the presence of long hydrocarbon chains promotes solubility in organic solvents. In addition, the research I conducted during my Part II project demonstrated that it is necessary for the anthracene unit to bear electron-rich substituents in order to facilitate fusion to the porphyrin periphery.[1] The molecular design of **91** and **92** was therefore predicted to limit aggregation, ensure solubility and enable ring closure under oxidative fusion conditions.

3.2.2 Synthetic Approaches to Anthracene-Linked Porphyrins

Porphyrins with two anthracene units linked to opposite *meso*-positions have been reported in the literature.[3-5] There are two main approaches to the synthesis of these compounds. The first route involves an acid-catalysed condensation reaction between a substituted dipyrromethane and an aldehyde. This method was employed by Osuka and co-workers in

the synthesis of **93**, and by Anderson and co-workers in the synthesis of **96** (Scheme 3.2). In both cases the major product was the corresponding hexaphyrin. This pathway has the advantage of requiring few reaction steps (although synthesis of the necessary anthracene-dipyrromethane may be non-trivial), but suffers from low yields (6% for **93** and 22% for **96**).

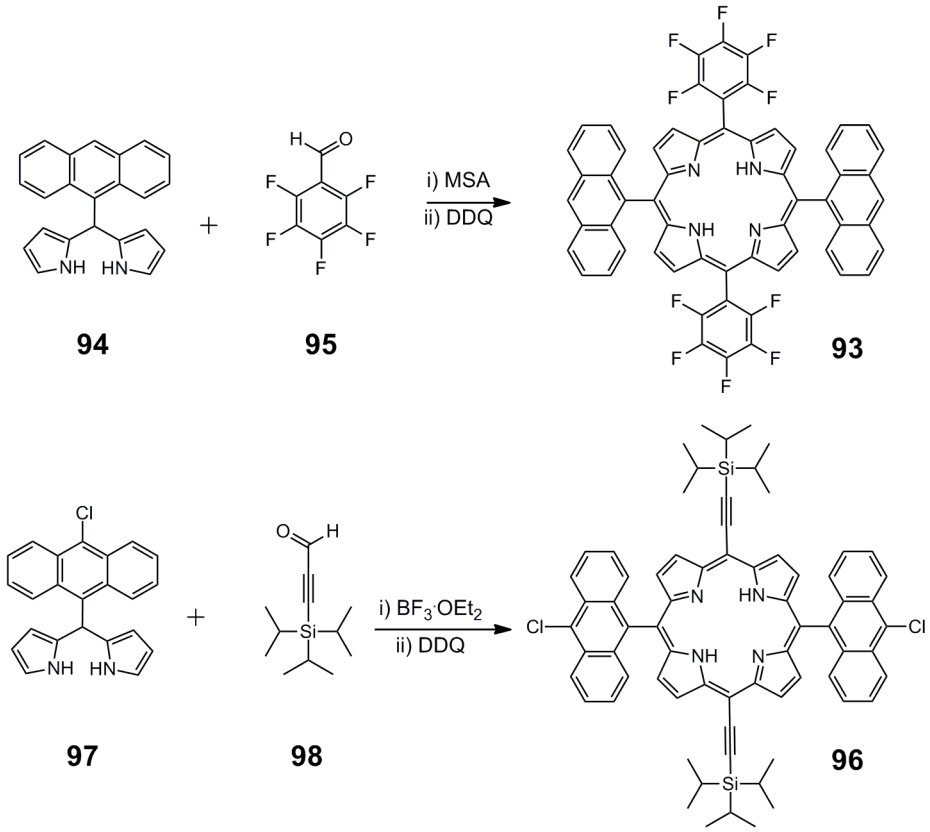

Scheme 3.2: Bis-anthracene linked porphyrins synthesised by Osuka (**93**) and Anderson (**96**) by condensation reaction.[3,5]

The second route involves a palladium-catalysed coupling reaction between a porphyrin and two anthracene units. Recently Bonifazi and co-workers have reported the synthesis of bis-anthracene linked porphyrins **99** and **100** in 10% — 12% yields (Scheme 3.3).[4] In this case the anthracene boronic esters (**101** and **102**) are formed by a palladium-catalysed coupling reaction between their bromoanthracene precursors and pinacolborane. These anthracene boronic esters then undergo a Suzuki reaction with a di-iodo porphyrin (**103**) to give the anthracene-linked products.

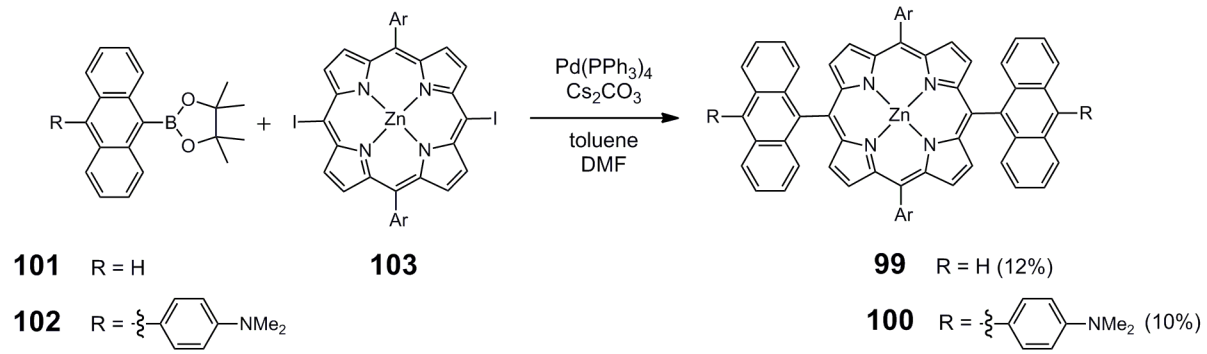

Scheme 3.3: Synthesis of bis-anthracene porphyrins **99** and **100** by Bonifazi and co-workers. Ar = 3,5-di(*t*-butyl)phenyl.[4]

It is not necessary that the boronic ester be carried by the anthracene unit rather than by the porphyrin. During my Part II project I demonstrated that it is possible to synthesise a mono-anthracene linked porphyrin in 36% yield by Suzuki coupling reaction between a porphyrin boronic ester and 10-bromo-1,8-bis(octyloxy)anthracene **72**.[1] The time consuming synthesis of anthracene **72** (Scheme 2.11) indicates that it would not be efficient to synthesise the analogous anthracene boronic ester as a precursor to the desired anthracene-porphyrin products.

The synthesis of porphyrins bearing two boronic ester groups has been reported in the literature.[6] Formation of porphyrin **104**, followed by a Suzuki coupling reaction with bromoanthracene **72** may therefore be expected to yield the desired bis-anthracene linked porphyrin **105** (Scheme 3.4). Such a route could result in simpler purification and higher yields of the bis-anthracene porphyrin, compared to the condensation method, but it is a longer pathway. The palladium-catalysed coupling route will also probably form a mono-anthracene linked porphyrin **106**, due to competing proto-deborylation of the porphyrin boronic ester under palladium-catalysed coupling conditions. This is advantageous as it means that both anthracene-linked porphyrin precursors to the target fused porphyrins may be synthesised in one reaction.

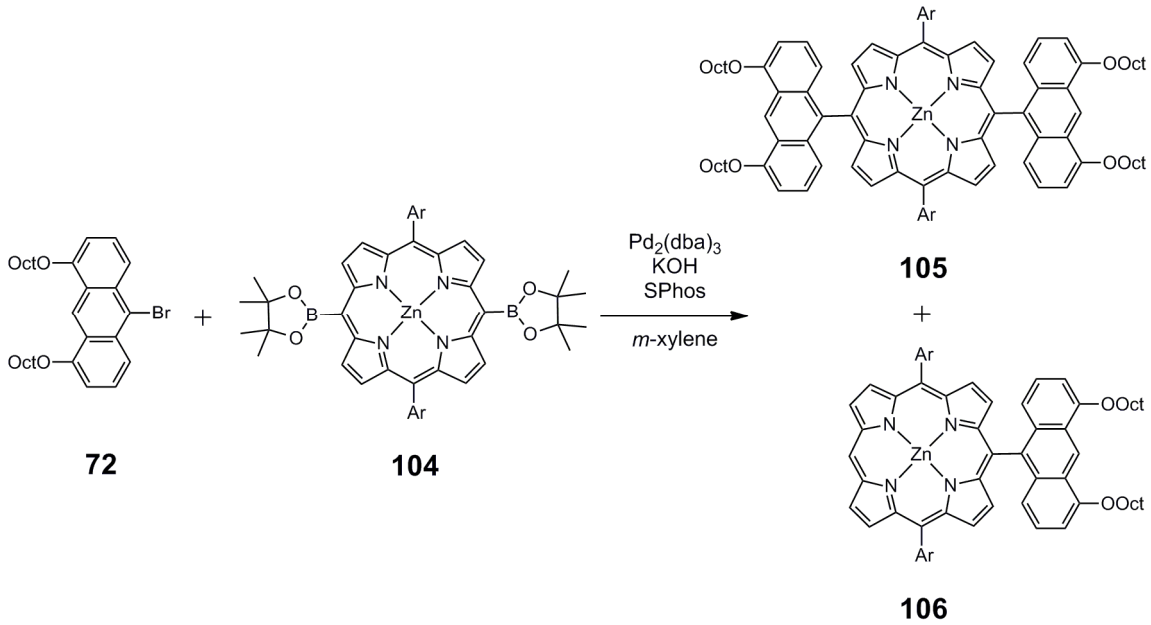

Scheme 3.4: Proposed route for Suzuki coupling reaction to form anthracene linked porphyrins **105** and **106**. Ar = 3,5-bis(octyloxy)phenyl.

With the synthetic route planned, I began the synthesis of the desired porphyrin boronic ester **104**. Using a modified literature procedure,[6] palladium-catalysed coupling of dibromoporphyrin (**108**) to pinacolborane gave **104** in 79% yield (Scheme 3.5).

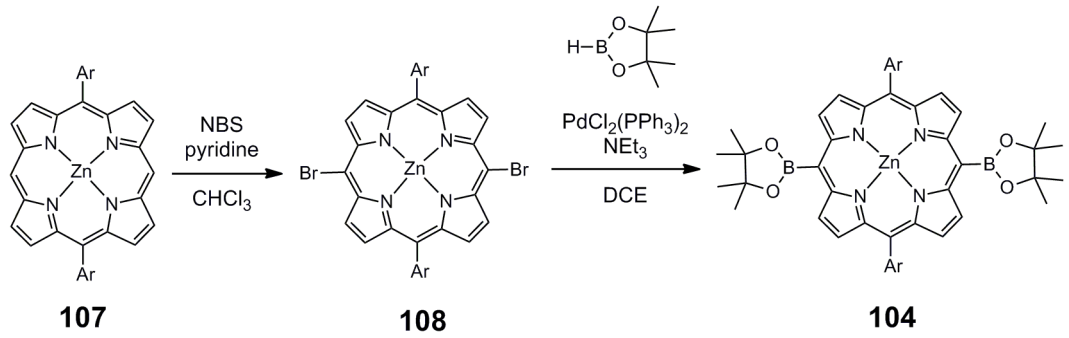

Scheme 3.5: Synthesis of porphyrin boronic ester **104**. Ar = 3,5-bis(octyloxy)phenyl.

Suzuki coupling of **104** and bromoanthracene **72** was carried out as described in Scheme 3.4 to give bis-anthracene porphyrin **105** in 16% yield, and mono-anthracene porphyrin **106** in 21% yield after purification.

3.2.3 Bis-Anthracene Fused Porphyrin Monomer

Fusion of bis-anthracene linked porphyrin **105** was initially attempted with ten equivalents of scandium(III) triflate and ten equivalents of DDQ in dry solvent (Scheme 3.6). Analysis of

the reaction mixture by TLC and ^{1}H NMR did not show the expected product, instead suggesting that the porphyrin core of **105** had been cleaved to generate a complex mixture of species.

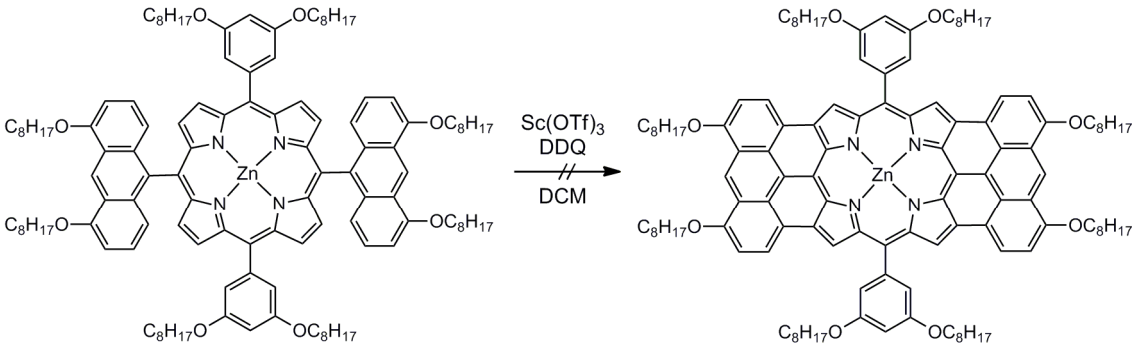

105 **91**

Scheme 3.6: Attempted fusion of porphyrin **105** with scandium(III) triflate and DDQ.

These findings were surprising given the success of the same fusion conditions for similar anthracene-porphyrin systems. It is however possible that the electron-rich 3,5-bis(octyloxy)phenyl substituents on the porphyrin react under the oxidative conditions, leading to decomposition of the molecule. As a result the unfused bis-anthracene porphyrin was re-designed to bear 3,5-di(*t*-butyl)phenyl groups, which are less electron rich yet still limit aggregation due to their bulkiness and non-planarity with the porphyrin core. The synthesis of bis-boronic ester **109**, which bears these 3,5-di(*t*-butyl)phenyl substituents, was achieved in 74% yield following an analogous pathway to that shown in Scheme 3.5.

A Suzuki reaction between the bis-boronic ester porphyrin **109** and bromoanthracene **72** gave the bis-anthracene linked porphyrin **110** in 47% yield, and mono-anthracene linked porphyrin **111** in 20% yield (Scheme 3.7).

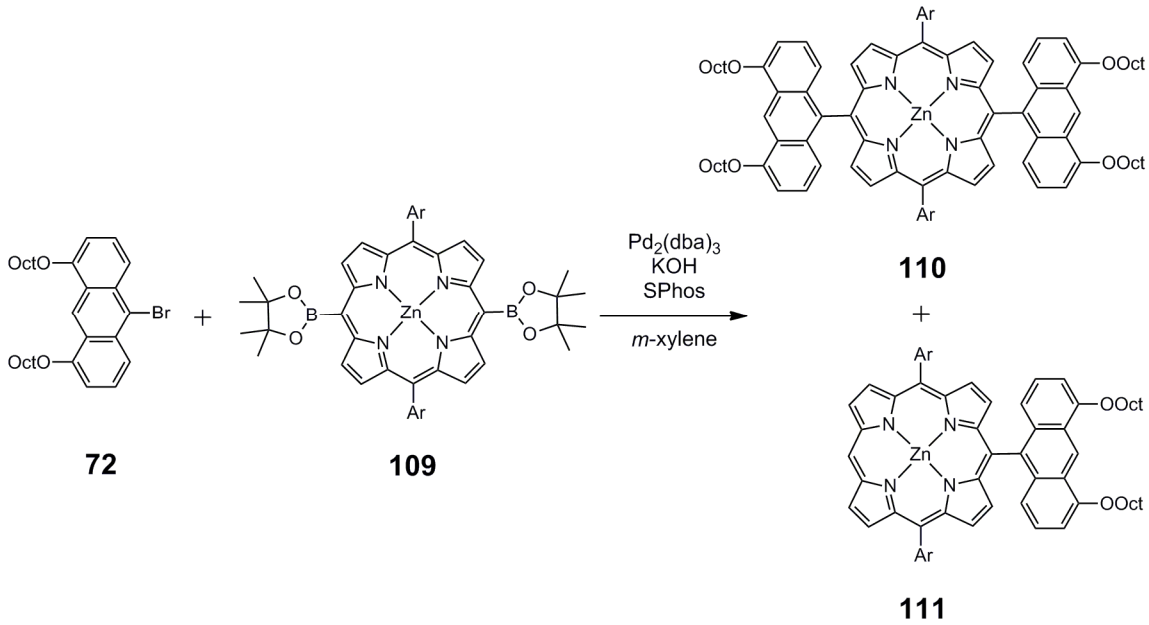

Scheme 3.7: Suzuki coupling reaction to form bis-anthracene linked porphyrin **110** and mono-anthracene linked porphyrin **111**. Ar = 3,5-di(*t*-butyl)phenyl

Fusion of **110** was attempted with ten equivalents of scandium(III) triflate and ten equivalents of DDQ (Scheme 3.8). Monitoring of the progress of the reaction by TLC showed complete consumption of **110**, and the formation of a dark red-purple product which was isolated by passing the reaction mixture over a silica gel plug. The UV-vis-NIR spectrum of this product showed a strong similarity to the mono anthracene-fused porphyrins previously synthesised, suggesting the product to be partially fused porphyrin **112**. Therefore I decided to subject this material to further oxidant to attempt to form the fully fused porphyrin.

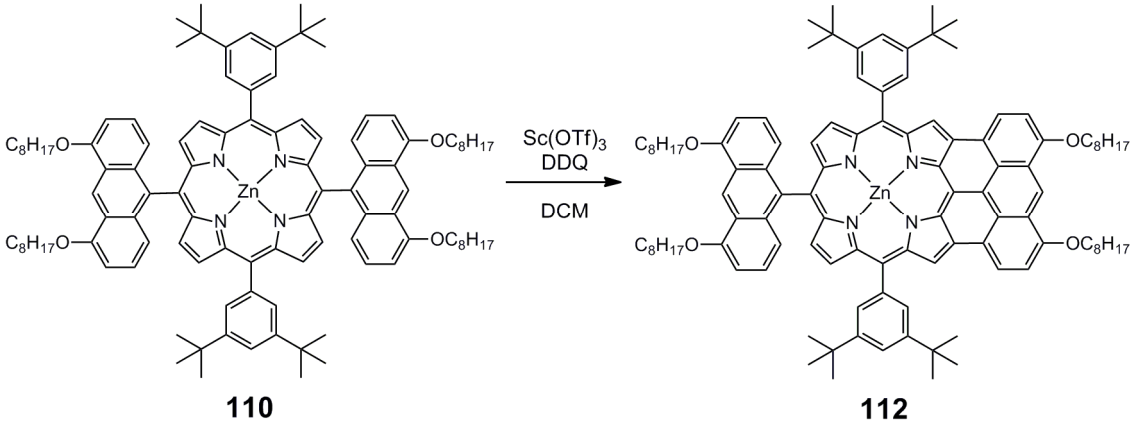

Scheme 3.8. Reaction of **110** with scandium(III) triflate and DDQ to form fused porphyrin **112**.

Upon treating **112** with further oxidant, TLC of the reaction mixture showed no reaction, even after 24 hours. Furthermore the UV-vis-NIR absorption spectrum of the crude reaction

mixture showed no change over this time. Upon repeating the procedure on another occasion, porphyrin **112** was observed to undergo a reaction to generate a mixture of products, but no fully fused **113** was isolated from the mixture.

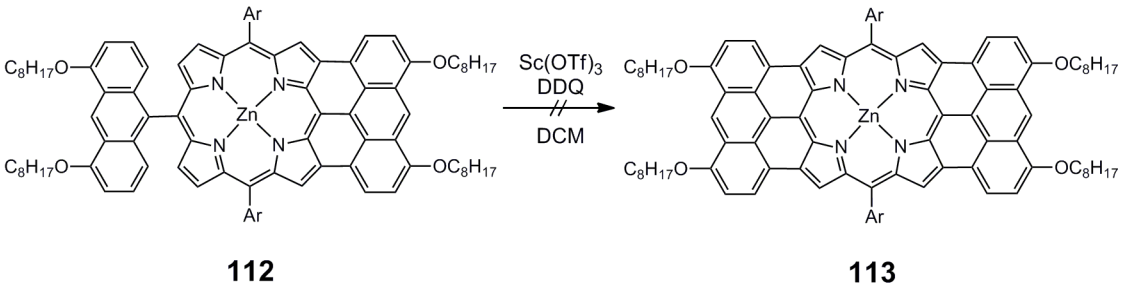

112 **113**

Scheme 3.9. Attempted fusion of partially fused porphyrin **112** to give fully fused porphyrin **113**. Ar = 3,5-di(*t*-butyl)phenyl.

Osuka and co-workers have reported the synthesis of *meso-meso, β-β, β-β* triply linked porphyrin dimers by oxidative ring-closure of *meso-meso* singly linked diporphyrin precursors with tris(4-bromophenyl)aminium hexachloroantimonate (BAHA).[7] These reaction conditions were attempted on porphyrin **110** (Scheme 3.10). TLC of the reaction mixture revealed it to contain predominantly demetalated **110**, together with side products that were shown by MALDI-TOF mass spectrometry to correspond to chlorinated derivatives of porphyrin **110**. UV-vis-NIR spectroscopy showed no absorption in the near-IR. Hence I concluded that no fused porphyrin products were formed in the reaction.

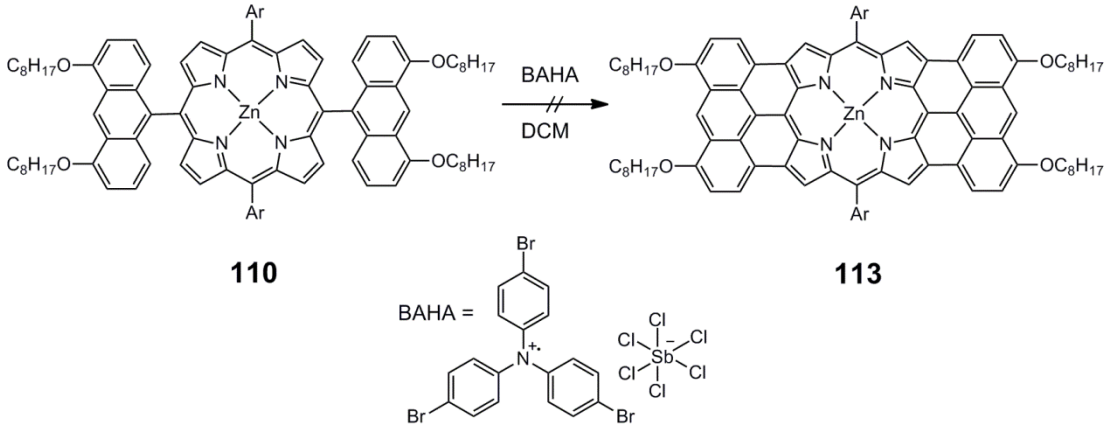

110 **113**

Scheme 3.10: Attempted fusion of **110** to give **113** with BAHA. Ar = 3,5-di(*t*-butyl)phenyl.

It has been reported that gold salts can oxidise zinc porphyrins to radical cation species,[8] which are intermediates in the oxidative ring-closure reaction. As a result, bis-anthracene linked porphyrin **110** was treated with gold(III) chloride and silver triflate using

a modified literature procedure (Scheme 3.11).[9] TLC of the reaction mixture showed the formation of demetalated **110** together with side products. UV-vis-NIR spectroscopy of the reaction mixture did not show any absorption in the near-IR, indicating that no fused porphyrin had been formed in the reaction.

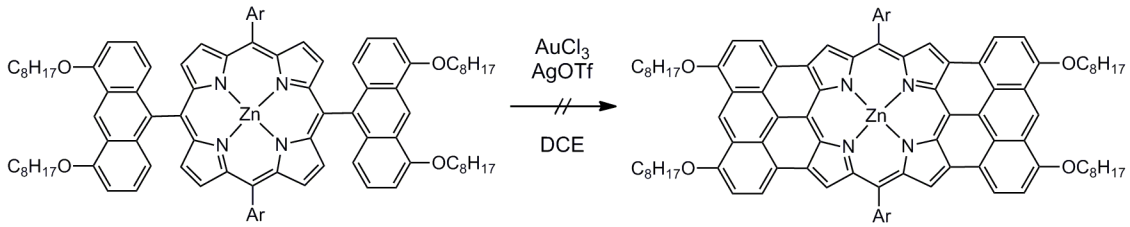

110 **113**

Scheme 3.11: Attempted fusion of **110** to give **113** with $AuCl_3$/AgOTf. Ar = 3,5-di(*t*-butyl)phenyl.

Iron(III) chloride has been widely employed as a reagent for oxidative ring-closure reactions.[10] Müllen and co-workers have employed this reagent in the synthesis of 'graphene nanoribbons' from branched polyphenylenes,[11] while Osuka and co-workers synthesised a fully fused nickel tetra-azulene porphyrin (**51**) from its unfused precursor (**114**) using the same reagent (Scheme 3.12).[12]

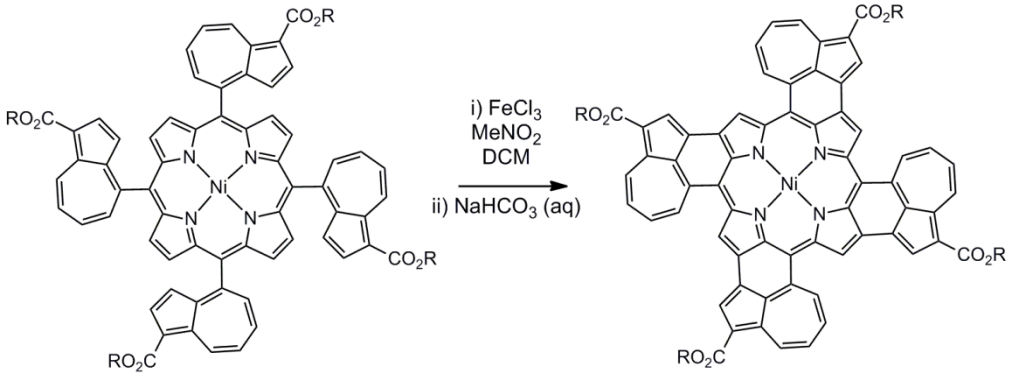

114 **51**

Scheme 3.12: Synthesis of a quadruply fused tetra-azulene porphyrin (**51**) by Osuka and co-workers with iron(III) chloride. R = 2,4,6-tri(*t*-butyl)phenyl.[12]

Fusion with iron(III) chloride was initially attempted on bis-anthracene linked zinc porphyrin **110** (Scheme 3.13). TLC showed complete consumption of bis-anthracene linked porphyrin **110** in 30 minutes. After passing over a short pad of silica to remove iron residues, analysis of the products showed only demetalated **110** together with partially fused porphyrin **112**.

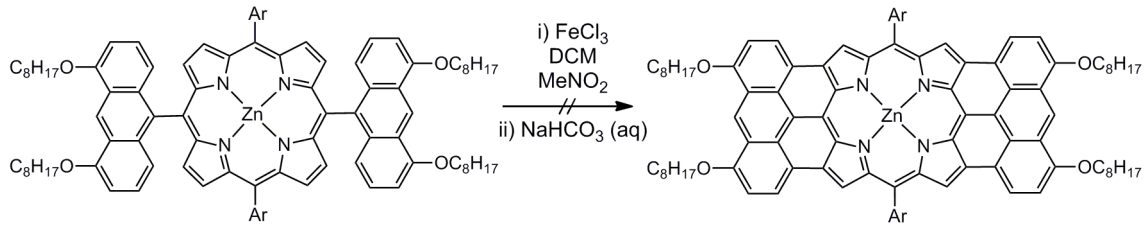

110 **113**

Scheme 3.13: Attempted fusion of **110** with iron(III) chloride. Ar = 3,5-di(*t*-butyl)phenyl.

From the results above I deduced that free-base porphyrins do not undergo oxidative ring-closure reactions. In order to employ iron(III) chloride as a reagent in the synthesis of fully fused bis-anthracene porphyrin **113**, it is necessary to replace the coordinated zinc metal with a metal which is more strongly bound in the porphyrin cavity. This is because partial hydrolysis of iron(III) chloride during the fusion reaction may generate hydrochloric acid, which can protonate the nitrogen atoms of the porphyrin cavity, causing demetalation. Nickel(II) is coordinated more strongly by the pyrrolic nitrogens of the porphyrin than zinc(II), and nickel porphyrins are resistant to demetalation in the presence of iron(III) chloride.

Bis-anthracene linked zinc porphyrin **110** was demetalated using TFA to yield the intermediate free-base porphyrin, which was reacted directly with nickel(II) acetylacetonate to give the nickel bis-anthracene porphyrin **115** in 92% yield over two-steps (Scheme 3.14).

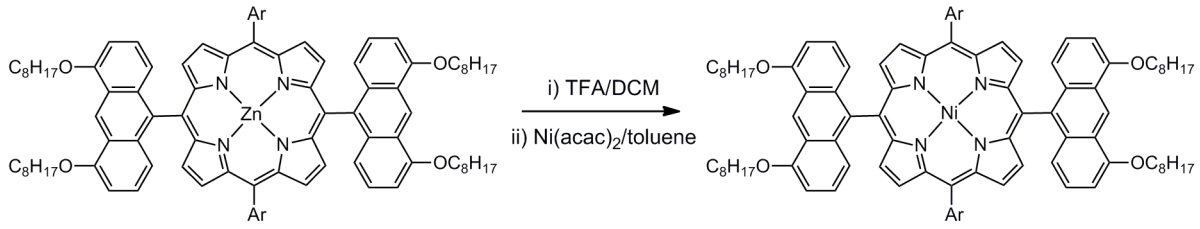

110 **115**

Scheme 3.14: Conversion of zinc porphyrin **110** to nickel porphyrin **115**. Ar = 3,5-di(*t*-butyl)phenyl.

Fusion of **115** was initially attempted following the conditions used by Osuka and co-workers in the synthesis of tetra-azulene fused porphyrin **51** (Scheme 3.15). Porphyrin **115** was dissolved in dry solvent and ten equivalents of iron(III) chloride were added at room temperature. The starting material was observed by TLC to be completely consumed after 30 minutes, and a dark red-purple product formed. The UV-vis-NIR spectrum of this

reaction mixture did not show any evidence of the desired fully fused bis-anthracene porphyrin. The dark red-purple product was isolated by silica chromatography in 81% yield and was identified as partially fused porphyrin **116**.

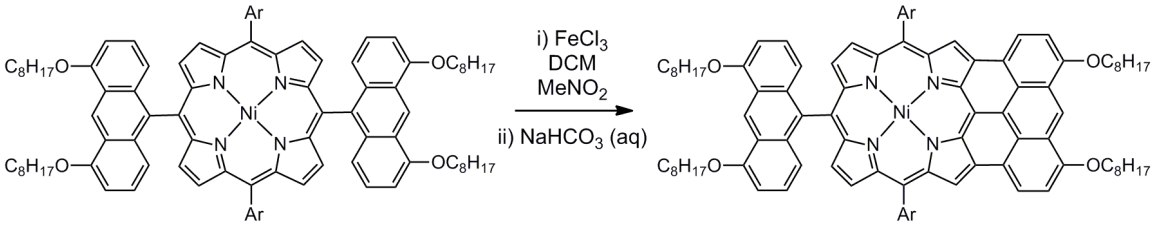

115 **116**

Scheme 3.15: Fusion of porphyrin **115** using $FeCl_3$. Ar = 3,5-di(*t*-butyl)phenyl.

Porphyrin **116** was subjected to a further ten equivalents of iron(III) chloride in an attempt to force the second anthracene unit to fuse to the porphyrin periphery (Scheme 3.16). After 30 minutes, TLC showed consumption of the starting material and the formation of a deep purple product. UV-vis-NIR spectroscopy of the crude reaction mixture showed absorption in the near-IR beyond that associated with partially fused porphyrin **116**. MALDI-TOF mass spectrometry of the crude reaction mixture showed the presence of **117**, together with chlorinated side products corresponding to fully fused porphyrin **117** bearing between one and four chlorine atoms substituting hydrogen atoms.

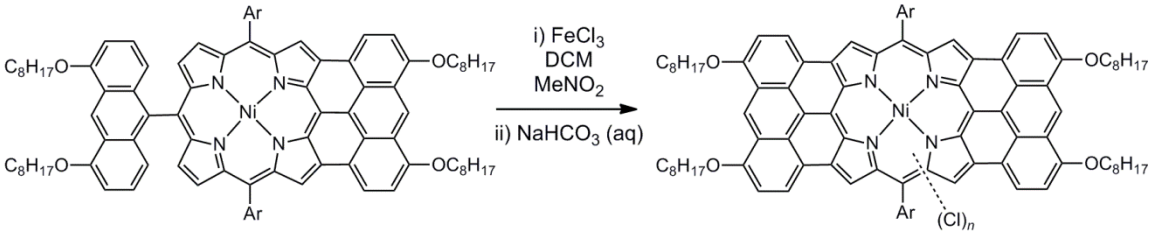

116 **117**

Scheme 3.16: Reaction of porphyrin **116** with $FeCl_3$ to form fully fused bis-anthracene porphyrin **117**. Ar = 3,5-di(*t*-butyl)phenyl, n = 0 — 4.

The tendency for iron(III) chloride to chlorinate products of oxidative ring-closure reactions has also been reported by Müllen and co-workers in their work on the formation of hexabenzocorranulenes (HBCs).[13] Several methods have been reported to suppress this chlorination, including the use of nitromethane as a solvent for the iron(III) chloride and bubbling argon through the reaction mixture to displace the HCl produced,[14] however

neither of these approaches prevented the formation of chlorinated side products when applied to the fusion of partially fused bis-anthracene porphyrin **116**.

Purification of fully fused bis-anthracene porphyrin **117** was carried out by silica gel chromatography. However, this compound was difficult to elute from the silica column due to its tendency to strongly adsorb to the silica, resulting in very inefficient purification. In addition, separation of fully fused porphyrin **117** from the chlorinated side-products proved exceeding difficult due to the very small differences in polarity between these compounds. Eventually a small fraction of **117** was isolated by silica gel chromatography, providing a clean MALDI-TOF mass spectrum which displayed a single peak corresponding to the mass of fully fused porphyrin **117**. The UV-vis spectrum of this fraction shows absorption into the near-IR, with a λ_{max} of 960 nm together with a greatly simplified spectral shape compared to partially fused porphyrin **116**, as expected for a chromophore of higher symmetry (Figure 3.2).

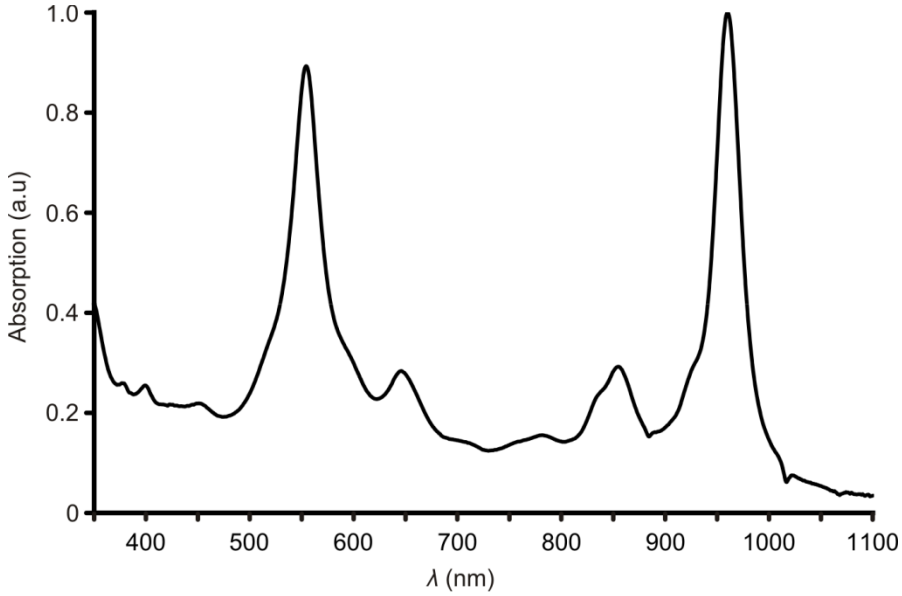

Figure 3.2: UV-vis-NIR absorption spectrum in $CHCl_3$ of fully fused bis-anthracene porphyrin **117**.

Unfortunately the ^{1}H NMR spectrum of the small sample of purified **117** displayed only broad peaks in the aromatic region which, due to the low concentration of the sample, were of low signal intensity. Large π-systems often readily oxidise to the corresponding radical cation which, being paramagnetic, gives rise to broad ^{1}H NMR signals.[15] Unfortunately addition of 10 μL of hydrazine hydrate to reduce such a species did not result

in any improvement to the ^{1}H NMR spectrum. Broad signals may also be a result of aggregation between molecules: high temperature ^{1}H NMR of the sample was attempted in 1,1,2,2-tetrachloroethane-d_2, but no resolution was observed, even at 140 °C, indicating that it is likely that strong aggregation of **117** was occurring.

3.2.4 Bis-Anthracene Fused Porphyrin Dimer

The decomposition of **105** under scandium(III) triflate/DDQ conditions indicated that the formation of dimer **92** from porphyrin **106** would be expected to suffer from similar problems. Porphyrin **111**, with less reactive *t*-butylphenyl side groups, was expected to be more stable than **106** under the fusion conditions. Porphyrin **111** was isolated as a side product of the Suzuki coupling reaction to form **110** in 20% yield. Thus the synthesis of a bis-anthracene fused porphyrin dimer (**118**) was initially attempted from porphyrin **111** (Scheme 3.17).

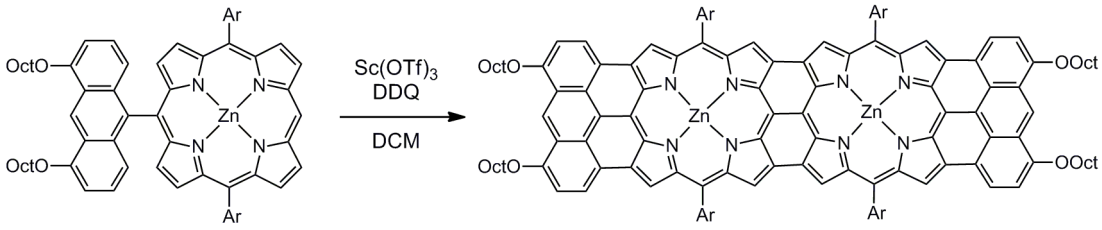

111 **118**

Scheme 3.17: Fusion of porphyrin **111** to form dimer **118** with scandium(III) triflate and DDQ. Ar = 3,5-di(*t*-butyl)phenyl.

Porphyrin **111** was treated with 15 equivalents of scandium(III) triflate and DDQ. After one hour TLC showed complete consumption of **111**, and the formation of a mixture of dark blue products was observed. MALDI-TOF mass spectrometry of the crude reaction mixture showed the presence of dimer **118**. Unfortunately, purification of **118** by silica gel chromatography proved to be exceedingly difficult due to its tendency to strongly adsorb to the silica gel and to elute as a broad band, suggesting the formation of aggregates. Hence it was impossible to separate the mixture of products formed in the fusion reaction and isolate dimer **118**. ^{1}H NMR spectroscopy of the mixture of products provided a featureless spectrum in the aromatic region, indicating strong aggregation between molecules.

I concluded that porphyrins **117** and **118** experience aggregation effects that are not significantly reduced by the presence of *t*-butyl aryl groups on the porphyrin ring periphery. While it is likely that these aryl groups prevent face-to-face π-stacking, it is possible that π-π interactions may occur in an offset arrangement between the anthracene moieties of separate molecules. These regions are exposed with little steric hindrance from the octyl chains to interrupt π-stacking, hence re-design of the anthracene unit to bear bulky substituents would lead to fused porphyrins with a far lower tendency to aggregate. This would not only facilitate efficient purification, but also enable characterisation of these compounds by NMR spectroscopy.

3.3 Re-Design of Anthracene Unit

3.3.1 Anthracene Unit with 2,6-Diisopropylphenoxy Substituents

In order to circumvent the recurring problems of aggregation, it was necessary to re-design the anthracene unit to bear bulky substituents in the 1- and 8-positions that are capable of preventing π-π interactions from occurring between anthracene units of the fused porphyrin systems.

Warren and co-workers have shown that aggregation of phthalocyanines may be reduced by the presence of 2,6-diisopropylphenoxy groups around the periphery of the phthalocyanine ring (**119**, Figure 3.3).[16] These aryl groups are forced by steric congestion to lie out of plane with respect to the macrocycle, with the bulky isopropyl groups lying above and below the plane of the phthalocyanine ring, thereby inhibiting the formation of columnar stacks.

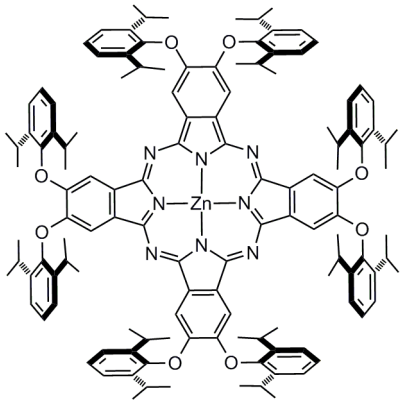

119

Figure 3.3: Facially encumbered phthalocyanine **119** synthesised by Warren and co-workers.[16]

As well as bearing bulky aryl ether substituents in the 1- and 8-positions, the required anthracene also needs to be connected to a leaving group in the 10-position which is suitable for Suzuki coupling to porphyrin boronic ester **109**. My previous work in the Anderson group demonstrated that direct bromination of an anthracene at the 10-position will not be possible if there are strongly electron donating substitutents in the 1- and 8-positions (Section 2.2.1).[1] In order to circumvent this problem of regioselectivity, I developed the synthetic pathway to bromoanthracene **72** shown in Scheme 2.11. This route makes use of poorly electron donating acetoxy protecting groups to direct bromination to the 10-position followed by hydrolysis and alkylation by S_N2 mechanism to give anthracene **72**. However unlike alkyl chains, aryl groups cannot be attached by S_N2 reaction. Hence an alternative pathway to a suitable anthracene was required.

It has been reported in the literature that it is possible to regiospecifically synthesise anthracenes bearing substituents in the 9- or 10-positions from the corresponding anthrones.[17,18] Müller and co-workers have shown that it is possible to synthesise anthrones with the desired regioselectively (protons *peri* to the 1- and 8-substituents) by reduction of anthraquinones using sodium dithionite in DMF and water.[19] Futhermore, Toyota and Makino have shown that conversion of an anthrone to a triflate is possible using lithium hexamethyldisilazide (LiHMDS) and triflic anhydride.[17] Triflates are suitable groups for Suzuki coupling reactions, hence anthracene triflate **120** was proposed as a new synthetic target. Scheme 3.18 summarises the proposed synthetic pathway to this anthracene.

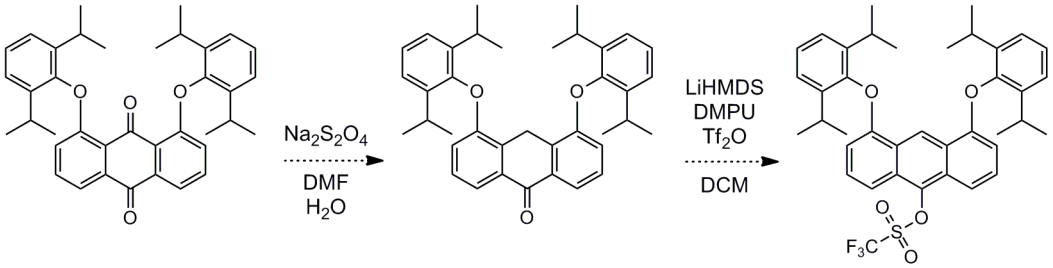

Scheme 3.18: Proposed synthetic pathway to anthracene triflate **120**.

Phenols have been shown to undergo nucleophilic aromatic substitution reactions with electron deficient aromatic systems.[16,20] 2,6-Diisopropylphenol (**123**) was heated in DMF with 1,8-dichloroanthraquinone (**124**) under basic conditions to give anthraquinone **121** in 53% yield after purification (Scheme 3.19).

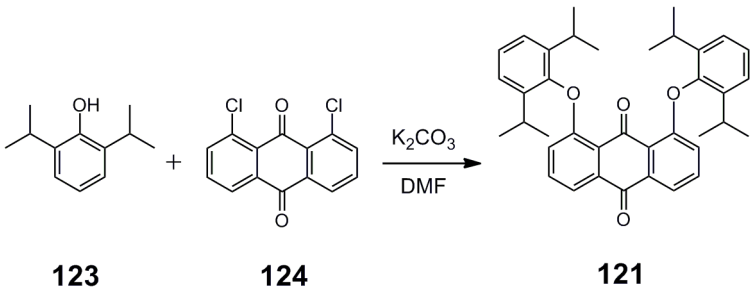

Scheme 3.19: Synthesis of **121** by nucleophilic aromatic substitution.

Reduction of anthraquinone **121** to anthrone **122** was initially attempted with ten equivalents of sodium dithionite, as described in Scheme 3.18. The reaction was monitored by TLC and ^{1}H NMR spectroscopy, however after four days the reaction mixture contained only unreacted anthraquinone **121**. Müller and co-workers reported the rate of anthraquinone reduction is highly dependent upon the substituents attached to the oxygen atoms in the 1- and 8-positions of the anthraquinone, with benzylic groups exhibiting longer reaction times than methyl groups.[19] In light of these results, it seemed possible that the bulky nature of the aryl groups of **121** may be responsible for the very slow rate of reaction. Hence the concentration of sodium dithionite was increased to attempt to speed up the rate of the reaction and force reduction, however no reaction was observed by ^{1}H NMR spectroscopy even after 100 equivalents of sodium dithionite were added and the mixture heated overnight.

Regioselective reduction of anthraquinones to anthrones with protons *peri-* to the 1- and 8-substituents has also been achieved using sodium borohydride, followed by an acidic work-up.[18] This procedure was applied to anthraquinone **121** (Scheme 3.20). The reaction mixture turned from yellow to a white suspension upon addition of ten equivalents of sodium borohydride over the course of an hour. TLC of this mixture indicated the consumption of **121** and the formation of a more polar product. However, upon washing with acid, the precipitate collected turned from white to yellow and, after neutralisation with aqueous sodium hydrogen carbonate, was shown by ^{1}H NMR spectroscopy to be only unreacted anthraquinone **121**. The reaction was repeated with a large excess of sodium borohydride (~100 equivalents), but again after acidic work-up no reaction was observed.

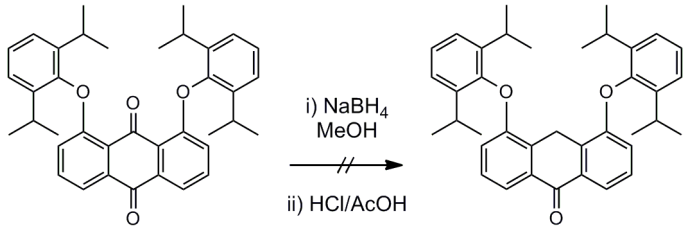

121 **122**

Scheme 3.20: Attempted reduction of anthraquinone **121** to **122** with sodium borohydride.

It seemed likely that anthraquinone **121** forms an intermediate product upon exposure to sodium borohydride, which fails to react further to form anthrone **122**, and which is converted back into anthraquinone **121** upon work-up. Such an intermediate may show poor solubility in methanol, like anthraquinone **121**, thereby limiting this second step. As a result, the reaction was repeated in a 1:1 mixture of THF and methanol, however again no reaction was observed by ^{1}H NMR spectroscopy after work-up. Possibly, the bulkiness of the aryl substituents may slow the rate of anthrone formation due to steric constraints. As a result the reaction time was increased, with the reduction in methanol being stirred for three days under nitrogen with a large excess of sodium borohydride (~100 equivalents). After this time the white precipitate was collected and washed with acid. Again, only starting material **121** was observed by ^{1}H NMR spectroscopy.

The difficulties encountered in the reduction of **121** with sodium borohydride led to attempted reactions with stronger reducing agents. Shyamasundar and Caluwe have shown

that reduction of 1,8-substituted anthrones with lithium aluminium hydride gives a mixture of the two possible anthrone isomers, with the desired isomer (with protons *peri* to the 1- and 8-substituents) as the major product.[21] Reduction of **121** with a solution of lithium aluminium hydride was attempted in dry THF as shown in Scheme 3.21. The reaction mixture changed from yellow to white upon addition of lithium aluminium hydride. TLC of this mixture showed the formation of a new, more polar component, together with consumption of the starting material. Upon work-up the mixture turned yellow in colour. ^{1}H NMR spectroscopy of the crude mixture showed it to be only unreacted anthraquinone **121**.

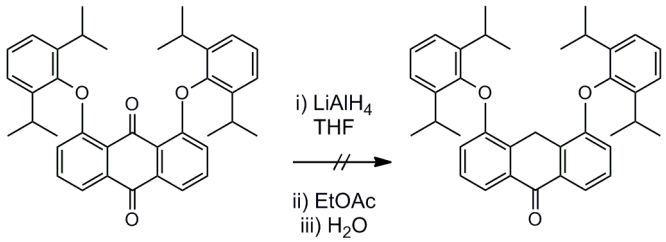

121 **122**

Scheme 3.21: Attempted reduction of anthraquinone **121** to anthrone **122** with $LiAlH_4$.

The apparent consumption of **121** (observed by TLC and colour change) during these hydride reductions is surprising given that only starting material is observed after work-up of the reactions. Most likely anthraquinone **121** forms a reversible complex with the reductant, without undergoing hydride transfer, which then collapses upon work-up to re-form **121**.

Müller and co-workers have reported the reduction of 1,8-dimethoxyanthraquinone to a mixture of 1,8-dimethoxyanthracene and the 1,8-dimethoxyanthrone with protons *peri* to the carbonyl group using zinc in aqueous ammonia.[18] This procedure was applied to anthraquinone **121** as shown in Scheme 3.22.

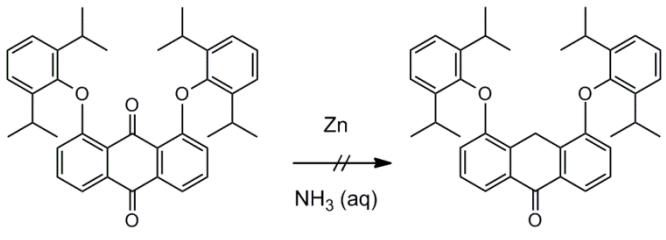

121 **122**

Scheme 3.22: Attempted reduction of anthraquinone **121** to anthrone **122** with zinc in aqueous ammonia.

The reaction was monitored by TLC, however after refluxing for eight hours with zinc in aqueous ammonia the reaction mixture appeared to contain predominantly starting material. The reaction mixture was left for a further 16 hours, however no further reaction was observed. After workup, the product collected was shown by ^{1}H NMR spectroscopy to be almost exclusively anthraquinone **121**.

From the reaction conditions trialled it would appear that it is not possible to reduce anthraquinone **121** to anthrone **122**. This result suggests the high degree of steric crowding exerted by the bulky 2,6-diisopropylaryl groups hinder attack at the carbonyl *peri-* to these aryl groups.

3.3.2 X-Ray Crystal Structure of Anthraquinone 121

Crystals of anthraquinone **121** were grown by vapour diffusion of methanol into a solution of **121** in chloroform, and the X-ray data was collected by Dr Amber Thompson, Department of Chemistry, University of Oxford. The crystal structure of **121** shows the high degree steric crowding about the oxygen atom (*peri-* to the 1- and 8-substituents), from the 2,6-diisopropylphenoxy groups (Figure 3.4).

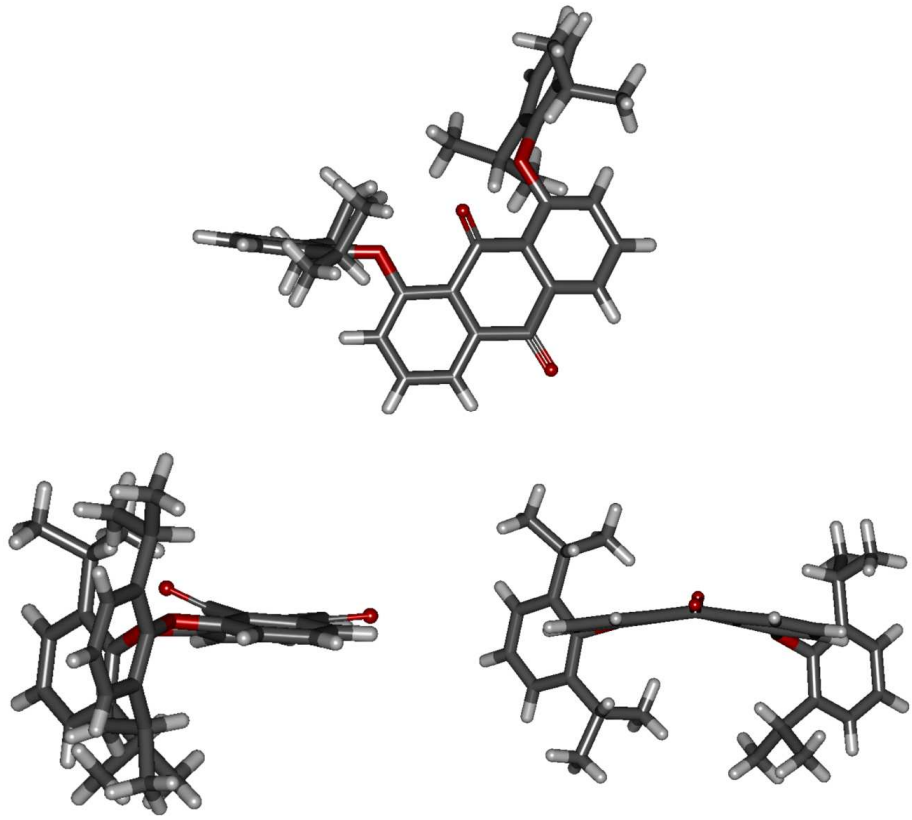

Figure 3.4: Three views of the molecular structure of **121** in the crystal. Hydrogens are shown to illustrate steric congestion.

From the crystal structure shown in Figure 3.4, it can be seen that anthraquinone **121** displays a bent structure, with the three rings of the anthraquinone core arranged in a non-planar geometry. In addition, the oxygen of the carbonyl group *peri-* to the 1,8-substituents is considerably bent away from the plane of the central anthraquinone ring. In order to determine whether these distortions from planarity are typical for 1,8-substituted anthraquinones, or whether such distortions may arise as a consequence of the bulky nature of the 2,6-diisopropylphenoxy substituents, a search of the Cambridge Structural Database (CSD) was conducted for anthraquinones with identical 1,8-substituents (other than hydrogen). The search was restricted to organic compounds excluding structures with known errors, polymeric structures, ions and structures determined by powder diffraction. The angles under investigation are shown in Figure 3.5, and are defined as the angle between the normals of the two planes of the terminal anthraquinone rings, and the angle between the oxygen atom *peri-* to the 1,8-substituents, the carbon atom it is bonded to, and the

carbon atom of the carbonyl group on the opposite side of the central anthraquinone ring. For anthraquinone **121** the values of these parameters are 16.57° and 160.26° respectively.

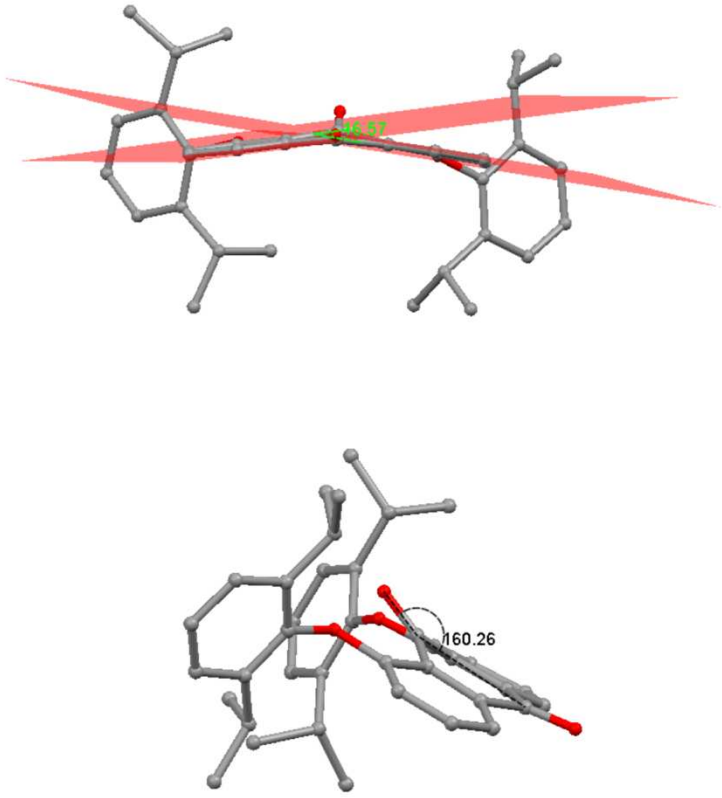

Figure 3.5: Angles under investigation. Top: the angle between the two planes of the terminal anthraquinone rings of **121** (found to be 16.57°). Bottom: the angle defined by three atoms — the oxygen atom *peri*- to the 1,8-substituents, the carbon atom it is bonded to, and the carbon atom of the carbonyl group on the opposite side of the central anthraquinone ring; angle found to be 160.26°. Hydrogens are omitted for clarity.

The search generated 44 hits, which included multiple results for some structures. By analysing the results, it became clear that anthraquinones with a single group bound across both the 1- and 8-positions show the greatest deviations from planarity for both angles under investigation. As shown in Figure 3.6, these 'tethered' anthraquinones show an angle between the normals of the planes of their terminal rings of about 15° or more, indicating a considerable degree of non-planarity; in general, the shorter the length of the tether, the larger the deviation from planarity. For anthraquinones with unlinked substituents in the 1- and 8-positions, those with substituents capable of undergoing hydrogen bonding with the *peri*- carbonyl oxygen, such as OH or NHR groups, display a smaller distortion from planarity across the anthraquinone system. In addition, those with

substituents larger than a methyl group display a greater degree of non-planarity, however there is little correlation between the bulkiness of these substituents and the non-planarity of the system. For example anthraquinones with *N*,*N*-diethyl-2-hydroxyacetamide, 2-methylnaphthyl and trimethylsilylethynyl substituents display a narrow distribution of angles with values of 11.65, 11.47 and 10.35° respectively, while clearly exerting very different steric constraints. In addition, dihydroxyanthraquinone has been reported to exhibit values ranging from 2.01 — 9.76°, illustrating that one compound can give a wide distribution of values due to the formation of different polymorphs. Anthraquinone **121** displays a greater degree of non-planarity than observed for other non-tethered anthraquinones, with a value of 16.57°, which may in part be due to the large degree of steric crowding exerted by the 2,6-diisopropyl groups of the phenoxy substituents. However the data obtained from the search of the CSD imply that it is not possible to draw conclusions about the magnitude of such an influence.

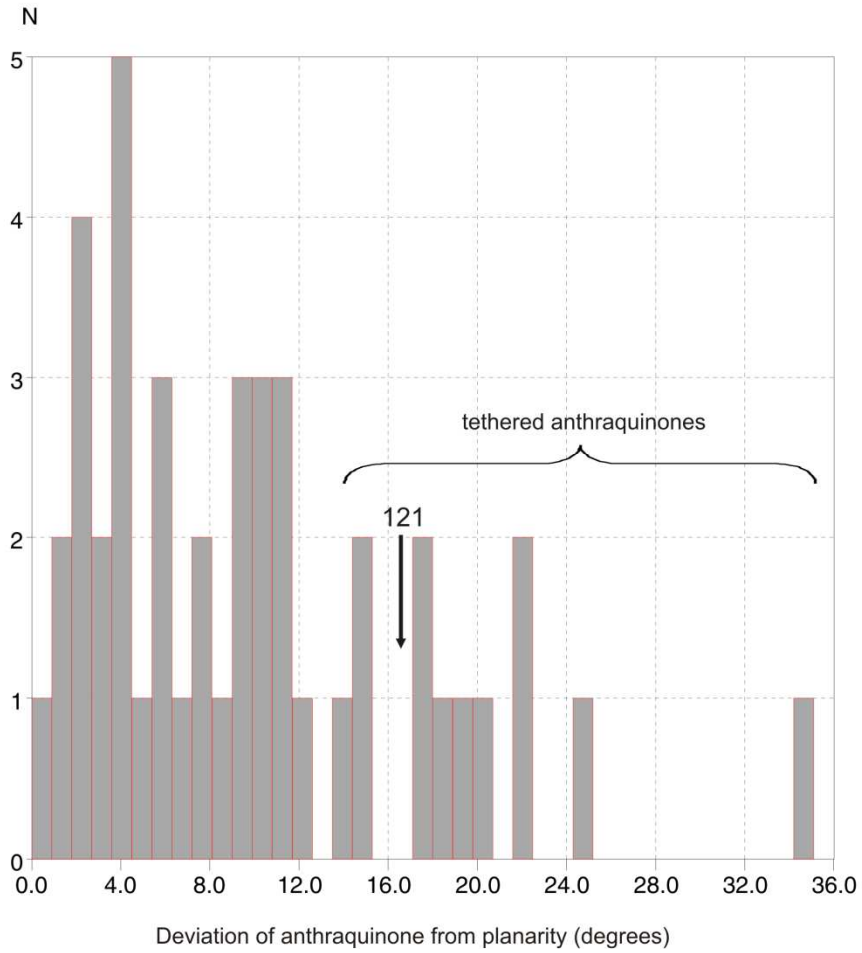

Figure 3.6: Histogram showing the distribution of angles depicting the deviation of anthraquinones from planarity from a search of the Cambridge Structural Database[22] using ConQuest (version 1.12).[23] Data were analysed using Vista.[24] The angle for anthraquinone **121** is depicted by an arrow, and is the only anthraquinone giving an angle greater than 15° without a covalent tether between the 1 and 8 positions.

As shown by the histogram in Figure 3.7, the angle between the oxygen atom *peri*- to the 1,8-substituents and the central anthraquinone ring may exhibit a wide range of values. Analysis of the data, revealed that the smallest angles (corresponding to a large deviation from planarity) are present in tethered anthraquinones bearing linked substituents in the 1- and 8-positions. The smallest value (134.2°) however was observed for one structure reported for 1,8-dimethoxyanthraquinone. This result appears to be anomalous given that another value for the same structure has been reported to be 166.90°, and values for analogous methylselanyl and methylthio compounds lie in the range 176.25° — 178.18°. I again found that the presence of hydrogen bonding between this oxygen and the substituents favours very small deviations from planarity. There appears to be little correlation between the size of the angle between the oxygen atom *peri*- to the 1,8-substituents and the central

anthraquinone ring, and the bulkiness of the 1- and 8-substituents, however the value of 160.26° observed for anthraquinone **121** appears to be smaller than for other untethered anthraquinones suggesting the 2,6-diisopropylphenoxy substituents may influence this parameter, although it is difficult to draw conclusions about the size of this effect.

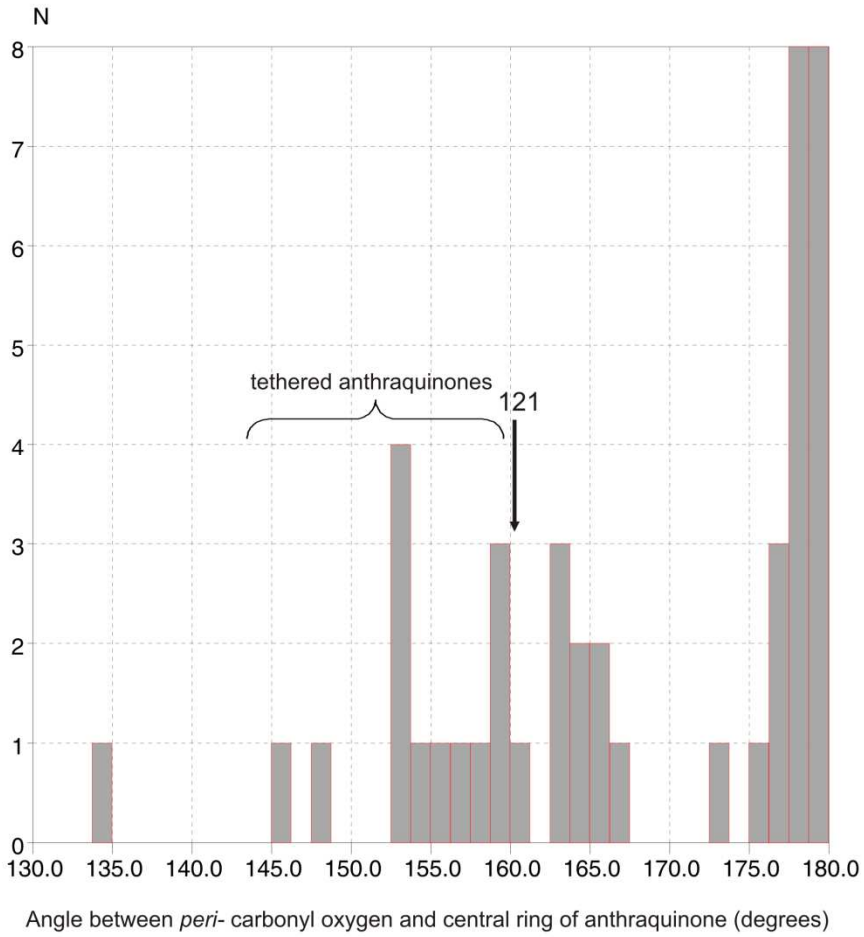

Figure 3.7: Histogram showing the distribution of angles depicting the angle between the oxygen atom *peri*- to the 1,8-substituents and the central anthraquinone ring from a search of the Cambridge Structural Database[22] using ConQuest (version 1.12).[23] Data were analysed using Vista.[24] The angle for anthraquinone **121** is depicted by an arrow.

A plot showing the relationship between the two angles under investigation is shown in Figure 3.8. It can been seen that there is a correlation between the degree of non-planarity of three rings of the anthraquinone system and the non-planarity of the oxygen atom *peri*- to the 1,8-substituents and the central anthraquinone ring. However, as mentioned above, the influence of the bulkiness of these 1,8-substituents on these parameters is not clear.

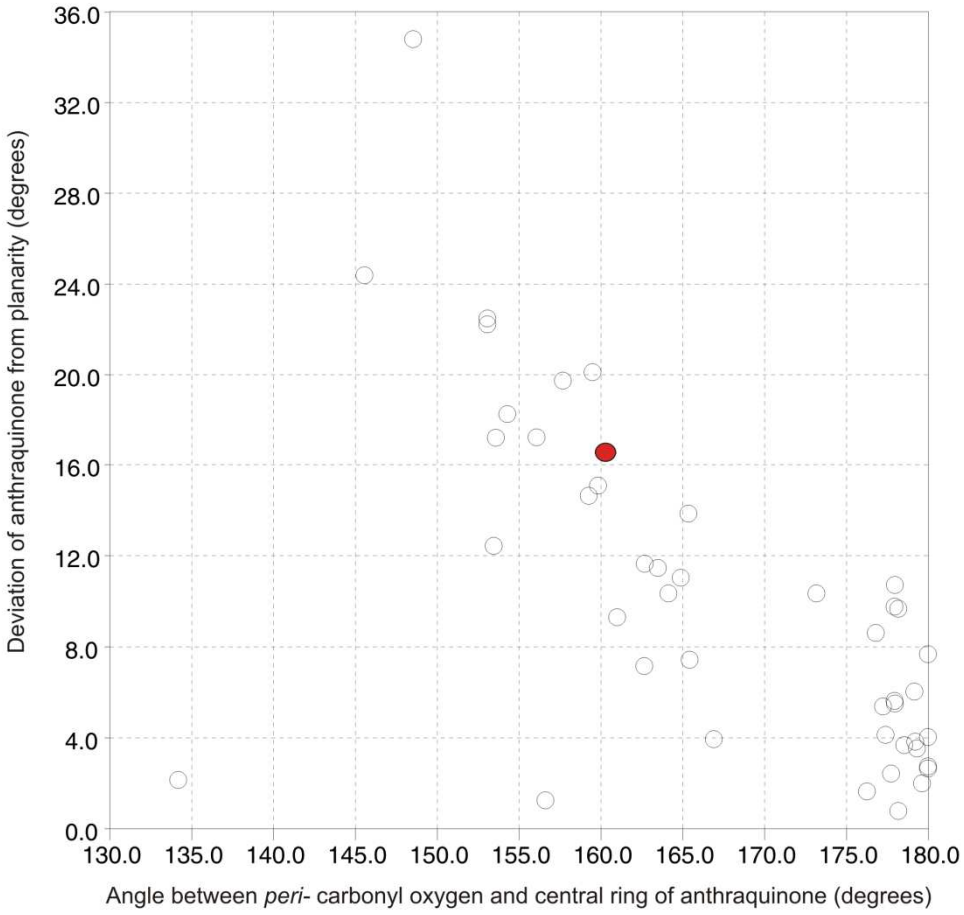

Figure 3.8: Plot showing the correlation between the non-planarity of the anthraquinone core, and that of the oxygen atom *peri*- to the 1,8-substituents (with respect to the central anthraquinone ring) for 1,8 substituted anthraquinones. Data for anthraquinone **121** are shown by a red circle.

From the discussion above it can be seen that, while it is difficult to draw conclusions about the magnitude of the influence of the 2,6-diispropylphenoxy groups of anthraquinone **121** on its distortions from planarity, this anthraquinone does show greater deviations from planarity than observed for other non-tethered anthraquinones. It is possible that such distortions affect the reactivity of the anthraquinone system and hence may be partially responsible for the difficulties encountered in the reduction of anthraquinone **121**.

3.3.3 Anthracene Unit with 2,4,6-Trimethylphenoxy Substituents

The problems encountered in the attempted synthesis of anthrone **122** from anthraquinone **121** indicated that an anthraquinone bearing aryl groups with less bulky substituents are required. I decided to employ 2,4,6-trimethylphenoxy groups as substituents on the

anthracene unit, as the *ortho*-methyl groups would favour a near-perpendicular arrangement of the aryl group relative to the anthracene. *Meta*- or *para*-substituents on the other hand may tolerate a smaller twist of the aryl group relative to the anthracene, and hence would be less effective at reducing aggregation in the target anthracene-fused porphyrin systems.

Synthesis of anthraquinone **125** bearing 2,4,6-trimethylphenoxy substituents was achieved in 51% yield by nucleophilic aromatic substitution of 1,8-dichloroanthraquinone **124**) with 2,4,6-trimethylphenol (**126**) (Scheme 3.23).

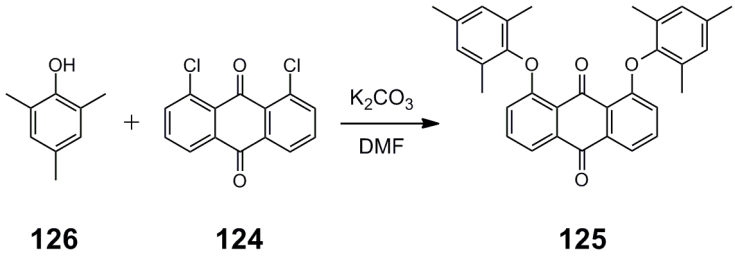

126 **124** **125**

Scheme 3.23: Synthesis of anthraquinone **125** by nucleophilic aromatic substitution.

Reduction of **125** to anthrone **127** was initially attempted with sodium dithionite (Scheme 3.24) After two days, ^{1}H NMR spectroscopy of the reaction mixture showed that no reaction had occurred.

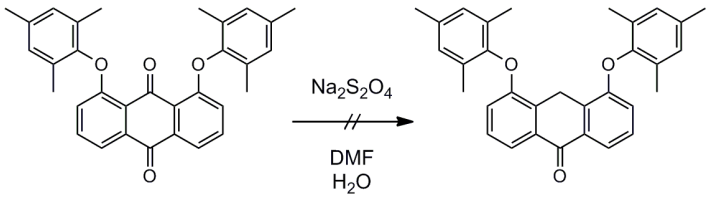

125 **127**

Scheme 3.24: Attempted reduction of **125** to **127** with $Na_2S_2O_4$.

Due to the lack of reactivity of **125** with sodium dithionite, I decided to attempt the synthesis of **127** by hydride reduction of **125** using the procedure reported by Müller and co-workers (Scheme 3.25).[18] Over the course of an hour, 20 equivalents of sodium borohydride were added to anthraquinone **125** and the mixture was stirred overnight. After acid work-up, ^{1}H NMR spectroscopy showed the solid to be a 1:6 mixture of the desired anthrone **127**, and anthraquinone **125**. Separation of this mixture proved unsuccessful by chromatography due to decomposition of **127** when in contact with silica gel.

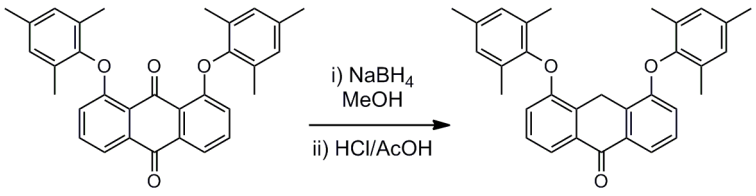

125 **127**

Scheme 3.25: Reduction of anthraquinone **125** to anthrone **127** by $NaBH_4$.

The decomposition of **127** during purification led to efforts being directed to force the reduction of **125** to completion. The reaction was repeated with a large excess of sodium borohydride (~100 equivalents), and the reaction mixture was stirred for three days; after acid work-up ^{1}H NMR spectroscopy showed **127** to be the only product. After washing with water, the isolated solid was dried to give **127** in 85% yield. Anthrone **127** was shown by 2D NOESY NMR spectroscopy to be the correct isomer due to coupling observed between protons of the *ortho*-methyl groups of the aryl ethers and the protons *peri* to these 1,8-substituents.

Conversion of anthrone **127** into triflate **128** was attempted with lithium hexamethyldisilazide (LiHMDS) and triflic anhydride (Scheme 3.26). In a similar reaction published by Toyota and Makino, hexamethylphosporamide (HMPA) was used as a co-solvent,[17] however for safety reasons I decided to substitute this very toxic solvent with the less toxic 1,3-dimethyl-3,4,5,6-tetrahydro-2(1*H*)-pyrimidinone (DMPU).

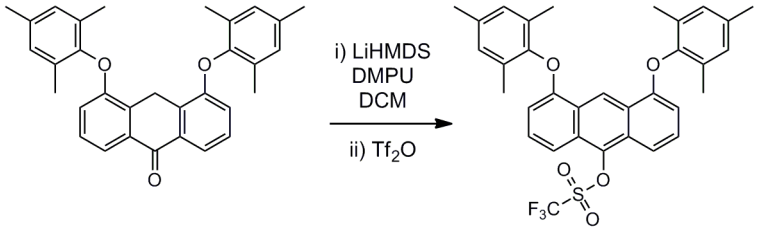

127 **128**

Scheme 3.26: Formation of triflate **128** from anthrone **127**.

The reaction proved to be successful and, after purification, anthracene triflate **128** was isolated in 31% yield. The low yield for this reaction is at least partially due to difficulties in separating DMPU from the product. To avoid these problems, the reaction was repeated in the absence of DMPU, which gave the anthracene triflate **128** in 55% yield.

3.4 Bis-Anthracene Fused Porphyrins Bearing 2,4,6-Trimethylphenoxy Substituted Anthracenes

3.4.1 Synthesis of Anthracene-Linked Porphyrins

The synthesis of bis-anthracene linked porphyrin **129** and mono-anthracene linked porphyrin **130** was achieved by Suzuki coupling, and the resulting products were isolated in 15% and 44% yields respectively (Scheme 3.27).

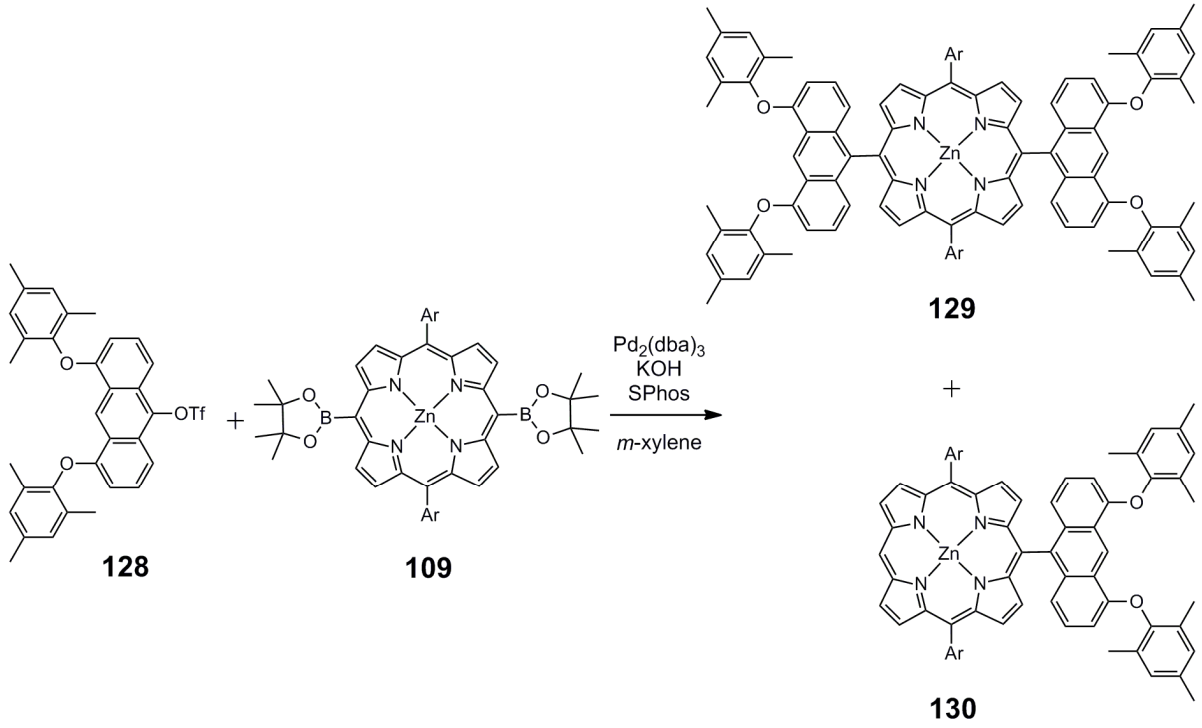

Scheme 3.27: Suzuki coupling pathway to anthracene linked porphyrins **129** and **130**. Ar = 3,5-di(*t*-butyl)phenyl.

3.4.2 Bis-Anthracene Fused Porphyrin Monomer

From the reaction conditions explored in the synthesis of fully fused bis-anthracene porphyrin **117** (Section 3.2.3), I decided that iron(III) chloride was the most promising reagent to use for oxidative ring-closure of bis-anthracene linked porphyrins. As a result zinc porphyrin **129** was demetalated and subjected to nickel insertion to give nickel porphyrin **131** in 92% yield over two steps, following the procedure shown in Scheme 3.14.

Fusion of **131** was initially attempted in dry solvent using ten equivalents of iron(III) chloride (Scheme 3.28). After 30 minutes TLC showed complete consumption of **131**,

together with formation of a red product. This red product was isolated by silica gel chromatography in 72% yield and identified to be partially fused porphyrin **132**.

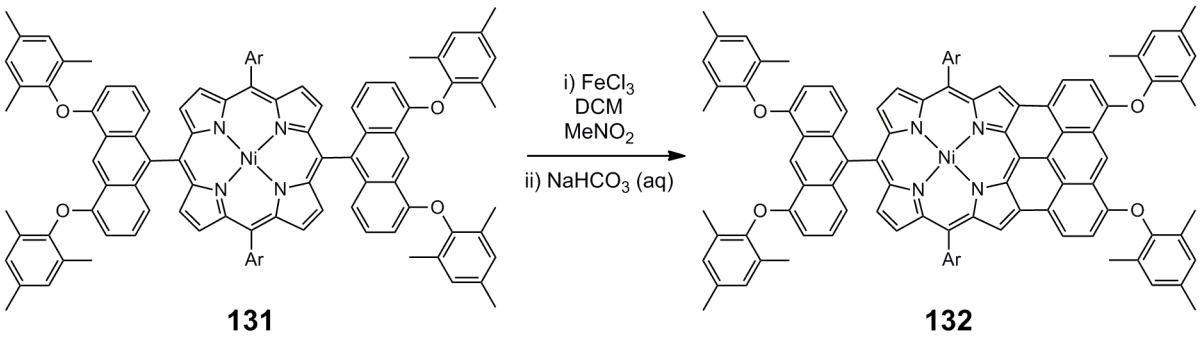

Scheme 3.28: Reaction of **131** with ten equivalents of $FeCl_3$ to give **132**. Ar = 3,5-di(t-butyl)phenyl.

Porphyrin **132** was subjected to a further ten equivalents of iron(III) chloride in an attempt to form the fully fused bis-anthracene porphyrin **133** (Scheme 3.29). After 10 minutes, TLC of the reaction mixture showed the consumption of **132** and the formation of purple material, while MALDI-TOF mass spectrometry revealed the presence of target porphyrin **133** together with several partially chlorinated and methylated fully fused bis-anthracene porphyrins. Separation of these products proved impossible by silica chromatography and by precipitation due to the similarity in polarity and solubility between fully fused bis-anthracene porphyrin **133** and the side products.

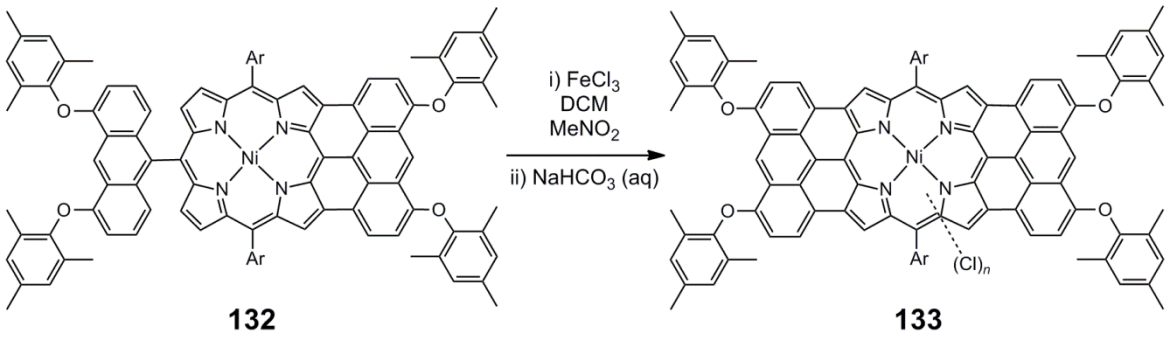

Scheme 3.29: Fusion of **132** to **133** with iron(III) chloride. Ar = 3,5-di(*t*-butyl)phenyl, n = 0 — 4.

The problems of chlorination and methylation encountered in the synthesis of fully fused bis-anthracene porphyrin **133** led to the screening of a wide range of reaction conditions in an attempt to prevent the formation of these side products. Besides exploring other iron(III) salts as oxidants, the fusion of partially fused porphyrin **132** to fully fused porphyrin **133** was also attempted in non-chlorinated solvents, and the solvent for the iron

salt was also varied. Furthermore, the addition of silver salts was explored as a method of scavenging chloride ions during the reaction to prevent their addition to fully fused porphyrin **133**. Table 3.1 summarises the results of the test reactions.

Table 3.1: Reaction conditions trialled for the fusion of **132** to **133**. All reactions were stirred for 10 minutes at room temperature under N_2. Crude reaction mixture investigated by MALDI-TOF mass spectrometry (dithranol matrix).

Solvent (porphyrin)	Solvent (iron salt)	Iron Salt	Ag Salt	Chlorination (1-4 chlorines)	Methylation	Additional Comments
DCM	$MeNO_2$	$FeCl_3$	None	Yes (1-4)	Yes	Mixture of products.
DCM	$MeNO_2$	$FeCl_3$	$AgPF_6$	Yes (1) on starting material	Yes	No di-fused products observed.
DCM	$MeNO_2$	$FeCl_3$	AgOTf	Yes (1)	Yes	Much less chlorination
Toluene	$MeNO_2$	$FeCl_3$	AgOTf	Yes (a little 1)	Yes	Much less chlorination.
DCM	$MeNO_2$	$Fe(acac)_3$	None	None	Yes	Mainly starting material observed.
DCM	$MeNO_2$	$Fe(NO_3)_3$	None	Yes (1) of starting material	No	Large mixture of products observed.
DCM	$MeNO_2$	$Fe(OTf)_3$	None	Yes (1-2)	Yes	Smaller degree of chlorination.
DCM	MeCN	$FeCl_3$	None	Yes (a lot of 1-2)	None	Mainly starting material.
DCM	MeCN	$FeCl_3$	AgOTf	Yes (a lot of 1)	None	Some starting material observed.
Toluene	MeCN	$Fe(OTf)_3$	AgOTf	None	None	Large mixture of products observed.

From Table 3.1 it can be seen that the use of acetonitrile instead of nitromethane as a solvent for the iron salt can suppress methylation of the fused porphyrin. Unfortunately

the poor solubility of iron(III) chloride in this solvent presented difficulties since it meant that a larger volume of acetonitrile was required to dissolve ten equivalents of iron(III) chloride. The poor solubility of partially fused porphyrin **132** in acetonitrile required the addition of a large volume of this solvent which reduced the concentration of **132** in solution, causing only a limited proportion of starting material to react. Table 3.1 also shows that the presence of silver triflate can reduce the extent of chlorination taking place during the reaction, although complete suppression was not observed.

From the reaction conditions tested in Table 3.1, the best conditions found for the formation of fully fused porphyrin **133** from partially fused porphyrin **132** were iron(III) chloride with silver triflate in a mixture of toluene and nitromethane. While these conditions did not totally suppress methylation and chlorination, the reaction did proceed to completion and the side products observed were both fewer in number and lower in intensity than seen for the initial reaction conditions. Upon purification of this reaction mixture, it was found that the bulky aryl ether groups of fully fused porphyrin **133** appeared to reduce aggregation of the porphyrin relative to octyloxy substituted bis-anthracene fused porphyrin **117**, enabling purification by silica chromatography without loss of product through strong adsorption to silica. Repeated chromatography followed by precipitation finally gave bis-anthracene fused porphyrin **133** in 15% yield.

^{1}H NMR spectroscopy of fully fused bis-anthracene porphyrin **133** in $CDCl_3$ showed broad peaks in the aromatic region. In order to reduce suspected radical species and observe sharp peaks, 10 μL of hydrazine hydrate was added to the NMR sample. The sample was shaken and poured into a separating funnel where 3 mL of water were added. The organic layer was separated and immediately transferred to an NMR tube and the ^{1}H NMR spectrum recorded. Following this method, the ^{1}H NMR spectrum displayed sharp peaks in the aromatic and aliphatic regions, demonstrating the success of the bulky aryl ether groups in limiting aggregation (Figure 3.9).

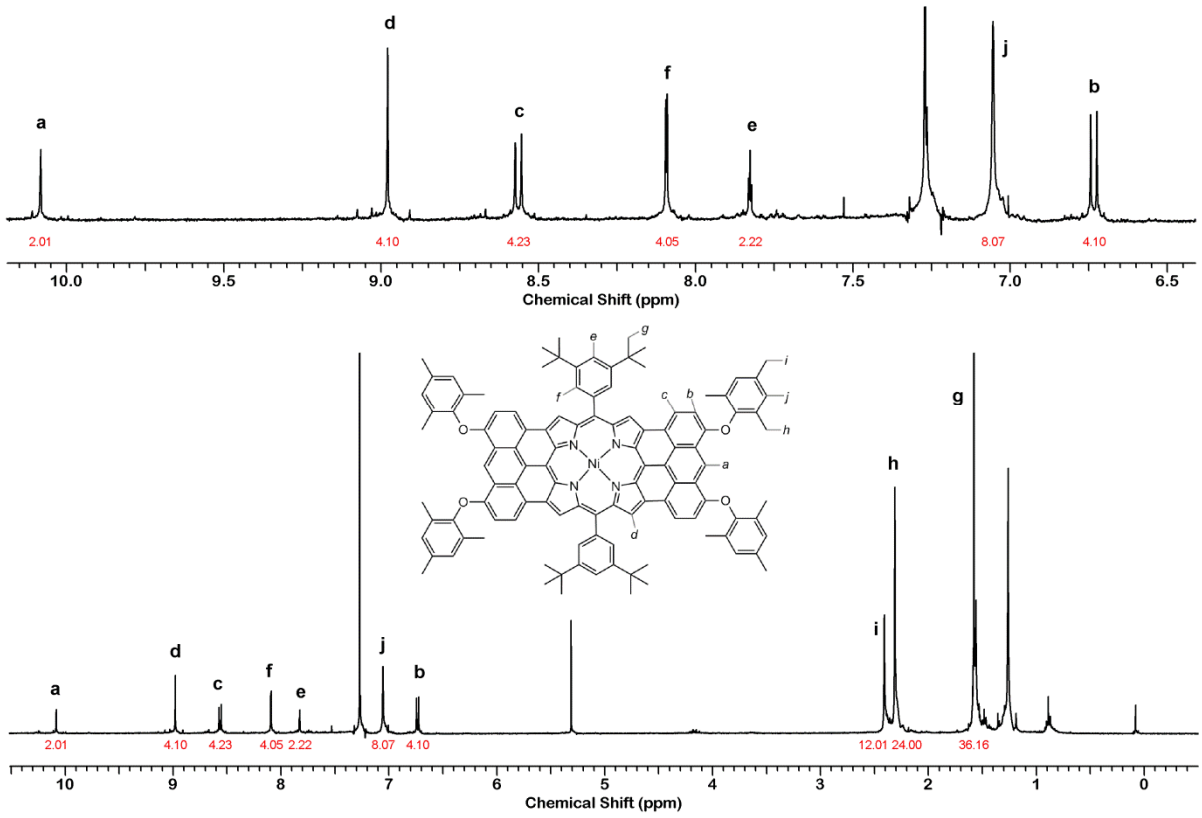

Figure 3.9: ^{1}H NMR spectrum of fully fused bis-anthracene porphyrin **133** (400 MHz, $CDCl_3$ with traces of N_2H_4, 298 K). Red numbers indicate peak integrals.

Increasing the concentration of the NMR sample resulted in broadening of the peaks in the ^{1}H spectrum rather than an increase in signal intensity, indicating that some aggregation was occurring. Attempts were made to record a ^{13}C NMR spectrum of fully fused bis-anthracene porphyrin **133**, however the signal to noise ratio in the aromatic region of the ^{13}C spectra was too poor to be able to distinguish peaks.

3.4.3 UV-vis-NIR Absorption Spectra of Anthracene-Porphyrins 131, 132 and 133

The UV-vis-NIR spectra of bis-anthracene linked porphyrin **131**, partially fused bis-anthracene porphyrin **132** and fully fused bis-anthracene porphyrin **133** are shown in Figure 3.10.

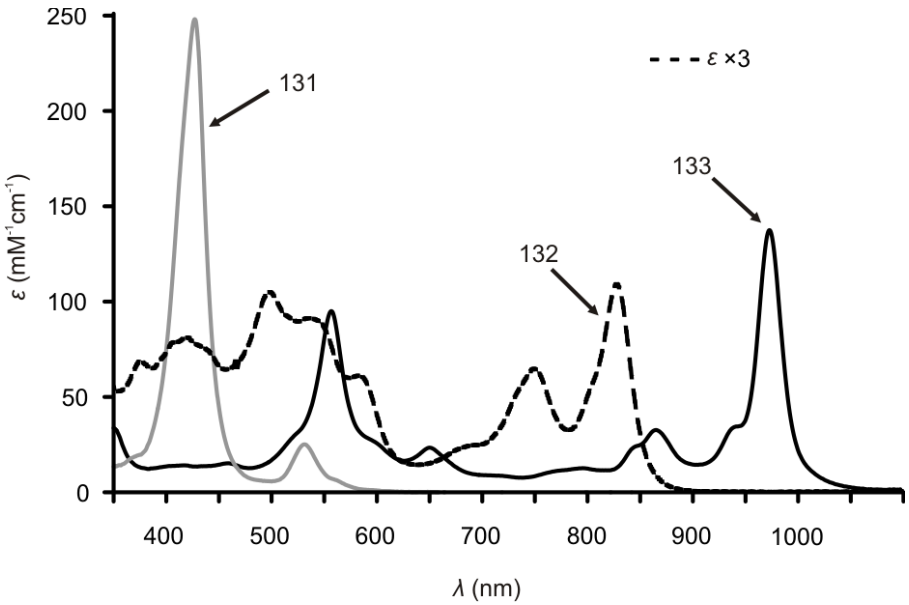

Figure 3.10: UV-vis-NIR absorption spectra in $CHCl_3$/1% pyridine for **131** (grey), **132** (ε × 3 for clarity, black dash) and **133** (solid black).

Unfused anthracene-linked porphyrin **131** shows absorption typical of a porphyrin monomer, with an intense Soret band at 427 nm.[12,25] Expansion of the π-system by fusion to an anthracene unit greatly perturbs the electronic structure of the system. As a result partially fused bis-anthracene porphyrin **132** displays a red-shifted absorption spectrum, with a λ_{max} at 828 nm, together with a highly distorted spectral shape and lower peak intensities.

Similar spectral properties have also been reported for other low-symmetry porphyrins such as mono-naphthalene (**48**), pyrene (**55**) and azulene (**49**) fused porphyrins (Figure 3.11).[12,26-28]

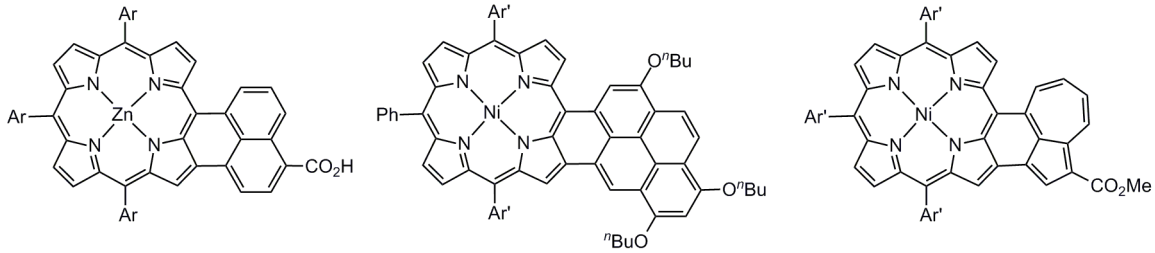

48 **55** **49**

Figure 3.11: Porphyrins fused to a single aromatic ring.[12,26,27] Ar = 2,4,6-trimethylphenyl, Ar' = 3,5-di(*t*-butyl)phenyl.

Mono-naphthalene fused zinc porphyrin **48** shows a λ_{max} in the near-IR of around 682 nm, however this broad Q-type absorption is five times lower in intensity than for the

corresponding Soret-type absorption.[27] This contrasts to anthracene-fused porphyrin **132** where the λ_{max} in the near-IR is both sharp and of a similar intensity to absorption in the Soret region. Mono-pyrene fused nickel porphyrin **55** exhibits a near-IR λ_{max} of 724 nm, together with several absorption peaks at higher energy.[26] Furthermore, mono-azulene fused porphyrin **49** displays very broad absorption of low intensity in the near-IR region, with no discernable peaks and a tail that reaches to around 1000 nm.[12] Comparison of this data with the spectrum of partially fused bis-anthracene porphyrin **132** suggests that the greater symmetry of the anthracene-fused porphyrin system may be responsible for the sharpness and high intensity of the near-IR absorption of **132**.

It can be concluded that the extent of perturbation of the porphyrin π-system upon fusion to an aromatic is dependent upon two main factors: the size of the aromatic unit and the number of bonds formed between this unit and the porphyrin upon fusion. Both factors influence the degree of red-shifting observed in the Q-band region of the absorption spectra. However the second factor also demonstrates that fusion across both β-positions creates a far more dramatic distortion of the spectral shape, and far greater similarities in intensity between Soret and Q band regions than fusion across just one β-position, reflecting both the greater degree of electronic communication and the higher symmetry of the triply linked system.

The fusion of the second anthracene unit of **132** to form fully fused bis-anthracene porphyrin **133** results in a chromophore of higher symmetry giving a simpler, sharper spectrum with higher peak intensities. This further expansion of the π-system results in a larger red-shift of the absorption spectrum relative to unfused porphyrin **131**, with **133** displaying a λ_{max} at 973 nm. The sharpness and intensity of this peak is unusual (ε = 1.4 × 10^5 M^{-1} cm^{-1}; fwhm = 300 cm^{-1}); Osuka and co-workers synthesised a porphyrin fused to two azulene units (**50**, Figure 3.12), however this system displays much broader absorption in the near-IR with maxima at 763, 898 and 1014 nm at lower intensities.

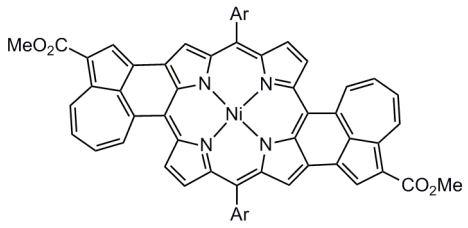

50

Figure 3.12: Bis-azulene fused porphyrin synthesised by Osuka and co-workers.[12] Ar = 3,5-di(*t*-butyl)phenyl.

Comparison of bis-anthracene fused porphyrin **133** to porphyrins fused to two naphthocycloheptanone units (**39** and **40**, Figure 3.13)[29] synthesised by Scott and co-workers, reveals that **133** displays longer wavelength absorption and higher intensities, with both *cis*-porphyrin **40** and *trans*-porphyrin **39** displaying a logε of 4.6 at their longest wavelength absorption maxima (705 nm for **39**, 681 nm for **40**) compared to the logε of 5.1 for porphyrin **133**.

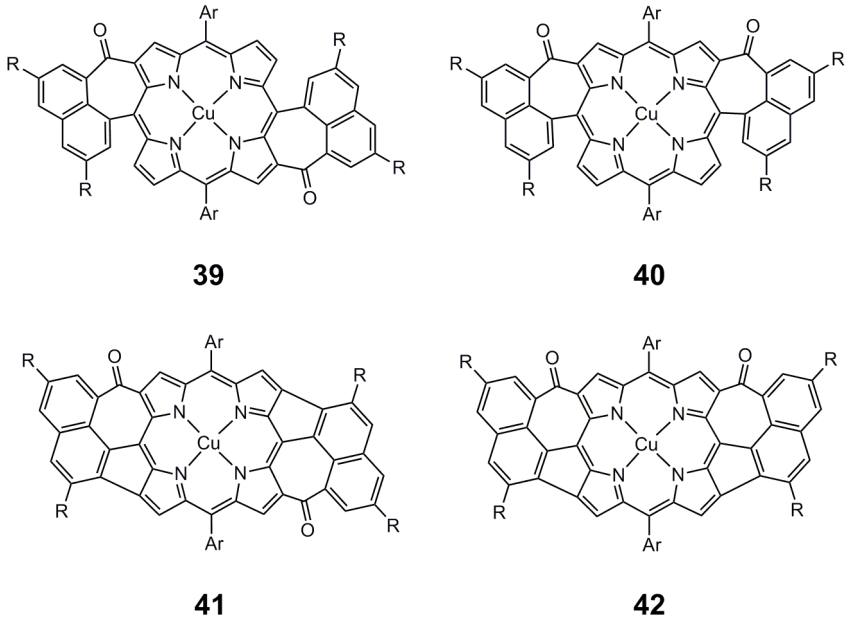

39 **40**

41 **42**

Figure 3.13: Bis(naphthocycloheptanone) and bis(naphthoazulenone)fused porphyrin systems synthesised by Scott and co-workers.[29] R = ^{t}Butyl, Ar = 2,4,6-trimethylphenyl.

Oxidation of **39** and **40** has been reported to yield bis(naphthoazulenone) fused porphyrins **41** and **42** respectively (Figure 3.13). These systems exhibit broad absorption in the near-IR with a λ_{max} at 1204 nm for *trans* porphyrin **41** and 894 nm for *cis* porphyrin **42**. These peaks have logε values of 3.9 and 4.2 respectively, which again are much lower than observed for

the λ_{max} of bis-anthracene fused porphyrin **133**. The broad nature of their near-IR absorption, together with the low peak intensities of these bis(naphthoazulenone) fused porphyrin systems, indicate a weaker electronic interaction between the porphyrin and the aromatic unit than for fully fused bis-anthracene porphyrin **133**. This confirms that anthracene units, with their noted geometry match to the porphyrin periphery, experience excellent conjugation with the porphyrin core upon fusion, displaying more intense near-IR absorption than observed for other fused porphyrin systems.

3.4.4 X-Ray Crystal Structure of Bis-Anthracene Fused Porphyrin Monomer 133

Crystals of fully fused bis-anthracene porphyrin **133** were grown by layered addition of methanol to a solution of **133** in chloroform. The crystals were thin, small and highly susceptible to solvent loss, however a low-resolution crystal structure was obtained from X-ray diffraction data collected at the Diamond Light Source (synchrotron beamline I19) by Dr Amber Thompson (Figure 3.14). The crystals of porphyrin **133** were found to be highly solvated, with 52% of the unit cell being occupied with disordered solvent (Figure 3.15).

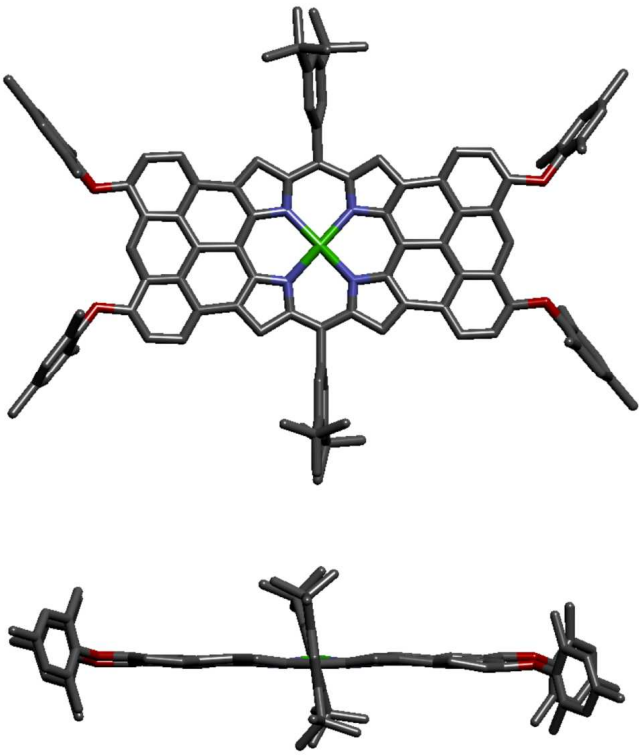

Figure 3.14: Two orthogonal views of the molecular structure of **133** in the crystal. Hydrogens omitted for clarity.

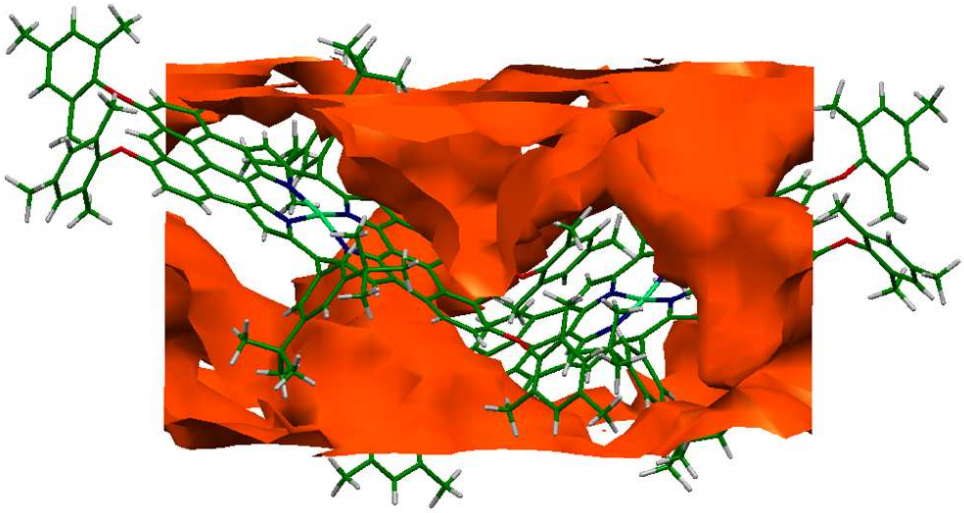

Figure 3.15: The solvent void surface for one unit cell of **133** is shown in orange. The solvent accessible void as calculated by PLATON/SQUEEZE is 52% of the unit cell volume.

The structure confirms a regular planar geometry of the π-system, and shows the twisted arrangement of the mesityl substituents relative to the anthracene-porphyrin core, which limits π-stacking. Porphyrin **133** packs in a herringbone arrangement with each porphyrin horizontally offset to the one above it. The poor quality of the X-ray diffraction data meant that a large number of restraints were required, preventing detailed analysis of the structure. Details of these restraints may be found in reference 30.[30]

3.4.5 Electrochemistry of Porphyrins 131, 132 and 133

Cyclic and square wave voltammetry were carried out on porphyrins **131**, **132** and **133** to determine their redox potentials. All measurements are quoted versus the ferrocene/ferrocinium redox couple. The cyclic and square wave voltammograms for bis-anthracene linked porphyrin **131** are shown in Figures 3.16 and 3.17 respectively. Porphyrin **131** has an E_1^{ox} of 0.61 V and an E_1^{red} of –1.86 V, giving an E_1^{ox}- E_1^{red} of 2.47 V, which is typical for an unfused porphyrin monomer.[31,32]

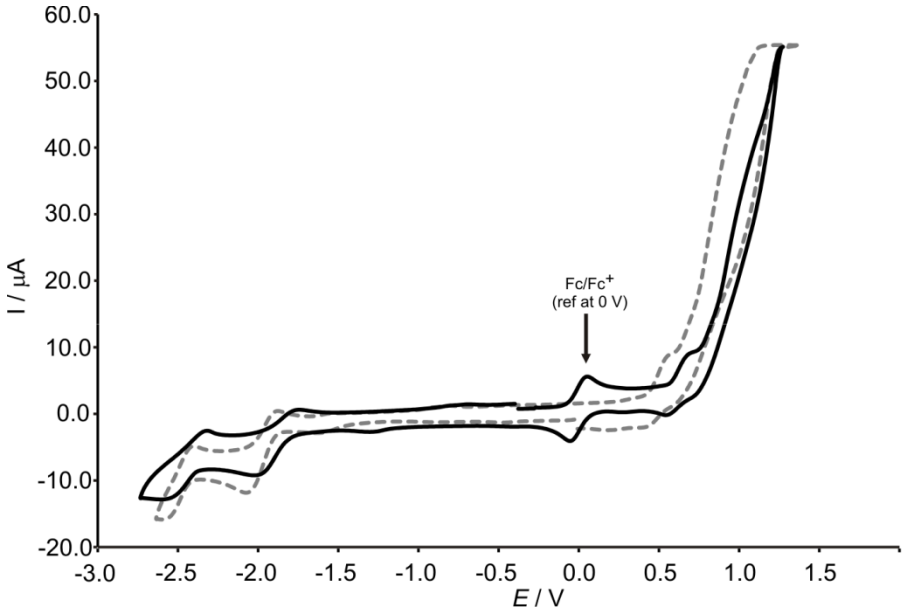

Figure 3.16: Cyclic voltammogram for unfused bis-anthracene linked porphyrin **131**, both with ferrocene (black), and without (grey). Cyclic voltammetry was carried out in THF with 0.1 M Bu_4NPF_6 at a scan rate of 100 mV s^{-1} using a glassy carbon working electrode, Pt counter electrode and $Ag/AgNO_3$ reference electrode.

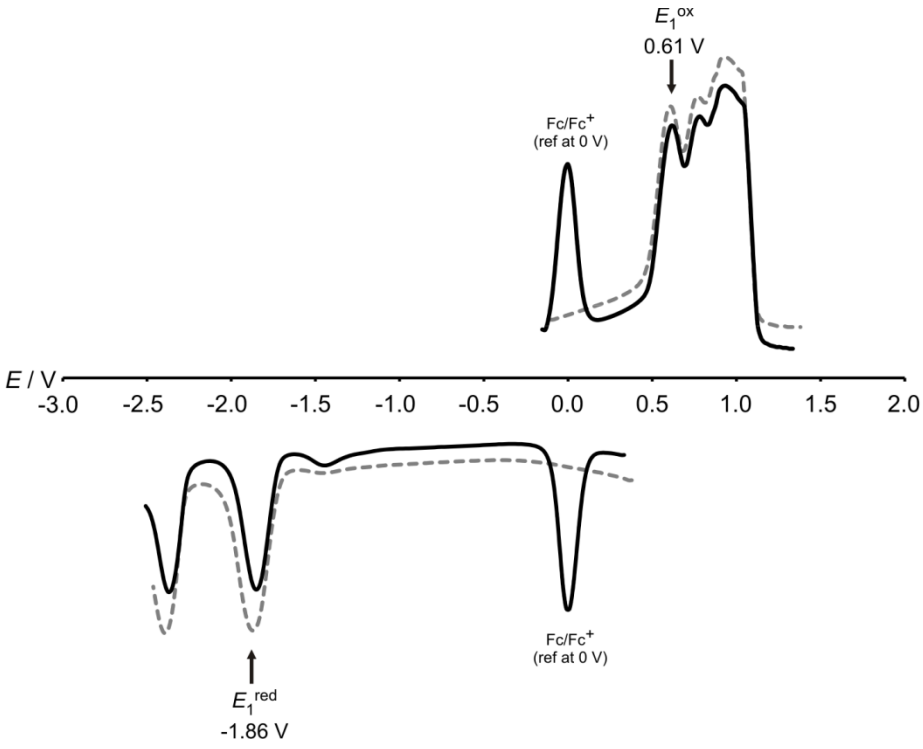

Figure 3.17: Square wave voltammogram for unfused bis-anthracene linked porphyrin **131**, both with ferrocene (black), and without (grey). Square wave experiments were recorded in THF with 0.1 M Bu_4NPF_6 at a square wave frequency of 8 Hz using a glassy carbon working electrode, Pt counter electrode and $Ag/AgNO_3$ reference electrode.

Fusion of one anthracene unit to the porphyrin ring increases electron delocalisation across the system. Porphyrin **132** displays an E_1^{ox} of 0.32 V and an E_1^{red} of –1.32 V leading to an E_1^{ox}- E_1^{red} separation of 1.64 V, which is smaller than for the unfused anthracene-linked porphyrin **131**, reflecting the increase in π-conjugation (Figures 3.18 and 3.19). This E_1^{ox}-E_1^{red} separation is slightly larger than for azulene-fused porphyrin **49**, which exhibits a value of 1.58 V, as expected from the larger red-shift in the UV-vis-NIR absorption spectrum of **49** compared to partially fused bis-anthracene porphyrin **132**.[12] However the first oxidation potential of partially fused bis-anthracene porphyrin **132** is lower than for both naphthalene-fused porphyrin **48** (0.59 V)[27] and, surprisingly, azulene-fused porphyrin **49** (0.38 V),[12] indicating that porphyrin **132** is easier to oxidise.

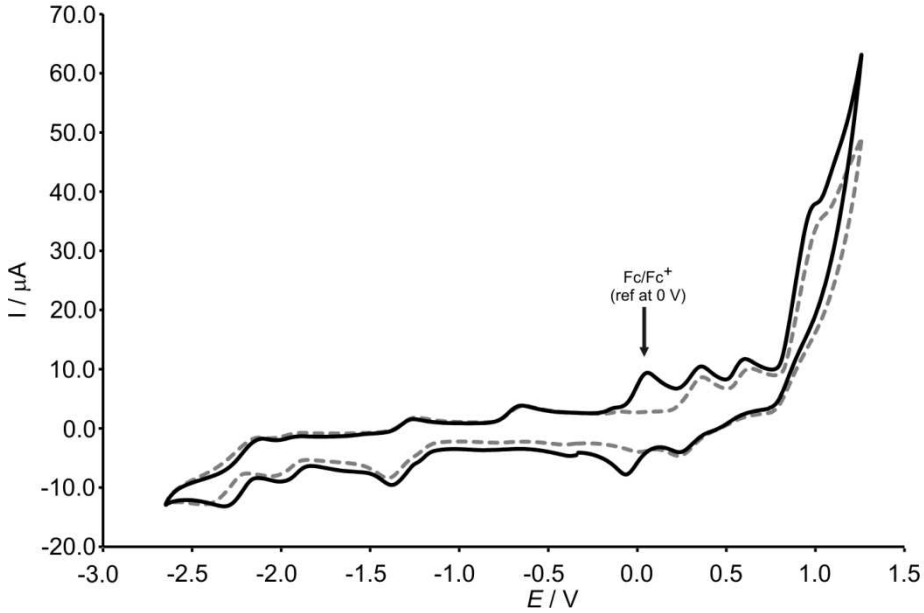

Figure 3.18: Cyclic voltammogram for partially fused bis-anthracene porphyrin **132**, both with ferrocene (black), and without (grey) Cyclic voltammetry was carried out in THF with 0.1 M Bu_4NPF_6 at a scan rate of 100 mV s^{-1} using a glassy carbon working electrode, Pt counter electrode and $Ag/AgNO_3$ reference electrode.

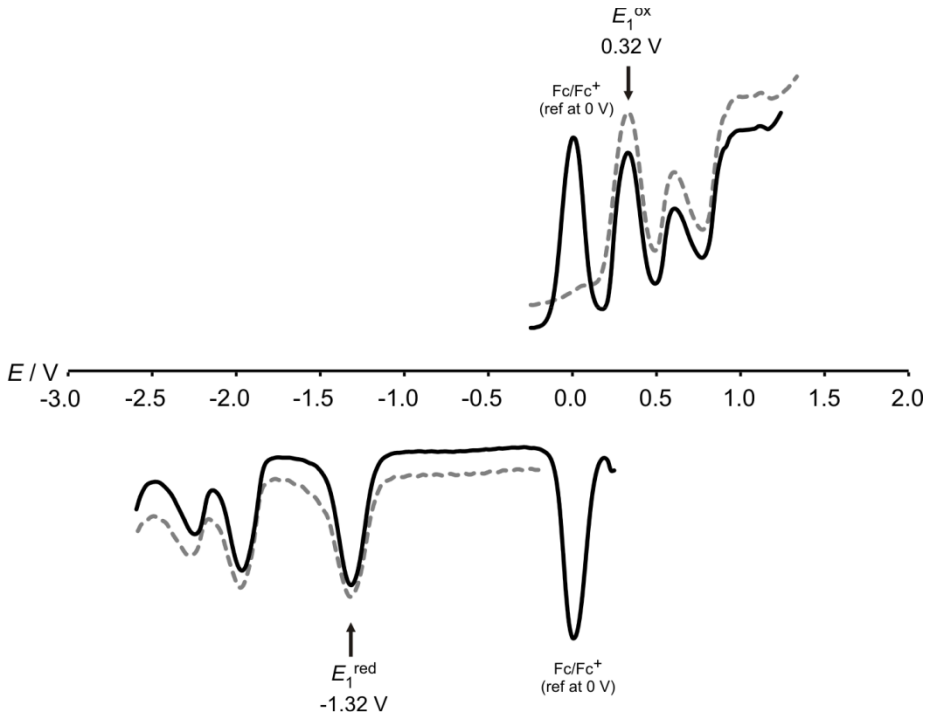

Figure 3.19: Square wave voltammogram for partially fused bis-anthracene porphyrin **132**, both with ferrocene (black), and without (grey). Square wave experiments were recorded in THF with 0.1 M Bu_4NPF_6 at a square wave frequency of 8 Hz using a glassy carbon working electrode, Pt counter electrode and $Ag/AgNO_3$ reference electrode.

Fully fused anthracene-porphyrin **133** shows an E_1^{ox} of 0.06 V and an E_1^{red} of –1.20 V, leading to an E_1^{ox}- E_1^{red} separation of 1.26 V (Figures 3.20 and 3.21). This value is smaller than observed for both unfused porphyrin **131** and partially fused bis-anthracene porphyrin **132**, reflecting the trend that the greater the degree of conjugation, the smaller the E_1^{ox}- E_1^{red} separation. This separation is only slightly larger than observed for bis-azulene fused porphyrin **50** (Figure 3.12) indicating a similar degree of electron delocalisation for both porphyrins. Furthermore, the first oxidation potential of fully fused bis-anthracene porphyrin **133** (0.06 V) is much lower than for azulene-porphyrin **50** (0.25 V) revealing that formation of a radical cation is far easier for porphyrin **133** than for **50**. The E_1^{ox}- E_1^{red} separation of fully fused bis-anthracene porphyrin **133** (1.26 V) lies between those of bis(naphthoazulenone) fused porphyrin systems **41** and **42** (1.17 V and 1.33 V respectively)[29] as expected from their near-IR λ_{max} values.

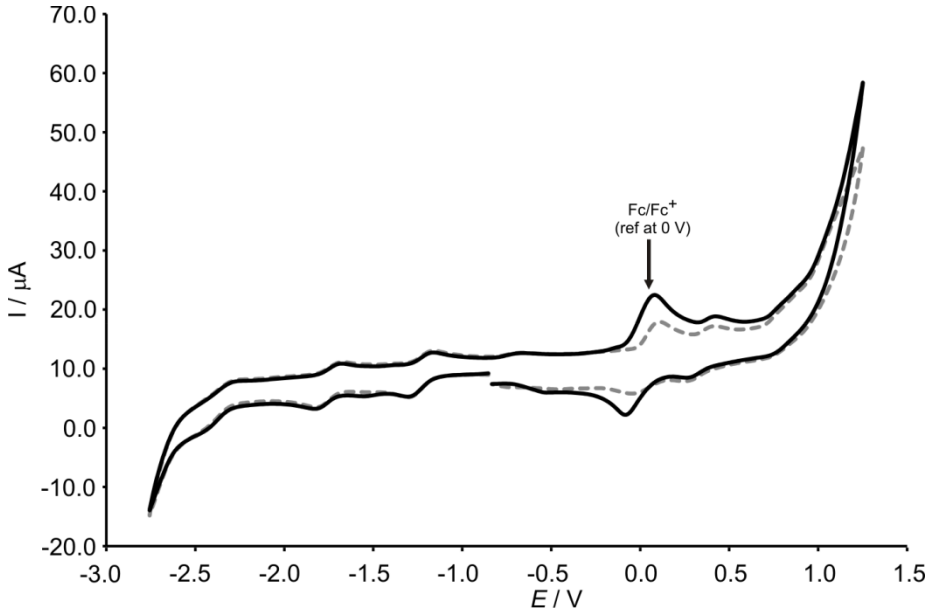

Figure 3.20: Cyclic voltammogram for fully fused bis-anthracene porphyrin **133**, both with ferrocene (black), and without (grey) Cyclic voltammetry was carried out in THF with 0.1 M Bu_4NPF_6 at a scan rate of 100 mV s^{-1} using a glassy carbon working electrode, Pt counter electrode and $Ag/AgNO_3$ reference electrode.

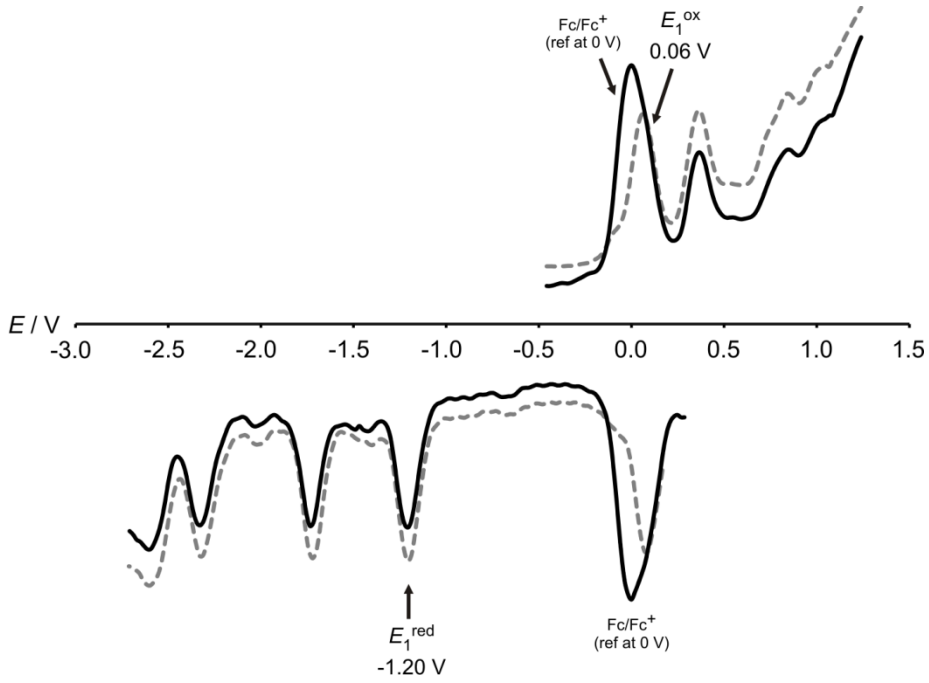

Figure 3.21: Square wave voltammogram for fully fused bis-anthracene porphyrin **133**, both with ferrocene (black), and without (grey). Square wave experiments were recorded in THF with 0.1 M Bu_4NPF_6 at a square wave frequency of 8 Hz using a glassy carbon working electrode, Pt counter electrode and $Ag/AgNO_3$ reference electrode.

The electrochemical gaps of anthracene-porphyrins **131, 132** and **133** match well with their optical gaps of 2.34, 1.50 and 1.28 eV respectively measured at their near-IR maxima. The surprisingly low first oxidation potentials of anthracene-fused porphyrins **132** and **133**, together with their small HOMO-LUMO gaps, suggest that these porphyrins could facilitate efficient charge transport. A summary of the electrochemical data for porphyrins **131**, **132** and **133** is given in Table 3.2.

Table 3.2: Summary of electrochemical data for porphyrins **131**, **132**, and **133** measured in THF with 0.1 M Bu_4NPF_6. $E_{g(opt)}$ refers to the optical gap measured at the longest wavelength absorption maxima for each of the compounds.

Compound	E_1^{ox} (V)	E_1^{red} (V)	E_1^{ox}-E_1^{red} (V)	$E_{g(opt)}$ (eV)
34	0.61	-1.86	2.47	2.34
35	0.32	-1.32	1.64	1.50
36	0.06	-1.20	1.26	1.28

3.4.6 Bis-Anthracene Fused Porphyrin Dimer

Anthracene-linked porphyrin **130** was isolated in 44% yield from the Suzuki coupling reaction shown in Scheme 3.27. This porphyrin was subjected to 15 equivalents of scandium(III) triflate and DDQ (Scheme 3.30).

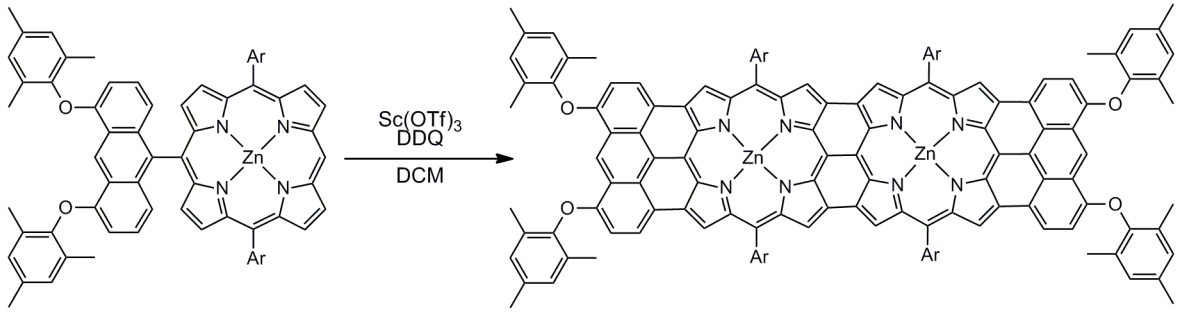

130 **134**

Scheme 3.30: Fusion of **130** to form dimer **134** with $Sc(OTf)_3$ and DDQ. Ar = 3,5-di(*t*-butyl)phenyl.

The complete consumption of mono-anthracene linked porphyrin **130** was observed after one hour, and many blue products were noted. The mixture was loaded onto a silica gel column in freshly distilled THF, and the fractions were analysed by MALDI-TOF mass spectrometry. The first fraction isolated gave a clean MALDI-TOF mass spectrum with

excellent isotopic resolution corresponding to fully fused dimer **134**, however subsequent fractions were shown to contain a large number of unidentified compounds of higher molecular weights. Upon monitoring the reaction over time by MALDI-TOF mass spectrometry, I found that longer reaction times, or an increase in the number of equivalents of oxidant, led to an increase in the formation of these high molecular weight side products. As a result the reaction time was reduced from one hour to 25 minutes. With these reaction conditions, fully fused dimer **134** was isolated in 13% yield.

^{1}H NMR spectroscopy of dimer **134** in $CDCl_3$ gave a featureless spectrum, possibly because the mesityl substituents on the anthracene units were not sufficiently bulky as to completely prevent aggregation between porphyrins. Coordination of pyridine to the zinc metal of a porphyrin can exert further steric effects to help to reduce π-stacking interactions. As a result, 10 μL pyridine-d_5 was added to the NMR sample, however under these conditions only broad peaks were observed in the ^{1}H NMR spectrum.

In order to try and force the porphyrin dimers to disaggregate I decided to run the ^{1}H NMR spectroscopy of fully fused dimer **134** in pure pyridine-d_5. The resulting ^{1}H NMR spectrum showed sharp peaks in the aromatic region, however the signals were of a very low intensity relative to the residual pyridine signals. Furthermore, these pyridine signals occur in the same region as those belonging to dimer **134**. Therefore, the intensity of the pyridine signals was reduced by utilising diffusion ordered ^{1}H DOSY spectroscopy. Under these conditions, sharp peaks were observed in both the aliphatic and aromatic regions of the spectrum and were assigned by 2D NOESY NMR spectroscopy to the protons of dimer **134** (Figure 3.22) however, even with repeated precipitations from pentane, it was not possible to remove all 'grease' impurities.

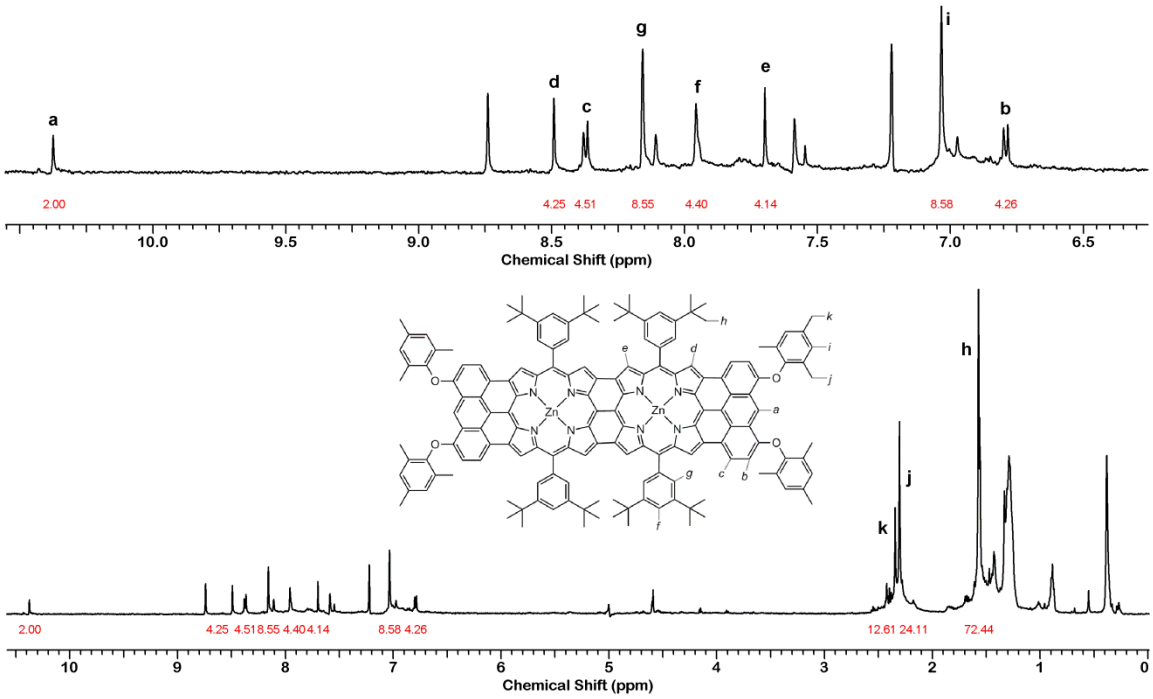

Figure 3.22: ^{1}H DOSY NMR spectrum of fully fused bis-anthracene dimer **134** (500 MHz, pyridine-d_5, 298 K). Red numbers indicate peak integrals.

Increasing sample concentration was not seen to increase peak intensity, probably due to aggregation effects. Unsurprisingly, ^{13}C NMR spectroscopy of dimer **134** failed to give a clear spectrum, with only a very poor signal to noise ratio seen, and indistinguishable peaks.

3.4.7 UV-vis-NIR Absorption Spectra of Anthracene-Porphyrins 130 and 134

The UV-vis-NIR absorption spectra of anthracene-linked porphyrin monomer **130** and bis-anthracene fused porphyrin dimer **134** are shown in Figure 3.23. Porphyrin **130** shows an absorption spectrum typical of a porphyrin monomer with a sharp, intense peak at 429 nm corresponding to the porphyrin Soret band. Fusion of **130** to form bis-anthracene fused porphyrin dimer **134** results in a drastic red-shift of the absorption spectrum, with dimer **134** displaying a λ_{max} of 1495 nm in the near-IR. Furthermore, the spectral shape is similar to that observed for bis-anthracene fused monomer **133** indicating that both chromophores are of the same D_{2h}- symmetry.

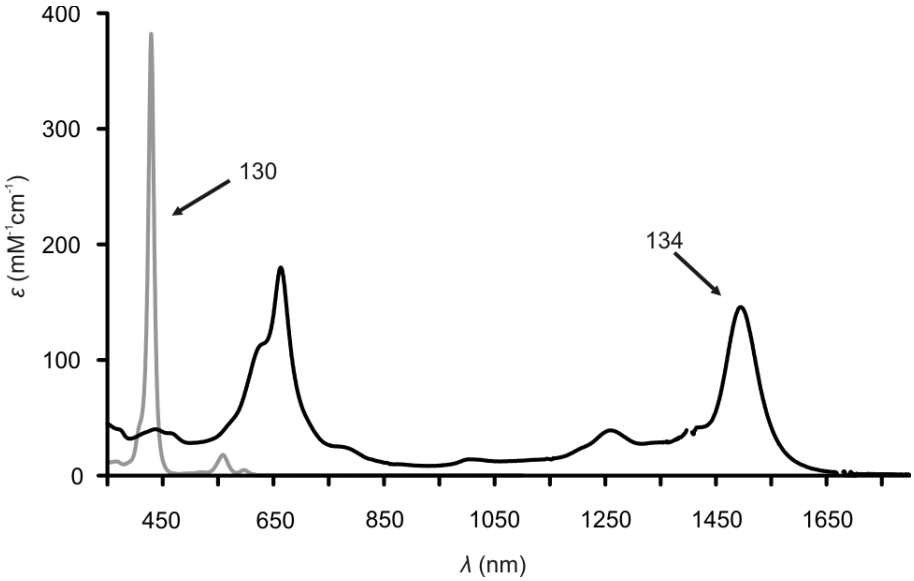

Figure 3.23: UV-vis-NIR absorption spectra in $CHCl_3$/1% pyridine for **130** (grey) and **134** (black).

The extensive absorption seen in the near-IR for dimer **134** is exceptional for a porphyrin dimer. Triply linked zinc porphyrin dimers such as **135** and **136** (Figure 3.24) have been reported in the literature and exhibit absorption spectra with a similar spectral shape to that of porphyrin **134**.[31,33,34] However the near-IR absorption of dimers **135** and **136** exhibit λ_{max} values of 1087 and 1061 nm respectively; addition of butylamine to dimer **136** red-shifts the λ_{max} to 1146 nm. From this comparison it can be seen that capping of a porphyrin dimer by fusion to two anthracene units red-shifts the near-IR absorption of the chromophore significantly, and decreases the optical gap by around 0.3 eV.

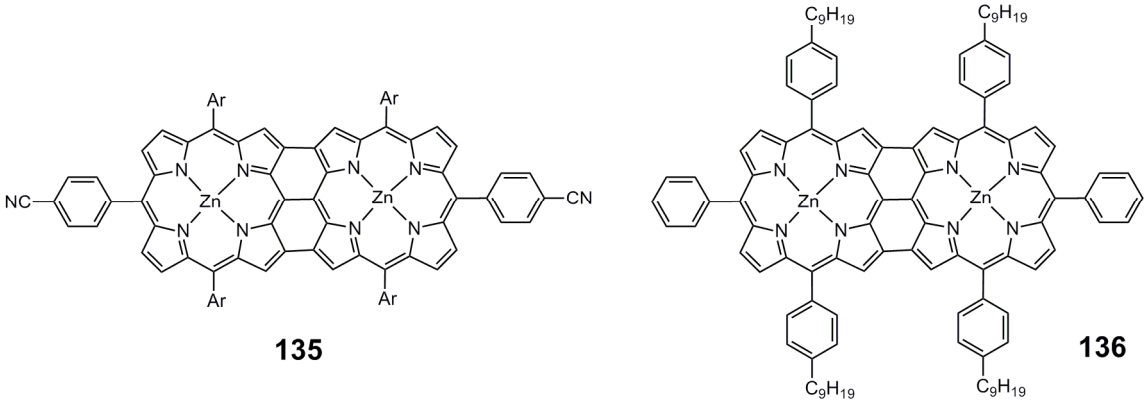

Figure 3.24: Porphyrin dimers **135** and **136**. Ar = 3,5-di(*t*-butyl)phenyl.[33,34]

Porphyrin trimers **137** and **138** (Figure 3.25) have also been reported in the literature.[33,34] These systems exhibit absorption spectra with very similar shape to that of dimer **134**, together with extensive absorption in the near-IR, demonstrating λ_{max} values of

1407 and 1494 nm for **137** and **138** respectively (the spectrum for **138** was recorded in the presence of butylamine). However while the intensity of absorption for trimer **138** is similar to that observed for dimer **134** (logε of 5.2 for both), trimer **137** exhibits a lower intensity of absorption with a logε of 4.7. This suggests that **137** may form aggregates in solution, even at low concentrations, in the absence of a coordinating solvent.

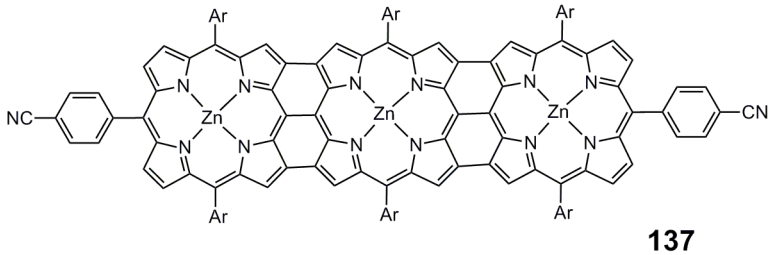

137

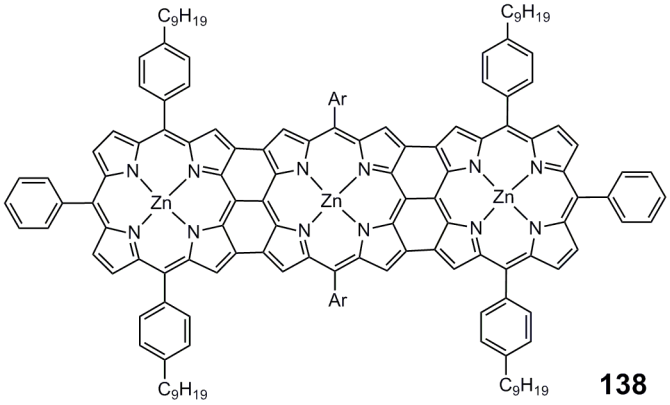

138

Figure 3.25: Porphyrin trimers **137** and **138**. Ar = 3,5-di(*t*-butyl)phenyl.[33,34]

It can be seen from these data that bis-anthracene fused porphyrins exhibit similar UV-vis-NIR absorption to triply linked porphyrin trimers. This suggests that conjugation between the anthracene and porphyrin units in fused dimer **134** is as extensive as that between three fused porphyrins. Triply linked porphyrin tapes have shown promise in the field of molecular wires,[35] hence it may be expected that bis-anthracene fused dimers may also demonstrate similar potential as charge transport materials.

The strong influence of the anthracene units upon the electronic structure of the fused porphyrin dimer **134** can be seen by comparison with bis-pyrene fused zinc porphyrin dimer **58** (Figure 3.26).[36] This dimer, synthesised by Thompson and co-workers after our publication of the synthesis of **134**, is similar in structure to bis-anthracene fused porphyrin dimer **134** and displays a UV-vis-NIR absorption spectrum with a similar spectral shape.

However the near-IR λ_{max} of bis-pyrene fused dimer **58** is much less red-shifted than for bis-anthracene fused porphyrin **134**, occurring at 1323 nm. This confirms the trend observed in Section 3.4.3, that the extent of delocalisation across a fused porphyrin system depends not only upon the size of the aromatic moiety being fused to the porphyrin, but also upon the number of bonds linking it to the porphyrin periphery.

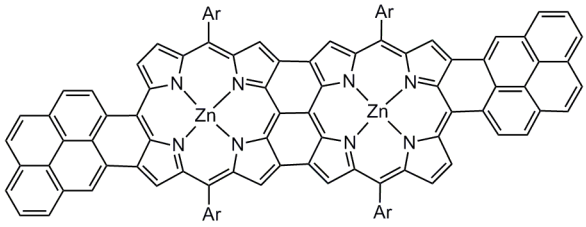

58

Figure 3.26: Bis-pyrene fused porphyrin dimer **58**.[36] Ar = 3,5-di(*t*-butyl)phenyl.

3.4.8 Electrochemistry of Porphyrins 130 and 134

Cyclic and square wave voltammetry were carried out on porphyrins **130** and **134** to determine their redox potentials. All measurements are quoted versus the ferrocene/ferrocinium redox couple. Mono anthracene-linked porphyrin **130** shows an E_1^{ox} of 0.44 V and an E_1^{red} of –1.96 V giving an E_1^{ox}- E_1^{red} of 2.40 V (Figures 3.27 and 3.28), typical for an unfused porphyrin monomer.[31,32]

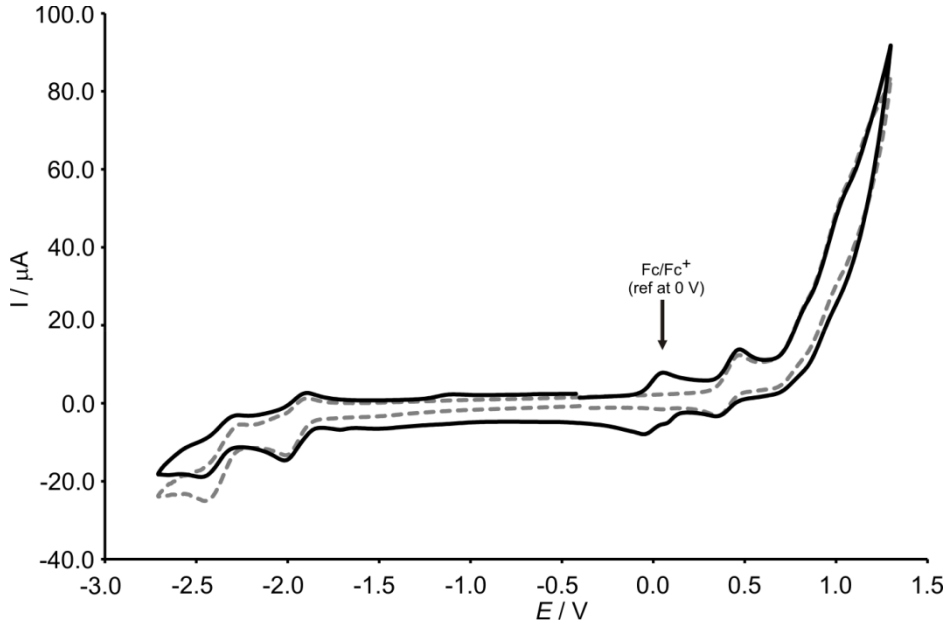

Figure 3.27: Cyclic voltammogram for unfused mono-anthracene porphyrin **130**, both with ferrocene (black), and without (grey). Cyclic voltammetry was carried out in THF with 0.1 M Bu_4NPF_6 at a scan rate of 100 mV s^{-1} using a glassy carbon working electrode, Pt counter electrode and $Ag/AgNO_3$ reference electrode.

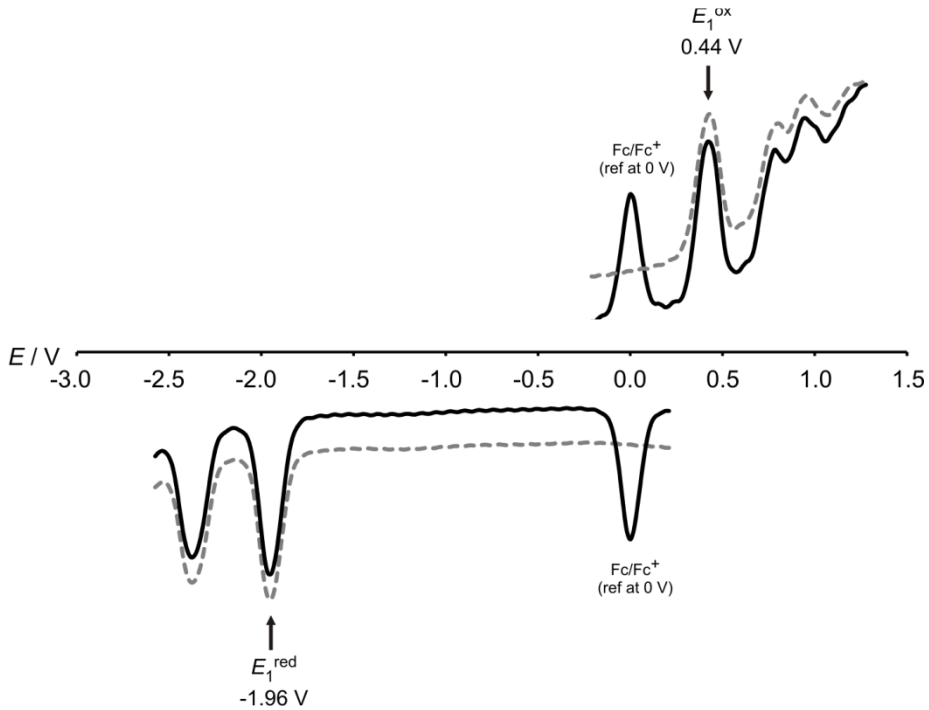

Figure 3.28: Square wave voltammogram for unfused mono-anthracene porphyrin **130**, both with ferrocene (black), and without (grey). Square wave experiments were recorded in THF with 0.1 M Bu_4NPF_6 at a square wave frequency of 8 Hz using a glassy carbon working electrode, Pt counter electrode and $Ag/AgNO_3$ reference electrode.

Fusion of **130** to form dimer **134** results in a drastic change to the cyclic and square wave voltammograms (Figures 3.29 and 3.30 respectively). The first oxidation peak, E_1^{ox}, of

porphyrin dimer **134** occurs at a potential of –0.24 V relative to ferrocene, which is far lower than for monomer **130**, while the first reduction peak, E_1^{red}, occurs at –1.01 V for dimer **134** which is a more positive potential than for unfused mono-anthracene linked porphyrin **130**. This leads to dimer **134** exhibiting an E_1^{ox}- E_1^{red} separation of 0.77 V which is nearly a third of the E_1^{ox}- E_1^{red} separation observed for monomer **130**. Furthermore, this electrochemical gap is close to the optical gap of 0.83 V measured at the near-IR λ_{max} for dimer **134**.

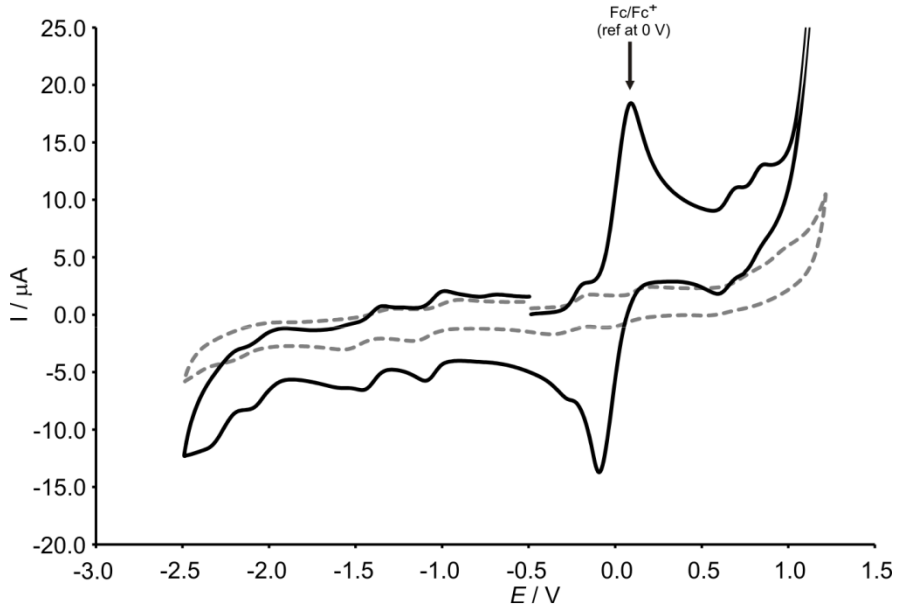

Figure 3.29: Cyclic voltammogram for bis-anthracene fused dimer **134**, both with ferrocene (black), and without (grey). Cyclic voltammetry was carried out in THF with 0.1 M Bu_4NPF_6 at a scan rate of 100 mV s^{-1} using a glassy carbon working electrode, Pt counter electrode and $Ag/AgNO_3$ reference electrode.

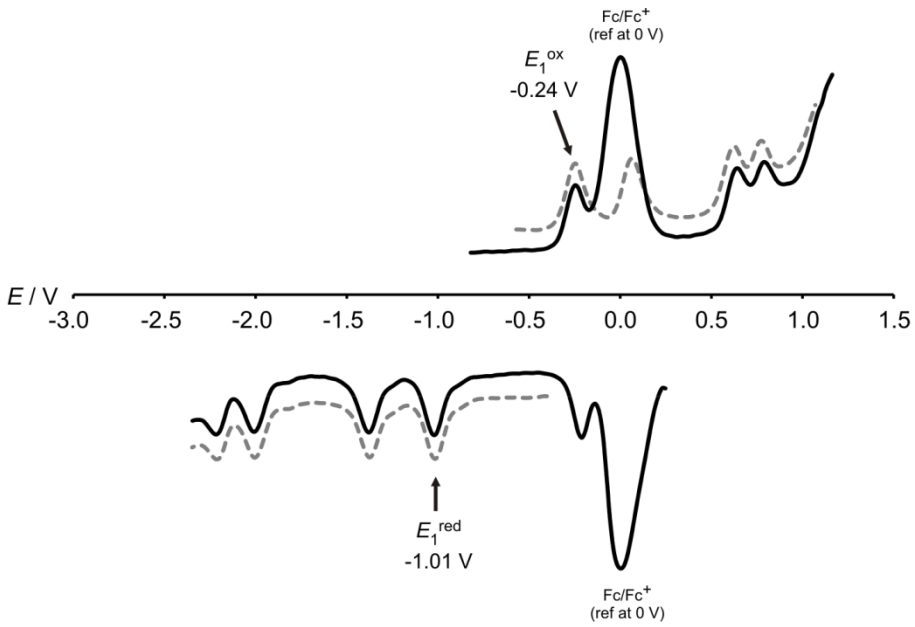

Figure 3.30: Square Wave voltammogram for bis-anthracene fused dimer **134**, both with ferrocene (black), and without (grey). Square wave experiments were recorded in THF with 0.1 M Bu_4NPF_6 at a square wave frequency of 8 Hz using a glassy carbon working electrode, Pt counter electrode and $Ag/AgNO_3$ reference electrode.

Comparison of these electrochemical data to those of triply linked porphyrin dimer **135** and trimer **137** illustrates the exceptional degree of electronic delocalisation in bis-anthracene fused dimer **134**. The electrochemical gap of 0.77 V observed for dimer **134** is much smaller than for triply linked porphyrin dimer **135** which has an E_1^{ox}- E_1^{red} separation of 1.22 V.[33] Triply linked porphyrin trimer **137** exhibits an electrochemical gap of 0.90 V, confirming the trend in HOMO-LUMO energy gaps seen from the UV-vis-NIR data in Section 3.4.7. Furthermore, the first oxidation potential of bis-anthracene fused porphyrin **134**, observed at -0.24 V, is far lower than for dimer **135** and trimer **137** (0.09 and 0.03 V respectively) indicating the ease of oxidation of dimer **134** and hence its potential for charge transport.[33]

In spite of demonstrating a near-IR λ_{max} which is blue-shifted with respect to trimer **137**, bis-pyrene fused porphyrin dimer **58** exhibits a smaller electrochemical gap of 0.84 V, and a first oxidation potential at -0.13 V.[36] In addition, dimer **58** displays an optical gap at the near-IR λ_{max} of 0.94 eV. These values are close to those observed for bis-anthracene fused porphyrin dimer **134**, however they confirm the conclusion that fusion of anthracene units to a porphyrin results in a higher degree of delocalisation than fusion of pyrene moieties.

These electrochemical investigations confirm the small HOMO-LUMO gap expected for bis-anthracene fused dimer **134** from the UV-vis-NIR spectrum. Furthermore they show that, while dimer **134** exhibits similar optical absorption as triply fused porphyrin trimers, dimer **134** is far easier to oxidise — a property which could be exploited for charge transport applications.

3.5 Conclusions

For the first time bis-anthracene fused porphyrin monomers and dimers have been synthesised and their optoelectronic properties investigated. Iron(III) chloride was used to form the fused monomers **132** and **133,** with silver triflate employed as a chloride ion scavenger. The fully fused end-capped dimer **134** was synthesised in a one-pot reaction from anthracene-linked porphyrin monomer **130** using scandium(III) triflate and DDQ.

Bulky aryl ether substituents have been shown to be effective at reducing aggregation problems observed for such large π-systems, allowing ^{1}H NMR spectra to be observed. The crystal structure of fully fused bis-anthracene porphyrin **133** demonstrates the planarity of the π-system as well as the perpendicular arrangement of the aryl ether groups, which sterically block the top and bottom face of the molecule.

The UV-vis-NIR absorption spectra of anthracene-fused porphyrins **132**, **133** and **134** show extensive absorption in the near-IR, which becomes more red-shifted with sequential fusion of anthracene units to the porphyrin core. Moreover, the spectral shape becomes greatly distorted as the symmetry of the π-system is reduced upon fusion of one anthracene unit. However fusion of two anthracene units to form either a bis-anthracene fused monomer or dimer creates more symmetrical D_{2h} chromophores which correspondingly exhibit a simpler spectral shape. The extent of the absorption into the near-IR, together with the high peak intensity and sharpness at the near-IR λ_{max} for these fused systems, is extraordinary. Comparison to analogous fused porphyrin systems reported in the literature shows that the anthracene unit, fused across the *meso* and β positions of the porphyrin, exerts a far stronger perturbation on the electronic structure of the porphyrin than many other aromatic systems including the larger aromatic ring, pyrene.[36]

Electrochemical measurements of **132**, **133** and **134** show an increase in electron delocalisation with the number of fused aromatic components in the anthracene-porphyrin system. These anthracene-fused porphyrins exhibit very small HOMO-LUMO gaps which match well with the optical gaps calculated, with dimer **134** demonstrating an E_1^{ox}- E_1^{red} separation of just 0.77 V. Moreover, the difference in E_1^{ox}- E_1^{red} separation of 0.45 V between triply linked porphyrin dimer **135** and bis-anthracene fused porphyrin dimer **134** indicates that the electrochemical properties of oligomeric porphyrin tapes can be efficiently tuned by capping with anthracene units. In addition, the first oxidation potentials of these anthracene-fused porphyrins are far lower than observed for other fused porphyrin systems reported in the literature. These results indicate that anthracene-fused porphyrins are readily oxidised and exhibit an excellent degree of electron delocalisation suggesting that they could exhibit promising charge transport properties.

3.6 References

(1) Davis, N. K. S.; Pawlicki, M.; Anderson, H. L. *Org. Lett.* **2008**, *10*, 3945-3947.

(2) Kamo, M.; Tsuda, A.; Nakamura, Y.; Aratani, N.; Furukawa, K.; Kato, T.; Osuka, A. *Org. Lett.* **2003**, *5*, 2079-2082.

(3) Krivokapic, A.; Anderson, H. L. *Org. Biomol. Chem.* **2003**, *1*, 3639-3641.

(4) Sooambar, C.; Troiani, V.; Bruno, C.; Marcaccio, M.; Paolucci, F.; Listorti, A.; Belbakra, A.; Armaroli, N.; Magistrato, A.; De Zorzi, R.; Geremia, S.; Bonifazi, D. *Org. Biomol. Chem.* **2009**, *7*, 2402-2413.

(5) Suzuki, M.; Osuka, A. *Org. Lett.* **2003**, *5*, 3943-3946.

(6) Hyslop, A. G.; Kellett, M. A.; Iovine, P. M.; Therien, M. J. *J. Am. Chem. Soc.* **1998**, *120*, 12676-12677.

(7) Tsuda, A.; Furuta, H.; Osuka, A. *J. Am. Chem. Soc.* **2001**, *123*, 10304-10321.

(8) Segawa, H.; Senshu, Y.; Nakazaki, J.; Susumu, K. *J. Am. Chem. Soc.* **2004**, *126*, 1354-1355.

(9) Sahoo, A. K.; Nakamura, Y.; Aratani, N.; Kim, K. S.; Noh, S. B.; Shinokubo, H.; Kim, D.; Osuka, A. *Org. Lett.* **2006**, *8*, 4141-4144.

(10) Sarhan, A. A. O.; Bolm, C. *Chem. Soc. Rev* **2009**, *38*, 2730-2744.

(11) Wu, J.; Gherghel, L.; Watson, M. D.; Li, J.; Wang, Z.; Simpson, C. D.; Kolb, U.; Müllen, K. *Macromolecules* **2003**, *36*, 7082-7089.

(12) Kurotobi, K.; Kim, K. S.; Noh, S. B.; Kim, D.; Osuka, A. *Angew. Chem. Int. Ed.* **2006**, *45*, 3944-3947.

(13) Feng, X.; Pisula, W.; Takase, M.; Dou, X.; Enkelmann, V.; Wagner, M.; Ding, N.; Müllen, K. *Chem. Mater.* **2008**, *20*, 2872-2874.

(14) Ito, S.; Wehmeier, M.; Brand, J. D.; Kübel, C.; Epsch, R.; Rabe, J. P.; Müllen, K. *Chem. Eur. J.* **2000**, *6*, 4327-4342.

(15) Pondaven, A.; Cozien, Y.; L'Her, M. *New J. Chem.* **1992**, *16*, 711-718.

(16) McKeown, N. B.; Makhseed, S.; Msayib, K. J.; Ooi, L. L.; Helliwell, M.; Warren, J. E. *Angew. Chem. Int. Ed.* **2005**, *44*, 7546-7549.

(17) Toyota, S.; Makino, T. *Tetrahedron Lett.* **2003**, *44*, 7775-7778.

(18) Prinz, H.; Burgemeister, T.; Wiegrebe, W.; Müller, K. *J. Org. Chem.* **1996**, *61*, 2857-2860.

(19) Prinz, H.; Wiegrebe, W.; Müller, K. *J. Org. Chem.* **1996**, *61*, 2853-2856.

(20) Brewis, M.; Clarkson, G. J.; Humberstone, P.; Makhseed, S.; McKeown, N. B. *Chem. Eur. J.* **1998**, *4*, 1633-1640.

(21) Shyamasundar, N.; Caluwe, P. *J. Org. Chem.* **1981**, *46*, 1552-1557.

(22) Allen, F. H. *Acta Crystallogr., Sect. B: Struct. Sci.* **2002**, *58*, 380-388.

(23) Bruno, I. J.; Cole, J. C.; Edgington, P. R.; Kessler, M.; Macrae, C. F.; McCabe, P.; Pearson, J.; Taylor, R. *Acta Crystallogr., Sect. B: Struct. Sci.* **2002**, *58*, 389-397.

(24) *Vista - A Program for the Analysis and Display of Data Retrieved from the CSD*, Cambridge Crystallographic Data Centre, 12 Union Road, Cambridge, UK
1994.

(25) Hayashi, S.; Tanaka, M.; Hayashi, H.; Eu, S.; Umeyama, T.; Matano, Y.; Araki, Y.; Imahori, H. *J. Phys. Chem. C.* **2008**, *112*, 15576-15585.
(26) Yamane, O.; Sugiura, K.; Miyasaka, H.; Nakamura, K.; Fujimoto, T.; Nakamura, K.; Kaneda, T.; Sakata, Y.; Yamashita, M. *Chem. Lett.* **2004**, *33*, 40-41.
(27) Tanaka, M.; Hayashi, S.; Eu, S.; Umeyama, T.; Matano, Y.; Imahori, H. *Chem. Commun.* **2007**, 2069-2071.
(28) Cammidge, A. N.; Scaife, P. J.; Berber, G.; Hughes, D. L. *Org. Lett.* **2005**, *7*, 3413-3416.
(29) Gill, H. S.; Harmjanz, M.; Santamaría, J.; Finger, I.; Scott, M. J. *Angew. Chem. Int. Ed.* **2004**, *43*, 485-490.
(30) Davis, N. K. S.; Thompson, A. L.; Anderson, H. L. *Org. Lett.* **2010**, *12*, 2124-2127.
(31) Fendt, L. A.; Fang, H.; Plonska-Brzezinska, M. E.; Zhang, S.; Cheng, F.; Braun, C.; Echegoyen, L.; Diederich, F. *Eur. J. Org. Chem.* **2007**, 4659-4673.
(32) Chang, D.; Malinski, T.; Ulman, A.; Kadish, K. M. *Inorg. Chem.* **1984**, *23*, 817-824.
(33) Cheng, F.; Zhang, S.; Adronov, A.; Echegoyen, L.; Diederich, F. *Chem. Eur. J.* **2006**, *12*, 6062-6070.
(34) Ikeue, T.; Aratani, N.; Osuka, A. *Isr. J. Chem.* **2005**, *45*, 293-302.
(35) Tagami, K.; Tsukada, M.; Matsumoto, T.; Kawai, T. *Phys. Rev. B* **2003**, *67*, 245324.
(36) Diev, V. V.; Hanson, K.; Zimmerman, J. D.; Forrest, S. R.; Thompson, M. E. *Angew. Chem. Int. Ed.* **2010**, *49*, 5523-5526.

Chapter 4: Tetra-Anthracene Fused Porphyrins[b]

Chapter 4 describes the synthesis and characterisation of a porphyrin fused to four anthracenes. Formation of the unfused tetra-anthracene linked porphyrin precursor is achieved by acid-catalysed tetramerisation of an anthracene-pyrrole intermediate. A subsequent eight-fold oxidative ring-closure reaction gives the fully fused tetra-anthracene porphyrin. This fused porphyrin monomer displays an extremely red-shifted UV-vis-NIR absorption spectrum and an electrochemical gap similar to those observed for triply linked porphyrin trimers. The crystal structure of this tetra-anthracene fused porphyrin shows that the molecules stack in a dimeric fashion in a near-eclipsed, twisted face-to-face arrangement. Finally, the potential of tetra-anthracene fused porphyrins as mesogens for discotic liquid crystals is explored.

[b] Part of this chapter has been published in *'A Porphyrin Fused to Four Anthracenes.'* Nicola K. S. Davis, Amber L. Thompson and Harry L. Anderson, *Journal of the American Chemical Society*, **2011**, *133*, 30—31.

4.1 Introduction

For over 35 years, chemists have been intrigued by the possibility of synthesising fused tetraanthracene porphyrins.[1] The high symmetry and discotic shape of such a molecule suggests that derivatives could form discotic liquid crystalline phases. In addition, the large number of electrons delocalised across the system implies that this compound could exhibit electrochemical properties which may facilitate charge generation and conduction along such stacks, together with sharp absorption in the near-IR.

Having achieved the fusion of one anthracene unit to a porphyrin with scandium(III) triflate and DDQ (Schemes 2.10 and 3.8),[2] a similar oxidative ring-closure pathway was expected to yield tetra-anthracene fused porphyrin **140** from unfused tetra-anthracene linked porphyrin **139** (Scheme 4.1).

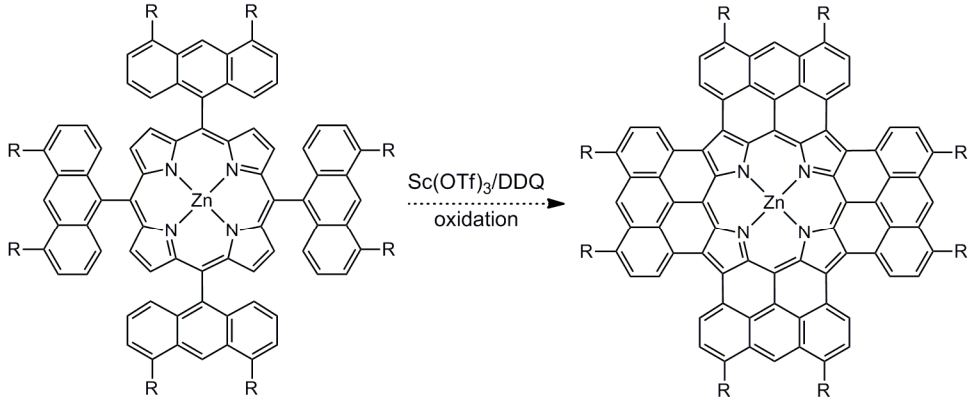

139 **140**

Scheme 4.1: Proposed reaction pathway for the synthesis of tetra-anthracene fused porphyrin **140** from the unfused precursor **139**. R represents solubilising side chains.

4.2 Synthesis of a Porphyrin Fused to Four Anthracenes

4.2.1 Molecular Design

The initial synthetic target, tetra-anthracene fused porphyrin **141**, is shown in Figure 4.1.

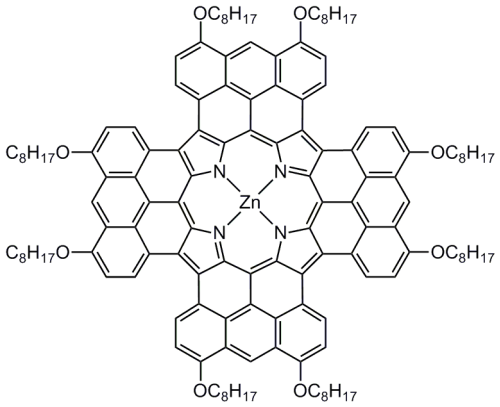

141

Figure 4.1: Target tetra-anthracene fused porphyrin **141.**

It has been shown by Yamane and co-workers that for fusion of a pyrene unit to a porphyrin to occur with scandium(III) triflate and DDQ, the pyrene must bear electron donating substituents.[3] This observation has also been shown to be true for the fusion of an anthracene to a porphyrin under the same conditions.[2] Hence I decided to attach electron-rich alkoxy substituents to the anthracene units in the 1- and 8-positions. Furthermore, these alkoxy groups should promote the solubility of the large anthracene-porphyrin π-system in organic solvents. Müllen and co-workers have shown that linking long alkyl chains, typically in the region of 12 carbon atoms in length, to the edge of hexa-*peri*-hexabenzocoronenes makes these systems sufficiently soluble in organic solvents as to allow characterisation by ^{1}H NMR spectroscopy.[4] As a result, I thought that the presence of eight octyloxy substituents around the periphery of tetra-anthracene fused porphyrin **141**, would convey enough solubility as to enable purification and characterisation of the compound.

The potential problem of aggregation, due to strong π-stacking between molecules of tetra-anthracene fused porphyrin **141**, was also considered in the molecular design. Given that coordination of zinc in the central porphyrin cavity would enable binding of an axial pyridine ligand, thereby sterically encumbering the face of the porphyrin molecule, I thought that this would successfully limit aggregation.

The design and subsequent synthesis of tetra-anthracene fused porphyrin **141**, was carried out simultaneously with the synthesis of bis-anthracene fused porphyrins **117** and **118** (Sections 3.2.3 and 3.2.4) which also bear octyloxy substituents on the anthracene units.

As a result, the problems of purification and characterisation encountered for these bis-anthracene fused porphyrins were unknown when the structure of tetra-anthracene fused porphyrin **141** was designed.

4.2.2 Synthetic Approaches to Tetra-Anthracene Linked Porphyrins

The formation of tetra-aryl porphyrins is often achieved by condensation of an aldehyde (bearing the aromatic unit, **142**) and pyrrole (**143**) under acid-catalysed conditions, to form a porphyrinogen **144** which is then oxidised to the corresponding porphyrin **145**, often followed by coordination of a metal ion to form **146** (Scheme 4.2).[5] The yield of the reaction depends upon many factors including the choice of solvent, the acid catalyst employed, the structure of the aldehyde and the concentration of the reagents. However for many tetra-aryl porphyrins the yields are reasonable, with tetra-phenyl porphyrin formed in yields of up to 68%.[6]

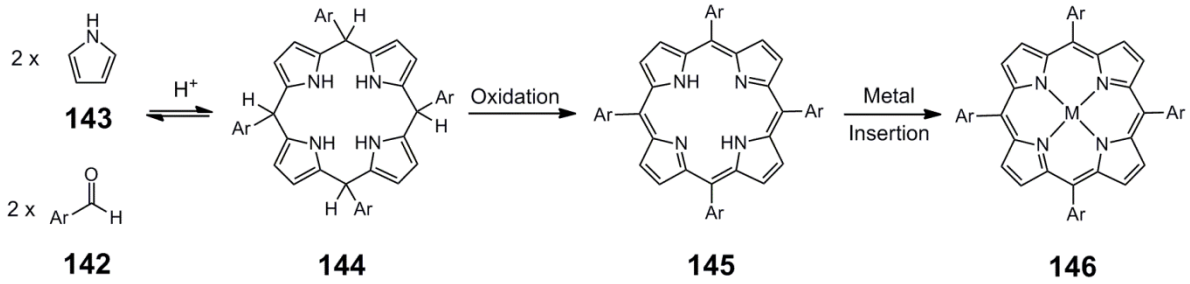

Scheme 4.2: Synthesis of tetra-aryl porphyrins (**145**) and metalloporphyrins (**146**), via a porphyrinogen intermediate (**144**), by acid catalysed condensation reaction.[5]

Tetra-anthracene linked porphyrin **67** (Figure 4.2) and its metalloporphyrin derivates have previously been reported in the literature.[7-15] The acid-catalysed condensation of pyrrole (**143**) and 9-formyl anthracene, following the reaction pathway shown in Scheme 4.2, has been attempted under many different conditions. In 1968 Treibs and Häberle synthesised tetra-anthracene porphyrin **67** by condensation of pyrrole (**143**) and 9-formyl anthracene in acetic acid and pyridine, however the yield of **67** was reported to be less than 1%.[10]

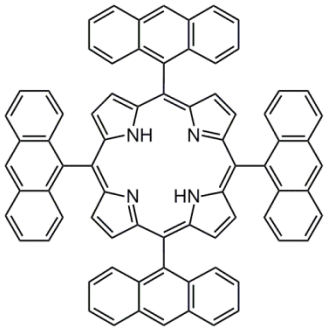

67

Figure 4.2: Tetra-anthracene linked porphyrin **67**.

Cense and Le Quan reported alternative conditions for the synthesis of tetra-anthracene linked porphyrin **67** in 1979, by condensation of pyrrole (**143**) and 9-formyl anthracene in propionic acid. However, the yield of the desired porphyrin was still very low, at only 0.2%.[7]

In recent years further studies into the formation of porphyrin **67** by acid-catalysed condensation have been carried out. In 2007 Tohara and Sato investigated the kinetics of tetra-anthracene porphyrinogen formation by condensation of pyrrole (**143**) and 9-formyl anthracene in chloroform the presence of $BF_3{\cdot}OEt_2$.[9] Surprisingly, it was found that under these conditions the maximum porphyrinogen concentration was reached just one minute after the reaction was started, with tetra-anthracene linked porphyrin **67** being isolated from the reaction mixture in 3% yield upon oxidation of the porphyrinogen with DDQ. In addition, it was reported that the concentration of the tetra-anthracene porphyrinogen decreases after one minute of reaction. Tohara and Sato suggest that this is due to the reversibility of porphyrinogen formation, and the presence of significant reversible and irreversible acid-catalysed side reactions called 'leak pathways' such as the formation of long anthracene-pyrrole oligomers.[9]

In the same year, Sarkar and co-workers reported the synthesis of free-base tetra-anthracene linked porphyrin **67** in 1.8% yield and the zinc porphyrin derivative in 2.5% yield, by condensation of pyrrole (**143**) and 9-formyl anthracene in DMF in the presence of concentrated HCl. In contrast to the work by Tohara and Sato, Sarkar and co-workers did not use extremely short reaction times to achieve these yields; the reaction mixture was

stirred for an hour after addition of the acid catalyst, and then refluxed for eight hours in air.[8] This suggests that the formation and stability of the tetra-anthracene porphyrinogen is highly sensitive to reaction conditions.

From the reaction conditions discussed above, it can be seen that the synthesis of tetra-anthracene linked porphyrins by condensation reactions occurs in very low yields. These low yields have been explained by some, such as Lindsey and co-workers, as arising from a steric clash between hydrogens of the anthracene periphery and the *meso*-hydrogen of the porphyrinogen intermediate (Figure 4.3 (a)).[16] However this fails to explain why similar sterically encumbered porphyrins, such as **147** (Figure 4.3 (b)), may be formed in yields of around 30% under standard $BF_3{\cdot}OEt_2$ catalysed condensation conditions from pyrrole (**143**) and the corresponding aldehyde.[17,18] It therefore seems likely that the electronic properties of the aromatic aldehyde, together with other factors such as solubility, also play a role in determining the success of the condensation reaction.

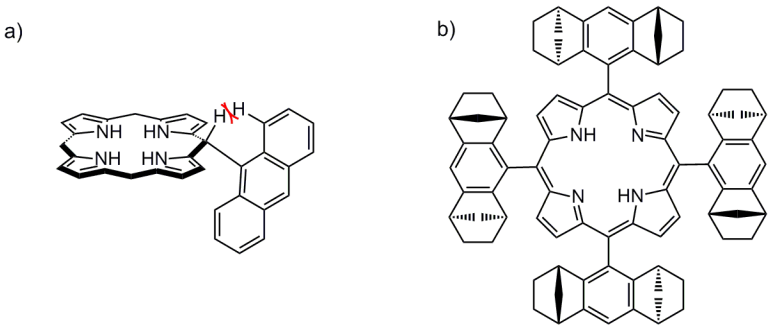

147

Figure 4.3: a) Steric clash between the *meso*-hydrogen of the porphyrinogen and the hydrogen of the anthracene unit.[16] Only one of the four anthracenes is shown for clarity. b) Structure of tetra-substituted porphyrin **147** which forms in 29% yield by condensation of the aromatic aldehyde with pyrrole (**143**) in the presence of $BF_3{\cdot}OEt_2$.[17]

Despite the low yields achieved for the condensation reaction of pyrrole (**143**) with a formylanthracene, the direct formation of tetra-anthracene linked porphyrin **67** by such a pathway has some potential attractions compared to alternative routes such as by palladium-catalysed coupling reactions. These palladium-catalysed pathways require the synthesis of a tetra-bromo or tetra-boronicester porphyrin followed by a four-fold coupling reaction which is likely to yield a large mixture of products which could be very difficult to

separate. As a result of the greater number of steps with potentially low yields, such a pathway is expected to result in overall yields comparable to those achieved by a condensation reaction. Hence I decided to attempt the synthesis of tetra-anthracene linked porphyrin **148** by condensation of formylanthracene **149** with pyrrole (**143**) (Scheme 4.3).

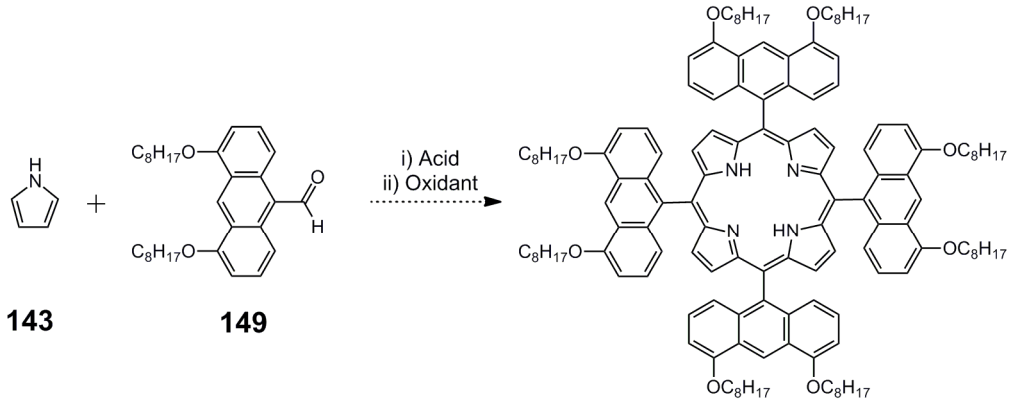

143 **149** **148**

Scheme 4.3: Proposed synthetic route to tetra-anthracene linked porphyrin **148**.

The first step in the formation of tetra-anthracene linked porphyrin **148** is the synthesis of 4,5-bis(octyloxy)anthracene-9-carbaldehyde (**149**). The formylation of anthracene at the central ring has been reported by use of a Vilsmeier-Haack reaction involving a substituted amide, such as methylformanilide, and $POCl_3$.[19] Initially, formylation was attempted on 1,8-dimethoxyanthracene (**150**) as a test reaction (Scheme 4.4). I had made **150** on a large scale during previous work, hence it seemed sensible to use anthracene **150** in order to explore the regioselectivity of the formylation reaction. Subjection of **150** to an excess of $POCl_3$ (~ 30 equivalents) in DMF resulted in complete consumption of the starting material and the formation of one major product and several side products, as observed by TLC.

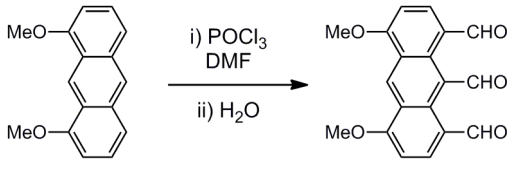

150 **151**

Scheme 4.4: Attempted formylation of **150** under Vilsmeier conditions.

^{1}H NMR spectroscopy of the crude mixture revealed the major product (~80% by integration) to be an unusual triply substituted anthracene (**151**) (as deduced from the presence of two singlets at 10.42 and 11.18 ppm in the ratio of 2:1 corresponding to the aldehyde peaks, three aromatic signals of one singlet and two doublets corresponding to the protons of the anthracene ring, and only one peak at 4.20 ppm corresponding to the methyl protons). There are no reports of an anthracene bearing three formyl groups in the 1-,8- and 9-positions in the literature, however such a compound may be expected to be synthetically useful for a variety of condensation reactions. When the reaction was repeated with only two equivalents of $POCl_3$, preliminary results indicated that no formylation was observed on the central ring, with only positions *para*- to the methoxy groups were substituted. These results demonstrate the strong electron donation by the methoxy groups into the aromatic system, increasing electron density at the positions *para*- to them.

In order to achieve regioselective formylation at the 10-position of the anthracene, the Vilsmeier reaction was attempted on 1,8-diacetoxyanthracene (**84**) (Scheme 4.5); the synthesis of anthracene **84** is shown in Scheme 2.11.[2] It was expected that the poorly electron donating nature of the acetoxy substituents would prevent formylation on the terminal rings, providing a regioselective route to formylanthracene **152** which could then undergo hydrolysis and alkylation to give formylanthracene **149**. However, no reaction was observed even after heating at 90 °C for 12 hours, indicating that the weak electron donating nature of the acetoxy groups reduces the reactivity of the whole molecule towards formylation.

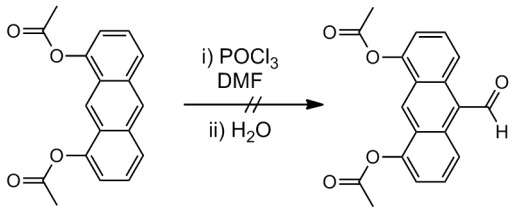

Scheme 4.5: Attempted formylation of 1,8-acetoxyanthracene **84** under Vilsmeier conditions.

The difficulties in synthesising formylanthracene **149** by Vilsmeier-Haack formylation indicated that another route to this aldehyde was required. It is well known that

aryl aldehydes may be synthesised by reaction of the corresponding organolithium species with DMF, followed by hydrolysis. Hence I decided to attempt the synthesis of formylanthracene **149** by lithium-halogen exchange of bromoanthracene **72** with *n*-butyllithium, followed by addition of DMF and subsequent aqueous acid work-up (Scheme 4.6). The synthesis of bromoanthracene **72** is shown in Scheme 2.11.[2]

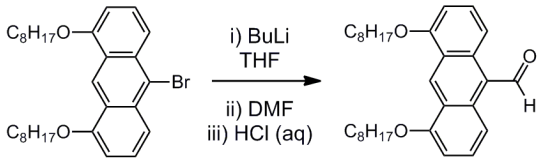

72 **149**

Scheme 4.6: Synthesis of formylanthracene **149**.

Following the reaction conditions shown in Scheme 4.6, a mixture of products was observed by TLC. Purification of this mixture was achieved by silica gel chromatography, to give the desired formylanthracene **149** in 60% yield.

Condensation of formylanthracene **149** with pyrrole (**143**) was attempted under several conditions as summarised in Table 4.1, following the pathway proposed in Scheme 4.3.

Table 4.1: Reaction conditions trialled for the synthesis of tetra-anthracene linked porphyrin **148**.

Acid	Solvent	Oxidant	Temp (°C)	Reaction Time (before oxidation)	Comments
HCl	DMF	DDQ	90	3 hours	Mixture of tarry products, no **149** observed
$BF_3{\cdot}OEt_2$	$CHCl_3$	DDQ	25	1 minute	No reaction.
$BF_3{\cdot}OEt_2$	$CHCl_3$	DDQ	25	16 hours	Mainly unreacted **149** present, some tarry products observed.
TFA	DCM	DDQ	35	18 hours	Mixture of tarry products, some unreacted **149** present.

The condensation of formylanthracene **149** with pyrrole (**143**) was initially attempted under conditions similar to those discussed above for the higher yielding syntheses of tetra-anthracene porphyrin **67**. Condensation in DMF, in the presence of HCl, to form the porphyrinogen was carried out according to the procedure reported by Sarkar and co-workers,[8] however oxidation was induced by the addition of DDQ rather than by refluxing in air to reduce the reaction time. After oxidation, the reaction mixture was shown by TLC to consist primarily of a large number of polar brown products.

Following the procedure reported by Tohara and Sato,[9] the condensation of formylanthracene **149** with pyrrole (**143**) was attempted in chloroform the presence of $BF_3{\cdot}OEt_2$ and quenched with DDQ after just one minute. Very little aldehyde was seen to react, with only traces of tarry side products observed by TLC. No porphyrin products were observed. In order to investigate whether a longer reaction time may favour porphyrinogen formation under these conditions, the reaction was repeated, with the reaction mixture stirred for 16 hours before being quenched with DDQ. Even with longer reaction time, very little formylaldehyde **149** was consumed, however a larger proportion of tarry products was observed, probably due to the polymerisation of pyrrole.

The failure of these reaction conditions to yield tetra-anthracene linked porphyrin **148** when applied to the condensation of formylanthracene **149** with pyrrole (**143**), prompted investigation of alternative conditions. Lindsey and co-workers have reported the use of TFA as an acid catalyst for porphyrin synthesis.[5] No reaction was observed however when formylanthracene **149** and pyrrole (**143**) were reacted under these conditions at room temperature and stirred for three hours. Warming the reaction mixture to 35 °C and stirring overnight resulted in the formation of many unidentifiable products, including tarry residues. No porphyrin products were observed, and TLC revealed unreacted formylanthracene **149** to be present in the reaction mixture.

With no tetra-anthracene porphyrin **148** detected from condensation reactions involving formylanthracene **149** and pyrrole (**143**), an alternative route was sought. It was thought possible that the steric bulk of the anthracene **149**, together with the electron rich nature of the system, is responsible for its low reactivity towards nucleophilic pyrrole. In order to solve this problem it was therefore necessary to explore the use of more reactive derivatives of formylanthracene **149**.

Volz and Schäffer have reported the synthesis of tetra-anthracene porphyrin **67** in 6.8% yield by reaction of pyrrole-2-carboxaldehyde with an anthracene lithiated at the central ring (**154**), followed by tetramerisation of the intermediate (**153**) formed (Scheme 4.7).[12] In order to test the reproducibility of this yield, I carried out this literature procedure, achieving porphyrin **67** in 6.5% yield, which is very close to the reported value. Two molecules of lithiated anthracene are required for the formation of each molecule of **153**; one molecule of lithiated anthracene deprotonates the pyrrolic nitrogen of pyrrole-2-carboxaldehyde, while the other attacks the electrophilic aldehyde group.

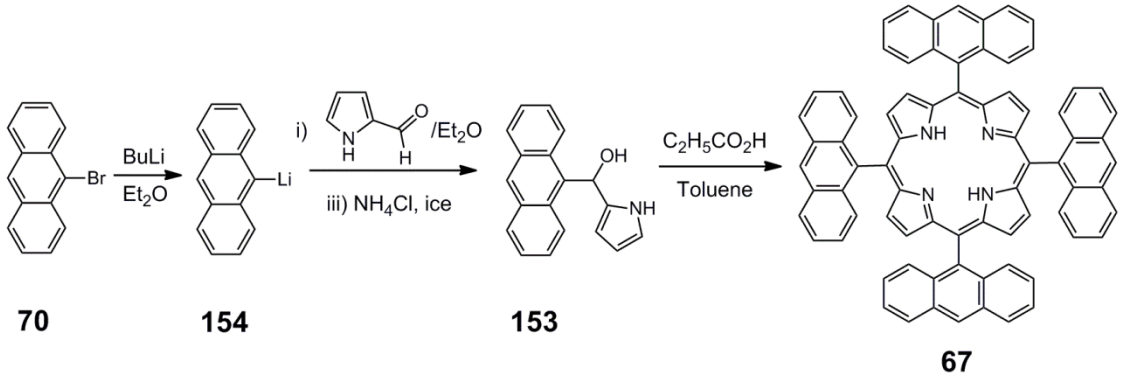

Scheme 4.7: Formation of tetra-anthracene porphyrin **67**, using an organolithium derivate of anthracene, reported by Volz and Schäffer.[12]

The higher yield of this reaction, compared to those explored above, is likely to be due to the high reactivity of the lithiated anthracene species which forces the formation of intermediate **153**. However undesired reactions, such as the polymerisation of pyrrolic species, compete with tetramerisation in the second step, resulting in the formation of many side products.

The pathway reported by Volz and Schäffer for tetra-anthracene linked porphyrin synthesis, shown in Scheme 4.7, may be expected to work well for bromoanthracene **72**. However, following the many difficulties encountered in the synthesis and purification of bis-anthracene fused porphyrins **117** and **118** due to aggregation (see Sections 3.2.3 and 3.2.4), I decided to modify the structure of the target tetra-anthracene linked porphyrin. Substitution of the octyloxy groups attached to the anthracene units for bulky aryl ether groups, was expected to facilitate the synthesis, purification and characterisation of the tetra-anthracene fused porphyrin (**155**) (Figure 4.4).

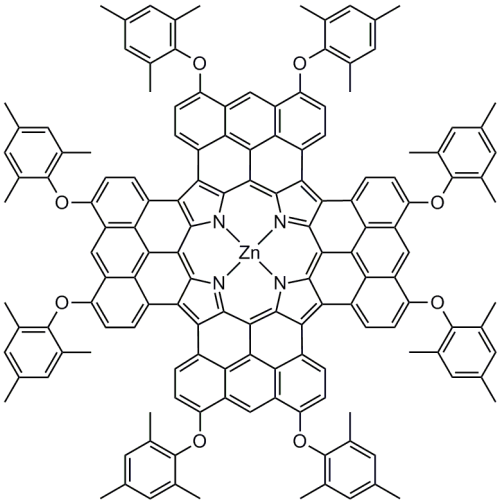

155

Figure 4.4: Target tetra-anthracene fused porphyrin **155** bearing bulky aryl ether substituents.

The first step towards the formation of tetra-anthracene fused porphyrin **155** is the synthesis of the substituted bromoanthracene precursor, in order that the synthetic route shown in Scheme 4.7 may be followed. As discussed in Chapter 2, regioselective bromination on the central ring of an anthracene bearing electron donating groups in the 1- and 8-positions, is non-trivial. In order to control the position of bromination, the synthesis of bromoanthracene **156** was initially attempted from anthracene triflate **128** (Scheme 4.8). The synthesis of anthracene triflate **128** is discussed in Section 3.3.3. Substitution of an aryl triflate by a bromide ion has been achieved by Kang and co-workers in the presence of copper(I) bromide.[20] Nucleophilic aromatic substitution of unactivated aromatic rings may occur in the presence of copper, either by ligand exchange or by catalysis.[21] Anthracene triflate **128** was therefore heated with a large excess of copper(I) bromide (~ 100 equivalents) and the extent of the reaction was monitored by TLC.

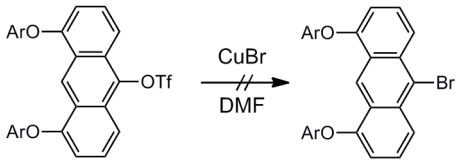

128 **156**

Scheme 4.8: Attempted synthesis of bromoanthracene **156** with CuBr. Ar = 2,4,6-trimethylphenyl.

After heating for two hours at 135 °C, TLC of the reaction mixture showed unreacted starting material, as well as several products which did not show fluorescence under short wavelength UV light, however analysis of the mixture did not reveal the presence of the desired anthracene product.

Thompson and co-workers have reported the conversion of aryl triflates to aryl bromides via aryl boronic ester intermediates.[22] The synthesis of these aryl boronic esters is reported to occur under palladium-catalysed coupling conditions, while copper(II) bromide facilitates their conversion to the corresponding aryl bromide. Palladium-catalysed coupling of anthracene triflate **128** with pinacolborane was attempted as shown in Scheme 4.9.

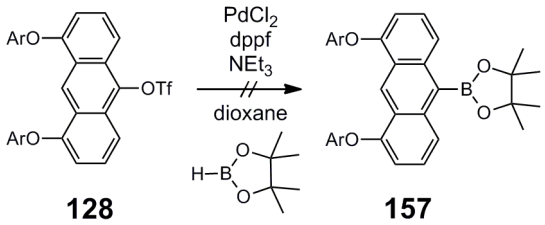

128 **157**

Scheme 4.9: Attempted synthesis of anthracene boronic ester **157** under palladium-catalysed coupling conditions. Ar = 2,4,6-trimethylphenyl.

After heating at 90 °C for two hours, TLC of the reaction mixture showed little consumption of the starting material, so the reaction was heated and stirred for a further 24 hours. After this time the starting material (**128**) was found to be the main component of the reaction mixture; none of the desired product (**157**) was observed.

The use of phosphorus tribromide for converting aliphatic alcohols into alkyl bromides is a well known synthetic procedure. This reagent has also been shown to be successful in reactions involving aromatic systems, such as the conversion of 2-hydroxyazulene to 2-bromoazulene.[23,24] It was therefore considered possible that phosphorus tribromide could react with anthrone **127** to form intermediates **158** and **159** which could then collapse, releasing phosphenous bromide, to form bromoanthracene **156** (Scheme 4.10).

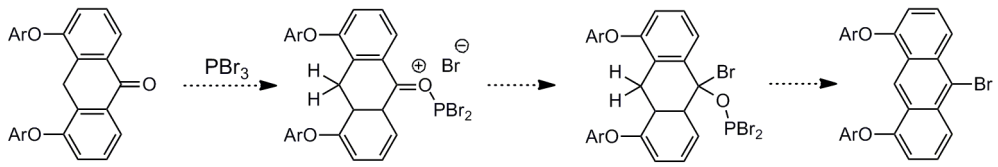

Scheme 4.10: Proposed pathway for the synthesis of bromoanthracene **156** from anthrone **127** with PBr_3. Ar = 2,4,6-trimethylphenyl.

After heating anthrone **127** at 90 °C with phosphorus tribromide in toluene, the mixture was quenched with excess water and a precipitate formed. The precipitate collected appeared by TLC to be mainly starting material. ^{1}H NMR spectroscopy of the crude mixture showed the primary component to be anthrone **127**, however additional signals of low intensity (~ 2% by integration of signals) in the aromatic region were also observed. It was thought that the reaction conditions above were possibly too mild for bromination to occur, hence the reaction was repeated in neat phosphorus tribromide at 110 °C (Scheme 4.11). TLC of the crude reaction mixture showed complete consumption of the starting material and the formation of two products. ^{1}H NMR spectroscopy of the crude reaction mixture showed the main component to be the desired bromoanthracene **156**, while the minor component (<10% by integration of signals) was identified as anthracene **160**.

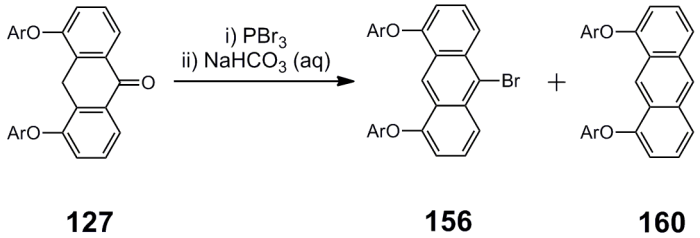

Scheme 4.11: Synthesis of bromoanthracene **156** from anthrone **127** with PBr_3. Ar = 2,4,6-trimethylphenyl.

Bromoanthracene **156** was obtained in 79% yield with a minor impurity of anthracene **160**. The small differences in polarity, together with the low solubility of the anthracene **160** and the desired bromoanthracene **156**, meant that separation of these compounds was impractical on a large scale. In addition, anthracene **160** is expected to form as a side product in the synthesis of tetra-anthracene linked porphyrin **161** (Scheme 4.12). Hence I decided that the crude reaction mixture formed from the bromination of anthrone

127 with phosphorus tribromide, should simply be passed through a short pad of silica gel in toluene and then used directly in the synthesis of tetra-anthracene linked porphyrin **161**, without separation of anthracenes **156** and **160**.

The synthesis of tetra-anthracene linked porphyrin **161** is shown in Scheme 4.12.

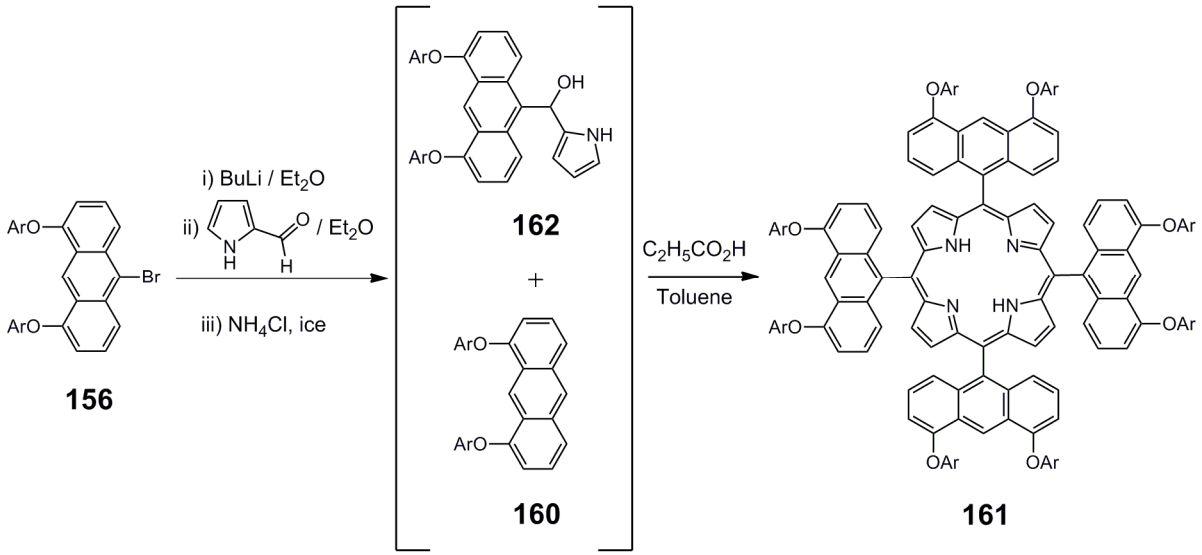

Scheme 4.12: Synthesis of tetra-anthracene linked porphyrin **161**. Ar = 2,4,6-trimethylphenyl.

It was found to be critical that the lithium-halogen exchange of bromoanthracene **156** with *n*-butyllithium, and subsequent addition of pyrrole-2-carboxaldehyde, was carried out in freshly distilled solvent. Following the procedure described by Volz and Schäffer,[12] the products of this reaction were not purified, but used directly in the synthesis of **161**; TLC of the crude reaction mixture did however confirm the presence of two products more polar than **156** (likely to be **160** and **162**), as well as the absence of **156**. Tetramerisation of **162** contained in this crude mixture, followed by purification by silica gel and SEC chromatography, gave the desired free-base tetra-anthracene linked porphyrin **161** in 9.6% yield (with respect to pyrrole-2-carboxaldehyde). Yields between 8.2 and 9.6% for this reaction were achieved on multiple occasions (with the reaction carried out on the 0.1 g scale with respect to pyrrole-2-carboxaldehyde). These yields are notably higher than those reported for any other tetra-anthracene linked porphyrins.

4.2.3 Fusion of a Tetra-Anthracene Linked Porphyrin

My work in Chapter 3 has shown that it is possible to fuse anthracene units to the porphyrin periphery in the presence of scandium(III) triflate and DDQ.[2] These conditions have also been reported to be successful in the fusion of aromatic units such as pyrene[3] and perylene groups[25] to the porphyrin periphery. Hence I decided to attempt the synthesis of tetra-anthracene fused porphyrin **155** using these conditions (Scheme 4.13)

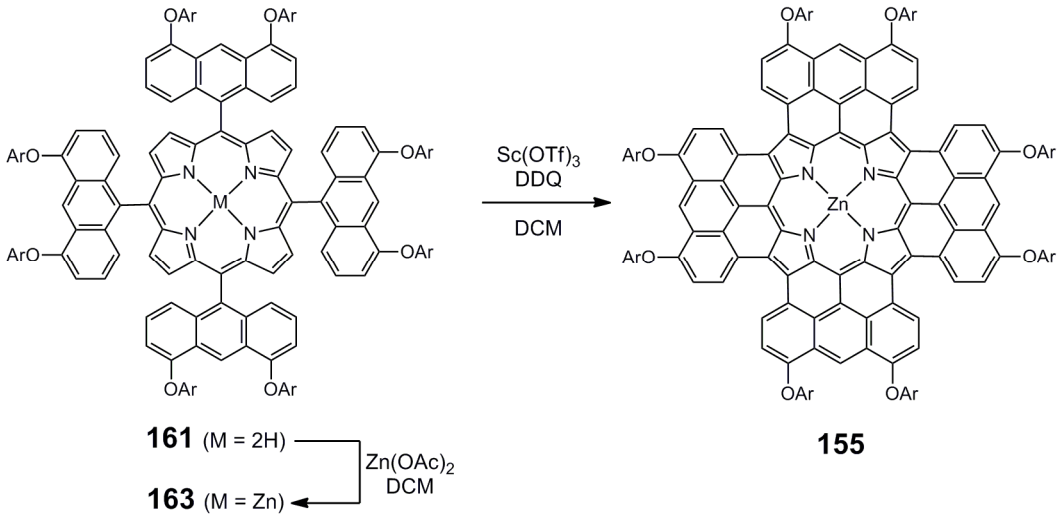

Scheme 4.13: Fusion of tetra-anthracene linked zinc porphyrin **163** with $Sc(OTf)_3$ and DDQ. Ar = 2,4,6-trimethylphenyl.

Tetra-anthracene linked zinc porphyrin **163** was formed in 89% yield from free-base porphyrin **161** by a zinc insertion reaction. Fusion of porphyrin **163** was attempted with 20 equivalents of scandium(III) triflate and DDQ, and the extent of the reaction was monitored by TLC. After 90 minutes, TLC of the reaction mixture showed the presence of unreacted starting material, together with a black side product. Unreacted zinc porphyrin **163** was separated from the black material by silica gel chromatography. The black component was thought to be fused porphyrin **155** however, analysis by ^{1}H NMR spectroscopy, displayed a featureless spectrum. This problem was thought to be due to facile oxidation of the large π-system, forming a radical cation which is paramagnetic and hence gives rise to very broad signals in the ^{1}H NMR spectrum. Hydrazine hydrate is often used to reduce paramagnetic lanthanide phthalocyanine complexes in order to record ^{1}H NMR spectra,[26] hence 10 μL of hydrazine hydrate was added to the NMR sample of black material formed from fusion of

tetra-anthracene linked porphyrin **163**. The ^{1}H NMR spectrum of this sample showed sharp peaks which appeared to arise from a mixture of compounds. MALDI-TOF mass spectrometry of the sample however confirmed the presence of the desired tetra-anthracene fused porphyrin **155**.

The fusion reaction of **163** with scandium(III) triflate and DDQ was repeated with a longer reaction time of three hours, after which time TLC showed total consumption of the starting material. However the reaction mixture again showed the presence of several compounds, including porphyrin **155** which proved impossible to separate. Hence in order to achieve a pure sample of a tetra-anthracene fused porphyrin an alternative synthetic route was sought.

Oxidative ring-closure reactions, which result in the fusion of aromatic units to a porphyrin core, have been achieved with iron(III) chloride for several nickel porphyrins bearing aromatic units.[27-29] This approach also proved to be successful for the synthesis of fully fused bis-anthracene porphyrins **117** and **133** (Chapter 3). Hence the synthesis of fully fused tetra-anthracene porphyrin **165** was attempted using iron(III) chloride (Scheme 4.14).

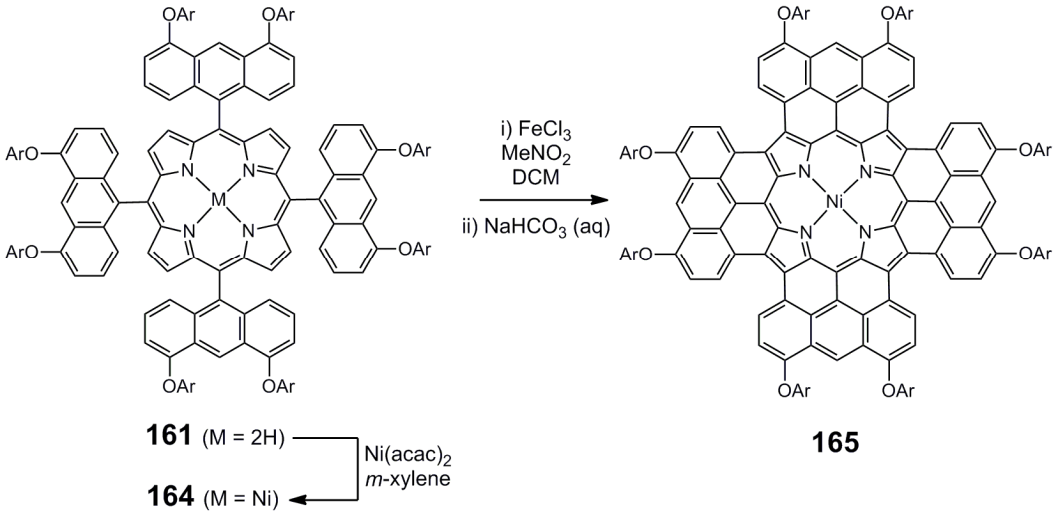

Scheme 4.14: Fusion of tetra-anthracene linked nickel porphyrin **164** with $FeCl_3$. Ar = 2,4,6-trimethylphenyl.

Insertion of nickel into the cavity of free-base porphyrin **161** proceeded in 84% yield to give tetra-anthracene linked nickel porphyrin **164**. Fusion of **164** was attempted with 40 equivalents of iron(III) chloride, and the extent of the reaction was monitored by TLC. After

30 minutes, TLC showed consumption of the starting material together with the formation many dark coloured products.

UV-vis-NIR spectroscopy of the crude reaction mixture showed broad absorption in the near-IR around 1400 nm, suggesting the formation of a highly conjugated system. After passing over a short pad of silica gel, the ^{1}H NMR spectrum of this reaction mixture (in $CDCl_3$ in the presence of 10 μL of hydrazine hydrate) was recorded. This spectrum showed several peaks in the aromatic region that could not be assigned to a single compound. MALDI-TOF mass spectrometry of this sample confirmed the presence of fully fused tetra-anthracene porphyrin **165**.

Purification of porphyrin **165** was achieved to give the desired tetra-anthracene fused porphyrin in 49% yield, however this purification process proved to be exceedingly challenging. Porphyrin **165** showed a tendency to strongly adsorb to silica gel, causing many difficulties in the chromatography of the compound, however it was found that addition of 5% triethylamine to the eluent partially overcame this problem. It was impossible to achieve good separation of **165** from the side products by silica gel chromatography, as decreasing the solvent polarity resulted in precipitation of both the porphyrin compound and the side products on the column. As a result, the material which was seen to elute from the silica gel column did not form discrete bands, but instead comprised of one very broad dark band. Many fractions of this band were collected and analysed by MALDI-TOF mass spectrometry to identify which fraction(s) contained porphyrin **165**.

^{1}H NMR spectroscopy of these combined fractions, in the presence of hydrazine hydrate, revealed a simplified spectrum with four signals of appropriate integration in the aromatic region which corresponded to tetra-anthracene fused porphyrin **165**. However the spectrum also showed the presence of several additional peaks in the aromatic region. Hence I decided to purify the sample further by size exclusion chromatography (SEC). This procedure separated a black fraction of higher molecular weight from the major green-blue fraction. Addition of hydrazine hydrate to a $CDCl_3$ solution of this green-blue material resulted in a darkening of the sample colour. ^{1}H NMR spectroscopy of this sample showed the presence of the four sharp aromatic peaks due to porphyrin **165**, as well as smaller broad

signals in the aromatic region. Surprisingly, three singlet peaks were observed around 7 ppm, the region corresponding to the aromatic *meta*-protons of the 2,4,6-trimethylphenyl groups.

After recording the ^{1}H NMR spectrum of the purified sample of porphyrin **165**, the sample was passed through a second SEC column. Again, black material of a higher molecular weight was separated from the green-blue band. It seemed likely that this material is a product of decomposition of tetra-anthracene fused porphyrin **165**, and its formation may be induced by the addition of hydrazine hydrate to the NMR sample.

In order to overcome this problem, a milder reducing agent was sought. Ng and co-workers have reported that sodium borohydride may be used to reduce paramagnetic lanthanide phthalocyanine compounds.[30,31] Hence a purified sample of porphyrin **165** in $CDCl_3$ was mixed with an excess of sodium borohydride (~ 1.0 mg). The MALDI-TOF mass spectrum of this sample showed only a peak corresponding to the mass of porphyrin **165**. The ^{1}H NMR spectrum recorded for this sample was very simple (Figure 4.5), and free from the peaks observed in the presence of hydrazine hydrate. Only a doublet and a singlet were observed above 7.5 ppm, corresponding to protons ***a*** and ***b*** of the anthracene units of porphyrin **165**; the second doublet of these anthracene units was observed around 6.5 ppm (proton ***c***). Surprisingly three singlet peaks were still observed around 7 ppm, one of which was identified as the *meta*-proton of the 2,4,6-trimethylphenyl groups, proton ***d***. The other two signals in this region, marked with a *, varied in intensity (relative to the peaks of porphyrin **165**) with sample concentration and temperature.

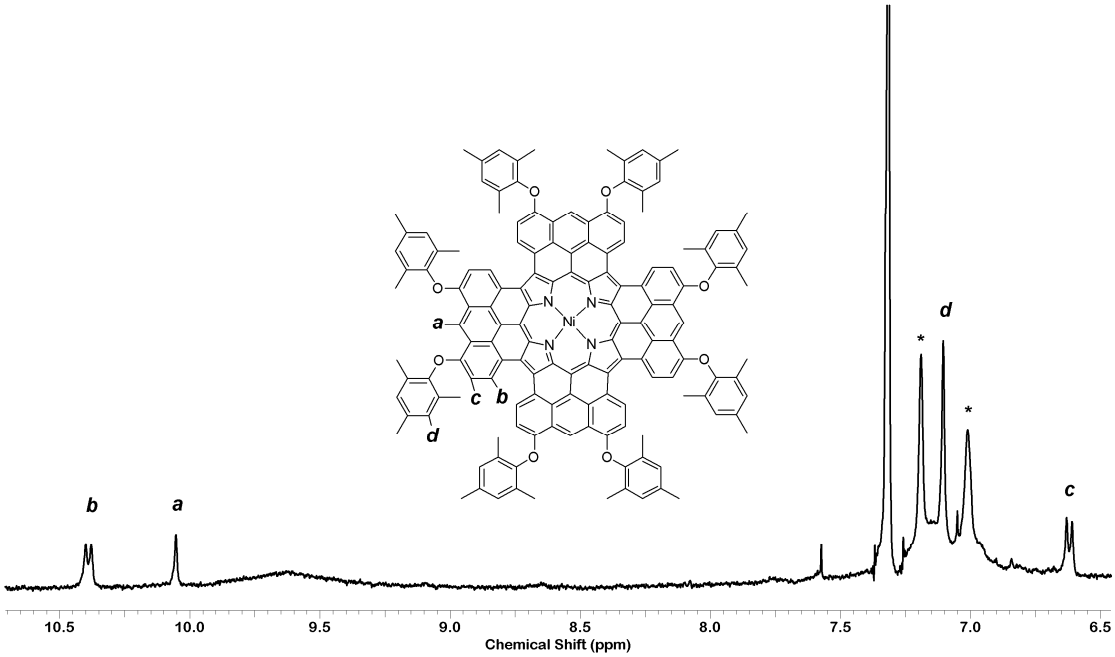

Figure 4.5: ^{1}H NMR spectrum of tetra-anthracene fused porphyrin **165** (400 MHz, $CDCl_3$ with $NaBH_4$, 298 K). Peaks corresponding to aromatic protons of the porphyrin are labelled ***a*-*d***, peaks labelled with * are thought to be due to aggregates of the porphyrin in the $CDCl_3$ sample.

It was considered possible that these peaks arose from aggregates of porphyrin **165**, hence the NMR solvent was changed to benzene-d_6 to increase the solubility of porphyrin **165**. The ^{1}H NMR spectrum of this sample displayed only four peaks in the aromatic region, as expected from the molecular structure of tetra-anthracene fused porphyrin **165**; the two signals thought to be from aggregate species were not observed (Figure 4.6). It is interesting to note that the chemical shift of the signal corresponding to proton ***a*** alters significantly upon changing the NMR solvent; in $CDCl_3$ the signal for proton ***a*** occurs upfield of that for proton ***b*** around 10.1 ppm, while in benzene-d_6 it occurs downfield of the signal for proton ***b*** at nearly 10.7 ppm.

While the bulky aryl ether substituents of tetra-anthracene porphyrin **165** hinder aggregation sufficiently for a ^{1}H NMR spectrum to be recorded, increasing the concentration of the sample in benzene-d_6 was not found to increase signal intensity. Hence it was necessary to record the ^{1}H NMR spectrum at low sample concentration (~ 1 mM). To remove the signal of benzene and its satellites from the ^{1}H NMR spectrum, and hence provide a clearer spectrum, a diffusion-ordered (DOSY) ^{1}H NMR spectrum was recorded.

Unfortunately, the necessarily low concentration of this sample resulted in the observation of a very poor signal to noise ratio in the ^{13}C NMR spectrum of tetra-anthracene fused porphyrin **165**, preventing a clear ^{13}C NMR spectrum from being obtained.

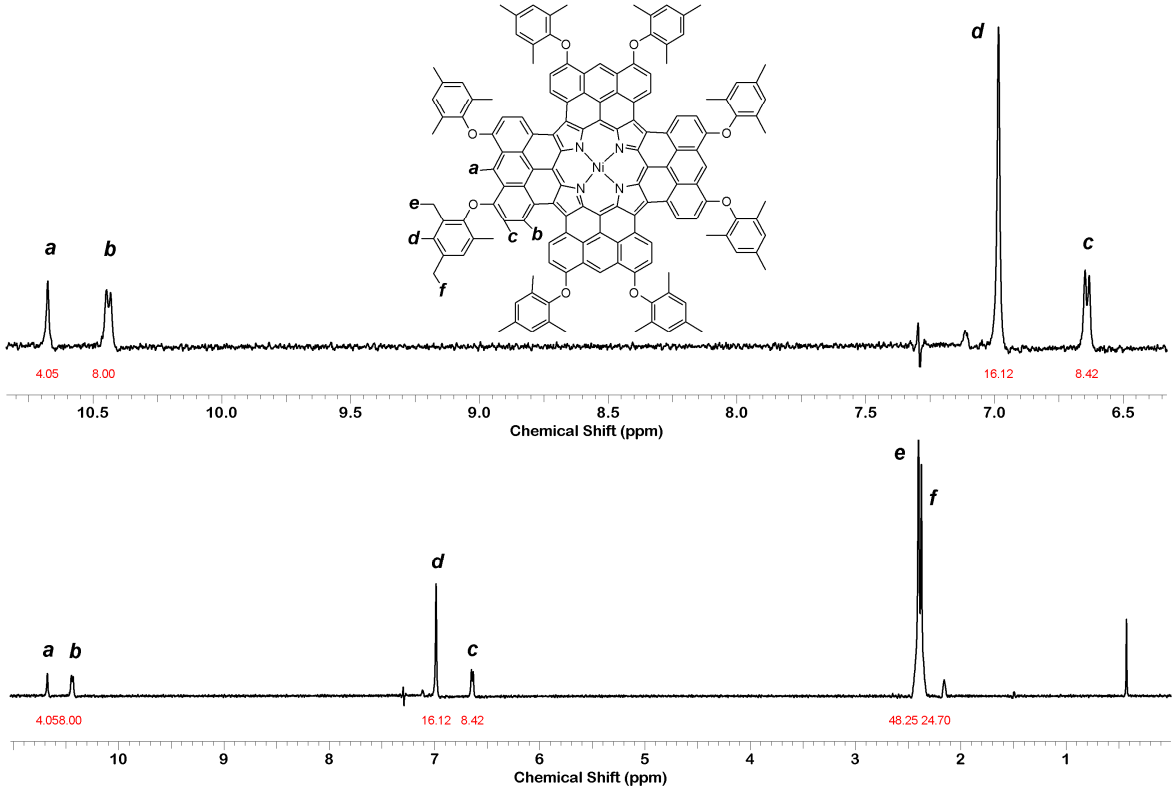

Figure 4.6: ^{1}H NMR spectrum of tetra-anthracene fused porphyrin **165** DOSY-edited so as not to show large solvent peak and satellites. (500 MHz, benzene-d_6 with 1.0 mg $NaBH_4$, 298 K). Red numbers indicate peak integrals.

4.3 Optoelectronic Properties of a Porphyrin Fused to Four Anthracenes

4.3.1 UV-vis-NIR Spectra of Tetra-Anthracene Porphyrins 164 and 165

The UV-vis-NIR spectra of tetra-anthracene fused porphyrin **165** and unfused tetra-anthracene linked porphyrin **164** are shown in Figure 4.7. The spectrum of fused porphyrin **165** was recorded with the addition of 0.5 mg of sodium borohydride to prevent the formation of radical cations of the porphyrin.

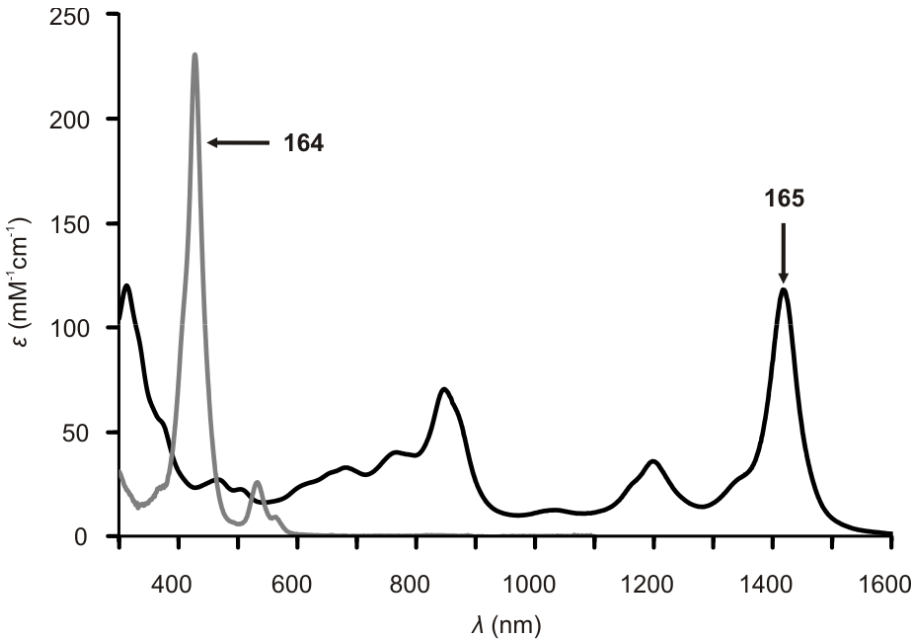

Figure 4.7: UV-vis-NIR absorption spectra in toluene for unfused porphyrin **164** (grey), and fully fused porphyrin **165** (solid black). The spectrum of **165** was recorded in the presence of 0.5 mg of $NaBH_4$ to prevent radical cation formation.

Anthracene-linked porphyrin **164** shows a UV-vis spectrum typical of an unfused nickel porphyrin monomer linked to four aromatic substituents at the *meso*-positions.[27] Upon fusion to form fully fused tetra-anthracene porphyrin **165** however, the spectral shape alters dramatically and the absorption is exceedingly red-shifted, with a longest wavelength absorption λ_{max} at 1417 nm. This near-IR absorption extends to a longer wavelength than for all other porphyrin monomers reported to date, including tetra-azulene fused nickel porphyrin **51** synthesised by Osuka and co-workers (Figure 4.8) which displays a long wavelength λ_{max} at 1136 nm and absorption to around 1250 nm.[27]

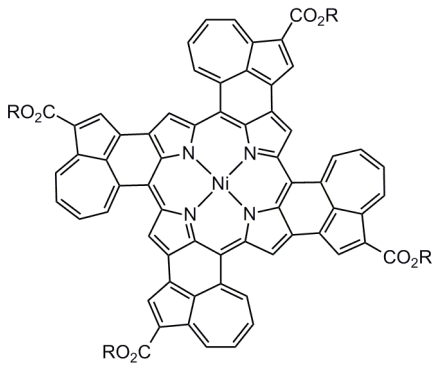

51

Figure 4.8: Tetra-azulene fused porphyrin **51** synthesised by Osuka and co-workers.[27]

Indeed, the longest wavelength absorption λ_{max} value for tetra-anthracene fused porphyrin **165** occurs at a wavelength that is comparable to those reported for triply linked porphyrin trimers (Figure 4.9: trimers **137** and **138** have long wavelength λ_{max} values of 1407 and 1494 nm respectively).[32-34]

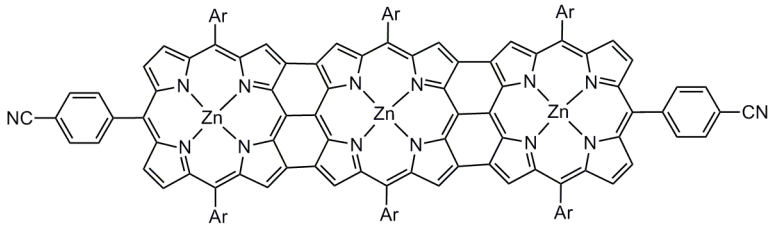

137

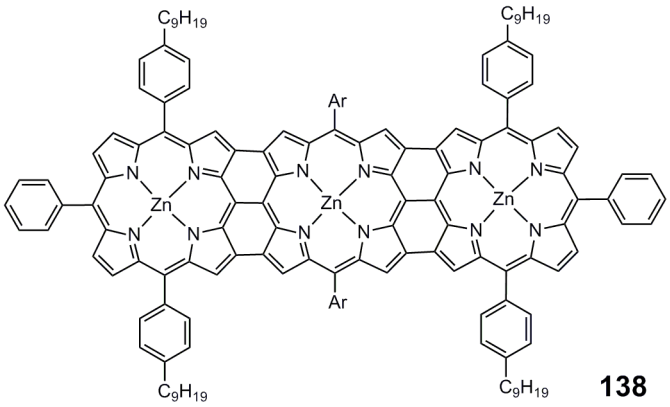

138

Figure 4.9: Porphyrin trimers **137** and **138**.[33,34] Ar = 3,5-di(*t*-butyl)phenyl.

The near-IR absorption of fused monomer **165** nearly extends as far as that of bis-anthracene fused dimer **134** (Section 3.4.7), which displays a λ_{max} at 1495 nm. Furthermore, the near-IR absorption peak of porphyrin **165** at 1417 nm is very intense and sharp (ε = 1.2 × 10^5 $M^{-1}cm^{-1}$; fwhm = 284 cm^{-1}), reflecting the high symmetry and rigid geometry of the fused system. This intensity is similar to that observed for triply linked porphyrin trimer **138** which exhibits a longest wavelength peak with ε = 1.7 × 10^5 M^{-1} cm^{-1}. However, the high intensity near-IR absorption demonstrated by porphyrin **165** is very unusual for porphyrin monomers fused to aromatic rings other than porphyrin units: tetra-azulene fused porphyrin **51** displays a very broad near-IR peak at 1136 nm with ε = 0.54 × 10^5 M^{-1} cm^{-1} (Figure 2.7).[27] This contrast in the intensity is likely to be due to the differences in the sharpness of near-IR absorption maxima between tetra-anthracene and tetra-azulene fused porphyrins. Broad

absorption for the latter system may arise from its lower symmetry and greater distortion from planarity, compared to the tetra-anthracene fused porphyrin, due to fewer sites of fusion and steric clashes between hydrogens of the azulene unit and the β-pyrrolic hydrogens of the porphyrin.

The exceedingly long wavelength absorption of tetra-anthracene fused porphyrin **165** may seem surprising, given the shift in λ_{max} of only 145 nm between mono- and bis-anthracene fused porphyrins **132** and **133** (Section 3.4.3). However a plot of optical gap (taken at the longest wavelength absorption maxima, and given in eV) versus the number of anthracenes fused to the porphyrin periphery shows that, after an initial sharp drop in energy upon fusion of one anthracene, the correlation between these two parameters is in fact linear (Figure 4.10). Hence it would appear that the near-IR absorption of **165**, giving an optical gap of 0.87 eV, is consistent with the decrease in HOMO-LUMO gap expected for the fusion of four anthracenes to the porphyrin.

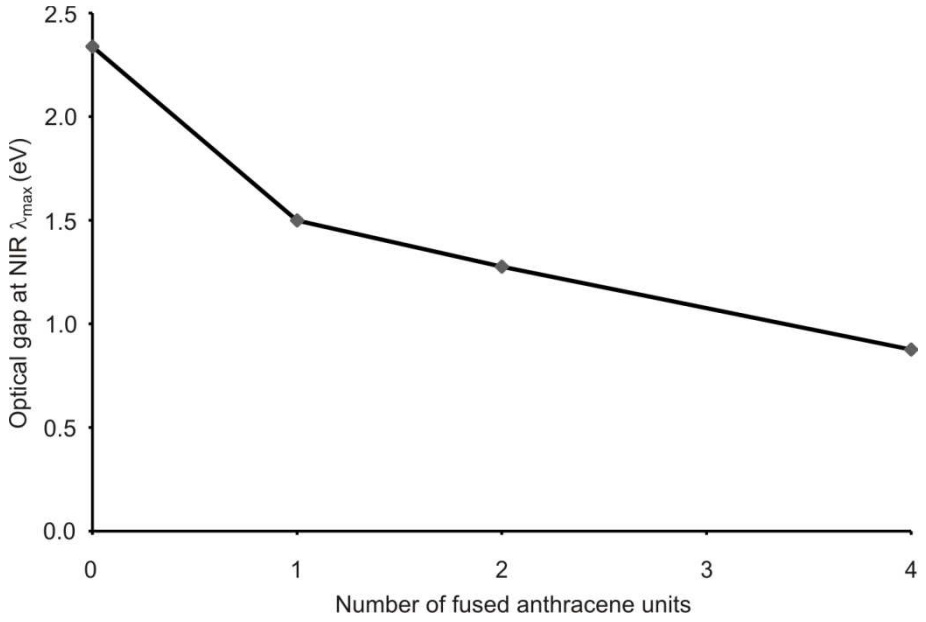

Figure 4.10: Graph showing the correlation between the optical gap (in eV) and number of anthracene units fused to the periphery of a nickel porphyrin. The optical gaps are taken at the near-IR absorption maxima for anthracene-linked porphyrin **131**, partially fused bis-anthracene porphyrin **132**, fully fused bis-anthracene porphyrin **133** (measured in $CHCl_3$/1% pyridine) and tetra-anthracene fused porphyrin **165** (measured in toluene/1% pyridine).

The exceptionally long wavelength λ_{max} exhibited in the UV-vis-NIR absorption spectrum of tetra-anthracene fused porphyrin **165**, is indicative of a very high degree of

electron delocalisation across the system. This is likely to arise from the many possible conjugation pathways through the system which occur when all four anthracenes are fused the β-positions of porphyrin **165**, thereby greatly increasing the extent of electronic communication between the anthracene units.

4.3.2 Electrochemical Properties of Tetra-Anthracene Porphyrins 164 and 165

In order to investigate the consequences of fusion on the electrochemical properties of a tetra-anthracene porphyrin system, cyclic and square-wave voltammetry were carried out on both unfused tetra-anthracene linked porphyrin **164** and fully fused tetra-anthracene porphyrin **165**. All measurements are quoted versus the ferrocene/ferrocinium redox couple. From these experiments, it was found that porphyrin **164** displays a first oxidation potential, E_1^{ox}, of 0.61 V and a first reduction potential, E_1^{red}, of –1.81 V giving an E_1^{ox}- E_1^{red} of 2.42 V (Figures 4.11 and 4.12), as expected for an unfused porphyrin monomer.[32,35]

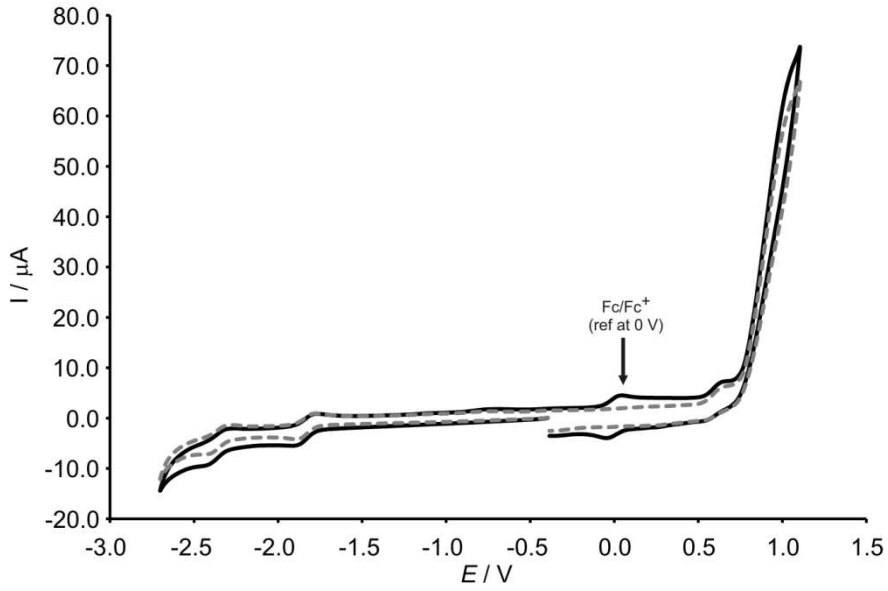

Figure 4.11: Cyclic voltammogram for unfused tetra-anthracene linked porphyrin **164**, both with ferrocene (black solid), and without (grey dash). Cyclic voltammetry was carried out in THF with 0.1 M Bu_4NPF_6 at a scan rate of 100 mV s^{-1} using a glassy carbon working electrode, Pt counter electrode and $Ag/AgNO_3$ reference electrode.

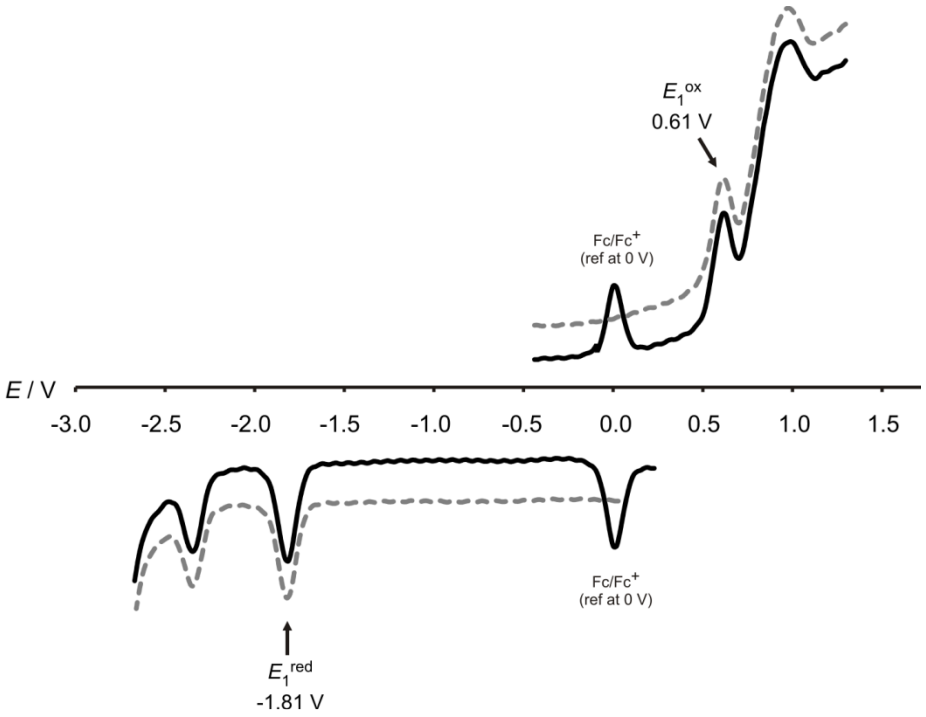

Figure 4.12: Square wave voltammogram for unfused tetra-anthracene linked porphyrin **164**, both with ferrocene (black solid), and without (grey dash). Square wave experiments were recorded in THF with 0.1 M Bu_4NPF_6 at a square wave frequency of 8 Hz using a glassy carbon working electrode, Pt counter electrode and $Ag/AgNO_3$ reference electrode.

Fusion of four anthracene units to the porphyrin core to give tetra-anthracene fused porphyrin **165**, dramatically alters the redox properties of the system, as shown by cyclic and square wave voltammetry (Figures 4.14 and 4.15 respectively). The E_1^{ox} value of fused porphyrin **165** at -0.44 V, is exceptionally low, even for a fused porphyrin system; triply linked porphyrin trimer **137** exhibits an E_1^{ox} value of 0.03 V,[33] while tetra-azulene fused porphyrin **51** displays an E_1^{ox} value of 0.13 V. Furthermore pyrene fused porphyrin dimer **58** (Figure 4.13) exhibits an E_1^{ox} value of -0.13 V which is considerably more positive than the value recorded for tetra-anthracene fused porphyrin **165**, despite both systems containing a very similar number of π-electrons.[36]

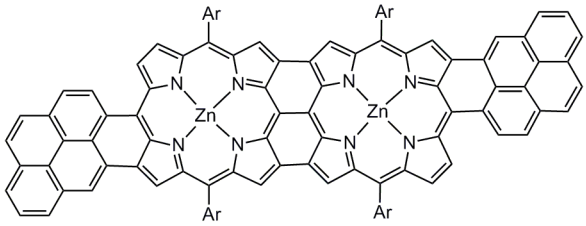

58

Figure 4.13: Pyrene fused porphyrin dimer **58** synthesised by Thompson and co-workers.[36] Ar = 3,5-di(*t*-butyl)phenyl.

The E_1^{red} value of tetra-anthracene fused porphyrin **165** was found to be -1.05 V which is more negative than observed for both triply linked porphyrin trimer **137** (-0.87 V)[33] and tetra-azulene fused porphyrin **51** (-0.88 V),[27] and similar to the value of E_1^{red} recorded for pyrene fused porphyrin dimer **58** (-0.97 V).[36]

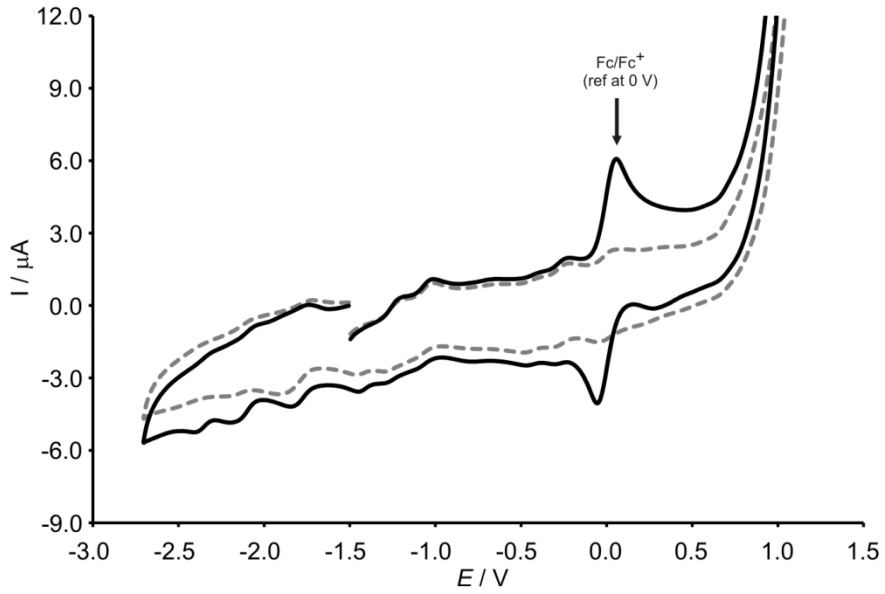

Figure 4.14: Cyclic voltammogram for fully fused tetra-anthracene porphyrin **165**, both with ferrocene (black solid), and without (grey dash). Cyclic voltammetry was carried out in THF with 0.1 M Bu_4NPF_6 at a scan rate of 100 mV s^{-1} using a glassy carbon working electrode, Pt counter electrode and $Ag/AgNO_3$ reference electrode.

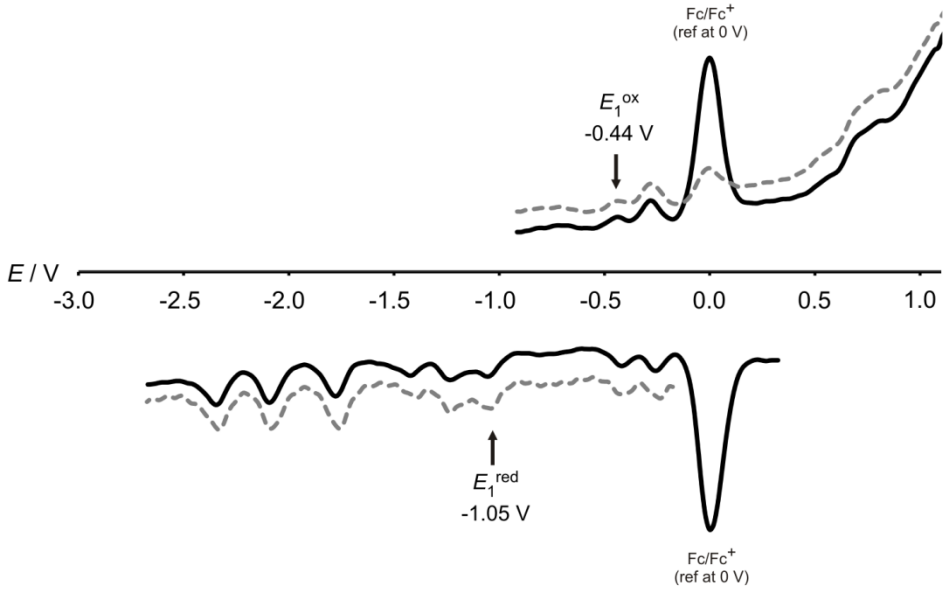

Figure 4.15: Square wave voltammogram for fully fused tetra-anthracene porphyrin **165**, both with ferrocene (black solid), and without (grey dash). Square wave experiments were recorded in THF with 0.1 M Bu_4NPF_6 at a square wave frequency of 8 Hz using a glassy carbon working electrode, Pt counter electrode and $Ag/AgNO_3$ reference electrode.

The electrochemical data obtained for tetra-anthracene porphyrins **164** and **165** are summarised in Table 4.2.

Table 4.2: Summary of electrochemical data for porphyrins **164**, and **165** measured in THF with 0.1 M Bu_4NPF_6.

Compound	E_1^{ox} (V)	E_1^{red} (V)	E_1^{ox}-E_1^{red} (V)
164	0.61	-1.81	2.42
165	-0.44	-1.05	0.61

The very small E_1^{ox}- E_1^{red} separation of just 0.61 V confirms that porphyrin **165** experiences a high degree of electron delocalisation across the system, as suggested by the exceedingly red-shifted absorption spectrum (Figure 4.7). The difference between the optical gap measured from the UV-vis-NIR absorption spectrum (0.87 V) and the electrochemical gap (0.61 V) may be due several factors, including the different choice of solvents used for the measurements, and the measurement of the optical gap at the near-IR maximum (rather than at the absorption onset or crossing point between absorption and emission spectra).

However both values indicate that tetra-anthracene fused porphyrin **165** possesses a very small HOMO-LUMO gap. Together with the high energy HOMO level, indicated by very negative value of E_1^{ox}, these values suggest that porphyrin **165** should readily undergo photogeneration of electron and hole pairs under low energy excitation, as well as exhibiting facile hole or electron injection in the bulk material of **165** by oxidation or reduction respectively. These properties are highly important in optoelectronic applications such as dye-sensitised solar cells and liquid crystalline semiconductors where efficient charge generation is critical.

4.4 X-Ray Crystal Structure of Fully Fused Tetra-Anthracene Porphyrin **165**

Crystals of tetra-anthracene fused porphyrin **165** were grown by diffusion of ethanol into a solution of porphyrin **165** in benzene, and analysed at 150 K with X-ray radiation using beamline I19 (EH1) at the Diamond Light Source by Dr Amber Thompson.

The crystal structure reveals that molecules of **165** form π-stacked dimers in the crystal (Figure 4.16), with two crystallographically independent porphyrin molecules.

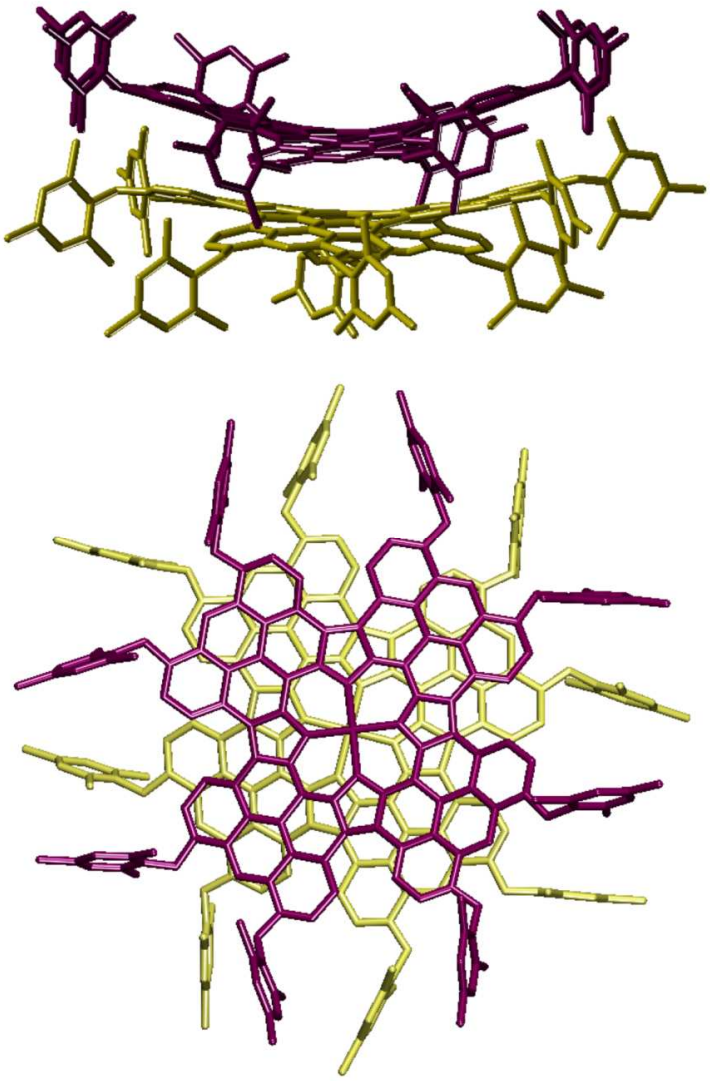

Figure 4.16: Two orthogonal views of the dimeric arrangement of tetra-anthracene fused porphyrin **165** in the crystal (hydrogens omitted for clarity). The two molecules of porphyrin **165** are shown in purple and yellow to clearly show their arrangement with respect to each other in the crystal.

The aryl ether substituents of one molecule appear to lie in between those of the second molecule due the steric demand they exert, such that the two porphyrins in the dimer are twisted by ~20° with respect to each other. The planes of the two molecules are almost parallel (angle between the mean planes of the 24-atom porphyrin cores: 1.4°), possibly to maximise the attractive π-π interactions between the π-systems of the two molecules. The mean distance of the core of one porphyrin to the plane of the other is 3.41 Å, with a Ni-Ni distance of 3.316(2) Å. A search of the Cambridge Structural Database (CSD) for Ni-Ni distances in porphyrin crystals was conducted to investigate whether the Ni-Ni distance

observed for the crystal structure of tetra-anthracene fused porphyrin **165**, is typical for nickel porphyrin systems. The van der Waals radius of nickel is 1.63 Å, hence the search was restricted to Ni-Ni distances of 3.2 — 6.4 Å to ensure the results correlated to distances between two adjacent porphyrin molecules. The results reveal that nickel porphyrins exhibit a bimodal distribution of Ni-Ni distances (Figure 4.17). Upon examination, it was found that the shorter distances (3-4 Å) were primarily found in crystal structures where porphyrin units exhibit a near-eclipsed face-to-face arrangement with respect to each other. Longer Ni-Ni distances (4 — 6.4 Å) were found to exist in crystal structures where the porphyrin units are not eclipsed, but exhibit a significant horizontal displacement with respect to each other. The Ni-Ni distance of 3.316(2) Å observed for tetra-anthracene fused porphyrin **165** in the crystal is therefore consistent with the observed near-eclipsed geometry of the dimeric pairs of porphyrin **165**. This distance does however fall on the shorter end of the distribution, indicating that monomers of porphyrin **165** pack more closely than most porphyrins exhibiting a near-eclipsed geometry, possibly due to the large size of the π-system generating more significant attractive van der Waals and π-stacking interactions.

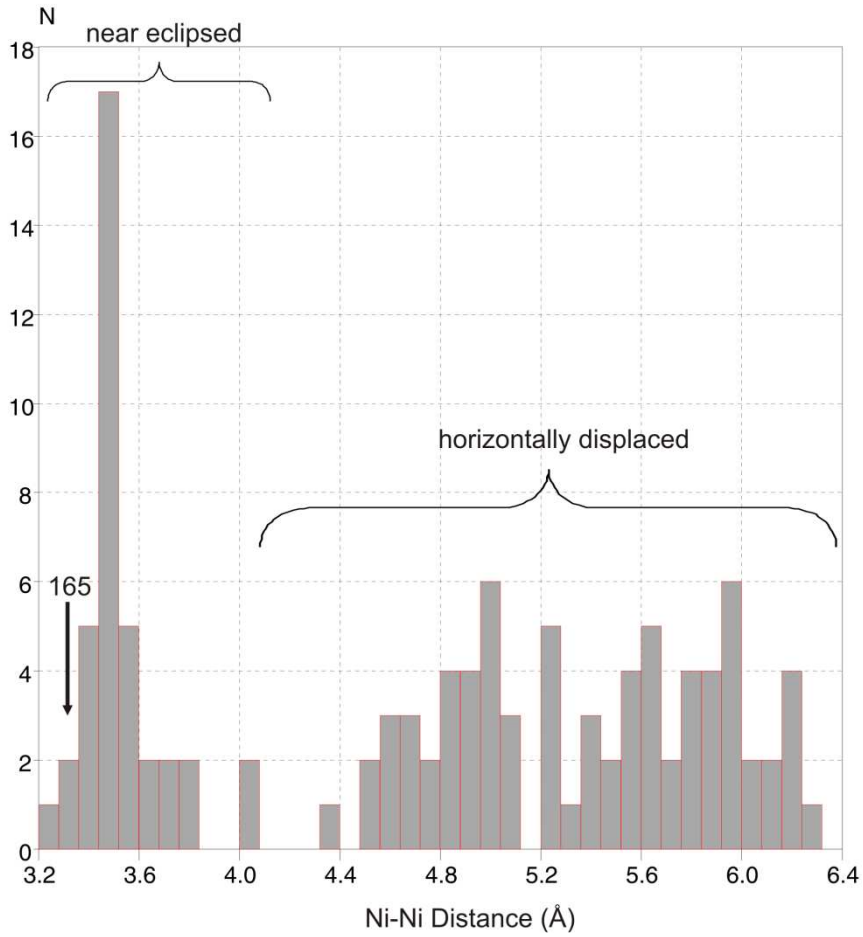

Figure 4.17: Histogram showing the distribution of Ni-Ni distances in porphyrins in the range 3.2-6.4 Å, from a search of the Cambridge Structual Database[37] using ConQuest (version 1.12).[38] Data were analyzed using Vista.[39] The Ni-Ni distance observed for porphyrin **165** is indicated by an arrow.

Both porphyrins in the π-stacked dimer adopt ruffled conformations; the mean deviation from planarity for the 24 atoms of each porphyrin core is 0.20 Å. This figure is well within the range of values reported for *meso*-tetrasubstituted nickel(II) porphyrins (Figure 4.18). The mean deviation from planarity of tetra-anthracene fused porphyrin **165** is, however, significantly less than observed for tetra-azulene fused porphyrin **51** (which is also observed to stack in dimeric pairs in the crystal).[27] This tetra-azulene fused porphyrin exhibits mean deviations from planarity of 0.40 and 0.46 Å for the two molecules in the dimeric pair, possibly due to the aforementioned steric clash between β-pyrrolic hydrogens of the porphyrin core and hydrogens of the azulene unit. Fusion across all porphyrin β-positions, as in the case of tetra-anthracene porphyrin **165**, removes such steric effects and facilitates the adoption of a more planar conformation.

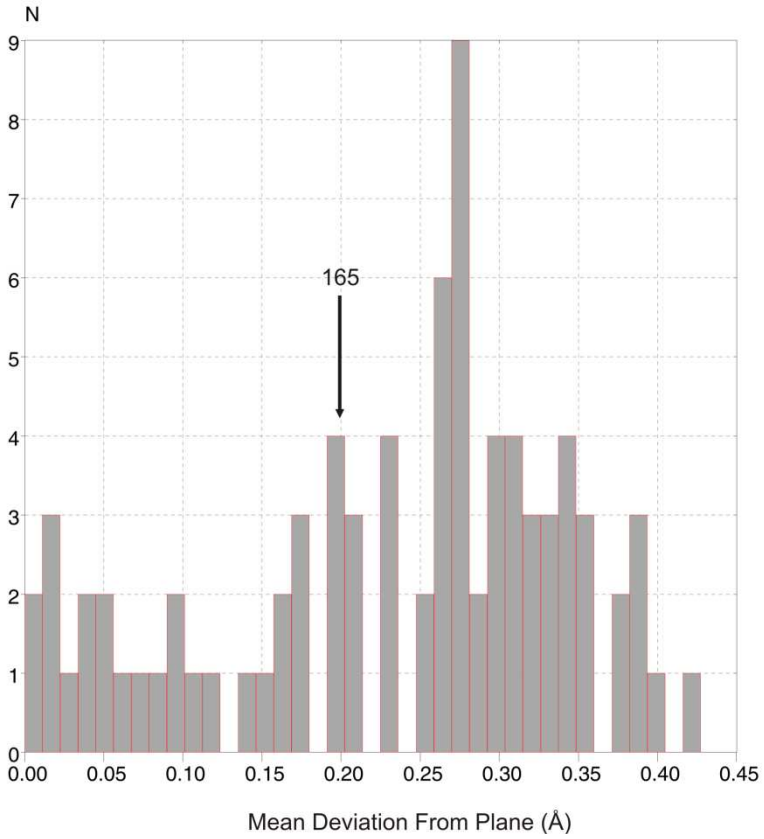

Figure 4.18: Histogram of out-of-plane distances for *meso*-tetrasubstituted nickel(II) porphyrins, from a search of the Cambridge Structural Database[37] using ConQuest (version 1.12).[38] The 'mean deviation from plane' was defined as the average deviation of the 20 carbon atoms and four nitrogen atoms of the porphyrin core from the mean plane of these 24 atoms. Data were analyzed using Vista.[39] The mean deviation from the plane observed for porphyrin **165** is indicated by an arrow.

The crystal structure of tetra-anthracene fused porphyrin **165** also reveals that dimeric pairs of molecules are surrounded by eight crystallographically distinct, ordered benzene solvent molecules, as well as significant volumes of disordered solvent. These ordered benzene rings demonstrate π-stacking interactions with the exposed faces of the anthracene-porphyrin core and the aryl side groups, resulting in the packing arrangement shown in Figure 4.19.

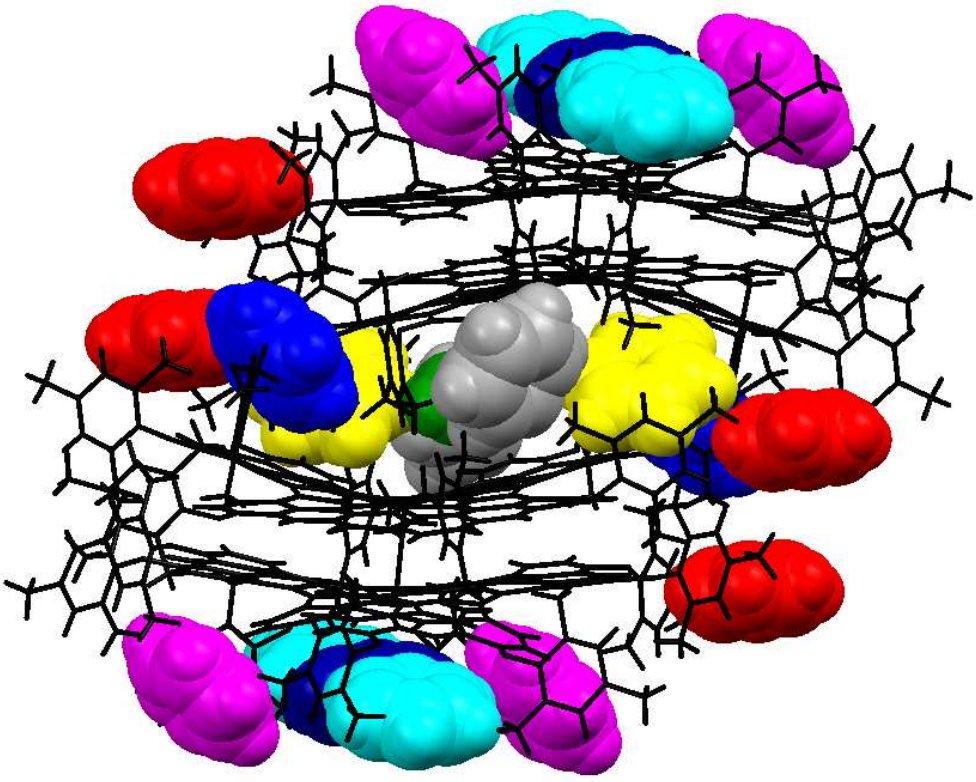

Figure 4.19: Packing diagram for **165** showing the eight crystallographically distinct ordered benzene solvent molecules (coloured red, blue, green, yellow, purple, pale blue, navy blue and grey). Two pairs of porphyrin dimer molecules are also shown (black, wire-frame).

The sterically bulky 2,4,6-trimethylphenyl groups of porphyrin **165**, besides dictating the twist angle between molecules in the dimer as mentioned above, also exert a steric effect above and below the plane of the anthracene-fused porphyrin system, preventing the formation of extended π-stacked columns. This indicates that substitution of the 2,4,6-trimethylphenyl groups for less bulky substituents could result in the formation of extended columnar arrays of porphyrin **165**. If the substituents are chosen to bear long alkyl chains, it is possible that liquid crystalline phases may be achieved.

4.5 Tetra-Anthracene Fused Porphyrins for Discotic Liquid Crystals

4.5.1 Molecular Design

As described in Section 1.2.3, the self-assembly of conjugated disc-shaped molecules into extended columnar stacks is driven by many factors including the size of the aromatic core, the nature of the peripheral substituents, and the planarity of the system.

Tetra-anthracene fused porphyrin **165** exhibits a large highly conjugated core, rigidified by fusion of the anthracene units across all of the β-positions of the porphyrin. Together with a mean deviation from planarity of only 0.20 Å, these factors indicate that the system may be expected to exhibit a small internal reorganisation energy. In addition, molecules of porphyrin **165** show a tendency to stack in a near-eclipsed arrangement, thereby maximising the π-orbital overlap between the stacked molecules such that a large transfer integral may be expected. Combined with the exceedingly low E_1^{ox} value of -0.44 V observed for tetra-anthracene fused porphyrin **165** (Section 4.3.2), these parameters suggest that the fused core of porphyrin **165** could enable excellent hole injection into, and charge transport through, columnar charge carrier systems.

In order to facilitate the formation of a liquid crystalline phase of a tetra-anthracene fused porphyrin system, it is necessary to replace the bulky aryl ether substituents of porphyrin **165** with less sterically encumbered groups, such as long alkyl chains. These peripheral substituents become disordered when the system is warmed, causing a partial breakdown of crystalline structure and hence the formation of a liquid crystalline phase. In addition, Müllen and co-workers have shown that the degree of insulation against charge recombination between columns strongly depends upon the length of these chains.[40] As a result of these requirements, target porphyrin **166** bearing long octadecyl chains was proposed as a likely candidate for the formation of liquid crystals (Figure 4.20).

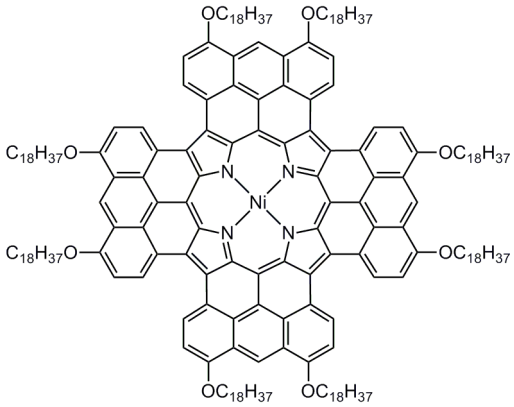

166

Figure 4.20: Target tetra-anthracene fused porphyrin **166** bearing long alkyl chains to aid formation of liquid crystalline phases.

The challenges encountered in the synthesis and purification of bis-anthracene fused porphyrins **117** and **118** bearing octyloxy chains (Chapter 3) were considered when designing the target molecule **166**. Aggregation effects due to π-stacking between the molecules of **166** are necessary for the formation of a liquid crystalline phase, but this may be expected to prevent the observation of a clear ^{1}H NMR spectrum of **166**, as found in the case of octyloxy substituted anthracene-fused porphyrins **117** and **118**. However, I thought that the extremely long octadecyl chains should convey sufficient solubility to the system to enable purification by silica gel and size exclusion chromatography. Characterisation of tetra-anthracene fused porphyrin **166** could be achieved by MALDI-TOF mass spectrometry and comparision of the UV-vis-NIR absorption spectrum with that of fused porphyrin **165**, which exhibits the same chromophore.

4.5.2 Attempted Synthesis of a Tetra-Anthracene Fused Porphyrin for Liquid Crystals

I propose that the synthesis of tetra-anthracene fused porphyrin **166** could be achieved by a similar route to that used for the synthesis of porphyrin **165** (Scheme 4.15).

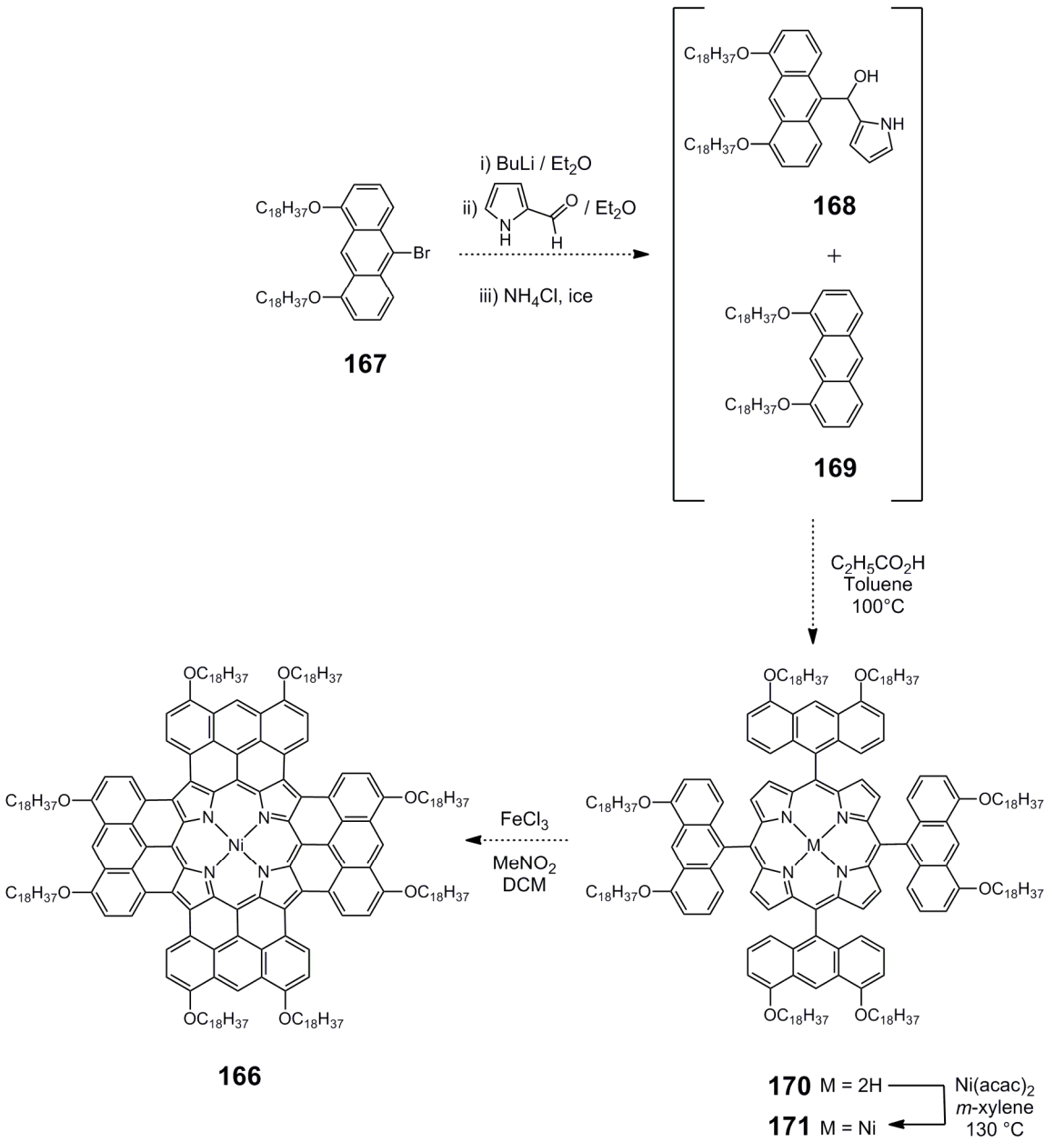

Scheme 4.15: Proposed synthetic pathway to fully fused tetra-anthracene porphyrin **166** bearing octadecyl substituents.

The first step in the formation of tetra-anthracene fused porphyrin **166** is the synthesis of bromoanthracene **167**. The synthetic pathway towards 10-bromo-1-8-octyloxyanthracene **72** (Scheme 2.11)[2] was impractical for the large scale synthesis of anthracene **167** due to the many steps involved, and the low yields achieved for some of the reactions. As a result, a pathway to bromoanthracene **167** was devised based upon the three step, high yielding synthesis of anthracene **156**. The first step in this synthesis is alkylation

of 1,8-dihydroxanthraquinone (**82**) to give 1,8-bis(octadecyloxy)anthraquinone **172**. This was initially attempted using iodooctadecane in the presence of potassium carbonate and 18-crown-6 (Scheme 4.16), following conditions which had proved successful in the alkylation of dihydroxyanthracene **86** with octylbromide (Scheme 2.11). However, when applied to the synthesis of **172**, no reaction was observed, even after three days. The reaction was repeated, increasing the number of equivalents of potassium carbonate, however still no reaction was observed.

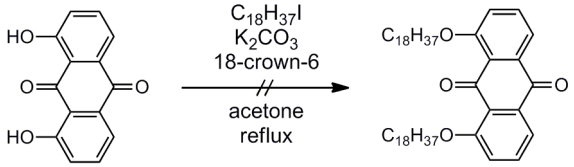

82 **172**

Scheme 4.16: Attempted synthesis of alkoxyanthraquinone **172**.

The difficulty in synthesising **172** by this standard alkylation procedure seems surprising, however it has been suggested by Gokel and co-workers that the inert behaviour of dihydroxyanthraquinone **82** towards alkylhaldies under these conditions is due to the formation of tight ion-pairs (such as **173**, Figure 4.21) which greatly reduces the nucleophilicity of the anthraquinone phenoxide anion.[41]

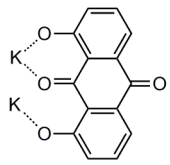

173

Figure 4.21: Tight ion-pair formed by dihydroxyanthraquinone in the presence of K_2CO_3.

Urankar and co-workers also encountered this problem in the alkylation of 1-hydroxyanthraquinones, and proposed that the use of tetralkylammonium salts would result in the formation of a looser ion-pair and hence a more reactive anion.[42] By employing a two phase procedure and a phase-transfer catalyst, it was shown that 1,8-dihydroxyanthraquinones can be readily alkylated by a variety of alkylbromides and iodides.

Synthesis of octadecyloxy substituted anthraquinone **172** was attempted under these conditions (Scheme 4.17) using tetrabutylammonium chloride.

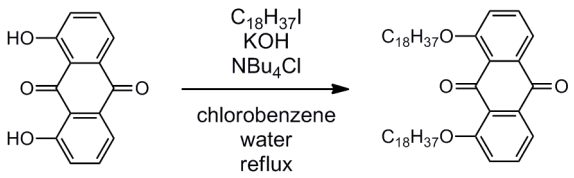

82 **172**

Scheme 4.17: Synthesis of alkoxyanthraquinone **172** by a phase-transfer catalysed procedure.

The progress of the reaction was indicated by the colour change from dark red to yellow-brown which was observed after stirring at reflux overnight. This colour change is due to the consumption of the anthraquinone 'phenoxide' ion (red) and the formation of alkylated anthraquinone (yellow). TLC of the reaction mixture after this colour change confirmed the consumption of the starting material and the formation of less polar yellow material. ^{1}H NMR spectroscopy of this mixture revealed it to contain anthraquinone **172** as the major component and the corresponding mono-alkylated anthraquinone as a bi-product. Purification of this mixture gave anthraquinone **172** in 40% isolated yield. This figure is comparable to the yield reported by Urankar and co-workers for the synthesis of 1,8-bis(hexyloxy)anthraquinone.[42]

Reduction of anthraquinone **172** to form anthrone **174** was initially attempted with sodium borohydride in methanol, followed by an acid work-up (Scheme 4.18). However even after three days, no reaction was observed.

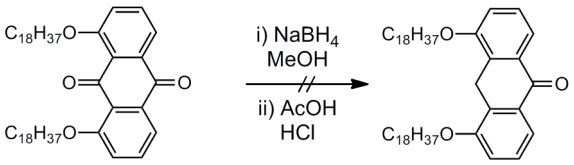

172 **174**

Scheme 4.18: Attempted reduction of anthraquinone **172** with $NaBH_4$.

In order to increase the reactivity of the anthraquinone towards sodium borohydride, cerium(III) chloride was added to a suspension of anthraquinone **172** in methanol. The reaction was monitored over three days, but again no product formation was observed.

It has been reported by Norvez that the low solubility of *peri*-alkoxyanthraquinones in methanol may prevent their reaction with sodium borohydride.[43] As a result, the reduction of anthraquinone **172** was repeated with an excess of sodium borohydride in THF with 10% methanol, following the procedure reported by Norvez for the analogous reduction of 1,4,5,8-tetrakis(methoxy)anthraquinone. After 30 minutes the reaction mixture changed colour from yellow to colourless, indicating the consumption of anthraquinone **172**. ^{1}H NMR spectroscopy of the crude mixture after acid work-up, showed a large mixture of products, one of which was identified as the desired anthrone **174**, and another as 1,8-bis(octadecyloxy)anthracene (**169**). Purification of this mixture by chromatography proved impossible due to the decomposition of anthrone **174** when in contact with silica gel.

I thought it possible that the difficulties encountered in the reduction of anthraquinone **172** to give anthrone **174** may, in part, be due to the greater electron donating capacity of octadecyloxy groups, compared to the aryl ether groups of anthraquinone **125** (Scheme 3.23), thereby decreasing the reactivity of anthraquinone **172** towards reduction. As a result, I decided to redesign the target anthraquinone to bear aryl ether groups with long pentadecyl side chains (**175**, Figure 4.22) in order to reduce the electron density of the anthraquinone system.

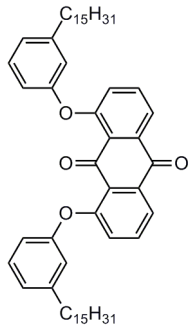

175

Figure 4.22: Target anthraquinone **175** bearing *m*-pentadecylphenoxy substituents.

The bulkier nature of the aryl substituents of anthraquinone **175** compared to the octadecyl substituents of anthraquinone **172** could potentially be expected to prevent the formation of extended π-stacked columns of the corresponding tetra-anthracene fused porphyrin derivative, and hence a liquid crystalline phase. However, Müllen and co-workers

have demonstrated that the presence of a phenyl linker group between the aromatic core and long alkyl chains of hexabenzocoronene (HBC) derivatives does not prevent the formation of liquid crystalline phases (Section 1.2.3).[44,45] In addition, the formation of π-stacked dimers of tetra-anthracene fused porphyrin **165**, rather than extended columnar arrays, is likely to be due to the steric influence of the methyl substituents of the aryl ether groups of porphyrin **165** above and below the plane of the porphyrin π-system. Hence removal of these *ortho* substituents is likely to be a key factor in favouring the formation of a liquid crystalline phase.

Due to time constraints the choice of aryl substituent for **175** however was limited by the availability of commercial phenols; while phenols with *para*-alkyl substituents are available, the length of the alkyl chain for such compounds was not considered long enough to favour liquid crystal formation. While the use of *meta*-substituted aryl groups in **175** may exert some steric influence over the packing of the final tetra-anthracene fused porphyrin, this was not considered to be likely to hinder liquid crystal formation. This conclusion was based upon consideration of the combined effect of there being only one alkyl chain per aryl group, together with the reduced steric effect of *meta*- versus *ortho*- substituents. Hence the formation of **175** may be expected to facilitate the synthesis of the corresponding tetra-anthracene fused porphyrin without compromising the possibility of the formation of a liquid crystalline phase of this porphyrin.

The synthesis of anthraquinone **175** was achieved in 42% yield by a nucleophilic aromatic substitution reaction between 1,8-dichloroanthraquinone (**124**) and 3-pentadecylphenol (**176**) (Scheme 4.19).

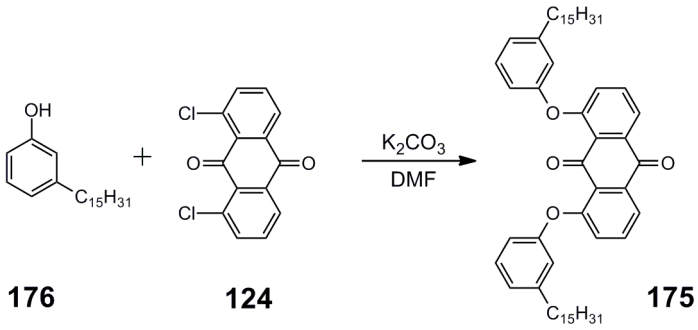

176 **124** **175**

Scheme 4.19: Synthesis of anthraquinone **175** by nucleophilic aromatic substitution.

Reduction of anthraquinone **175** with a large excess of sodium borohydride (~ 100 equivalents) was initially attempted under the same conditions as those shown in Scheme 4.18, with methanol as the solvent. The progress of the reaction was indicated by a change in colour of the reaction mixture from yellow to colourless, signifying consumption of anthraquinone **175**. After acid work-up, ^{1}H NMR spectroscopy revealed a complex mixture of products which could not be identified. However the presence of a peak at ~ 4.3 ppm suggested that the desired anthrone had indeed been formed during the reaction. Unfortunately separation of the anthrone from the large mixture of side-products proved impossible by silica gel chromatography, and partial decomposition of the product was observed when it was in contact with silica gel. The reaction was repeated with a smaller excess of sodium borohydride in order to try to reduce the number of products formed, however ^{1}H NMR spectroscopy of the crude mixture after acid work-up showed the presence of starting material together with a range of products

The presence of a long alkyl chain in anthraquinone **175** was thought to reduce its solubility in polar solvents. Hence the reduction reaction was repeated in THF with 10% methanol in an attempt to improve its solubility. The reaction mixture turned from yellow to colourless upon addition of sodium borohydride, indicating that anthraquinone **175** was being consumed. Upon acid work-up, ^{1}H NMR spectroscopy of the crude products displayed a very similar set of signals to that observed when the reaction was carried out in methanol alone. Again, purification of this mixture proved impossible.

It was concluded that the presence of a very long alkyl chain in anthraquinone **175** increases its non-polar nature, compared to 2,4,6-trimethylphenoxy substituted anthraquinone **125**. The effect of such a change in polarity and solubility causes a subtle change in the reactivity of the anthraquinone system towards sodium borohydride. Screening of different solvent systems, or reducing agents, may be expected to yield the desired anthrone, with hydrogens *peri*- to the 1,8-substituents, in high yields as found for 2,4,6-trimethylphenoxy substituted anthrone **127**. Alternatively, it may be possible to synthesise octadecyl bromoanthracene **167** following the reaction pathway shown in Scheme 2.11 for the analogous 10-bromo-(1,8-bisoctyloxy)anthracene **72**. However this pathway

involves several time consuming and low yielding steps, making it a far less attractive route, since the formation of a tetra-anthracene linked porphyrin by the procedure shown in Scheme 4.15 requires large quantities of bromoanthracene. Unfortunately, time constraints meant that it was not possible to undertake the exploration of these reaction conditions in this work.

4.6 Conclusions

Synthesis of a porphyrin fused to four anthracenes has been achieved for the first time, to create a chromophore initially proposed by Yen in 1975.[1] In the process of achieving this goal many new developments were made in the field of anthracene chemistry, providing new approaches to the regioselective bromination and reduction of 1,8-substituted anthracenes. The use of such bromoanthracenes in the synthesis of tetra-anthracene porphyrin species was explored, with the synthesis of tetra-anthracene linked free base porphyrin **161** being achieved in a 9.6% yield — a higher yield than reported for any other tetra-anthracene linked porphyrin systems.

The fusion of tetra-anthracene linked porphyrins was explored under several conditions before the fusion of tetra-anthracene linked nickel porphyrin **164** was achieved with iron(III) chloride to give the fully fused porphyrin **165** in 49% yield.

The challenging purification and characterisation of this porphyrin highlighted the subtle effects of the choice of NMR solvent, and both the need for and choice of reducing agent, highly important in the observation of a clear ^{1}H NMR spectrum. The exceedingly simple set of only six signals observed in the ^{1}H NMR spectrum of tetra-anthracene fused porphyrin **165** are a testimony of the high symmetry of the system.

The UV-vis-NIR spectrum of tetra-anthracene fused porphyrin **165** shows a large red-shift compared to the absorption spectrum of unfused porphyrin **164**, with a λ_{max} in the near-IR at 1417 nm. The small optical gap associated with such a near-IR maximum has been shown to be consistent with those recorded for mono- and bis-anthracene fused porphyrins, with a linear decrease in optical gap observed as the number of anthracene units

fused to the porphyrin increases. This indicates the strong effect fusion of anthracene units has on the electronic structure of the porphyrin system. Indeed, the near-IR absorption exhibited by **165** occurs at a longer wavelength than those reported for all other porphyrin monomers, indicating the exceedingly novel properties of this near-IR dye. Furthermore, the high intensity and sharpness of the near-IR absorption demonstrated by tetra-anthracene fused porphyrin **165** is indicative of its high degree of electron delocalisation and the planarity, symmetry and rigidity of the system. Indeed the absorption of porphyrin **165** is comparable to that observed for many triply linked porphyrin trimer systems. Such long wavelength near-IR absorption suggests that porphyrin **165** may exhibit nonlinear optical properties at wavelengths suitable for applications in the field of telecommunications (circa 1500 nm).[46,47]

The electrochemistry of tetra-anthracene fused porphyrin **165** was investigated and it was revealed that the first oxidation occurs at just -0.44 V; a value more negative than observed for any similar fused porphyrin systems. The high energy HOMO expected to correlate to such a negative oxidation potential is likely to facilitate hole-injection in the bulk material by oxidation, rendering tetra-anthracene fused porphyrin **165** and its derivatives of potential use in charge carrier systems. In addition the exceedingly small E^1_{ox}-E^1_{red} separation of only 0.61 V suggest that the photogeneration of electrons and holes in **165** may be expected to occur at low energies, indicating that tetra-anthracene fused porphyrins may find application in near-IR photovoltaic devices.

The crystal structure of tetra-anthracene fused porphyrin **165** confirms the connectivity of the system, and demonstrates the tendency for the molecules of **165** to stack in dimeric pairs in a near-eclipsed face-to-face arrangement with a small twist angle. This geometry was shown to result in a short Ni-Ni distance of 3.316(2) Å. In the absence of the methyl groups of the aryl ether substituents, it may be expected that the dimeric pairs of tetra-anthracene fused porphyrins could extend to form long columnar arrays.

The synthesis of a tetra-anthracene fused porphyrin capable of forming liquid crystal phases was attempted. However it proved impossible to synthesise the necessary anthrone precursor bearing substituents with long alkyl chains. Future work in this area is necessary

to understand the complexities of anthrone synthesis. Once these hurdles are overcome, it may be possible to access a tetra-anthracene fused porphyrin with long alkyl substituents, capable of forming liquid crystal phases. Measurement of charge transport in such a system would be of great interest, given the exceedingly promising electrochemical properties recorded in Section 4.3.2.

4.7 References

(1) Yen, T. F. *The Role of Trace Metals in Petroleum*; Ann Arbor Science Publishers: Ann Arbor, 1975.

(2) Davis, N. K. S.; Pawlicki, M.; Anderson, H. L. *Org. Lett.* **2008**, *10*, 3945-3947.

(3) Yamane, O.; Sugiura, K.; Miyasaka, H.; Nakamura, K.; Fujimoto, T.; Nakamura, K.; Kaneda, T.; Sakata, Y.; Yamashita, M. *Chem. Lett.* **2004**, *33*, 40-41.

(4) Herwig, P.; Kayser, C. W.; Müllen, K.; Spiess, H. W. *Adv. Mater.* **1996**, *8*, 510-513.

(5) Lindsey, J. S.; Hsu, H. C.; Schreiman, I. C. *Tetrahedron Lett.* **1986**, *27*, 4969-4970.

(6) Gradillas, A.; del Campo, C.; Sinisterra, J. V.; Llama, E. F. *J. Chem. Soc., Perkin Trans. 1* **1995**, 2611-2613.

(7) Cense, J. M.; Le Quan, R. M. *Tetrahedron Lett.* **1979**, 3725-3728.

(8) Kumar, A.; Maji, S.; Dubey, P.; Abhilash, G. J.; Pandey, S.; Sarkar, S. *Tetrahedron Lett.* **2007**, *48*, 7287-7290.

(9) Tohara, A.; Sato, M. *J. Porphyrins Phthalocyanines* **2007**, *11*, 513-518.

(10) Treibs, A.; Häberle, N. *Justus Liebigs Ann. Chem.* **1968**, *718*, 183-207.

(11) Volz, H.; Herb, G. *Z. Naturforsch. B.* **1984**, *39*, 1393-1398.

(12) Volz, H.; Schäffer, H. *Chem. Ztg.* **1985**, *109*, 308-309.

(13) Harden, G. J.; Coombs, M. M. *J. Chem. Soc., Perkin Trans. 1* **1995**, 3037-3042.

(14) Vzorov, A. N.; Dixon, D. W.; Trommel, J. S.; Marzilli, L. G.; Compans, R. W. *Antimicrob. Agents Chemother.* **2002**, *46*, 3917-3925.

(15) Scharbert, B. In *Ger. Offen.*; Hoechst A. G.: Germany, 1995.

(16) Lindsey, J. S.; Wagner, R. W. *J. Org. Chem.* **1989**, *54*, 828-836.

(17) Halterman, R. L.; Jan, S. T. *J. Org. Chem.* **1991**, *56*, 5253-5254.

(18) Halterman, R. L.; Mei, X. *Tetrahedron Lett.* **1996**, *37*, 6291-6294.

(19) Fieser, L. F.; Hartwell, J. L. *J. Am. Chem. Soc.* **1938**, *60*, 2555-2559.

(20) Choi, D. H.; Chon, J. Y.; Kang, J. *Bull. Korean Chem. Soc.* **2009**, *30*, 23-24.

(21) Bunnett, J. F.; Zahler, R. E. *Chem. Rev.* **1951**, *49*, 273-412.

(22) Thompson, A. L. S.; Kabalka, G. W.; Akula, M. R.; Huffman, J. W. *Synthesis* **2005**, 547-550.

(23) Yokoyama, R.; Ito, S.; Okujima, T.; Kubo, T.; Yasunami, M.; Tajiri, A.; Morita, N. *Tetrahedron* **2003**, *59*, 8191-8198.

(24) Ito, S.; Ando, M.; Nomura, A.; Morita, N.; Kabuto, C.; Mukai, H.; Ohta, K.; Kawakami, J.; Yoshizawa, A.; Tajiri, A. *J. Org. Chem.* **2005**, *70*, 3939-3949.

(25) Jiao, C.; Huang, K. W.; Guan, Z.; Xu, Q. H.; Wu, J. *Org. Lett.* **2010**, *12*, 4046-4049.

(26) Pondaven, A.; Cozien, Y.; L'Her, M. *New J. Chem.* **1992**, *16*, 711-718.

(27) Kurotobi, K.; Kim, K. S.; Noh, S. B.; Kim, D.; Osuka, A. *Angew. Chem. Int. Ed.* **2006**, *45*, 3944-3947.

(28) Tanaka, M.; Hayashi, S.; Eu, S.; Umeyama, T.; Matano, Y.; Imahori, H. *Chem. Commun.* **2007**, 2069-2071.

(29) Jiao, C.; Huang, K. W.; Chi, C.; Wu, J. *J. Org. Chem.* **2011**, *76*, 661-664.

(30) Bian, Y. Z.; Chen, X. H.; Wang, D. Y.; Choi, C. F.; Zhou, Y.; Zhu, P. H.; Ng, D. K. P.; Jiang, J. Z.; Weng, Y. X.; Li, X. Y. *Chem. Eur. J.* **2007**, *13*, 4169-4177.
(31) Jiang, J.; Liu, W.; Cheng, K. L.; Poon, K. W.; Ng, D. K. P. *Eur. J. Inorg. Chem.* **2001**, 413-417.
(32) Fendt, L. A.; Fang, H.; Plonska-Brzezinska, M. E.; Zhang, S.; Cheng, F.; Braun, C.; Echegoyen, L.; Diederich, F. *Eur. J. Org. Chem.* **2007**, 4659-4673.
(33) Cheng, F.; Zhang, S.; Adronov, A.; Echegoyen, L.; Diederich, F. *Chem. Eur. J.* **2006**, *12*, 6062-6070.
(34) Ikeue, T.; Aratani, N.; Osuka, A. *Isr. J. Chem.* **2005**, *45*, 293-302.
(35) Chang, D.; Malinski, T.; Ulman, A.; Kadish, K. M. *Inorg. Chem.* **1984**, *23*, 817-824.
(36) Diev, V. V.; Hanson, K.; Zimmerman, J. D.; Forrest, S. R.; Thompson, M. E. *Angew. Chem. Int. Ed.* **2010**, *49*, 5523-5526.
(37) Allen, F. H. *Acta Crystallogr., Sect. B: Struct. Sci.* **2002**, *58*, 380-388.
(38) Bruno, I. J.; Cole, J. C.; Edgington, P. R.; Kessler, M.; Macrae, C. F.; McCabe, P.; Pearson, J.; Taylor, R. *Acta Crystallogr., Sect. B: Struct. Sci.* **2002**, *58*, 389-397.
(39) *Vista - A Program for the Analysis and Display of Data Retrieved from the CSD*, Cambridge Crystallographic Data Centre, 12 Union Road, Cambridge, UK
(1994).
(40) Warman, J. M.; Piris, J.; Pisula, W.; Kastler, M.; Wasserfallen, D.; Müllen, K. *J. Am. Chem. Soc.* **2005**, *127*, 14257-14262.
(41) Yoo, H. K.; Davis, D. M.; Chen, Z.; Echegoyen, L.; Gokel, G. W. *Tetrahedron Lett.* **1990**, *31*, 55-58.
(42) Robello, D. R.; Eldridge, T. D.; Urankar, E. J. *Org. Prep. Proced. Int.* **1999**, *31*, 433-439.
(43) Norvez, S. *J. Org. Chem.* **1993**, *58*, 2414-2418.
(44) van de Craats, A. M.; Warman, J. M.; Fechtenkötter, A.; Brand, J. D.; Harbison, M. A.; Müllen, K. *Adv. Mater.* **1999**, *11*, 1469-1472.
(45) Fechtenkötter, A.; Saalwächter, K.; Harbison, M. A.; Müllen, K.; Spiess, H. W. *Angew. Chem. Int. Ed.* **1999**, *38*, 3039-3042.
(46) Ramaswami, R. *IEEE Commun. Mag.* **2002**, *40*, 138-147.
(47) Brédas, J. L.; Adant, C.; Tackx, P.; Persoons, A.; Pierce, B. M. *Chem. Rev.* **1994**, *94*, 243-278.

Chapter 5: Anthracene-Porphyrins for Dye-Sensitised Solar Cells[c]

This chapter examines the mode of operation of a dye-sensitised solar cell (DSSC) and presents the various parameters which determine the efficiency of cell performance. Porphyrins are introduced as building blocks for organic sensitisers, and the suitability of fused porphyrins as panchromatic dyes is discussed. The molecular design and synthesis of an anthracene-linked and anthracene-fused porphyrin for use in DSSCs is presented, and the optoelectronic properties of these dyes are investigated. Finally, the photovoltaic performance of these dyes in dye-sensitised solar cells is presented and discussed.

[c] Part of this chapter has been included in the following paper: *'Towards a Porphyrin-Based Panchromatic Sensitizer for Dye-Sensitized Solar Cells.'* James M. Ball, Nicola K. S. Davis, James Wilkinson, Joël Teuscher, James Kirkpatrick, Robert Gunning, Harry L. Anderson, Henry J. Snaith. This paper is pending submission to *The Journal of Materials Chemistry*.

5.1. Dye-Sensitised Solar Cells

5.1.1 Operation of a Dye-Sensitised Solar Cell

The basic components of a dye-sensitised solar cell (DSSC), together with a description of the key desirable steps in the operation of such a device are shown in Figure 1.18. There are many competing processes which may act to reduce the overall cell performance.[1] Figure 5.1 shows both the desirable and undesirable processes.[2]

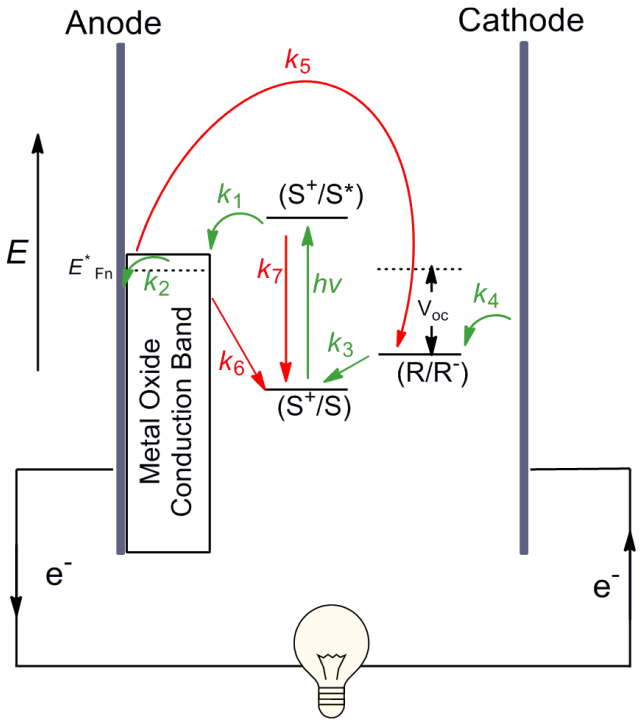

Figure 5.1: Schematic diagram showing desirable processes (green) and competing undesirable processes (red) in the operation of a DSSC.[1,2] The open circuit voltage, V_{oc}, is set by the difference between the Fermi level for electrons (E^*_{Fn}) in the metal oxide and the potential of the R/R^- redox couple in the electrolyte. k_1 = charge injection from the excited state of the dye into the metal oxide conduction band, k_2 = diffusion of electrons through metal oxide, k_3 = regeneration of dye, k_4 = hole migration from redox couple to cathode, k_5 = reduction of redox couple R/R^- by electrons from the metal oxide conduction band, k_6 = recombination of dye cation with electrons from the metal oxide conduction band, k_7 = relaxation of excited state of the dye to its ground state.

Absorption of light by the dye sensitiser (S) generates an excited state (S*) which may either undergo the desired charge injection process (with rate k_1), or relax back to the ground state either by fluorescence or by non-radiative decay processes (with rate k_7). In order for charge injection to be successful, k_1 must be greater than k_7. Once the charge has been injected into the metal oxide conduction band, it may also undergo one of several fates,

namely diffusion through the semiconducting metal oxide to the electrode (at rate k_2), recombination with the dye cation (k_6), or reduction of the redox couple R/R^- (at rate k_5) giving rise to a 'dark current'. In order for a DSSC to operate efficiently, k_2 must be faster than both k_5 and k_6, as these undesirable competing processes reduce the number of electrons taking part in the operational cycle, thereby reducing both the short-circuit current density (J_{SC}) and the open-circuit voltage (V_{OC}). Provided k_5 and k_6 are slower than k_2 and k_3, the oxidised dye will be reduced by the redox couple R/R^-. The circuit is completed by hole migration from R/R^- to the cathode in a process with rate k_4.[1]

Typically electron injection (k_1) has been found to occur on ultrafast timescales (10^{12} — 10^{15} s^{-1}),[3,4] while the recombination process with rate k_6 occurs on the micro to millisecond timescale.[3,5,6] In contrast, the singlet excited state lifetimes of sensitisers such as ruthenium complexes and porphyrins have been found to lie on the nanosecond timescale,[3,7] while the rate of dye regeneration (k_3) is in the microsecond to nanosecond time domain for the typical electron donor I^-.[8,9] The rate of the dark current process (k_5) is typically relatively slow for the I^-/I_3^- couple, with lifetimes occurring on the millisecond to second timescale,[5,8] while the rate of movement of electrons through the metal oxide layer (k_2) ranges from milliseconds to seconds.[6] While this rate of electron transport through the metal oxide is far slower than in semiconductors such as silicon, the absence of 'minority carriers' (i.e. holes) in the oxide means that recombination losses due to defects in the lattice are not encountered for DSSC devices, in contrast to conventional silicon based photovoltaic cells.[10,11]

5.1.2 Quantifying Cell Efficiency

As can been seen from the discussion above, the efficiency of a DSSC depends upon a complex interplay of factors. In order to measure the effect such factors have on the function of a solar cell however, it is necessary to define several parameters by which to quantify the performance of a DSSC. Hence the figures of merit for DSSC devices are now introduced.

The short-circuit photocurrent density (J_{SC}) of a cell is the maximum current (per unit area) which may flow through the device. This occurs when the applied voltage across

the DSSC is zero, i.e. the cell is short-circuited, and hence no work is done.[12] J_{SC} is related to short-circuit current, I_{SC}, by

$$J_{SC} = \frac{I_{SC}}{A}$$

where A is the area over which the illumination occurs. J_{SC} depends upon many factors including the incident spectrum, the intensity of the incident light, the absorption spectrum of the sensitiser, the probability of charge injection and the diffusion rate of the electrons through the metal oxide (which depends upon the structure of the metal oxide layer, as described for titanium dioxide in Section 5.1.3).[13]

The open-circuit voltage (V_{OC}) is the maximum voltage the DSSC can provide. This occurs when there is zero current i.e. V_{OC} is the voltage applied to supply a current to the cell in forward bias which negates the photocurrent; the load has infinite resistance so there is no net current.[12] V_{OC} is determined by the difference in the Fermi-level for electrons in the metal oxide conduction band and the potential of the redox couple in the electrolyte (Figure 5.1), however it is also affected by the magnitude of the current generated by illumination and the rate of unfavourable recombination reactions, as both of these factors affect the population of the conduction band and hence the position of the Fermi level.[14]

If a plot is made of J against V (a current density — voltage curve) a new parameter, the fill factor (FF) may be determined (Figure 5.2). FF is defined as the ratio of the maximum power output of the DSSC per unit area, divided by the maximum theoretical power output of the cell (as defined by J_{SC} and V_{OC}),[8] giving the equation

$$FF = \frac{P_{out}}{V_{OC} J_{SC}}$$

and

$$P_{out} = V_{mp} J_{mp}$$

where V_{mp} and J_{mp} are the voltage and current density at the maximum observed power output respectively. V_{OC} may be found from the intercept of the J — V curve with the x axis

while J_{SC} may be found from the y intercept.[8] In an ideal DSSC, all of the electrons injected into the conduction band of the metal oxide would reach the electrodes, however due to recombination processes, resistance, and leakage of current through the cell, this behaviour is not observed.[12] Hence P_{out} is always less than the maximum theoretical power output; the nearer the FF is to unity, the more rectangular the shape of the J — V curve, and the better the cell performance.[8]

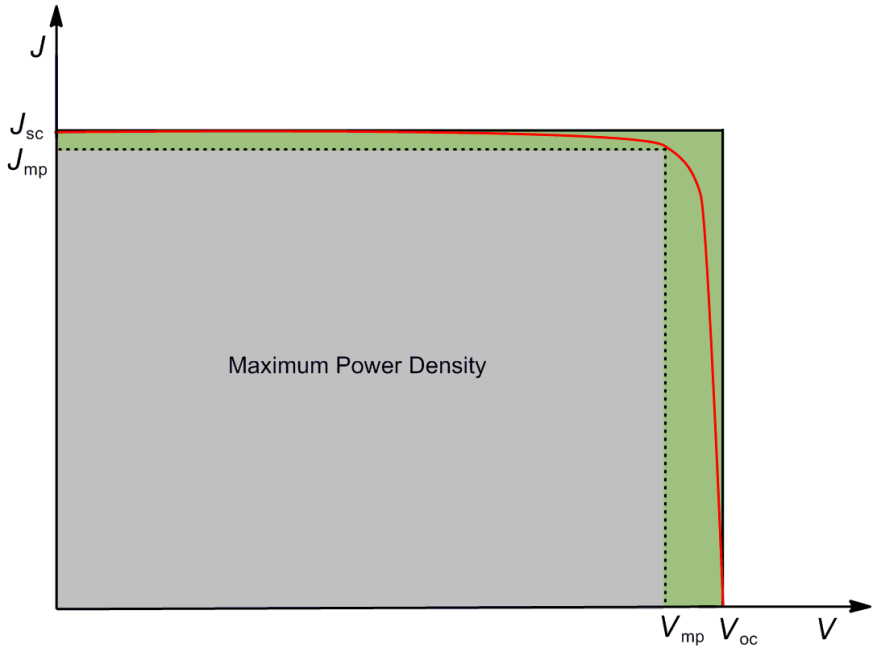

Figure 5.2: Schematic plot of current density (J) against voltage (V) for a DSSC (red line). The maximum power density is given by $J_{mp} \times V_{mp}$ and is shown by the grey box. This value falls below the theoretical maximum power output given by $J_{SC} \times V_{OC}$ (shown by the green box) due to recombination and resistance losses. The fill factor (FF) corresponds to the ratio of the area covered by the grey box relative to that covered by the green box.

The incident photon to current conversion efficiency (IPCE), also known as the 'external quantum efficiency',[8] is defined as the number of electrons (generated by light) which enter the external circuit, divided by the number of photons which strike the cell at a given wavelength.

$$\mathbf{IPCE}(\lambda) = \frac{\textbf{no. of electrons in circuit}}{\textbf{no. of incident photons}}$$

For an ideal cell every photon would generate an electron which would then enter the circuit, hence the IPCE would be 1 (or 100% as IPCE values are usually given as percentages). The IPCE can be also be written as

$$\mathbf{IPCE}(\boldsymbol{\lambda}) = \mathbf{LHE}(\boldsymbol{\lambda}) \times \boldsymbol{\varphi}_{\mathbf{inj}} \times \boldsymbol{\eta}_{\boldsymbol{c}}$$

where LHE(λ) is the light harvesting efficiency at wavelength λ, φ_{inj} is the quantum yield of electron injection into the metal oxide layer of the DSSC, and η_c is the efficiency of charge collection at the counter electrode,[8] which is dependent upon several factors including the rate of unfavourable processes such as charge recombination.

LHE(λ) is given by

$$\mathbf{LHE}(\boldsymbol{\lambda}) = \mathbf{1} - \mathbf{10}^{-\mathbf{A}}$$

where A is the absorbance of the dye adsorbed on the metal oxide layer. Hence to achieve high IPCE values, and therefore a large J_{SC}, it is necessary for the dye to absorb light over a wide range of wavelengths with large extinction coefficients, and for the dye to exhibit good surface coverage of the titanium dioxide.[15]

The parameters discussed above give rise to an overall solar-to-electrical energy conversion efficiency, η, given by

$$\boldsymbol{\eta} = \frac{\boldsymbol{V}_{\mathbf{mp}}\boldsymbol{J}_{\mathbf{mp}}}{\boldsymbol{I}_{\boldsymbol{in}}} = \frac{\boldsymbol{V}_{\mathbf{oc}}\boldsymbol{J}_{\mathbf{sc}}\boldsymbol{FF}}{\boldsymbol{I}_{\boldsymbol{in}}}$$

where I_{in} is the intensity of the incident light.

These figures of merit are dependent upon factors such as the spectrum and intensity of the incident light, and the temperature of the system. Hence standard conditions of Air Mass (AM) 1.5 G spectrum (Figure 5.3, where $\mathbf{AM} = \frac{\mathbf{1}}{\mathbf{cos}\boldsymbol{\varphi}}$ and φ is the average angle of elevation of the sun which is 42°),[8] incident light intensity of 1000 W m^{-2} and temperature of 298 K are used when testing devices.[12]

Figure 5.3: The photon flux of the AM 1.5 G spectrum at 1000 W m^{-2} (solid line) and calculated photocurrent (dashed line).[8]

5.1.3 Factors Affecting DSSC Efficiency

From the discussion in Section 5.1.1, it can be seen that the rates of both the desirable and undesirable processes occur over a range of timescales. These rates may be affected by many factors including, but not limited to, the nature of the metal oxide layer, the choice of electrolyte, and the choice of dye sensitiser.

Titanium dioxide (anatase) is the most common metal oxide used in DSSC devices, although other oxides such as zinc oxide (ZnO) and tin oxide (SnO_2) have also been used, the latter of which exhibits a conduction band around 0.5 eV lower in energy than titanium dioxide.[6,8] Tin oxide can therefore be used in DSSCs incorporating dyes with low energy excited states, although such systems would be expected to exhibit a lower open circuit voltage (V_{oc}).[8]

The role of the metal oxide is to block the interface between the anode (usually composed of glass coated with fluorine-doped tin oxide, FTO) and the redox couple R/R^- (usually I^-/I_3^- for liquid electrolyte cells), as well as providing a surface for the anchoring of dye sensitiser molecules.[1] O'Regan and Grätzel showed in their groundbreaking publication,[11] that use of a rough surface composed of titanium dioxide nanoparticles greatly improved the efficiency of DSSC devices, compared to those incorporating a smooth titanium dioxide surface. This is because the nanoparticles of titanium dioxide produce a surface area that is over 1000 times greater than for a smooth film, allowing a much larger proportion of

dye to adsorb for a given area, thereby greatly increasing the light harvesting properties of the device.[5,11] The particle size has been shown to strongly influence DSSC efficiencies; smaller particle sizes result in more dye adsorption, while larger particles lead to a better diffusion rate of electrons through the layer. This latter effect is due to the fact that electron traps (localised states, which exist below the conduction band) appear to be located on the surface of the titanium dioxide particles.[16,17] Particles of around 20 nm in diameter have been found to strike a balance between these competing factors of surface area and electron transport.[8] The porosity of the titanium dioxide particles may also strongly influence the efficiency of the DSSC, with high porosity favouring penetration of the electrolyte, containing the I^-/I_3^- redox couple, into the titanium dioxide layer, thereby enabling efficient dye regeneration.[5,6] However increasing the porosity of the film decreases the coordination number of the titanium dioxide particles, reducing the ability for electrons to move through the material.[8,18] It has been found that the optimal porosity for the titanium dioxide layer is therefore between 50% and 60%.[6,19]

The thickness of this titanium dioxide layer is also important. As the thickness of the film increases, the probability of trapping and recombination of electrons also increases due to the greater number of grain boundaries and particles the electrons must cross.[6,20] Furthermore, the slow diffusion rate of the I^-/I_3^- redox couple through the electrolyte also suggests that a thin layer of titanium dioxide is desirable to reduce the distance the I_3^- must travel in order to reach the cathode.[21] However a thicker titanium dioxide film enables greater light absorption due to the adsorption of more dye molecules.[6] Hence these factors must be balanced to produce a device with high efficiencies; in the case of liquid electrolyte DSSCs, the thickness of the titanium dioxide layer is usually in the region of 10 μm.[8]

The composition of the liquid electrolyte is also a key parameter. The I^-/I_3^- redox couple is the couple of choice due to its slow rate of recombination with electrons from the titanium dioxide, its rapid rate of dye regeneration, and its fast kinetics of electron uptake at the cathode.[6,8] However the volatility of iodine and the electrolyte solvent means that the cells must be sealed and, in addition, the I^-/I_3^- redox couple can be corrosive towards the platinum electrode, hence alternative redox couples have been investigated. The use of the

redox couple Br^-/Br_2, has been shown to give larger V_{OC} values than for the I^-/I_3^- redox couple due to its more positive redox potential, however devices incorporating this redox couple have been found to display rather low efficiencies. In addition the value of J_{SC} was found to be lower when the Br^-/Br_2 redox couple was employed, possibly due to ineffective dye regeneration due to the small energy gap between the potential of the redox couple and the HOMO of the dye.[22,23] The $SeCN^-/(SeCN)_3^-$ and $SCN^-/(SCN)_3^-$ redox couples, with more positive redox potentials than the I^-/I_3^- redox couple, have also been investigated in both titanium and tin oxide DSSC devices.[24-26] It was thought that such couples would result in larger open circuit voltages due to their more positive redox potentials. However the $SCN^-/(SCN)_3^-$ redox couple has been shown to exhibit slow kinetics of dye regeneration,[26] and instability at room temperature, rendering it an impractical system. On the other hand, the $SeCN^-/(SeCN)_3^-$ couple has been found to be noncorrosive, absorb less visible light than the I^-/I_3^- redox couple and operate over a wide temperature range.[26] However this redox couple has been found by Meyer and co-workers to exhibit a slower rate of dye regeneration than for the I^-/I_3^- couple for acetonitrile based electrolytes, with efficiencies, though promising, still far behind those of cells incorporating the I^-/I_3^- redox couple.[24,25] In contrast, Grätzel and co-workers have found the $SeCN^-/(SeCN)_3^-$ couple to be highly successful when employed in ionic liquid electrolyte DSSCs.[26]

Transition metal based systems have also been explored as redox mediators, with DSSCs incorporating cobalt complexes exhibiting efficiencies of up to 8% in low intensity light.[27] Ferrocenes have also been investigated for this purpose however such systems have been shown to experience very high rates of recombination (k_5, Figure 5.1) as well as decomposition in the presence of common additives such as 4-*tert*-butylpyridine (4TBP). The rate of the unfavourable recombination reaction may be decreased by Atomic Layer Deposition (ALD) of alumina on the titanium dioxide surface, however multiple layers of alumina have been shown to slow electron injection (k_1).[28] As such, despite much research in the area, the I^-/I_3^- redox couple is still the most common system employed for liquid electrolytes.

The choice of electrolyte solvent also plays a role in determining the efficiency of a DSSC device. The main requirements for the solvent are that it should possess long term stability, low volatility and low viscosity (to ensure high diffusion coefficients for the redox couple). Organic solvents such as 3-methoxypropionitrile (MPN) have been shown to demonstrate good cell performances: the low volatility and high photostability of MPN, together with its low toxicity, make it a commonly used solvent.[29] In addition, the presence of imidazolium iodides have been shown to improve solar cell performance due to a variety of possible factors including the adsorption of imidazolium cations on to the titanium dioxide surface,[30,31] an increase in electron diffusion coefficient through the titanium dioxide and an increase in conductivity of the electrolyte.[32] Hence it is common to mix such imidazolium species with low viscosity, low volatility organic solvents such as MPN to create high performance robust electrolytes.[33,34] Ionic liquids are one class of material which also display low volatilities and high chemical and thermal stabilities, with imidazolium species being the most widely studied.[8] However their high viscosity has been shown to impede ion mobility and hence decrease cell performance.[35] One solution to this problem is the formation of eutectic mixtures to reduce melting points, creating 'solvent free electrolytes'.[36] Such mixtures are particularly attractive electrolytes for solar cells fabricated from flexible and lightweight plastics, since they do not contain organic solvents (which may permeate the walls of such devices).[37]

The concentration of lithium salts has been shown to have a strong influence on the performance of DSSCs. Lithium ions have been shown to adsorb (at low concentrations) or intercalate (at high concentrations) into the surface of the titanium dioxide layer and hence affect the energy of the conduction band,[38] shifting the potential towards more positive values by up to one volt (depending upon the ion concentration).[39,40] This behaviour was shown by Redmond and Fitzmaurice to be independent of the counter anion however, it has been suggested that the magnitude of this shift would be less dramatic for titanium dioxide films bearing dye sensitisers attached by carboxylic acid groups, due to the presence of protons from this anchor group. The shifts in the conduction band potential of titanium dioxide induced by lithium ions, makes electron injection from the sensitiser into the

conduction band more thermodynamically favourable.[41] This property is particularly useful for increasing the electron injection rate of sensitisers with excited state oxidation potentials close to the reduction potential of bare titanium dioxide. However the use of lithium ions to shift the conduction band of titanium dioxide reduces the open circuit voltage, hence a balance of these factors must be considered when optimising the efficiency of a DSSC device.[8]

Additives such as 4-*tert*-butylpyridine (4TBP) act to increase the open circuit voltage by shifting the conduction band of the titanium dioxide to higher energies. This may be achieved through the removal of coordinated protons due to the basicity of 4TBP, or by the displacement of cations such as lithium ions.[42] In addition, the electron lifetime significantly increases upon addition of 4TBP, corresponding to a decrease in the rate of the unfavourable recombination process k_5 (Figure 5.1). This is thought to be due to several factors such as steric blocking of the titanium dioxide by the bulky 4TBP groups, preventing the electrolyte from reaching the surface, and coordination of 4TBP to iodine in the electrolyte, reducing the concentration of free iodine. Since the unfavourable recombination reactions are faster for iodine than for triodide,[43] this may result in an increase in electron lifetime.[42]

Obviously a vital component of a DSSC is the dye sensitiser. The main structural factors governing the design of the dye to produce the greatest efficiencies have already been outlined in Section 1.2.6; further considerations surrounding the design of novel sensitisers for DSSC devices are now discussed.

5.2 Porphyrins as Sensitisers for Dye-Sensitised Solar Cells

5.2.1 Background

Since O'Regan and Grätzel published their seminal paper in 1991 detailing the construction of efficient dye-sensitised solar cells (DSSCs) based on a ruthenium complex sensitiser,[11] a great deal of intensive research has been carried out in order to explore new ruthenium-free organic chromophores capable of rivalling such dyes. As discussed in Section 1.2.6, these new compounds are expected to exhibit several properties which make them attractive

alternatives to ruthenium complexes including lower cost, simpler purification (and hence processability), and non-toxic nature. In addition, the optoelectronic properties of these organic chromophores may be tailored to meet the device requirements due to the high level of structural flexibility of organic systems. In order to produce organic dyes capable of efficient light harvesting, the design principles outlined in Section 1.2.6 must be considered.

Porphyrins are one class of compounds which has received much attention for application in the field of DSSCs.[44-47] Their similarity to the structure of chlorophyll, nature's highly efficient light harvester, makes these chromophores an obvious choice for such devices. In addition, porphyrins exhibit absorption of light across the UV-vis spectrum with high extinction coefficients, with values in the region of 10^5 M^{-1} cm^{-1} for a typical Soret band (around 400 — 500 nm) and 10^4 M^{-1} cm^{-1} for typical Q-bands (around 550 — 650 nm). The intensity and spectral shape of the porphyrin absorption spectrum may be tuned by peripheral modifications to the macrocycle (Section 1.3 and Chapter 2) or by coordination of a variety of metal ions in the central cavity. Many papers have been published regarding the use of porphyrins in DSSCs, with the efficiencies of these devices typically reported in the region of 5% — 7%. In contrast, devices based upon ruthenium complexes have consistently reached efficiencies of over 11%. However, recently Diau, Grätzel and co-workers have reported power conversion efficiencies of 10.06 and 11.00% for devices containing porphyrins conjugated to pyrene groups (**177**, Figure 5.4 (a))[48] and bearing donor-acceptor moieties (**178**, Figure 5.4 (b))[49] respectively, demonstrating that, by careful choice of peripheral substituents, porphyrins may yet offer a feasible alternative to ruthenium dyes.

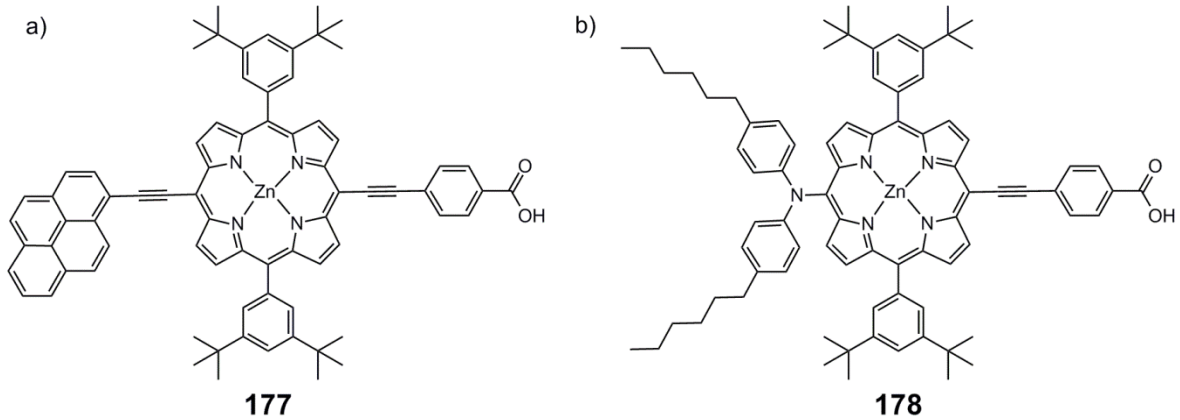

177 **178**

Figure 5.4: Porphyrin sensitisers for DSSCs demonstrating high power conversion efficiencies of 10.06% (**177**)[48] and 11.00% (**178**).[49]

One approach towards increasing the performance of porphyrin based DSSCs, is to elongate the π-system of the porphyrin. This may be achieved either by linking aromatic groups to the porphyrin by alkyne linkers or by direct fusion of the porphyrin ring periphery to aromatic units (Section 1.3.1). In the former case, the absorption spectrum is red-shifted, however the spectral shape remains similar to that of the unsubstituted porphyrin with distinct Soret and Q-bands, meaning that some regions of the visible spectrum still exhibit very low absorption. In the case of porphyrins fused to aromatic groups, the structural modifications result in a reduction in symmetry of the porphyrin core, hence provoking a dramatic distortion of the spectral shape, such that absorption may be both red-shifted and occur over a broad range of wavelengths. This facilitates the panchromatic absorption of light with strong absorption extending into the near-IR, where around 50% of solar radiation falls. Since J_{SC} depends upon the integration of the product of incident photon flux and the IPCE value for the cell over the range of wavelengths where light is absorbed, it may be expected that DSSCs incorporating such dyes will demonstrate enhanced cell performance.[8,15] The next section provides an overview of sensitisers based upon such fused-porphyrin chromophores and examines the efficiency of the resulting DSSC devices.

5.2.2 Fused Porphyrins for Dye-Sensitised Solar Cells

As discussed in Chapter 2, the fusion of aromatic moieties to a porphyrin core is an area of research which has gained much attention in recent years. However, while a wide variety of fused porphyrin systems are now accessible, few have been tested in DSSC devices.

Imahori and co-workers were the first to explore the use of porphyrins fused to aromatic units as sensitisers for dye-sensitised solar cells, with naphthalene-fused porphyrins (Figure 5.5).[50,51] Porphyrins **46**, **48**, **179** and **180** all bear bulky 2,4,6-trimethylphenyl groups in order to reduce aggregation and hence limit self-quenching processes. In addition, all of these dyes bear carboxylic acid anchor groups to allow them to attach to the metal oxide surface (titanium dioxide in these studies). As shown in Scheme 2.5, fusion of a naphthalene unit to a porphyrin to create fused porphyrin **48**, results in a red-shift in the absorption spectrum of around 130 nm compared to the unfused precursor,

with longest wavelength absorption maxima extending to 682 nm. In addition to exhibiting a red-shift, the absorption peaks broaden and absorption in the Q-band region increases in intensity relative to that in the Soret band region.

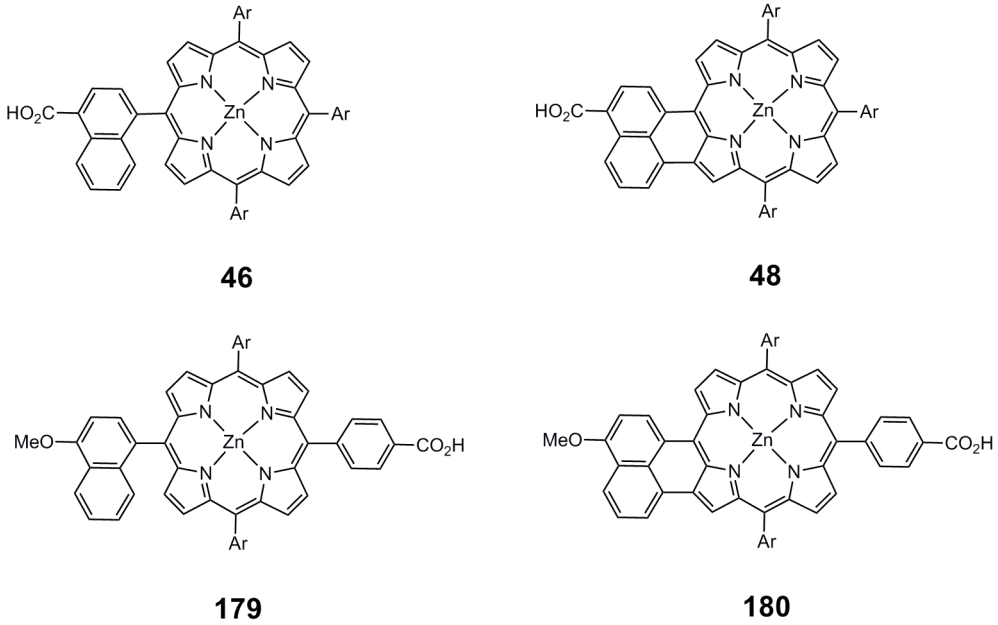

Figure 5.5: Naphthalene-fused porphyrins tested by Imahori and co-workers in photovoltaic devices.[50,51]

When incorporated in DSSC devices, fused porphyrin **48** gave the highest solar-to-electrical energy conversion efficiency, η, of 4.1%; the efficiency of the unfused analogue (**46**) in contrast was found to be 2.8%. The greater efficiency observed for **48** is believed to be due to the increase in J_{SC} from 6.7 mA cm^{-2} to 10.6 mA cm^{-2} upon fusion (V_{OC} values are similar for both dyes). However, the maximum IPCE value for **48** is lower than for **46** (55% and 59% respectively). It has been suggested that the greater strain present in **48** (due to the steric clash between the β-pyrrolic hydrogen of the porphyrin ring and the hydrogen of the naphthyl group) could accelerate nonradiative relaxation processes of the excited state, thereby decreasing the quantum yield of charge injection.[51] These factors are partially counteracted by the increased electronic coupling between the dye and the titanium dioxide layer for porphyrin **48** compared to **46** (due to the greater electron density localised on the carboxylic acid anchor group in the LUMO of **48** compared to **46**, as shown by DFT calculations). Combined with the improved light harvesting abilities of the fused dye, (due to absorption over a wider range of wavelengths) a large increase in J_{SC} and hence η is

observed for **48**. Naphthalene-fused porphyrin **180** displays an absorption spectrum which is very similar to that of **48**, however it was found to exhibit an η of 1.1%; unfused porphyrin **179** in contrast, exhibits an η of 3.4%. The lower efficiency of fused porphyrin **180** compared to its unfused analogue is attributed to the smaller localisation of electron density near the anchor group in the LUMO of **180** compared to **179**, resulting in poorer electronic coupling between the porphyrin and the titanium dioxide. However, unfused porphyrin **46**, with its higher efficiency, exhibits very similar electron densities to fused porphyrin **180** on the anchor group in the LUMO, suggesting that other factors must also contribute to the surprisingly low efficiency of fused porphyrin **180**, such as increased aggregation and fast relaxation of excited states. It may therefore be concluded that π-extended porphyrins with a planar geometry, high extinction coefficients and bulky peripheral substituents (to limit aggregation) would give rise to larger η values.

Quinoxaline-fused porphyrins have also been investigated by Imahori and co-workers as dyes for photovoltaic devices (Figure 5.6).[52-54]

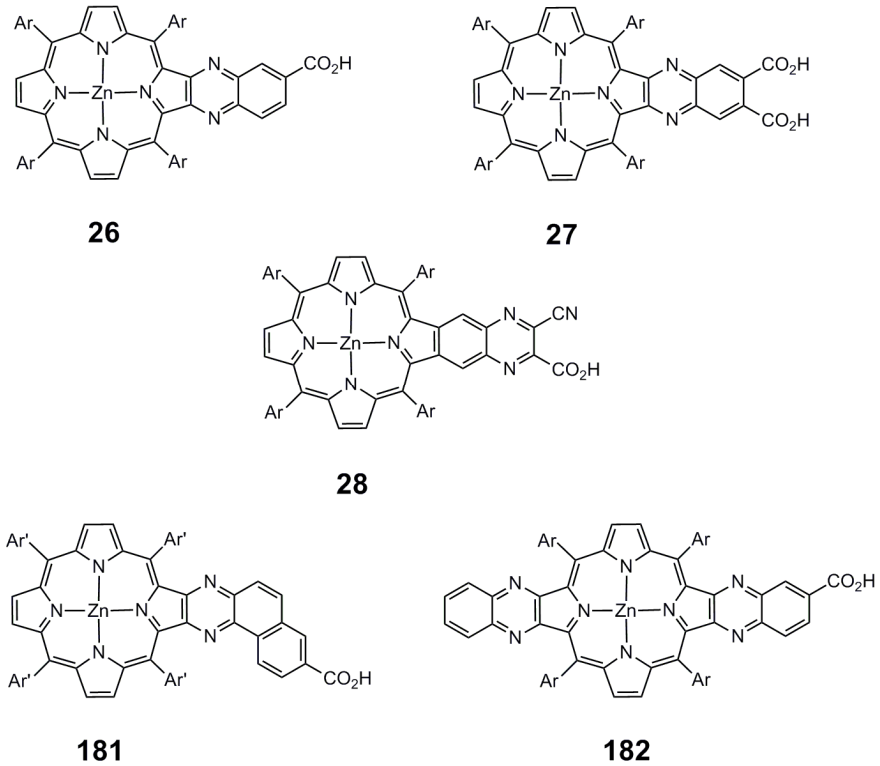

Figure 5.6: Quinoxaline-fused porphyrin systems tested by Imahori and co-workers in DSSC devices.[52-54] Ar = 2,4,6-trimethylphenyl, Ar' = 3,5-di(*t*-butyl)phenyl.

Comparison of the performance of porphyrins **26** and **27** in DSSC devices shows that **26** gives rise to a higher efficiency (η = 5.2%) than **27** (η = 4.0%). Given the strong similarities between the absorption spectra of these two dyes, and the comparable surface coverages, the difference in efficiencies is believed to be due to lower φ_{inj} and η_c values for **27**.[52] This view is supported by DFT calculations which reveal that the electron density on the carboxylic acid linker groups of **27** is smaller than for **26**, indicating a poorer degree of electronic coupling between the titanium dioxide surface and the dye and hence lowering φ_{inj}. Furthermore, from measuring the current-voltage curve under dark conditions, it appears that **27** exhibits a higher degree of charge recombination than **26**.[52] This negative effect is compensated to some degree by the increased favourability of charge injection, due to proton binding at the titanium dioxide surface which lowers the energy of the conduction band. As **27** has twice the number of acidic protons as **26**, the conduction band of titanium dioxide may be expected to lie at lower energies for a device incorporating **27** compared to one incorporating **26**, hence favouring charge injection.[52]

In order to induce broader peaks in the absorption spectra of quinoxaline-fused porphyrins, unsymmetrical dyes **181** and **28** were synthesised by Imahori and co-workers.[53] In addition, the cyano group of porphyrin **28** was expected to increase electron density on the anchor group in the LUMO, thereby facilitating electron injection from the dye into the conduction band of the titanium dioxide. These dyes were co-adsorbed onto the titanium dioxide surface with chenodeoxycholic acid (CDCA) which is known to decrease aggregation between dye molecules. Under these conditions it was found that porphyrin **181** gave rise to η = 5.1%, while porphyrin **28** exhibited η = 0.8%. As a reference, porphyrin **26** was found to give η = 6.3% under these conditions. It is suggested that the lower efficiency of **181** compared to **26** may be due to slightly smaller electron densities on the anchor group in the LUMO. However, porphyrin **28** has been shown to exhibit large electron densities on the carboxylic acid group in the LUMO yet still exhibits a very low η value. This has been rationalised by the short fluorescence lifetime of **28** (decreasing the value of φ_{inj}), and the tilted orientation of the dye relative to the titanium dioxide surface (due to coordination of

both the carboxyl group and the adjacent nitrogen atom). Coordination of pyrazine molecules is expected to raise the energy of the titanium dioxide conduction band, resulting in a large V_{OC}. The observation that porphyrin **28** in fact displays a modest V_{OC} of 0.51 V, may be due to several factors including the tilted packing arrangement of **28** which decreases the distance between the titanium dioxide and the dye, possibly facilitating rapid charge recombination between electrons in the conduction band and the cation of the porphyrin. Furthermore, **28** has been shown to exhibit a larger dark current than **181** and **26**, again possibly due to this packing arrangement which allows a closer approach of the electrolyte to the titanium dioxide surface.

Bis-quinoxaline fused porphyrin **182** exhibits red-shifted absorption relative to the other porphyrins shown in Figure 5.6 indicating improved light harvesting capabilities. The DSSC device incorporating **182** with coadsorbed CDCA was found to give η = 4.7%, i.e. a lower efficiency than observed for porphyrin **26**.[54] The high light harvesting efficiency of porphyrin **182** suggests that the smaller J_{SC} and V_{OC} values observed (compared to porphyrin **26**) arise from a lower electron injection quantum yield and/or lower charge collection efficiency. It has been proposed that a lower value of φ_{inj} may arise from slightly weaker coupling between the carboxylic acid anchor group and the titanium dioxide, although alternatively the potentially more tilted packing of **182** compared to **26** may result in faster charge recombination between electrons in the conduction band and dye cation. In addition, **182** exhibits a slightly larger dark current than **26** which may be expected to negatively affect η_c values and result in a smaller V_{OC}.[54] The results of these studies into quinoxaline-fused porphyrins suggest that many factors compete to affect the efficiency of a DSSC and that the magnitude of such influences is difficult to predict from structural considerations.

Imahori and co-workers have also investigated aryl-fused porphyrin **183** as a sensitiser for DSSC devices (Figure 5.7). This porphyrin exhibits a broader, red-shifted Soret band relative to the unfused precursor **184**, as well as weak absorption extending to nearly 800 nm.[55]

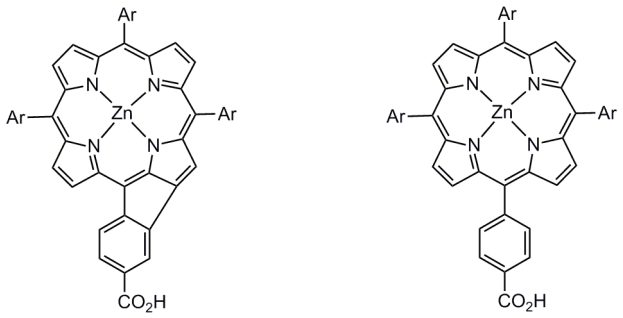

183 **184**

Figure 5.7: Aryl-linked (**184**) and aryl-fused (**183**) porphyrins synthesised by Imahori and co-workers for application in DSSC devices.[55] Ar = 2,4,6-trimethylphenyl.

However despite the better light harvesting capabilities of porphyrin **183**, the efficiency of a DSSC device incorporating this dye is lower than observed for those using unfused porphyrin **184** with η = 0.3% for **183** and 4.6% for **184**. The surprisingly low efficiency observed for porphyrin **183** has been shown to be due to very low IPCE values, however the explanation for such poor photocurrent generation is unclear. It has been suggested that reduced electron injection into the titanium dioxide conduction band may account for such observations, however the energy level of the excited state of porphyrin **183** has been shown to sit 1.9 eV higher in energy than the conduction band of the titanium dioxide, indicating that electron injection is thermodynamically feasible.

Yeh and co-workers have recently investigated the use of diporphyrins in DSSC devices including fused and acetylene linked dimers **185**, **186** and **187** (Figure 5.8).[56] These dyes all exhibit absorption into the near-IR with longest wavelength λ_{max} values at 753, 845 and 1169 nm respectively.

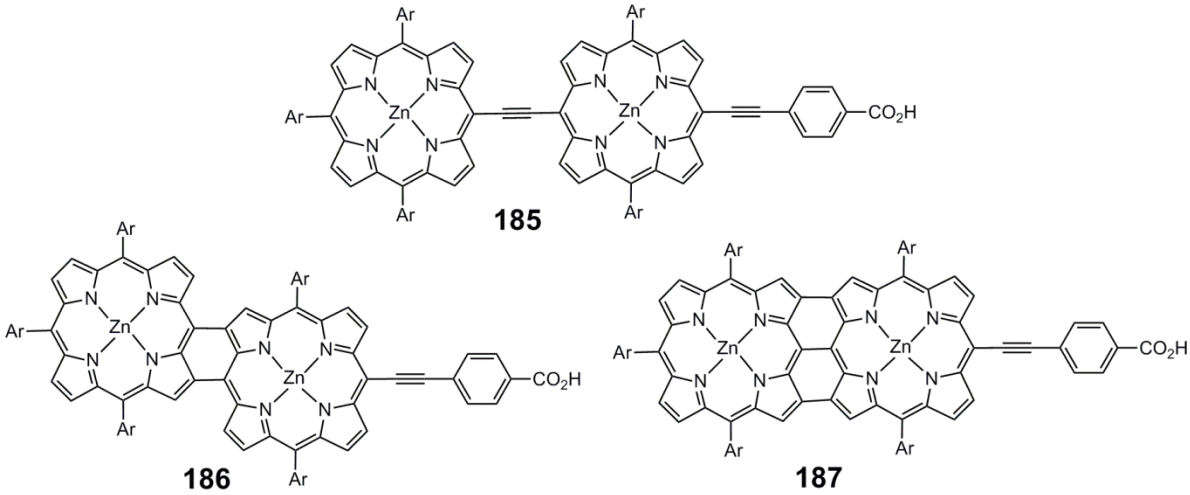

Figure 5.8: Diporphyrins synthesised by Yeh and co-workers for use in DSSC devices.[56]
Ar = 3,5-di(*t*-butyl)phenyl.

Investigations into DSSC devices incorporating these dyes show that porphyrin **185** gives rise to an efficiency of 4.1% which is similar to values reported by Officer and co-workers for porphyrin dimer **188** (3.8%) and by Kim and co-workers for **189** (4.2%) (Figure 5.9).

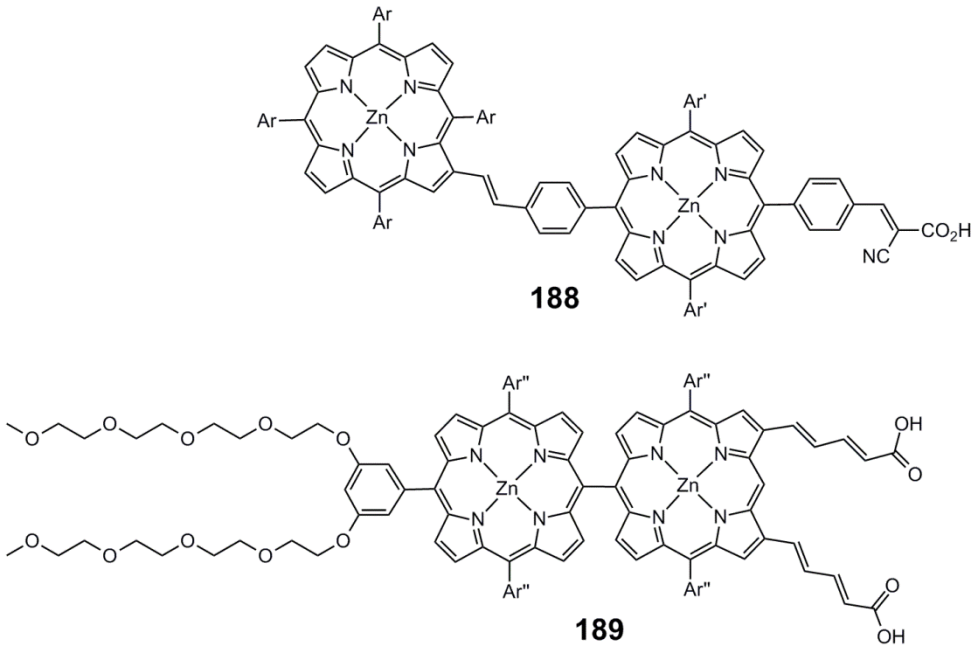

Figure 5.9: Dimers synthesised by Officer and co-workers (**188**) and Kim and co-workers (**189**). Ar = 3,5-dimethylphenyl, Ar' = 4-methylphenyl, Ar" = 3,5-di(*t*-butyl)phenyl.[57,58]

In contrast it was not possible to obtain efficiencies for devices containing fused porphyrins **186** and **187** due to their exceedingly low efficiencies of conversion of incident

photons to current.[56] Investigation of the electrochemistry of **186** and **187** revealed excited state energy levels at -0.53 and -0.32 eV respectively (versus the Normal Hydrogen Electrode, NHE) compared to the TiO_2 conduction band energy of -0.5 eV, implying that ineffective electron injection into the conduction band of the titanium dioxide is likely to be the reason for the poor IPCE values. The fact that only tiny IPCE values were observed in the visible region for porphyrins **186** and **187** suggests that relaxation of higher excited states to lower excited states competes with electron injection from these higher energy states.[56] It should be noted however that these investigations were carried out with titanium dioxide fulfilling the role of the metal oxide and with an electrolyte composed of lithium iodide (0.1 M), iodine (0.05 M), 1-propyl-3-methylimidazolium iodide (0.6 M) and 4TBP (0.5 M) in a solvent mixture containing acetonitrile and valeronitrile (volume ratio 1:1). It may be possible to obtain larger IPCE values for porphyrins **186** and **187** if the metal oxide were replaced with tin oxide as this has a lower energy conduction band. Alternatively, altering the electrolyte composition could result in high IPCE values, since 4TBP is known to raise the energy of the titanium dioxide conduction band. Electrolytes without 4TBP and with a high concentration of lithium iodide (in the region of 2.0 M) have been shown to facilitate good IPCE values for osmium and ruthenium complexes which exhibit thermodynamically unfavourable charge injection due to low lying excited state energy levels.[59] Hence the use of a lithium iodide rich electrolyte could lower the energy of the titanium dioxide conduction band sufficiently as to enable charge injection.

Finally, very recently perylene anhydride fused porphyrins have been investigated as sensitisers for DSSC devices by Wu and co-workers (Figure 5.10).[60]

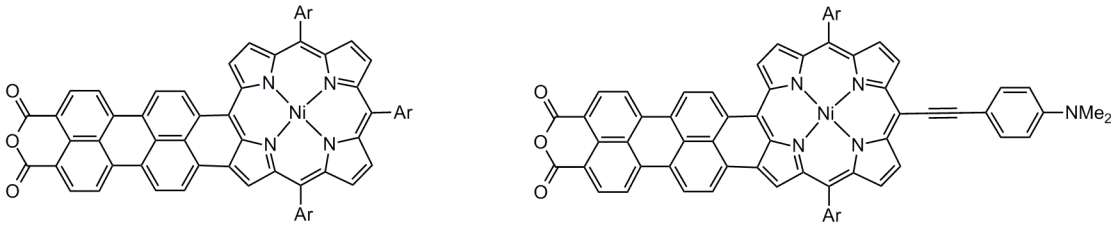

190 **191**

Figure 5.10: Perylene fused porphyrins synthesised by Wu and co-workers.[60] Ar = 3,5-di(*t*-butyl)phenyl.

These dyes exhibit strong absorption in the near-IR with longest wavelength maxima at 805 and 847 nm for porphyrins **190** and **191** respectively, with porphyrin **191** showing absorption to around 1000 nm. Calculations of the excited state energy levels of **190** and **191** show that they are of a similar energy to that of the conduction band of titanium dioxide, implying that charge injection may be inefficient. However, both **190** and **191** give IPCE values over a wide spectral range, with highest efficiencies around 30%. In addition porphyrin **191** exhibits an IPCE response to nearly 1000 nm, which is one of the furthest near-IR responses observed for ruthenium-free dyes. The overall solar-to-electrical energy conversion efficiencies of these devices were found to be 1.26% for porphyrin **190** and 1.36% for porphyrin **191**. The larger efficiency for porphyrin **191** compared to **190**, is likely to be due to its increased π-conjugation (arising from the presence of a conjugated amino group), resulting in a more red-shifted absorption spectrum and hence a larger light harvesting efficiency. The performance of these dyes could be optimised by increasing the lifetimes of their excited states by coordination of a different metal ion such as zinc. In addition there is evidence to suggest that these dyes experience aggregation in solution (as shown by their broad ^{1}H NMR spectra) which may result in quenching of the excited states. Hence it may be necessary to introduce bulky substituents to the perylene moiety to reduce this aggregation and improve device performance.

5.3 Anthracene-Fused Porphyrins for Dye-Sensitised Solar Cells

From the discussion above, it can be seen that fused porphyrins show promise as panchromatic dyes for DSSC devices. While the efficiencies of cells incorporating these sensitisers show a wide range of values, and undoubtedly require optimisation through careful choice of metal oxide, electrolyte and numerous other parameters, their ability to harvest light into the near-IR is an important development in solar cell technology.

Porphyrins fused to a single anthracene unit have been shown to exhibit strong absorption into the near-IR (Figures 2.12 and 3.10), with an absorption spectrum which correlates well to the AM 1.5 G solar radiation spectrum (Figure 5.3). As such, modification

of this chromophore to enable binding of the molecule to a metal oxide surface could be expected to yield a sensitiser capable of efficient light harvesting across the whole visible region and into the near-IR. The molecular design of such an anthracene-fused porphyrin is now discussed.

5.3.1 Molecular Design

The synthetic targets for this new class of sensitiser for DSSC devices are shown in Figure 5.11.

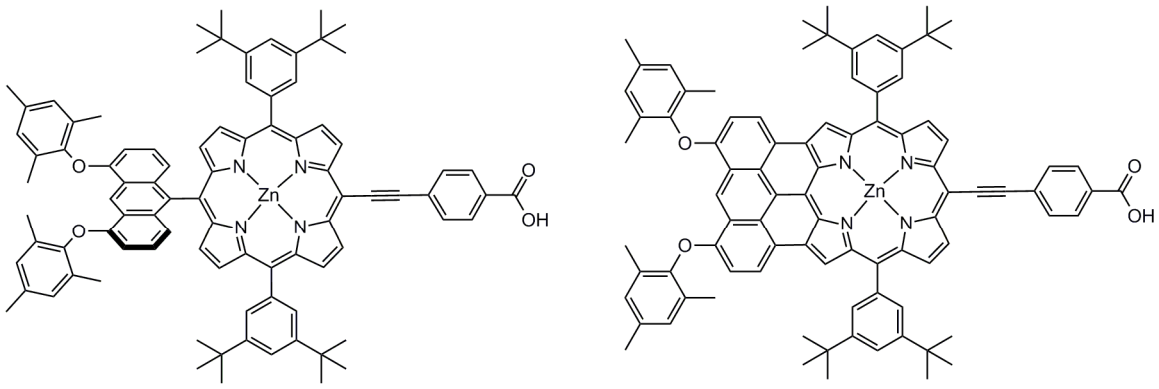

192 **193**

Figure 5.11: Molecular structures of the proposed anthracene-porphyrin sensitisers for DSSC devices.

In order to meet the sensitiser requirements outlined in Section 1.2.6, several features have been included into the molecular design of these anthracene-porphyrin dyes.

First, fusion of an anthracene unit to the porphyrin core to yield anthracene-fused porphyrins elongates the π-system and is expected to result in broad, intense absorption across the visible and near-IR regions. In order to investigate the effect of this expansion of the π-system on DSSC performance, fused porphyrin **193** was proposed as the target compound and unfused anthracene-porphyrin **192** was proposed as a reference dye.

Second, in order to facilitate charge injection into the metal oxide conduction band, and to reduce charge recombination between this metal oxide and the dye cation, the HOMO energy level of the dye should be localised away from the surface at which the dye is bound. In addition, the LUMO level should be spatially close to the metal oxide surface.[61] In order to achieve these requirements, the anthracene moiety of **192** and **193** was designed to bear

electron rich aryl ether groups. These are expected to increase the electron density on the anthracene units in the HOMOs of the two dyes, while the electron withdrawing nature of the carboxylic acid group may be expected to increase its electron density in the LUMO of the two dyes.

The tendency for porphyrins to aggregate through π-stacking interactions is well known and can result in decreased efficiencies, when these dyes are incorporated into DSSC devices, due to self-quenching processes.[62,63] Cell efficiency may be improved by co-adsorption of the bulky acid CDCA which acts to disperse the porphyrin monomers across the surface of the metal oxide, however this limits the degree of dye coverage which may be achieved.[63] Other solutions to the problem of aggregation include the use of a ligating species such as pyridine in the electrolyte which may coordinate to the metal centre of the porphyrin and hence block the face of the macrocycle towards π-stacking interactions.[64] Use of these additives, while limiting aggregation, may however affect many other components of the DSSC device, for example adsorption of CDCA on to the metal oxide surface is known to influence the energy level of the conduction band. An alternative to these approaches is to design the dye itself to bear sterically bulky peripheral substituents. Following this approach, porphyrins **192** and **193** were designed to bear bulky 2,4,6-trimethylphenoxy groups on the anthracene units, and 3,5-di(*t*-butyl)phenyl substituents on the porphyrin periphery. From the work carried out on bis-anthracene and tetra-anthracene fused porphyrins (Chapters 3 and 4), these substituents have been found to be successful in limiting the effects of aggregation for such systems.

In addition to preventing aggregation, these aryl substituents are also very hydrophobic and hence may be expected to improve the stability of the DSSC devices by preventing traces of water from approaching the anchor group of the dye (a common cause of dye desorption).[61]

It is possible for the porphyrin macrocycle to bind to a variety of metal ions, however zinc was chosen to sit in the central cavity of porphyrins **192** and **193** as zinc porphyrins are known to have long-lived singlet excited states (> 1 ns). In addition, these excited states are

often higher in energy than those of the free-base porphyrin, resulting in faster electron injection kinetics.[44,65]

It has been shown that conjugated linker groups result in higher DSSC efficiencies for both porphyrin and phthalocyanine sensitisers, than insulating linker groups.[65-67] Ethyne bridges facilitate a coplanar arrangement of two aromatic groups, due to a decrease in the steric effects, and enable efficient conjugation between them. As such, ethyne bridges have been shown to facilitate strong electronic communication between directly linked porphyrin macrocycles, and between porphyrins and other aromatic groups.[68-70] As a result, the commonly used phenylethynyl group was chosen to link the porphyrin macrocycle to the anchor group.

Carboxylic acid groups are widely used as binding groups for sensitisers due to their ability to form strong linkages to the metal oxide surface. Several binding modes have been suggested for the interaction between titanium dioxide and carboxylic acid groups, including the formation of ester linkages, hydrogen bonding, and bridging (involving both oxygen atoms of the carboxyl group).[67,71-74] In addition, carboxylic acids promote strong electronic coupling between the excited state of the dye and the titanium dioxide.[67] While other anchor groups such as sulfonic and phosphonic acids may be expected to exhibit superior binding due to their greater acidity, these groups have been shown to give rise to lower efficiencies, suggesting that electronic coupling is the more important factor in determining cell performance.[67] In addition, it is thought that single carboxylic acid groups favour perpendicular binding of the porphyrin to the titanium dioxide surface (rather than lying flat in a horizontal fashion). This allows good surface coverage of the dye, thereby enhancing the light harvesting properties of the system. As a result of the factors discussed above, porphyrins **192** and **193** were designed to bear carboxylic acid anchor groups to facilitate strong binding and good electronic coupling to the metal oxide surface of the DSSC devices.

During their work on naphthalene-fused porphyrins for DSSC devices, Imahori and co-workers suggested that cell performance for porphyrins **48** and **180** was limited by accelerated nonradiative relaxation of the excited state of the porphyrin, due to the strain induced by interactions between the naphthalene and the porphyrin ring.[50,51] It was

proposed that cell performance could therefore be improved by employing porphyrin sensitisers with extended π-conjugation and a planar geometry. Porphyrin **193** possesses these properties, hence it may be considered likely that this porphyrin will show superior cell performance to naphthalene-fused porphyrins.

In order to establish whether electron injection and dye regeneration are thermodynamically favourable, it is necessary to investigate the optoelectronic properties of the target porphyrins as it is not possible to predict the energy levels of such systems from values found for similar structures, due to subtle effects such as those exerted by differences in the central metal ion and peripheral substituents.

5.3.2 Synthesis of Anthracene-Porphyrins for DSSC Devices

The initial synthetic approach towards porphyrins **192** and **193** is shown in Scheme 5.1. Anthracene-linked porphyrin **130** was synthesised by a Suzuki coupling reaction, as shown in Scheme 3.27. Bromination of this anthracene-porphyrin was carried out with a slight excess of NBS and was found to give porphyrin **194** as the only product in 95% yield. Fusion of an anthracene moiety to the porphyrin core has been shown to occur in the presence of either scandium(III) triflate and DDQ or iron(III) chloride (Chapters 3 and 4). However, iron(III) chloride induces demetalation of zinc porphyrins during the fusion reaction, creating unfused free-base anthracene-linked porphyrins which are not able to undergo fusion. Hence it was decided to employ the milder scandium(III) triflate and DDQ conditions in the synthesis of anthracene-fused porphyrin **196**.

When subjected to these fusion conditions in dry solvents, anthracene-linked porphyrin **194** showed no reaction after 30 minutes according to TLC monitoring, an observation confirmed by UV-vis spectroscopy. The reaction was then heated to 35 °C for a further 30 minutes, however UV-vis spectroscopy of this mixture did not reveal the presence of any anthracene-fused products. This surprising result may be due to the electron withdrawing inductive effect of the bromine atom attached to the porphyrin, which may deactivate the ring towards fusion under these conditions, thereby favouring other undesired reactions.

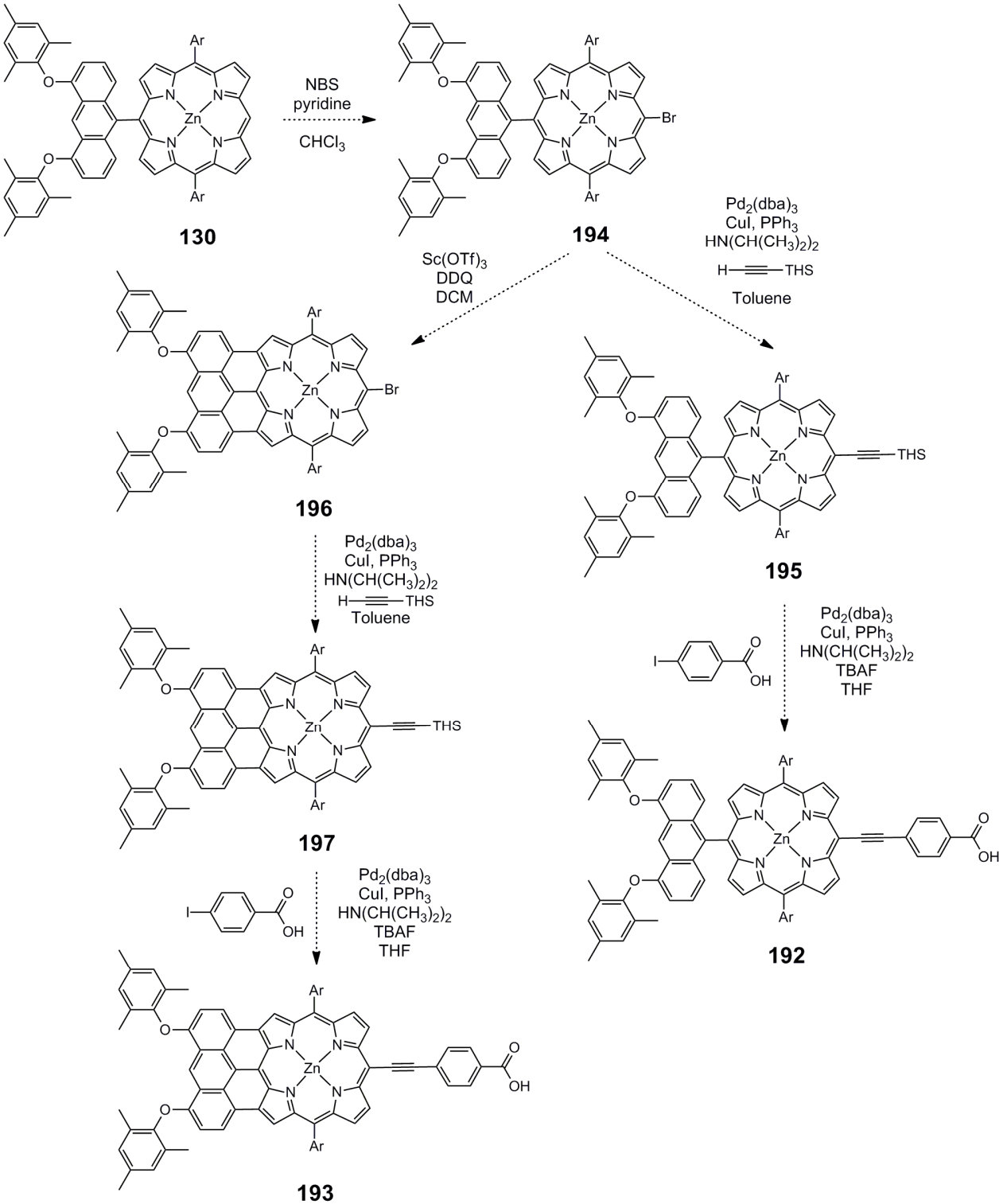

Scheme 5.1: Proposed route for the synthesis of anthracene-porphyrins **192** and **193**.
Ar = 3.5-di(*t*-butyl)phenyl.

I decided to employ the stronger oxidant iron(III) chloride in order to form anthracene-fused porphyrin **196**. When subjected to this reagent in dry solvents, porphyrin

194 was shown by TLC to be consumed and two products were formed. UV-vis-NIR spectroscopy of the crude mixture of products showed the presence of absorption in the near-IR, suggesting the formation of a fused product. MALDI-TOF mass spectrometry confirmed that the mixture contained the desired fused porphyrin **196** together with demetalated **194**. Unfortunately, while it was possible to remove the free-base porphyrin by silica gel chromatography, the low solubility of porphyrin **196**, together with its tendency to adsorb on silica gel, led to many difficulties in purification. It was impossible to isolate a pure sample of porphyrin **196**.

It was thought that further purification of these products may be achieved after carrying out the in situ deprotection and Sonogashira coupling reaction with trihexylsilylacetylene (THS acetylene) to form **197**, since this product was expected to be far more soluble. Unfortunately, subjection of impure porphyrin **196** to this palladium-catalysed coupling reaction led to the observation of unreacted starting material, together with mixture of unidentifiable products of similar polarity. As a result, it was impossible to separate the components of the mixture. It seems likely that the low solubility of porphyrin **196** may limit its reactivity, although it is possible that the electronic influence of the fused anthracene moiety also affects the reactivity of the brominated *meso*-position.

In order to circumvent these problems, I decided to re-design the synthetic pathway to anthracene-porphyrins **192** and **193** by first synthesising THS acetylene-porphyrin **195** and then attempting the fusion reaction. The synthesis of porphyrin **195** was carried out by Sonogashira coupling as described in Scheme 5.1. After three hours, TLC showed the reaction to have reached completion and silica-gel chromatography of the crude reaction mixture afforded the desired acetylene-linked porphyrin **195** in 56% yield.

Fusion of **195** was initially attempted with scandium(III) triflate and DDQ (Scheme 5.2), as the use of iron(III) chloride could induce unfavourable reactions at the triple bond, as well as inducing demetalation of the porphyrin core.

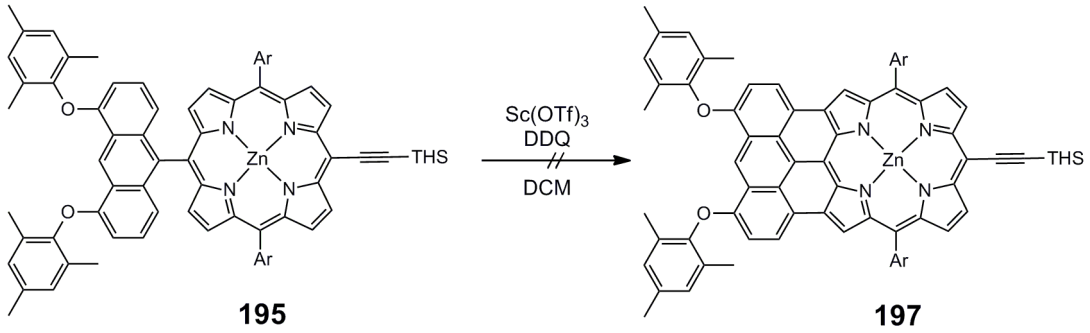

Scheme 5.2: Attempted synthesis of anthracene-fused porphyrin **197** using $Sc(OTf)_3$ and DDQ. Ar = 3.5-di(*t*-butyl)phenyl.

Porphyrin **195** was subjected to these reaction conditions at room temperature, however TLC of the reaction mixture after an hour showed little consumption of the starting material. The mixture was heated to reflux in order to force the fusion reaction, however TLC showed that these conditions resulted in only partial consumption of the starting material, together with the formation of material which adhered to the baseline of the TLC plate. UV-vis-NIR spectroscopy of this crude reaction mixture did not reveal the presence of any of the desired, fused, product hence purification of this mixture was not attempted.

Fusion of porphyrin **195** was then attempted with iron(III) chloride (Scheme 5.3) and the extent of the reaction was monitored by TLC.

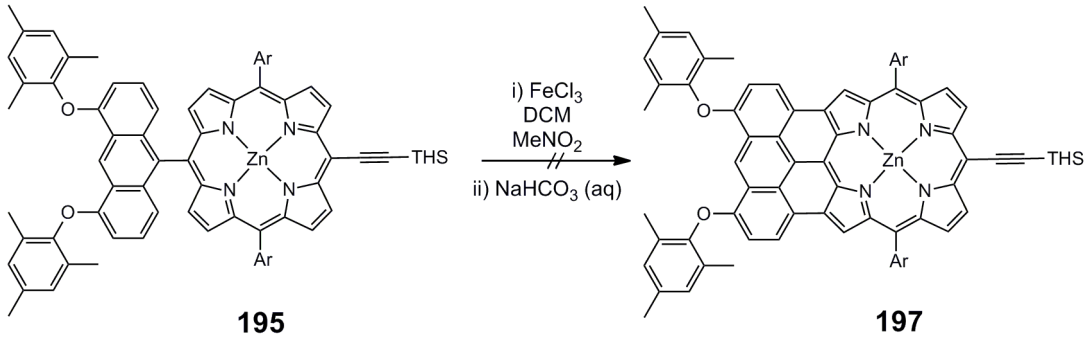

Scheme 5.3: Attempted fusion of anthracene-porphyrin **195** with $FeCl_3$. Ar = 3.5-di(*t*-butyl)phenyl.

After 30 minutes porphyrin **195** was totally consumed and several products were observed, the major component of which was thought to be demetalated **195**. MALDI-TOF mass spectrometry confirmed that the crude reaction mixture contained demetalated **195**, together with a large mixture of products at much higher molecular weights, including a peak corresponding to bis-acetylene linked dimer **198** (Figure 5.12). No peak corresponding

to the desired anthracene-fused porphyrin **197** was observed, hence separation of this reaction mixture was not attempted.

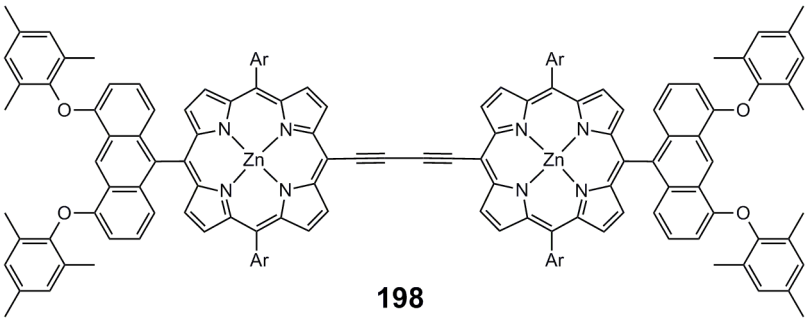

Figure 5.12: Acetylene-linked dimer **198** observed by MADLI-TOF mass spectrometry as a by-product of the fusion reaction shown in Scheme 5.3. Ar = 3.5-di(*t*-butyl)phenyl.

The problems encountered in the fusion of **195** to form **197** may be due to the lability of the trihexylsilyl (THS) group protecting the triple bond. Hence I decided to employ the triisopropylsilyl (TIPS) group as a protecting unit, since its increased steric bulk renders this group more robust.

Porphyrin **194** and triisopropylsilylacetylene were subjected to Sonogashira coupling conditions as shown in Scheme 5.4. TLC of the reaction mixture showed the formation of one major product; this mixture was purified by silica gel chromatography to give porphyrin **199** in 82% yield.

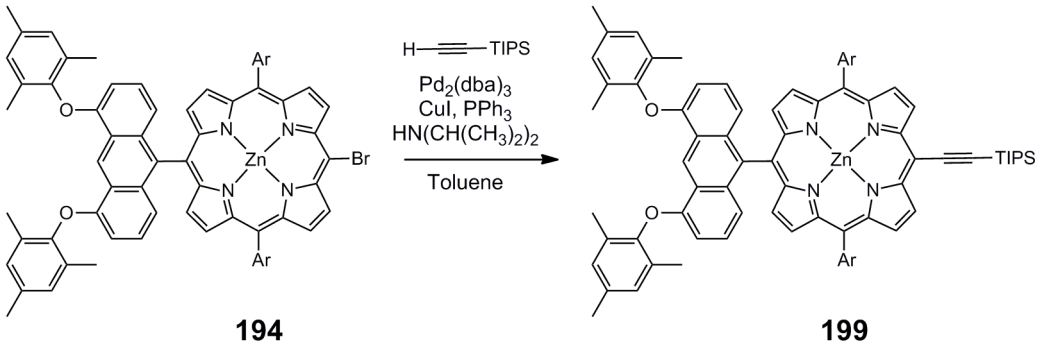

Scheme 5.4: Sonogashira coupling to form TIPS protected porphyrin **199**. Ar = 3.5-di(*t*-butyl)phenyl.

Given that subjection of THS protected porphyrin **195** with scandium(III) triflate and DDQ led to little reaction of the starting material, I decided to attempt the fusion of TIPS protected porphyrin **199** with the stronger oxidant iron(III) chloride (Scheme 5.5).

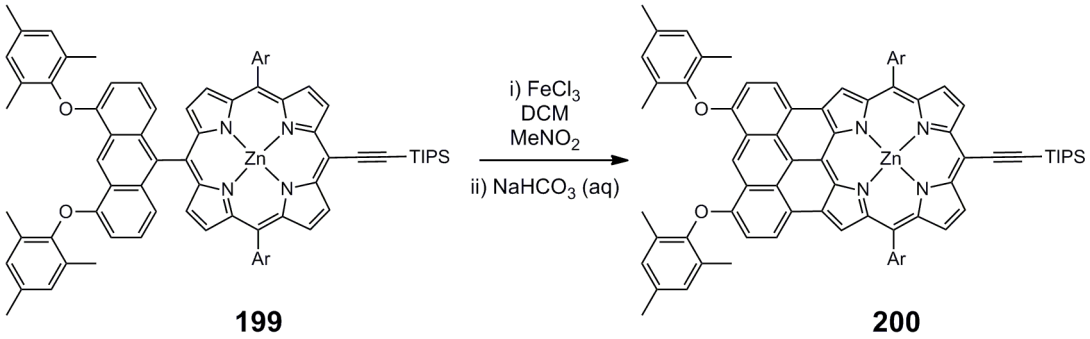

Scheme 5.5: Fusion of TIPS protected porphyrin **199** with $FeCl_3$ to form anthracene-fused porphyrin **200**. Ar = 3.5-di(*t*-butyl)phenyl.

After stirring **199** with iron(III) chloride for 30 minutes, TLC of the reaction mixture showed consumption of the starting material and the formation of demetalated **199**, together with two purple products of similar polarity which only moved from the baseline in the presence of pyridine. Addition of further iron(III) chloride did not result in the consumption of the free-base porphyrin, confirming that only metalated porphyrins are capable of undergoing fusion to an anthracene unit. UV-vis-NIR spectroscopy of the crude reaction mixture showed strong absorption corresponding to a free-base porphyrin, together with weaker absorption in the region of 800 nm, corresponding to the formation of anthracene-fused porphyrin products. Separation of the reaction mixture by silica gel chromatography proved difficult due to the very similar polarities of the fused products. It seemed likely that these products were a mixture of the desired porphyrin **200** and its free-base analogue (formed by demetalation after fusion).

The difficulty in separating the fused products, together with the fact that it is not possible to fuse an anthracene unit to the periphery of a free-base porphyrin, made it necessary to reduce the degree of demetalation encountered in this fusion reaction. In order to achieve this goal, 20 equivalents of anhydrous zinc(II) chloride were introduced into the reaction mixture in expectation that any free-base porphyrins formed during the reaction would undergo zinc re-insertion in situ. Upon carrying out this reaction however, the same mixture of products was observed as was found in the absence of anhydrous zinc(II) chloride, perhaps due to protonation of the free-base porphyrins by hydrochloric acid, produced by

partial hydrolysis of iron(III) chloride during the fusion reaction. Hence a new approach to the fusion of porphyrin **199** was developed.

In order to force the fusion of **199** towards the desired product **200**, porphyrin **199** was subjected to ten equivalents of iron(III) chloride and 50 equivalents of anhydrous zinc(II) chloride, and stirred for 30 minutes. This resulted in the observation of a mixture of products by TLC. After this time, ten equivalents of 'proton sponge' (1,8-bis(dimethylamino)naphthalene) were added (in order to neutralise any acid present, and facilitate zinc insertion) and the reaction mixture was stirred for a further 30 minutes. TLC of the reaction mixture after addition of this base showed the presence of only two species, one of which was identified as the unfused zinc porphyrin **199** while the other was shown by UV-vis-NIR spectroscopy to be a fused porphyrin. A further ten equivalents of iron(III) chloride were added to the reaction mixture and the cycle was repeated for a second and third time. After the third addition of proton sponge, TLC showed the presence of one major product (thought to be the desired anthracene-fused porphyrin **200**) together with some unreacted starting material. Silica gel chromatography of this mixture proved successful, giving zinc porphyrin **200** in 63% yield.

Synthesis of the fused target product **193** was initially attempted by an in situ deprotection and coupling reaction (Scheme 5.6). Such a one-pot procedure reduces the concentration of deprotected acetylene groups present in the reaction mixture at any given time, thereby reducing the extent of side reactions, such as homo-coupling.

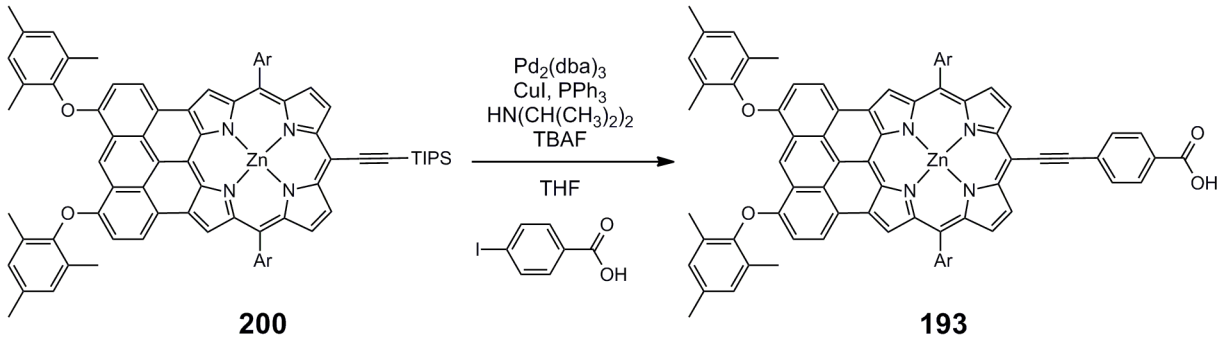

Scheme 5.6: In situ deprotection and coupling reaction to form anthracene-fused porphyrin **193**. Ar = 3.5-di(*t*-butyl)phenyl.

These conditions resulted in the consumption of porphyrin **200** and the formation of several polar products. Silica gel chromatography of the reaction mixture proved difficult due to the tendency for the products to adsorb onto the silica. Increasing the percentage of methanol in the eluent reduced the extent of this problem, but in doing so it became impossible to separate the porphyrinic products from each other and from unreacted 4-iodobenzoic acid.

In order to avoid such purification problems, I decided to attempt the in situ deprotection and coupling reaction with a 4-iodobenzoic ester. Methyl-4-iodobenzoate (**202**) was prepared in 87% yield from 4-iodobenzoic acid (**201**) following a standard literature procedure (Scheme 5.7).[75]

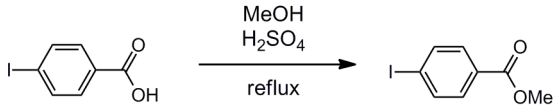

201 **202**

Scheme 5.7: Synthesis of methyl-4-iodobenzoate (**202**) from 4-iodobenzoic acid (**201**).

Coupling of anthracene-fused porphyrin **200** with ester **202** proceeded under the conditions shown in Scheme 5.6, to give anthracene-fused porphyrin **203** in 83% yield after purification (Figure 5.13 (a)). An analogous coupling reaction was carried out between unfused anthracene-linked porphyrin **199** and ester **202** to give anthracene-linked porphyrin **204** in 74% isolated yield (Figure 5.13 (b)). As expected, purification of these porphyrins was achieved by silica gel chromatography without encountering problems of adsorption and low solubility.

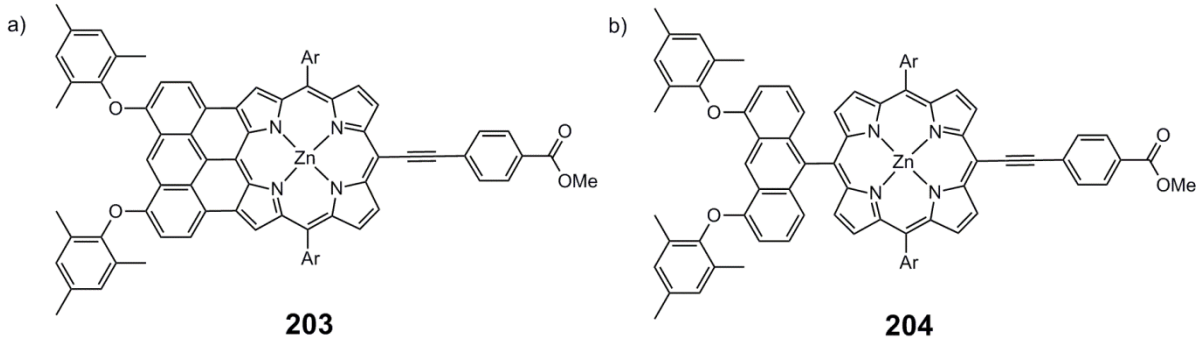

203 **204**

Figure 5.13: a) Anthracene-fused porphyrin ester **203** and b) Anthracene-linked porphyrin ester **204** obtained by in situ deprotection and coupling of ester **202** to porphyrins **200** and **199** respectively. Ar = 3.5-di(*t*-butyl)phenyl.

Hydrolysis of porphyrin **204** in basic conditions gave the target compound **192** in 81% yield (Scheme 5.8). Since MALDI-TOF mass spectrometry and ^{1}H NMR spectroscopy of the crude reaction mixture showed that porphyrin **192** was the only species formed under these conditions, purification was achieved by removal of salts through washing with water, followed by precipitation from DCM and pentane. Hydrolysis of fused porphyrin **203** was achieved under the same conditions, giving target compound **193** in 86% yield.

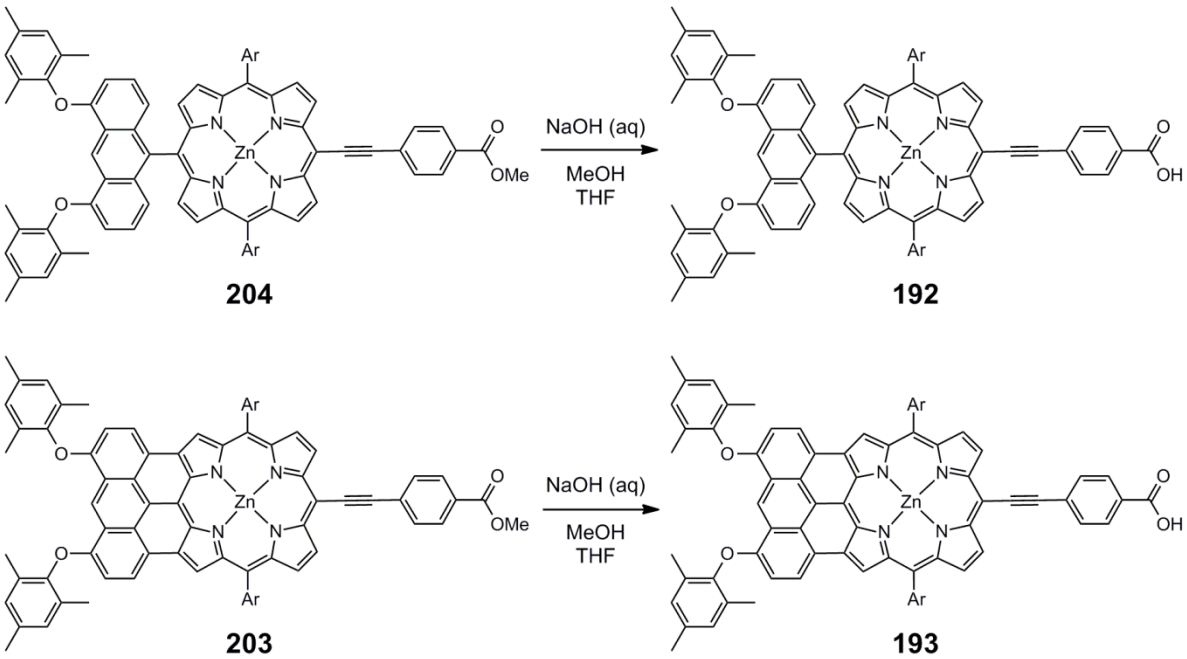

Scheme 5.8: Hydrolysis of anthracene-porphyrins **204** and **203** to give target compounds **192** and **193** respectively. Ar = 3.5-di(*t*-butyl)phenyl.

5.3.3 UV-vis-NIR Absorption Spectra of Anthracene-Porphyrins 192 and 193

The UV-vis-NIR absorption spectra of anthracene-porphyrins **192** and **193**, recorded in chloroform with 1% pyridine are shown in Figure 5.14.

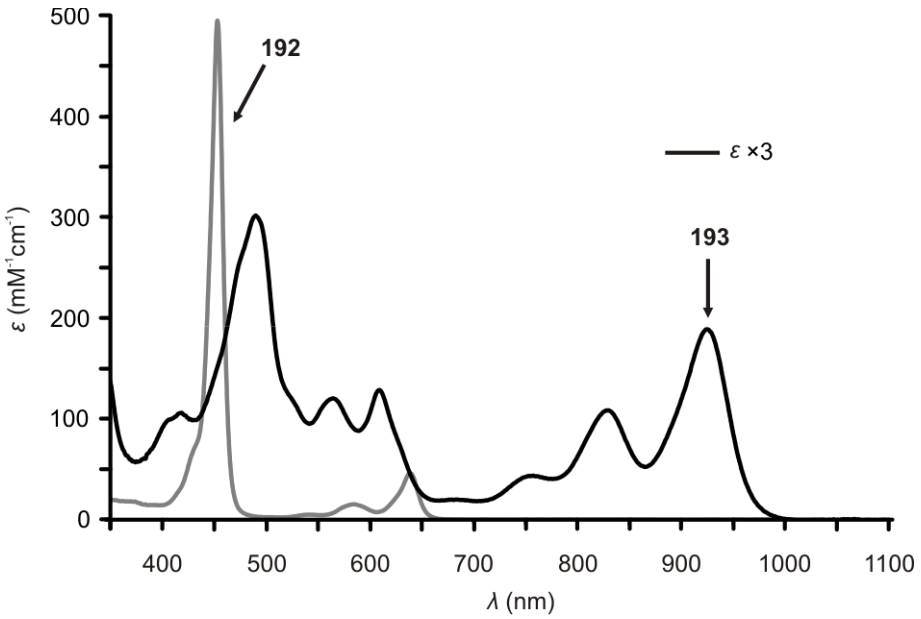

Figure 5.14: UV-vis-NIR absorption spectra in $CHCl_3$/1% pyridine for unfused anthracene-linked porphyrin **192** (grey), and anthracene-fused porphyrin **193** (ε × 3 for clarity, solid black).

The absorption spectrum of anthracene-linked porphyrin **192** exhibits a spectral shape similar to that of unfused anthracene-porphyrin **130**, however both the Soret and Q-bands of **192** are red-shifted and show an increase in intensity, due to extension of the π-system by conjugation with the ethynylphenyl group.[68] As expected from the UV-vis-NIR absorption spectrum of mono anthracene-fused porphyrin **132** synthesised in Chapter 3, anthracene fused porphyrin **193** demonstrates a dramatically red-shifted absorption spectrum compared to unfused anthracene-linked porphyrin **192** (longest wavelength λ_{max} shifts from 639 nm for **192** to 924 nm for **193**), together with broader absorption. The intensity of absorption shown by porphyrin **193** at its longest wavelength near-IR λ_{max} is greater than for **132** by nearly a factor of two. This may be explained by the more red-shifted absorption of **193** due to increase in conjugation arising from the presence of the ethynylphenyl group as mentioned above. The strong panchromatic absorption of **193** may be expected to facilitate excellent light harvesting by this dye when incorporated into DSSC devices.

5.3.4 Electrochemistry of Anthracene-Porphyrins 192 and 193

Cyclic and square wave voltammetry were carried out on porphyrins **192** and **193** to determine their redox potentials. All values are reported relative to the ferrocene/ferrocinium redox couple. The first oxidation peak of unfused anthracene-linked porphyrin **192**, E_1^{ox}, occurs at 0.46 V (Figures 5.15 and 5.16) which is very similar to that observed for mono-anthracene linked zinc porphyrin **130** synthesised in Chapter 3 (0.44 V). The first reduction peak of porphyrin **192**, E_1^{red}, occurs at -1.74 V which is more positive than observed for porphyrin **130** (-1.96 V), resulting in an E_1^{ox}- E_1^{red} separation of 2.20 V for porphyrin **192**. This suggests that the red-shift in UV-vis-NIR absorption of porphyrin **192** compared to **130**, arises from a decrease in the energy of the LUMO level, rather than an increase in HOMO energy.

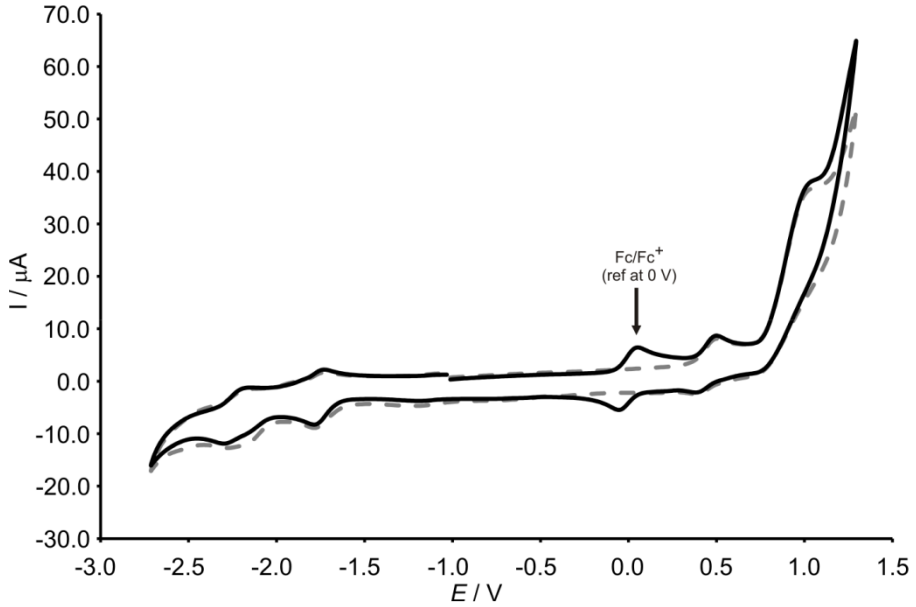

Figure 5.15: Cyclic voltammogram for unfused anthracene linked porphyrin **192**, both with ferrocene (black solid), and without (grey dash). Cyclic voltammetry was carried out in THF with 0.1 M Bu_4NPF_6 at a scan rate of 100 mV s^{-1} using a glassy carbon working electrode, Pt counter electrode and $Ag/AgNO_3$ reference electrode.

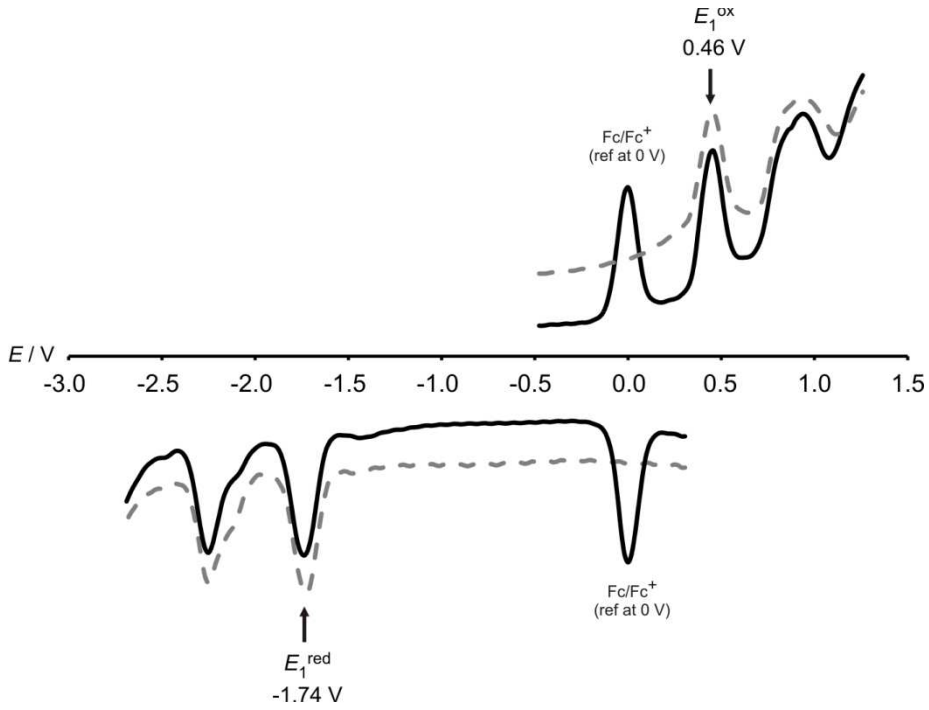

Figure 5.16: Square wave voltammogram for unfused anthracene-linked porphyrin **192**, both with ferrocene (black solid), and without (grey dash). Square wave experiments were recorded in THF with 0.1 M Bu_4NPF_6 at a square wave frequency of 8 Hz using a glassy carbon working electrode, Pt counter electrode and $Ag/AgNO_3$ reference electrode.

The cyclic voltammetry and square wave measurements for anthracene-fused porphyrin **193** are shown in Figures 5.17 and 5.18 respectively. It can be seen that porphyrin **193** exhibits an E_1^{ox} value of 0.17 V and an E_1^{red} value of -1.30 V, leading to an E_1^{ox}- E_1^{red} separation of 1.47 V. When compared to partially fused bis-anthracene nickel porphyrin **132** synthesised in Chapter 3 (E_1^{ox} = 0.32 V, E_1^{red} = -1.32 V), it can be seen that the larger degree of conjugation present in porphyrin **193** results in a smaller HOMO-LUMO gap. In addition, it can be seen that the HOMO of porphyrin **193** lies at significantly higher energy than porphyrin **132**. This is likely to be at least partially due to the influence of the different metal cations coordinated by the central cavity of the porphyrin macrocycle, as nickel porphyrins typically exhibit more positive oxidation potentials than zinc porphyrins.[76]

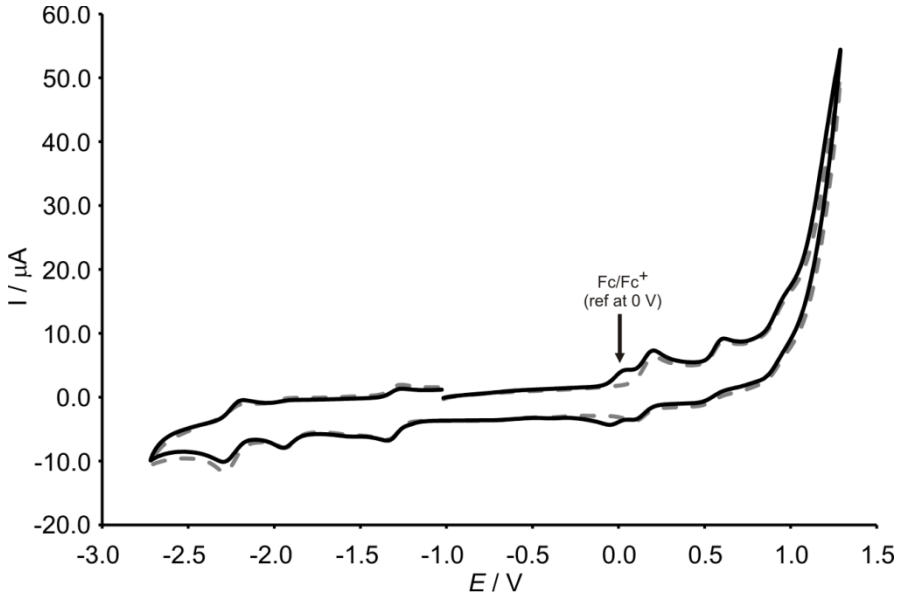

Figure 5.17: Cyclic voltammogram for anthracene-fused porphyrin **193**, both with ferrocene (black solid), and without (grey dash). Cyclic voltammetry was carried out in THF with 0.1 M Bu_4NPF_6 at a scan rate of 100 mV s^{-1} using a glassy carbon working electrode, Pt counter electrode and $Ag/AgNO_3$ reference electrode.

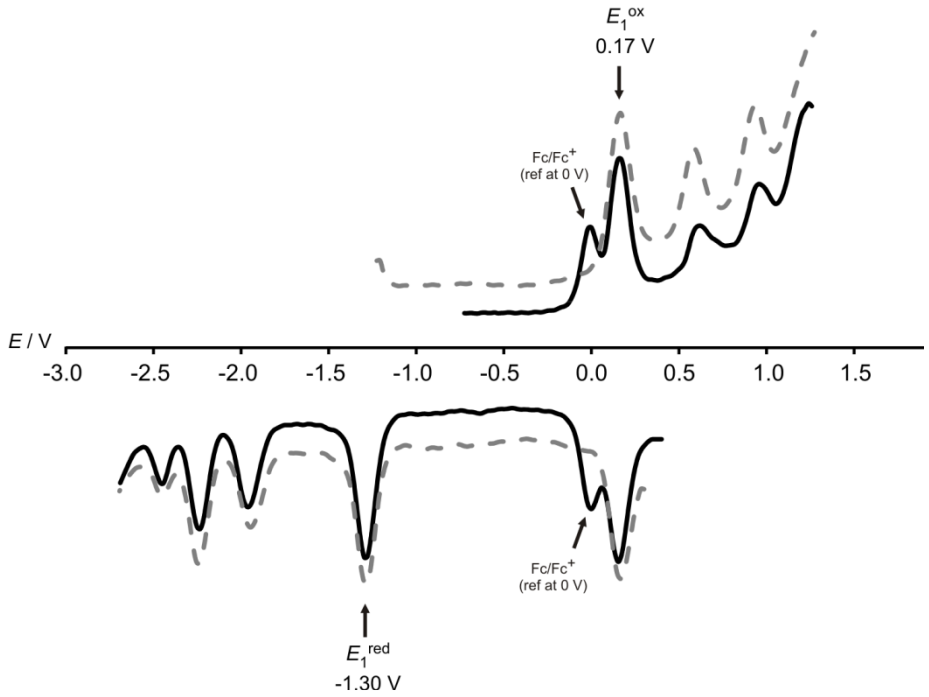

Figure 5.18: Square wave voltammogram for anthracene-fused porphyrin **193**, both with ferrocene (black solid), and without (grey dash). Square wave experiments were recorded in THF with 0.1 M Bu_4NPF_6 at a square wave frequency of 8 Hz using a glassy carbon working electrode, Pt counter electrode and $Ag/AgNO_3$ reference electrode.

5.3.5 Estimating the Redox Potentials of the First Excited State

In order to investigate whether charge injection by a sensitiser is thermodynamically favourable, it is necessary to determine the energy of its first excited state. The energy of this state may be estimated from the following equation

$$E(S^*/S^+) = E(S/S^+) + \Delta E_{0-0}(S/S^*)$$

where E(S*/S⁺) is the Fermi energy level of the oxidation potential of the first excited state relative to vacuum, E(S/S⁺) is the Fermi energy level of the oxidation potential of the HOMO relative to vacuum, and $\Delta E_{0\text{-}0}$(S/S*) is the energy of the 0-0 transition between the lowest energy vibrational levels in the ground and excited states.[8]

Since it is simpler to reference electrochemical measurements to standards such as the Normal Hydrogen Electrode (NHE) than to vacuum, the equation above may be expressed as

$$\Phi(S^*/S^+) = \Phi(S/S^+) - \Delta E_{0-0}(S/S^*)$$

where Φ(S*/S⁺) and Φ(S/S⁺) are the oxidation potentials of the first excited state and the ground state of the dye respectively, with respect to the NHE.[77]

The value for $\Delta E_{0\text{-}0}$(S/S*) is often found from the onset of emission in photoluminescence spectra, or from the point at which the absorption and photoluminescence spectra for a dye intersect. In the case of porphyrin **193** it was not possible to record a photoluminescence spectrum because the wavelengths of emission fall beyond the limit exhibited by our detector. However, the value of $\Delta E_{0\text{-}0}$(S/S*) was instead estimated for porphyrins **192** and **193** by taking the energy of the longest wavelength at which the absorption exhibited by these porphyrins reaches 10% of their furthest near-IR absorption maxima. This technique is commonly employed when difficulties arise in recording photoluminescence spectra.[8]

The Gibbs free energy for electron injection from the excited state of the dye into the conduction band of a metal oxide is given by

$$\Delta G_{inj} = \Phi(S^*/S^+) - E_{cb}$$

where E_{cb} is the energy of the conduction band edge of the metal oxide (relative to the NHE). For titanium dioxide, the energy of the conduction band edge is usually quoted as -0.5 V.[8] The calculated excited state energies and free energies for electron injection (into the titanium dioxide conduction band) for unfused anthracene-linked porphyrin **192** and anthracene-fused porphyrin **193**, are summarised in Table 5.1.

Table 5.1: Electrochemical, optical and thermodynamic data for porphyrins **192**, **193** and **205** carried out in THF. [a]First oxidation potential given relative to NHE, where Fc/Fc^+ = +0.80 V vs NHE in THF.[78,79] [b]Absorption onset calculated at 10% of the longest wavelength near-IR absorption maximum.

Dye	$E(S/S^+)$ /V vs Fc/Fc^+	$E(S/S^+)^a$ /V vs NHE	$\Delta E_{0\text{-}0}(S/S^*)^b$ /eV	$E(S^+/S^*)^a$ /V vs NHE	ΔG_{inj} /eV
192	0.46	1.26	1.89	-0.63	-0.13
193	0.17	0.97	1.28	-0.31	0.19
205	0.40	1.20	1.95	-0.75	-0.25

In addition, Table 5.1 also presents electrochemical, optical and thermodynamic data for porphyrin **205** (Figure 5.19) which bears an unsubstituted *meso*-position. This porphyrin was synthesised by James Wilkinson (Anderson Group) who also carried out the electrochemical measurements on this particular dye. This compound was thought to be an interesting reference molecule, as comparison of its DSSC performance to that of porphyrin **192** would enable the influence of an unfused anthracene unit to be investigated.

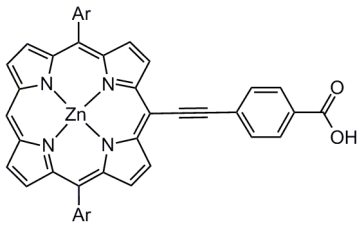

205

Figure 5.19: Reference porphyrin **205** synthesised by James Wilkinson.

Analysis of the data presented in Table 5.1 and Figure 5.20 indicates that charge injection is most favourable for porphyrin **205**, with anthracene-linked porphyrin **192** also displaying thermodynamically favourable free energy of charge injection.

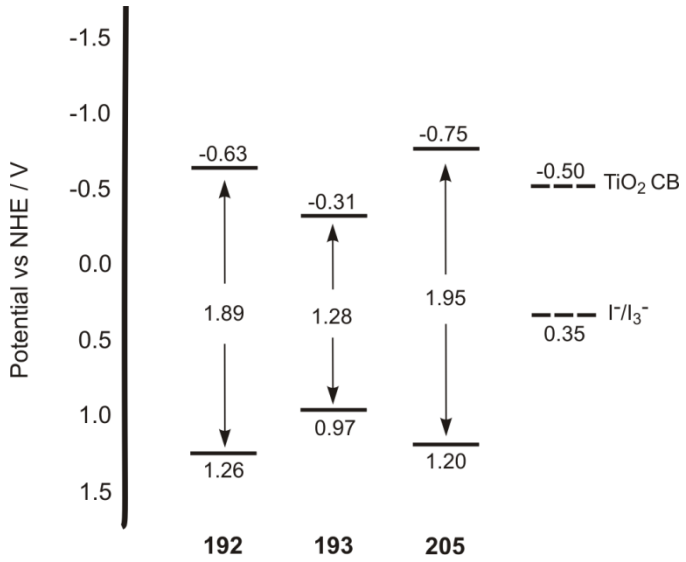

Figure 5.20: Schematic diagram showing the energy levels of porphyrins **192**, **193** and **205** relative to the conduction band (CB) of TiO_2 and the I^-/I_3^- redox couple based on the data in Table 5.1.

It would appear from the data for porphyrin **193** that charge injection for this dye is not thermodynamically favourable, due to the fact that the energy of the first excited state lies below that of the titanium dioxide conduction band. While this may be expected to result in poor performance of porphyrin **193** when incorporated into a DSSC device, it should be noted that the energy of the titanium dioxide conduction band edge depends greatly on the cell conditions as discussed in Section 5.1.3. For example, it has been found that changes in electrolyte composition such as the concentration of lithium ions, are capable of lowering the energy of this level by around one volt. In addition, adsorption of the dye onto the titanium dioxide surface also lowers the energy of the conduction band due to interaction of the protons with the surface states. Furthermore, tin oxide has been shown to exhibit a conduction band which lies 0.5 V lower in energy than that of titanium dioxide, implying that use of this metal oxide with porphyrin **193** would enable thermodynamically favourable charge injection. Hence with the correct choice of electrolyte and metal oxide surface, it may be expected that porphyrin **193** could also exhibit energetically favourable charge injection. Finally, it should be noted that the data shown in Figure 5.20 only give an approximation of the energy levels; the potentials of the Fc/Fc^+ couple, the I^-/I_3^- couple, and the TiO_2 conduction band versus NHE have many published figures, and the redox potentials of the dye sensitisers themselves may differ from those reported here when in electrolyte solution.

The error in such electrochemical measurements has been reported as in the region of 0.1 V.[80]

All of the porphyrins under investigation (**192**, **193** and **205**) have ground state oxidation potentials which are significantly more positive than that of the I^-/I_3^- redox couple, which lies at around +0.35 V vs NHE,[8] hence all of these dyes may be expected to exhibit a large thermodynamic driving force for regeneration.

5.4 Photovoltaic Testing and Characterisation of Porphyrins **192**, **193** and **205**

Photovoltaic device construction and cell testing was carried out by Dr James Ball in the Dr Henry Snaith Group, Department of Physics, University of Oxford.

5.4.1 DSSC Construction

The DSSCs were prepared in a low dust 'clean room' by the following procedure. Sheets of glass coated with a fluorine-doped tin oxide (FTO) layer were screen-printed with a porous layer of 20 nm sized titanium dioxide particles (7 μm thick) and then sintered by heating to 500 °C. The sheets were then treated with a 15 mM titanium tetrachloride solution in deionised water at 70 °C for one hour before being re-sintered at 500 °C. These electrodes were then cut to size and submerged for four hours in a 150 μM solution of dye dissolved in a 1:1 chloroform/ethanol solvent mixture. Upon removal from the dye solution, the electrodes were rinsed with ethanol and allowed to dry before being assembled with the counter electrode. This counter electrode was prepared separately from sheets of FTO coated glass, and into each electrode a small hole was introduced by sand-blasting. The electrodes were then platinised (platinising solution: 50 mM chloroplatinic acid in ethanol), doctor bladed and then heated to 450 °C for 20 minutes. The two electrodes were joined together by melting a 25 μm thick *Surlyn* gasket, and the internal space between the two electrodes was filled with a liquid electrolyte by a vacuum back filling technique. The hole was then sealed with a *Surlyn* sheet and cover glass.

AM 1.5 G light at 100 mW cm^{-2} was generated using an ABET solar simulator calibrated using an NREL calibrated silicon reference cell with a KG5 filter to minimise spectral mismatch.[81] *J/V* curves were measured with a Keithley 2400 unit. A metal aperture was used to mask the DSSC devices to give a defined active area and to remove any edge effects.

IPCE spectra were measured for DSSC devices across the visible spectrum under short-circuit conditions. The IPCE spectral response was taken under monochromatic light with an intensity of approximately 1 mW cm^{-2} and the response calibrated with a silicon reference diode.

5.4.2 Testing of Devices Incorporating a Standard Robust Electrolyte with a Titanium Dioxide Layer

Initially the devices were made with a standard robust electrolyte composed of 0.8 M 1,3-dimethylimidizolium iodide; 0.15 M iodine; 0.5 M 1-methylbenzimidazole; 0.1 M guanadinium thiocyanate in 2-methoxypropionitrile (MPN). In addition to testing porphyrin dyes **192**, **193** and **205**, indoline dye **D102** (Figure 5.21) was employed as a reference dye. This sensitiser has been shown to give high efficiencies (6.1%) when incorporated into titanium dioxide based DSSCs, which are comparable to those recorded for the widely used ruthenium based dye N3 under the same conditions (6.3%).[82]

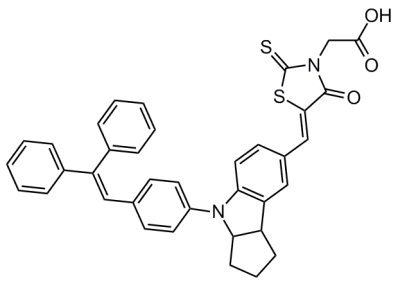

D102

Figure 5.21: Structure of reference dye **D102**.[82]

Typical *J/V* curves obtained for DSSC devices incorporating dyes **D102**, **192**, **193**, and **205** are shown in Figures 5.22 and 5.23 respectively.

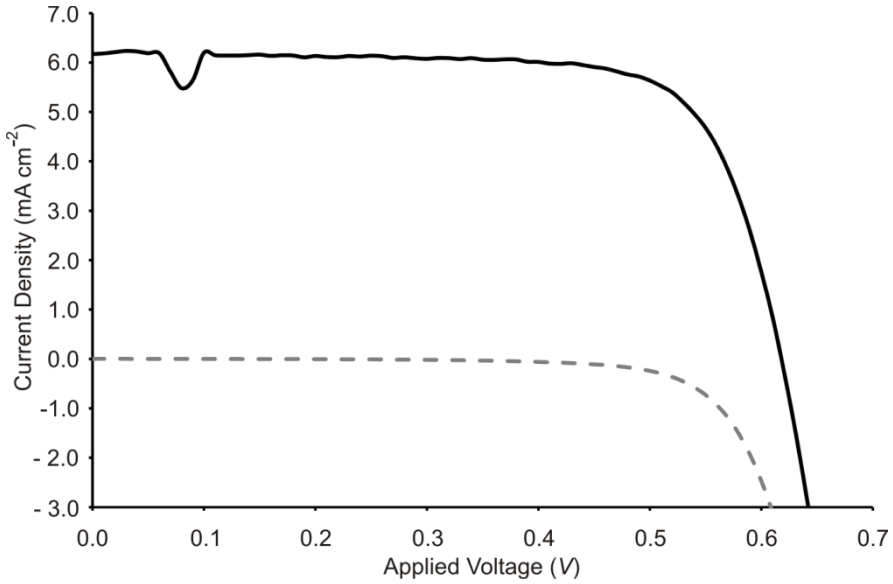

Figure 5.22: *J*/*V* curves for DSSC containing **D102** measured under 100 mW cm^{-2} illumination (solid black line) and in the dark (grey dashed line).

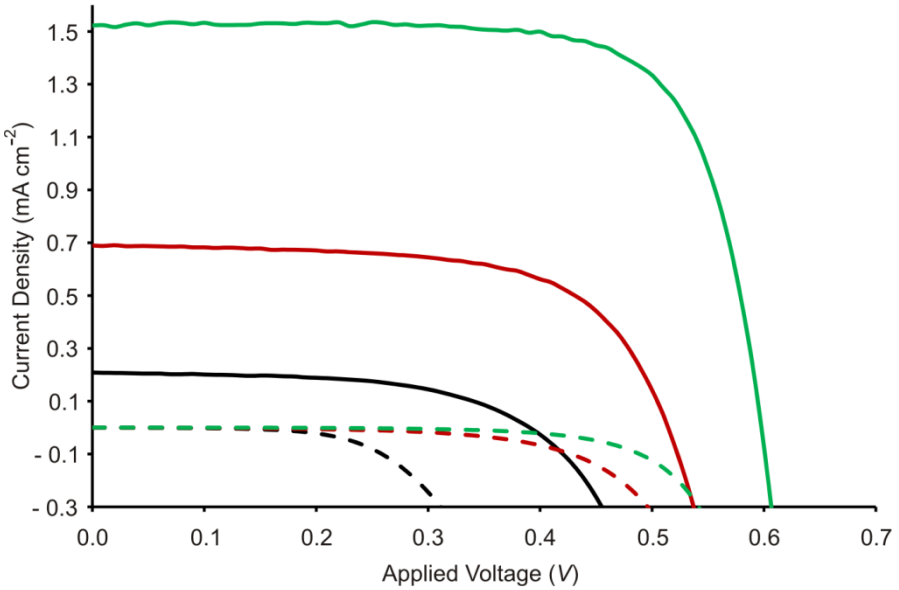

Figure 5.23: *J*/*V* curves for DSSC containing unfused anthracene porphyrin **192** (green), anthracene-fused porphyrin **193** (black) and porphyrin **205** (red), measured under 100 mW cm^{-2} illumination (solid lines) and in the dark (dashed lines).

A summary of the data obtained from these *J*/*V* curves shown is shown in Table 5.2.

Table 5.2: Summary of characteristic solar cell data for titanium dioxide devices incorporating dyes **D102**, unfused anthracene-porphyrin **192**, anthracene-fused porphyrin **193** and porphyrin **205**.

Dye	J_{SC} (mA cm^{-2})	V_{OC} (V)	FF	η (%)
D102	6.17	0.62	0.73	2.80
192	1.52	0.60	0.73	0.66
193	0.21	0.39	0.55	0.04
205	0.69	0.51	0.64	0.22

The efficiency of devices incorporating **D102** is lower than has been reported in the literature,[82] however, these devices have not been optimised for thickness and do not contain a scattering layer or antireflection coating, which are typical components in high efficiency devices. In addition it should be noted that it is not uncommon for different research groups to report different efficiencies for devices of the same construction. A significant factor in rationalising the relatively large J_{SC} value for **D102**, is the high IPCE response this dye exhibits over the whole visible region (Figure 5.24).

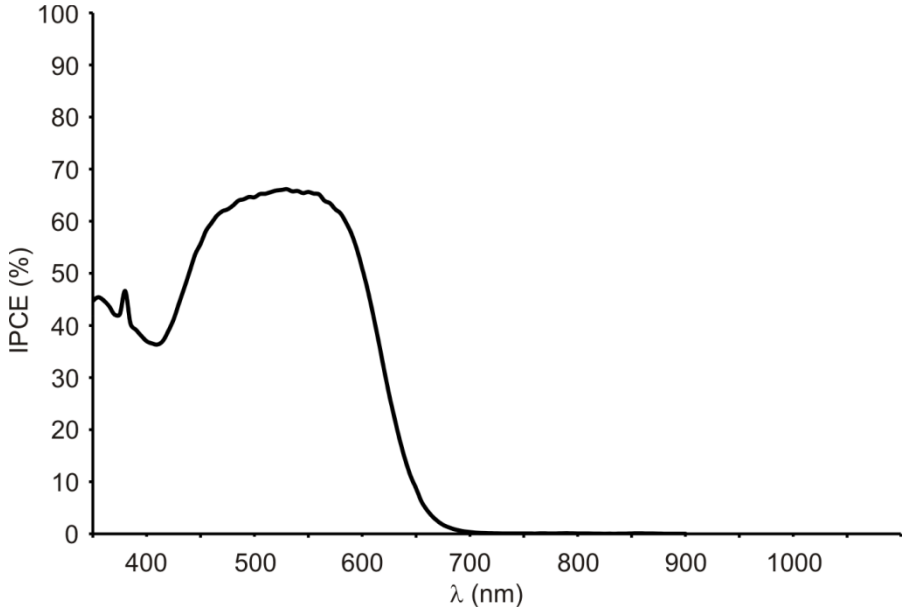

Figure 5.24: IPCE plot for reference dye **D102**.

Of the porphyrin dyes tested, unfused anthracene-linked porphyrin **192** gives the highest efficiency and exhibits the highest J_{SC} and V_{OC} values, while anthracene-fused porphyrin **193** gives the lowest values for all of the measured parameters. The higher

efficiency of **D102** compared to porphyrin **192** is almost entirely due to a higher J_{SC} value which arises from its broader IPCE response together with larger IPCE values across the whole spectrum. Since **D102** exhibits absorption of UV-vis light on titanium dioxide with similar magnitude to that of unfused porphyrin **192**, this suggests that the higher IPCE values for **D102** arise from larger φ_{in} and/or η_c values.

The greater efficiency of devices containing unfused anthracene-linked porphyrin **192** compared to porphyrin **205** may seem surprising, given the more favourable free energy of charge injection estimated for porphyrin **205**. However anthracene-porphyrin **192** exhibits a more red-shifted absorption spectrum, manifested by a smaller value of $\Delta E_{0\text{-}0}$(S/S*) for porphyrin **192** compared to porphyrin **205** (Table 5.1). In addition, porphyrin **192** has been shown to exhibit stronger UV-vis absorption when adsorbed onto titanium dioxide. It is likely that a combination of these factors gives rise to the larger IPCE values, and hence a larger J_{SC} observed for porphyrin **192** compared to porphyrin **205** (Figures 5.25 and 5.26).

The anthracene unit of porphyrin **192** is also twisted significantly with respect to the porphyrin macrocycle, thereby exerting considerable steric hindrance towards aggregation, and hence limiting self-quenching effects. Porphyrin **205** in contrast does not exhibit such strong steric hindrance and hence may be more prone to aggregation. In addition, the bulky anthracene unit of porphyrin **192** may be expected to suppress the dark current of the cell by inhibiting contact between the electrolyte and the titanium dioxide surface. Together, these factors offer a possible explanation for the larger V_{OC} observed for porphyrin **192** compared to porphyrin **205**.

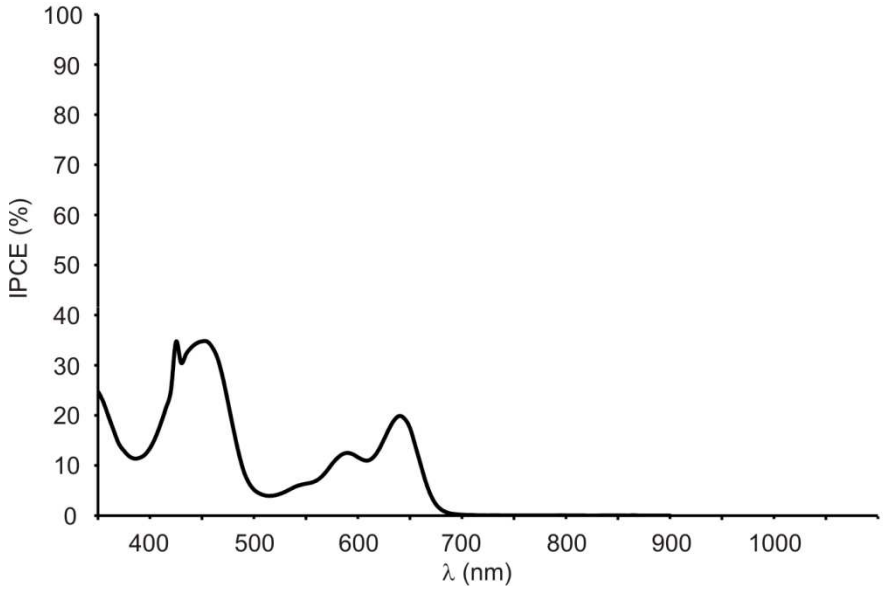

Figure 5.25: IPCE plot for unfused anthracene-porphyrin **192**.

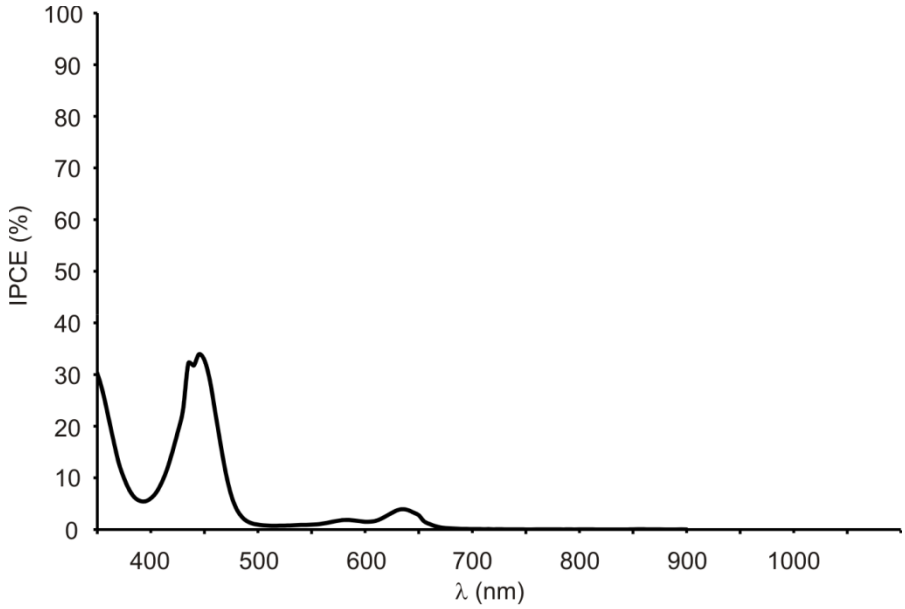

Figure 5.26: IPCE plot for porphyrin **205**.

The performance of anthracene-fused porphyrin **193** as a sensitiser for these DSSC devices is scientifically interesting, and may be rationalised from the data given in Table 5.1. The low value of J_{SC} is likely to be due to the first excited state of porphyrin **193** lying below that of the titianium dioxide conduction band, hence resulting in poor charge injection. As seen from the IPCE plot for anthracene-fused porphyrin **193** (Figure 5.27), some light harvesting occurs in the visible region between 400 and 600 nm, probably due to charge

injection into the titanium dioxide conduction band from higher excited states of the dye. However, the low values of response recorded in this region suggest rapid relaxation of such excited states to the first excited state from which charge injection is unfavourable.

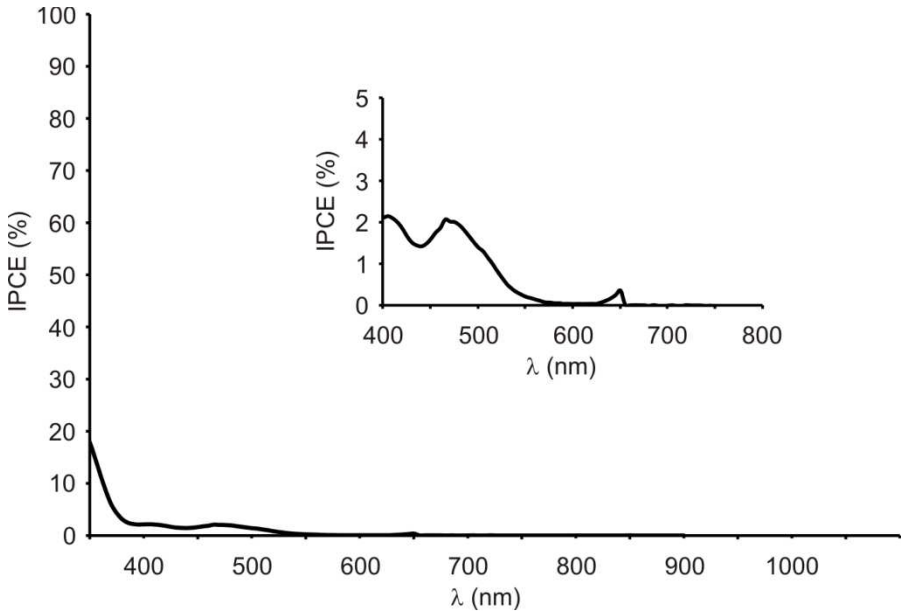

Figure 5.27: IPCE plot for anthracene-fused porphyrin **193**. The inset plot shows a magnified region of the graph.

Anthracene-fused porphyrin **193** exhibits an appreciable V_{OC} value, although it is lower than for unfused anthracene-linked porphyrin **192** and porphyrin **205**. The lower V_{OC} observed for porphyrin **193** may be due several factors; the reduced degree of electron injection observed for **193** means a smaller number of electrons are available to populate the conduction band, hence resulting in a more positive Fermi level than expected for devices incorporating unfused porphyrin **192**, and thereby resulting in a lower V_{OC}. There have been several reports that large, planar porphyrins may facilitate binding of I_3^- close to the titanium dioxide surface.[83,84] The larger dark current which would arise from such binding (due to a greater recombination between the electrons in the titanium dioxide and the I^-/I_3^- redox couple in the electrolyte) would also reduce V_{OC}. In addition, the higher energy HOMO of porphyrin **193** compared to porphyrins **192** and **205** means that this energy level lies closer to that of the I^-/I_3^- redox couple, possibly reducing the driving force for dye regeneration.

In order to be sure that the poor performance of anthracene-fused porphyrin **193** in DSSC devices is not due to poor cation regeneration by the electrolyte, transient absorption measurements were carried out by Dr Joël Teuscher, Department of Physics, University of Oxford.

The nanosecond laser flash photolysis (transient absorbance spectroscopy) technique was applied to dye-sensitised, 2 μm-thick, transparent titanium dioxide mesoporous films deposited on glass.

Pulsed excitation (λ_{ex} 510 nm, 7 ns pulse duration, 10 Hz repetition rate) was carried out by an Ekspla NT340 series Nd:YAG laser. The laser beam output was expanded by a lens to irradiate a large cross-section of the sample, whose surface was kept at a 30° angle to the excitation beam. The laser fluence on the sample was kept at a low level (< 40 mJ cm^{-2} per pulse). The probe light, produced by a continuous wave xenon arc lamp, was first passed through a monochromator (Acton Research Corporation, SpectraPro-2150i), various optical elements, the sample, and then through a second monochromator (Acton Research Corporation, SpectraPro-2300i), before being detected by a fast photomultiplier tube module (Hamamatsu, H9858-20). Data waves were recorded on a Tektronix DPO3054 oscilloscope. Satisfactory signal-to-noise ratios were typically obtained by averaging over 256 laser shots.

It can be seen from Figures 5.28, 5.29 and 5.30 that the radical cation of porphyrin **193** shows measurable transient difference absorption in the absence of electrolyte, but almost negligible values when electrolyte is present. In addition, it is only possible to measure cation lifetime in the absence of electrolyte (Figure 5.30), suggesting rapid regeneration of the dye on a nanosecond timescale. These results confirm that dye regeneration occurs rapidly and is not the limiting factor in the DSSC performance of anthracene-fused porphyrin **193**. Hence it is likely that inefficient electron injection from the dye into the titanium dioxide conduction band is the primary cause of the poor DSSC performance of porphyrin **193**.

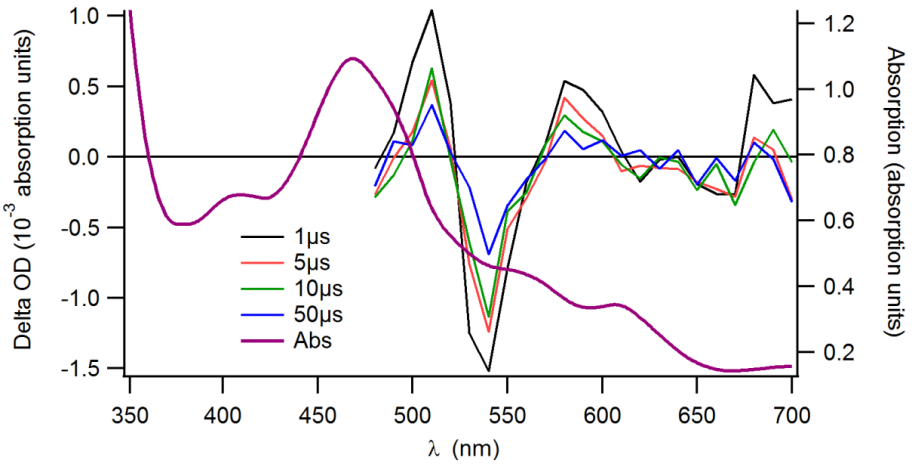

Figure 5.28: Transient difference absorption (Delta OD) spectra of porphyrin **193** on titanium dioxide as a function of wavelength in the absence of electrolyte for different times after irradiation; 1 µs (black), 5 µs (red), 10 µs (green), 50 µs (blue). The absorption spectrum of anthracene-fused porphyrin **193** on titanium dioxide is shown by the purple trace.

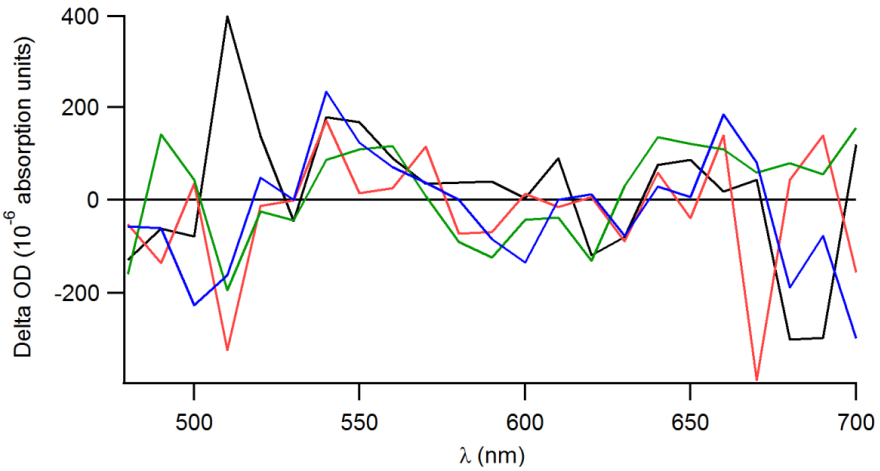

Figure 5.29: Transient difference absorption (Delta OD) spectra of porphyrin **193** on titanium dioxide as a function of wavelength in the presence of electrolyte for different times after irradiation; 1 µs (black), 5 µs (red), 10 µs (green), 50 µs (blue).

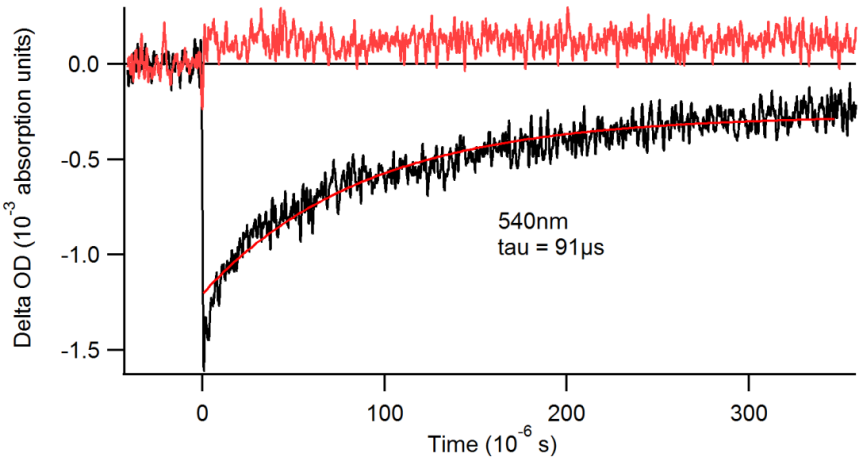

Figure 5.30: Transient difference absorption (Delta OD) spectra of porphyrin **193** on titanium dioxide in the presence of electrolyte as a function of time at 540 nm. Measurements carried out in the absence of electrolyte are shown in black, while those in the presence of electrolyte are shown in red. The red line on top of the black curve represents the fit used to find the lifetime of the cation.

5.4.3 Frontier Molecular Orbital Profiles of Porphyrins 192, 193 and 205

To better understand the reasons for the low efficiencies of porphyrins **192**, **193** and **205**, I carried out semi-empirical calculations using HyperChem software with the PM3 method. The frontier molecular orbital profiles of **192**, **193** and **205** derived from these calculations are shown in Figure 5.31.

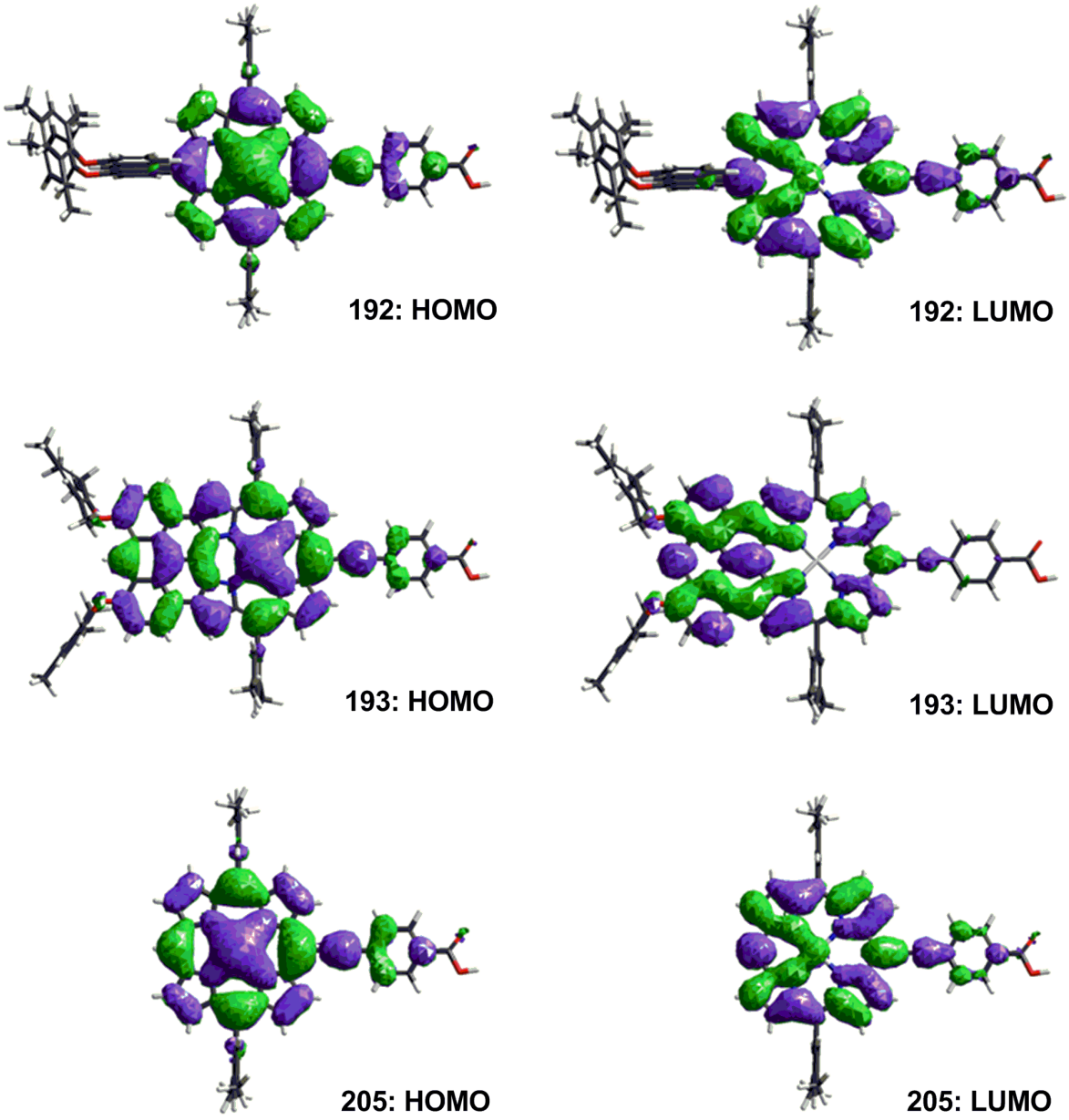

Figure 5.31: Frontier molecular orbital profile of anthracene-linked porphyrin **192** (top), anthracene-fused porphyrin **193** (middle) and porphyrin **205** (bottom) calculated by PM3 semi-empirical methods. HOMO (left) and LUMO (right).

In addition, DFT calculations were also performed for porphyrins **192**, **193** and **205**. These calculations were carried out by Dr James Kirkpatrick, Mathematical Institute, University of Oxford. Geometries and orbital energies were computed using Becke's three parameter hybrid density functional (B3LYP)[85] using a split double zeta basis function with added polarization functions (6-31g*)[86] for all row 1-3 atoms and Steven's effective core

potential basis set on the metal (CEP-31).[87] The frontier molecular orbitals calculated for **192**, **193** and **205** by these methods are shown in Figure 5.32.

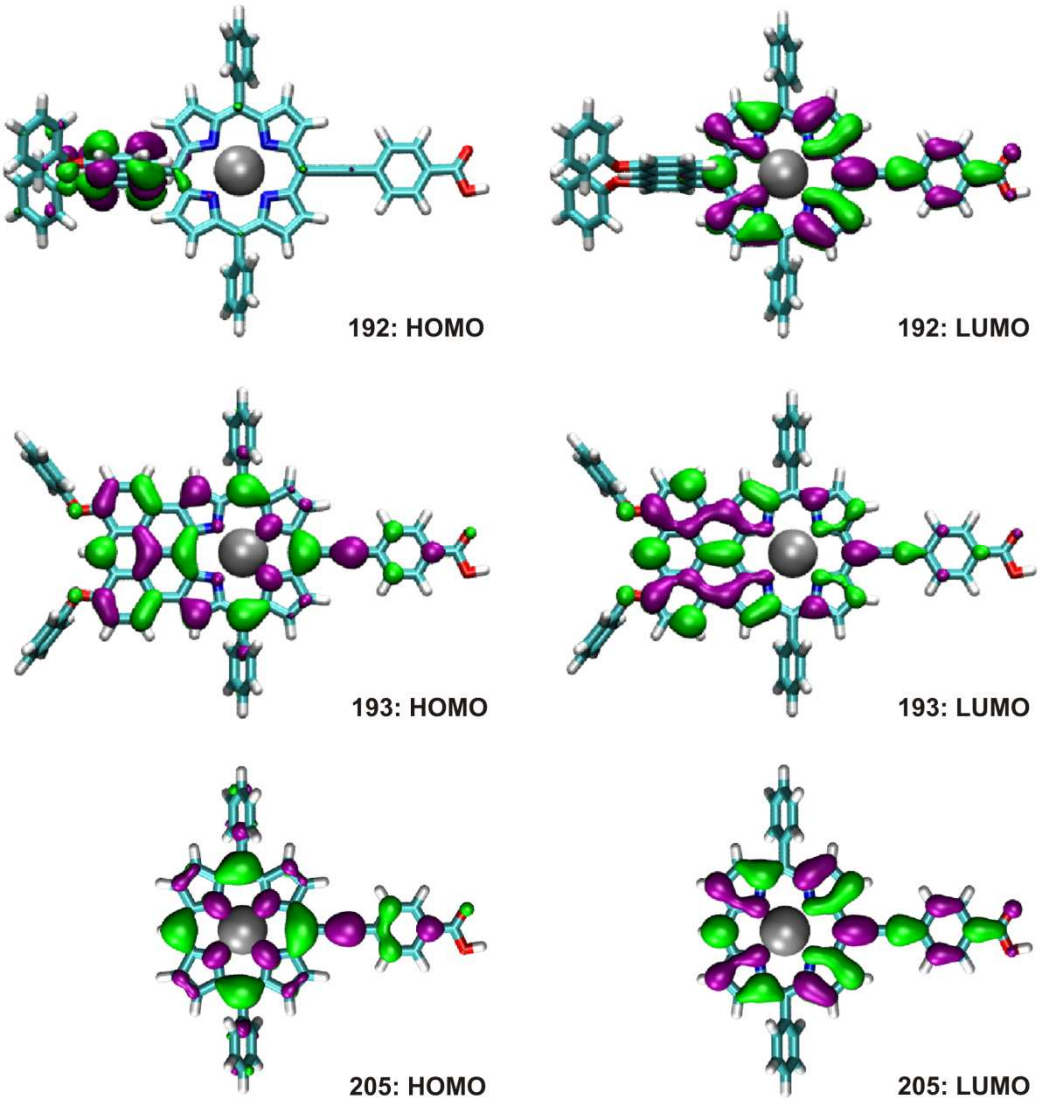

Figure 5.32: Frontier molecular orbital profiles of anthracene-linked porphyrin **192**, anthracene-fused porphyrin **193**, and porphyrin **205** calculated by DFT methods. HOMOs (left) and LUMOs (right). Methyl and *t*-butyl groups are truncated in the calculations.

It can be seen that for porphyrins **193** and **205**, these DFT results match well to those obtained using PM3, however for porphyrin **192** the HOMO is based on the anthracene moiety according to DFT calculations, but is porphyrin based from PM3 calculations. Examination of the energy levels for the HOMO, HOMO-1 and HOMO-2 of porphyrin **192** by DFT calculations shows that they lie very close in energy at -5.035, -5.052 and -5.290 eV respectively. In addition, it was found that the HOMO-2 level calculated by the PM3 method

matches well to the HOMO calculated by DFT. The different frontier molecular orbital profiles calculated by these two methods is likely to be due to their different treatment of the central zinc ion, which is less accurate for the PM3 method, potentially leading to subtle changes in the energies of the orbitals and hence a different ordering.

Both DFT and PM3 methods give similar frontier molecular orbital profiles for the LUMO levels of porphyrins **192**, **193** and **205**. It can be seen that porphyrins **192** and **205** have small electron densities on the carboxylic acid group in their LUMOs, while porphyrin **193** has negligible electron density on this group in its LUMO. This may give rise to poor electronic coupling between the dyes and the metal oxide surface, particularly for anthracene-fused porphyrin **193**, adversely affecting the process of electron injection. The appreciable electron density located on the adjacent aryl group for porphyrins **192** and **205** however, allows the electron density in the LUMO to sit closer to the metal oxide surface than for porphyrin **193**, which exhibits only very small electron densities on this aryl group in the LUMO. This arrangement may facilitate electron injection from porphyrins **192** and **205** into the conduction band of the metal oxide, contributing to the higher efficiencies observed for devices incorporating these dyes compared to porphyrin **193**.

The energies of the S_0-S_1 transitions for porphyrins **192**, **193** and **205** were also determined using time dependant B3LYP and were found to be 2.06, 1.60 and 2.19 eV respectively. These values are slightly larger than those observed by electrochemistry (Section 5.3.4) and from the near-IR absorption onset (Table 5.1), probably due to solvent effects (DFT calculations are performed with the assumption that the molecule is in a vacuum). However these values match well to the observed trend of a decrease in HOMO-LUMO separation as the degree of conjugation increases. The HOMO energy levels calculated for porphyrins **192**, **193** and **205** by DFT are -5.04, -4.55 and-5.10 eV respectively which are less negative than the values found by electrochemistry of -5.26, -4.97 and -5.13 eV (calculated from HOMO = - [4.8 + E_1^{ox}]), again probably due to solvent stabilisation effects.

5.4.4 Improving the IPCE Response of Porphyrin 193

As mentioned in Section 5.1.3, the conduction band of tin oxide lies lower in energy than that of titanium dioxide by around 0.5 eV, hence the free energy of electron injection from porphyrin **193** would be predicted to be thermodynamically favourable for this metal oxide. It may therefore be expected that use of tin oxide would result in a larger J_{SC} value for devices incorporating porphyrin **193**. On the other hand, lowering the conduction band of the metal oxide by employing tin oxide will decrease V_{OC}. The use of a high concentration of lithium ions in a titanium dioxide device would be expected to have a similar effect on these parameters. The purpose of these investigations however, revolves around exploring the possibility of harnessing near-IR light in photovoltaic devices, hence improving the IPCE response of porphyrin **193** would be a significant step towards this goal; improvement to overall cell efficiency will require the optimisation of many other parameters and is not the focus of this work.

Devices incorporating tin oxide were made in a similar fashion to the titanium dioxide cells described in Section 5.4.1 with the following modifications. Tin oxide was deposited by spray pyrolysis deposition of butyl tin chloride ($BuSnCl_3$) at 450 °C onto a sheet of FTO-coated glass to create a compact layer, followed by screen printing a mesoporous layer of tin oxide particles onto this surface. The sheet was then heated to 500 °C and allowed to cool. The sheets were either directly used in cell fabrication, or treated with a 20 mM magnesium acetate dihydrate solution in ethanol at 100 °C for one minute before being rinsed with ethanol and incorporated into photovoltaic devices. The electrolyte used in these devices is the standard robust electrolyte described in Section 5.4.2. The data achieved from these devices is summarised in Table 5.3.

Table 5.3: Summary of characteristic solar cell data for tin oxide devices incorporating dyes **D102**, unfused anthracene-porphyrin **192**, anthracene-fused porphyrin **193** and porphyrin **205** with the robust electrolyte described in Section 5.4.2.

	With MgO				Without MgO			
Dye	J_{SC} (mA cm^{-2})	V_{OC} (V)	*FF*	η (%)	J_{SC} (mA cm^{-2})	V_{OC} (V)	*FF*	η (%)
D102	5.96	0.57	0.55	1.87	6.86	0.37	0.55	1.38
192	0.97	0.55	0.70	0.37	2.65	0.33	0.55	0.47
193	0.004	0.16	0.35	0.00023	0.21	0.14	0.39	0.011
205	0.27	0.44	0.64	0.07	0.78	0.29	0.56	0.13

Devices were made both with and without the presence of magnesium oxide layer on top of the tin oxide surface. Tin oxide, besides having a lower energy conduction band than titanium dioxide (which may facilitate electron injection), also demonstrates much higher charge mobilities.[88] However tin oxide is more acidic than titanium dioxide, decreasing the degree of dye adsorption. In addition, the position of the tin oxide conduction band gives rise to lower values of V_{OC} than observed for titanium dioxide cells, together with fast recombination processes. The presence of a magnesium oxide layer has been shown in some cases to enhance performance of tin oxide devices, often demonstrating larger V_{OC} values than observed for devices with 'bare' tin oxide surfaces.[88] This is due to several factors including increased dye adsorption and suppression of unfavourable recombination processes.[89]

As seen from Table 5.3, the trends for the four dyes across each of the parameters follows those observed for the titanium dioxide devices described in Section 5.4.2, with **D102** exhibiting the best cell performance, followed by unfused anthracene-linked porphyrin **192**, then porphyrin **205** and finally anthracene-fused porphyrin **193**. Larger V_{OC} values are observed for all of the tin oxide devices incorporating a layer of magnesium oxide, compared to tin oxide devices without the layer, however the values of J_{SC} are significantly smaller for the porphyrin-based cells with the magnesium oxide layer. These effects may in part be due to the higher energy of the conduction band edge of magnesium oxide compared to tin oxide,

which thereby reduces the driving force for charge injection from the dye, while increasing V_{OC}.

In the absence of a magnesium oxide layer, the efficiencies of all of the porphyrin based cells improve due to the larger values of J_{SC}; the **D102** cells show a smaller increase in J_{SC} under these conditions, hence the larger reduction in V_{OC} results in a decreased efficiency compared to the **D102** device incorporating magnesium oxide. The improvement in cell performance observed for those incorporating porphyrin sensitisers is particularly notable for the devices employing anthracene-fused porphyrin **193** as the sensitiser, where J_{SC}, and hence the efficiency, increases by around two orders of magnitude in the absence of magnesium oxide. This is likely to be due to an increase in the favourability for charge injection from the dye into the low energy tin oxide conduction band.

Compared to the data obtained from the titanium dioxide devices described in Section 5.4.2, it can be seen that the values observed for all of the parameters are generally lower when titanium dioxide is replaced by tin oxide, even when a magnesium oxide layer is added. The difficult balance of reducing charge recombination and achieving a reasonable V_{OC} while still facilitating charge injection, appears to limit the performance of these tin oxide devices.

One of the main challenges facing the development of photovoltaic devices is creating cells capable of harvesting light in the near-IR. IPCE plots show the efficiency of charge generation from light hitting the cell at different wavelengths, and hence provide an indication of the light harvesting capabilities of the sensitiser. Porphyrin **193**, with its UV-vis-NIR absorption spectrum extending out to nearly 1000 nm, may be expected to show a strong spectral response in the near-IR however, when incorporated into a titanium dioxide device with the standard robust electrolyte, only a small IPCE response was observed in the visible region, as shown in Figure 5.27. In addition, the overall cell performance with this sensitiser was poor, as described in Section 5.4.2. While the cell performance exhibited by porphyrin **193** was equally meagre when incorporated into tin oxide devices, the IPCE plot encouragingly shows increased light harvesting in the near-IR (Figures 5.33 and 5.34). Although these IPCE values are low, they demonstrate that, while many other parameters

require significant modification to achieve an optimised device, the use of metal oxides with lower energy conduction bands than titanium dioxide can indeed facilitate charge injection, thereby enabling light harvesting beyond 1000 nm.

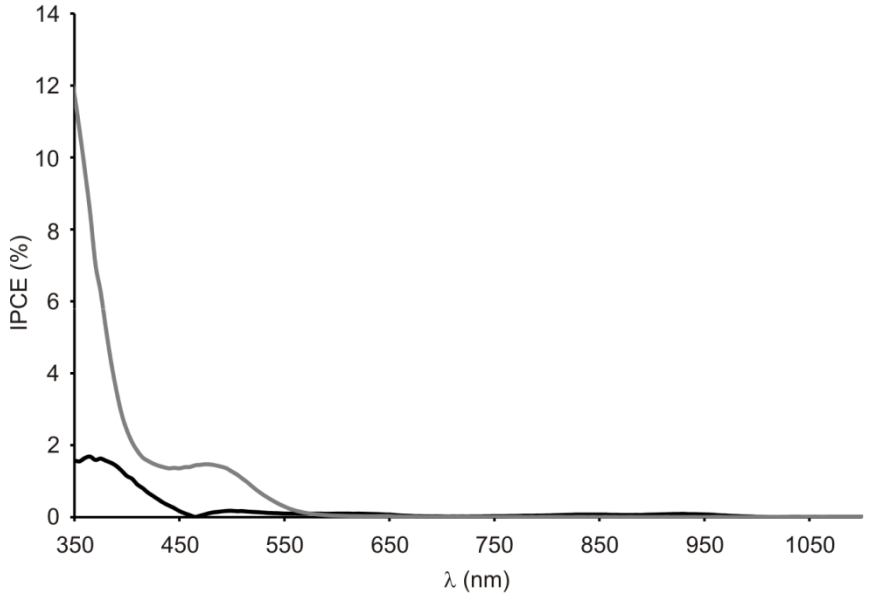

Figure 5.33: IPCE plots for devices incorporating anthracene-fused porphyrin **193** as a sensitiser: SnO_2 without MgO layer using standard robust electrolyte (black line) and titanium dioxide with standard robust electrolyte (grey line).

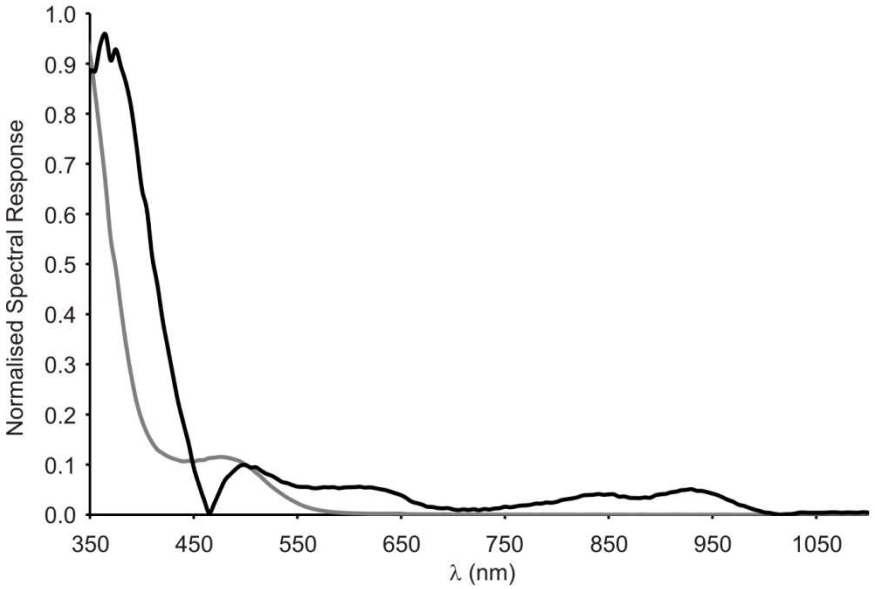

Figure 5.34: Normalised spectral response for devices incorporating anthracene-fused porphyrin **193** as a sensitiser: SnO_2 without MgO layer using standard robust electrolyte (black line) and titanium dioxide with standard robust electrolyte (grey line).

In order to avoid the problems associated with the use of tin oxide, an alternative approach towards increasing charge injection from anthracene-fused porphyrin **193** was

investigated. As described in Section 5.1.3, it is well known that lithium cations can strongly influence the position of the titanium dioxide conduction band through adsorption or intercalation with the surface of the metal oxide. Hence devices were constructed with a titanium dioxide layer, but with an electrolyte incorporating a high concentration of lithium ions. The devices were prepared as described in Section 5.4.1, however the composition of the electrolyte was chosen to be 2 M LiI and 0.1 M I_2 in MPN. This electrolyte was chosen as it is very similar to the 2 M LiI and 0.1 M I_2 in γ-butyrolactone electrolyte successfully employed by Bignozzi and co-workers for photovoltaic devices incorporating osmium and ruthenium polypyridine complexes, which absorb light into the near-IR (up to around 1100 nm).[59] The data achieved from incorporating **D102** and porphyrin **193** into these lithium ion rich devices is summarised in Table 5.4.

Table 5.4: Summary of characteristic solar cell data for titanium dioxide devices incorporating dyes **D102** and anthracene-fused porphyrin **193** with and electrolyte composed of 2 M LiI and 0.1 M I_2 in MPN.

Dye	J_{SC} (mA cm^{-2})	V_{OC} (V)	FF	η (%)
D102	13.39	0.33	0.41	1.76
193	1.43	0.11	0.40	0.06

While the V_{OC} values are lower for both **D102** and anthracene-fused porphyrin **193** in titanium dioxide cells with the lithium ion rich electrolyte compared to those with the standard robust electrolyte, the values of J_{SC} are much higher — in the case of porphyrin **193** this value has increased by a factor of seven. The decrease in both V_{OC} and FF results in **D102** exhibiting a lower efficiency in the presence of the lithium ion rich electrolyte than the standard robust electrolyte, however anthracene-fused porphyrin **193** shows an improvement in efficiency under the high concentration of lithium ions due to the great improvement in J_{SC}.

The IPCE plot for porphyrin **193** in the lithium ion rich devices is shown in Figure 5.35. While the IPCE values themselves are low across the spectrum, it is clear that these devices show a greatly improved spectral response, compared to the titanium dioxide devices with the standard robust electrolyte, exhibiting light harvesting to over 1050 nm.

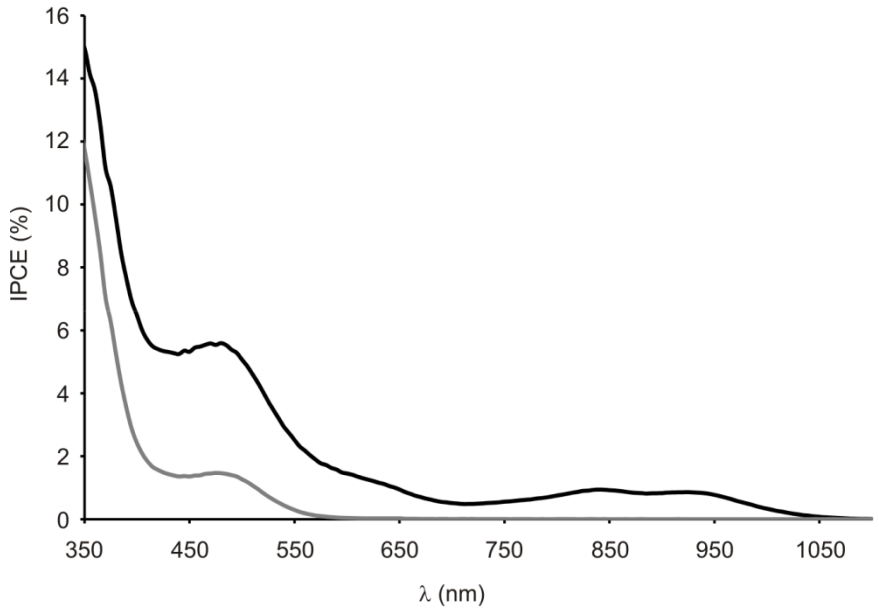

Figure 5.35: IPCE plots for devices incorporating anthracene-fused porphyrin **193** as a sensitiser: lithium ion rich electrolyte (black line) and titanium dioxide with standard robust electrolyte (grey line).

5.5 Conclusions

The synthesis of anthracene-linked and anthracene-fused porphyrins for use in photovoltaic devices has been achieved for the first time, offering valuable insights into the possibility of harvesting light in the near-IR region of the solar spectrum.

The syntheses of anthracene-linked and anthracene-fused porphyrins **192** and **193** respectively, demonstrate the need for a careful choice of acetylene protecting group in the precursor molecules, with only triisopropylsilyl groups being robust enough to enable fusion of the anthracene unit to the porphyrin periphery. The use of proton sponge, together with zinc(II) chloride, in parallel with the iron(III) chloride fusion conditions, was found to give anthracene-fused zinc porphyrin **200** in 63% yield. This is an elegant way to circumvent the problems of demetalation commonly encountered for zinc porphyrins when subjected to iron(III) chloride. This new approach towards fusion provides a simple way to access zinc porphyrins fused to aromatic moieties without having to rely on scandium(III) triflate and DDQ. This is particularly useful in the many cases demonstrated where the scandium(III) triflate reaction conditions either do not give the desired product, or where the product is difficult to purify from side products or residues of the DDQ oxidant.

The UV-vis-NIR spectra of porphyrins **192** and **193**, together with their electrochemical properties were investigated in order to estimate the Gibbs free energy of electron injection from the dye into the conduction band of titanium dioxide. From these calculations it was clear that reference porphyrin **205** had the most favourable free energy of electron injection, while anthracene-fused porphyrin **193** had a positive value, corresponding to the process of electron injection into the titanium dioxide conduction band being thermodynamically unfavourable for this dye.

Photovoltaic devices were initially constructed for porphyrins **192** and **193** with a titanium dioxide layer. **D102** and porphyrin **205** were also studied in these photovoltaic devices as reference dyes to enable useful conclusions to be drawn regarding the effect of the dye's molecular structure on the performance of cells. When incorporated into these titanium dioxide photovoltaic devices with the standard robust electrolyte, anthracene-linked porphyrin **192** showed the best cell performance of the porphyrin sensitisers, with an efficiency of 0.66%, while unsubstituted porphyrin gave a lower efficiency of 0.22%. This may be due to the greater steric bulk and red-shifted absorption of **192** compared to **205**. Anthracene-fused porphyrin **193** displayed a poor cell performance, with an efficiency of only 0.04%. Transient absorption spectroscopy confirmed that regeneration of the dye cation of porphyrin **193** occurs on the nanosecond timescale. Hence the modest efficiency of porphyrin **193** is likely to be due to a very low rate of electron injection from the dye into the conduction band of the titanium dioxide, due to the low lying excited state of porphyrin **193**. To circumnavigate this problem, tin oxide was employed as the metal oxide layer since it has a conduction band at lower energy than titanium dioxide, hence it was predicted to facilitate electron injection. In addition, devices were constructed both with and without an additional magnesium oxide layer since this the presence of such a layer has been reported to reduce recombination reactions and improve V_{OC}. While in both cases the overall cell performances for all dyes were poorer than for the titanium dioxide devices, the use of tin oxide (without magnesium oxide) improved the IPCE response of the porphyrin **193** considerably, enabling

light harvesting to occur to 1000 nm. This is one of the furthest red-shifted responses for ruthenium-free DSSCs.

Increasing the concentration of lithium ions in the electrolyte is known to strongly influence the position of the conduction band edge of titanium dioxide. Hence devices were made with a titanium dioxide layer and an electrolyte containing 2 M LiI. Under these conditions, anthracene-fused porphyrin **193** gave a much improved spectral response compared to that observed for both tin oxide and titanium dioxide devices employing the standard robust electrolyte. With the high concentration of lithium ions present, light harvesting was achieved above 1050 nm which is an exceptionally long wavelength for spectral response. The overall cell efficiency for porphyrin **193**, while still poor, was improved relative to the earlier devices due to the far higher value of J_{SC} achieved in these lithium ion rich cells.

From PM3 and DFT calculations, it was seen that one of the factors which could be limiting the cell performance of porphyrins **192**, **193** and **205** is the low level of electron density located on the anchor group of the dyes in their LUMOs. However, while porphyrins **192** and **205** show low electron densities in the LUMO on their carboxylic acid groups, the electron densities on the nearby aryl groups are much higher, allowing better electronic communication between the dye and the metal oxide surface than for porphyrin **193**. One approach to solving this problem could be re-designing porphyrin **193** to bear the carboxylic acid linker group on the anthracene-end of the fused system, to give porphyrin **206** (Figure 5.36 (a)). This would ensure a spatially closer arrangement of the porphyrin LUMO and the metal oxide conduction band edge, facilitating electron injection. However, such a molecule may be expected to experience strong aggregation due to the unhindered anthracene-porphyrin section of the molecule; the use of bulky groups around this periphery may hinder adsorption of the dye onto the metal oxide surface. In addition, an anthracene unit bearing a carboxylic acid group may not be electron rich enough to enable fusion of the anthracene to the porphyrin to occur. A different approach to improving the performance of anthracene-fused porphyrin **193** would be to attach electron withdrawing groups, such as fluorine atoms, to the aryl group adjacent to the carboxylic acid to create porphyrin **207** (Figure 5.36 (b)).

This would be expected to increase the electron density on the linker group in the LUMO, thereby increasing the electronic communication between the carboxylic acid group and the metal oxide surface, hence aiding electron injection.

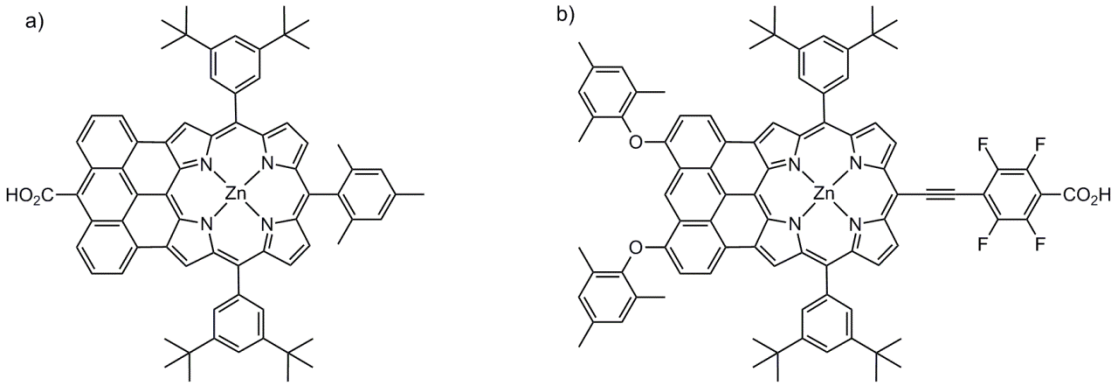

206 **207**

Figure 5.36: Potential anthracene-fused porphyrin targets expected to exhibit stronger electronic communication between the dye and the metal oxide surface than anthracene-fused porphyrin **193**.

One of the greatest challenges facing the field of photovoltaics at present is how to harvest light in the near-IR. The problem of poor electron injection from the dye to the metal oxide conduction band has frequently been reported for organic near-IR absorbing chromophores. The work in this chapter has explored solutions to this problem, resulting in anthracene-fused porphyrin **193** giving a spectral response to over 1050 nm in titanium dioxide devices with a lithium ion rich electrolyte. While optimisation of these devices is required to provide reasonable cell efficiencies, the observation of an IPCE response at such long wavelength is a significant step forwards in the design of near-IR photovoltaic devices.

5.6 References

(1) Yum, J. H.; Chen, P.; Grätzel, M.; Nazeeruddin, M. K. *ChemSusChem* **2008**, *1*, 699-707.
(2) Robertson, N. *Angew. Chem. Int. Ed.* **2006**, *45*, 2338-2345.
(3) Trachibana, Y.; Haque, S. A.; Mercer, I. P.; Durrant, J. R.; Klug, D. R. *J. Phys. Chem. B* **2000**, *104*, 1198-1205.
(4) Benkö, G.; Kallioinen, J.; Korppi-Tommola, J. E. I.; Yartsev, A. P.; Sundström, V. *J. Am. Chem. Soc.* **2002**, *124*, 489-493.
(5) Luque, A.; Hegedus, S. *Handbook of Photovoltaic Science and Engineering*; Wiley, 2003.
(6) Hagfeldt, A.; Grätzel, M. *Chem. Rev.* **1995**, *95*, 49-68.
(7) Haque, S. A.; Palomares, E.; Cho, B. M.; Green, A. N. M.; Hirata, N.; Klug, D. R.; Durrant, J. R. *J. Am. Chem. Soc.* **2005**, *127*, 3456-3462.
(8) Hagfeldt, A.; Boschloo, G.; Sun, L.; Kloo, L.; Pettersson, H. *Chem. Rev.* **2010**, *110*, 6595-6663.
(9) Ardo, S.; Meyer, G. J. *Chem. Soc. Rev* **2009**, *38*, 115-164.
(10) Snaith, H. J.; Schmidt-Mende, L. *Adv. Mater.* **2007**, *19*, 3187-3200.
(11) O'Regan, B.; Grätzel, M. *Nature* **1991**, *353*, 737-740.
(12) Nelson, J. *The Physics of Solar Cells*; Imperial College Press: London, 2003.
(13) Miller, A. J.; Hatton, R. A.; Chen, G. Y.; Silva, S. R. P. *Appl. Phys. Lett.* **2007**, *90*, 023105.
(14) Snaith, H. J. *Adv. Funct. Mater.* **2010**, *20*, 13-19.
(15) Tachibana, Y.; Hara, K.; Sayama, K.; Arakawa, H. *Chem. Mater.* **2002**, *14*, 2527-2535.
(16) Zhu, K.; Kopidakis, N.; Neale, N. R.; van de Lagemaat, J.; Frank, A. J. *J. Phys. Chem. B* **2006**, *110*, 25174-25180.
(17) Kopidakis, N.; Neale, N. R.; Zhu, K.; van de Lagemaat, J.; Frank, A. J. *Appl. Phys. Lett.* **2005**, *87*, 202106.
(18) Benkstein, K. D.; Kopidakis, N.; van de Lagemaat, J.; Frank, A. J. *J. Phys. Chem. B* **2003**, *107*, 7759-7767.
(19) van de Lagemaat, J.; Benkstein, K. D.; Frank, A. J. *J. Phys. Chem. B* **2001**, *105*, 12433-12436.
(20) Hagfeldt, A.; Björkstén, U.; Lindquist, S. E. *Sol. Energy Mater. Sol. Cells* **1992**, *27*, 293-304.
(21) Ito, S.; Zakeeruddin, S. M.; Humphry-Baker, R.; Liska, P.; Charvet, R.; Comte, P.; Nazeeruddin, M. K.; Péchy, P.; Takata, M.; Miura, H.; Uchida, S.; Grätzel, M. *Adv. Mater.* **2006**, *18*, 1202-1205.
(22) Hara, K.; Horiguchi, T.; Kinoshita, T.; Sayama, K.; Arakawa, H. *Sol. Energy Mater. Sol. Cells* **2001**, *70*, 151-161.
(23) Ferrere, S.; Zaban, A.; Gregg, B. A. *J. Phys. Chem. B* **1997**, *101*, 4490-4493.
(24) Oskam, G.; Bergeron, B. V.; Meyer, G. J.; Searson, P. C. *J. Phys. Chem. B* **2001**, *105*, 6867-6873.

(25) Bergeron, B. V.; Marton, A.; Oskam, G.; Meyer, G. J. *J. Phys. Chem. B* **2005**, *109*, 937-943.
(26) Wang, P.; Zakeeruddin, S. M.; Moser, J. E.; Humphry-Baker, R.; Grätzel, M. *J. Am. Chem. Soc.* **2004**, *126*, 7164-7165.
(27) Nusbaumer, H.; Zakeeruddin, S. M.; Moser, J. E.; Grätzel, M. *Chem. Eur. J.* **2003**, *9*, 3756-3763.
(28) Hamann, T. W.; Farha, O. K.; Hupp, J. T. *J. Phys. Chem. C* **2008**, *112*, 19756-19764.
(29) Boschloo, G.; Lindström, J.; Magnusson, E.; Holmberg, A.; Hagfeldt, A. *J. Photochem. Photobiol., A* **2002**, *148*, 11-15.
(30) Shi, C.; Dai, S.; Wang, K.; Pan, X.; Guo, L.; Zeng, L.; Hu, L.; Kong, F. *Sol. Energy Mater. Sol. Cells* **2005**, *86*, 527-535.
(31) Hara, K.; Nishikawa, T.; Kurashige, M.; Kawauchi, H.; Kashima, T.; Sayama, K.; Aika, K.; Arakawa, H. *Sol. Energy Mater. Sol. Cells* **2005**, *85*, 21-30.
(32) Kambe, S.; Nakade, S.; Kitamura, T.; Wada, Y.; Yanagida, S. *J. Phys. Chem. B* **2002**, *106*, 2967-2972.
(33) Wang, P.; Klein, C.; Humphry-Baker, R.; Zakeeruddin, S. M.; Grätzel, M. *Appl. Phys. Lett.* **2005**, *86*, 123508.
(34) Shi, D.; Pootrakulchote, N.; Li, R.; Guo, J.; Wang, Y.; Zakeeruddin, S. M.; Grätzel, M.; Wang, P. *J. Phys. Chem. C* **2008**, *112*, 17046-17050.
(35) Gorlov, M.; Kloo, L. *Dalton Trans.* **2008**, 2655-2666.
(36) Bai, Y.; Cao, Y.; Zhang, J.; Wang, M.; Li, R.; Wang, P.; Zakeeruddin, S. M.; Grätzel, M. *Nat. Mater.* **2008**, *7*, 626-630.
(37) Gao, F.; Wang, Y.; Shi, D.; Zhang, J.; Wang, M.; Jing, X.; Humphry-Baker, R.; Wang, P.; Zakeeruddin, S. M.; Grätzel, M. *J. Am. Chem. Soc.* **2008**, *130*, 10720-10728.
(38) Tennakone, K.; Wickramanayake, S. W. M. S.; Samarasekara, P.; Fernando, C. A. N. *Phys. Status Solidi A* **1987**, *104*, K57-K60.
(39) Redmond, G.; Fitzmaurice, D. *J. Phys. Chem.* **1993**, *97*, 1426-1430.
(40) Enright, B.; Redmond, G.; Fitzmaurice, D. *J. Phys. Chem.* **1994**, *98*, 6195-6200.
(41) Tachibana, Y.; Haque, S. A.; Mercer, I. P.; Moser, J. E.; Klug, D. R.; Durrant, J. R. *J. Phys. Chem. B* **2001**, *105*, 7424-7431.
(42) Boschloo, G.; Häggman, L.; Hagfeldt, A. *J. Phys. Chem. B* **2006**, *110*, 13144-13150.
(43) Green, A. N. M.; Chandler, R. E.; Haque, S. A.; Nelson, J.; Durrant, J. R. *J. Phys. Chem. B* **2005**, *109*, 142-150.
(44) Martínez-Díaz, M. V.; de la Torrea, G.; Torres, T. *Chem. Commun.* **2010**, *46*, 7090-7108.
(45) Imahori, H.; Umeyama, T.; Ito, S. *Acc. Chem. Res.* **2009**, *42*, 1809-1818.
(46) Radivojevic, I.; Varotto, A.; Farley, C.; Drain, C. M. *Energy Environ. Sci.* **2010**, *3*, 1897-1909.
(47) Walter, M. G.; Rudine, A. B.; Wamser, C. C. *J. Porphyrins Phthalocyanines* **2010**, *14*, 759-792.
(48) Wang, C. L.; Chang, Y. C.; Lan, C. M.; Lo, C. F.; Diau, E. W. G.; Lin, C. Y. *Energy Environ. Sci.* **2011**, *4*, 1788-1795.

(49) Bessho, T.; Zakeeruddin, S. M.; Yeh, C. Y.; Diau, E. W. G.; Grätzel, M. *Angew. Chem. Int. Ed.* **2010**, *49*, 6646-6649.
(50) Tanaka, M.; Hayashi, S.; Eu, S.; Umeyama, T.; Matano, Y.; Imahori, H. *Chem. Commun.* **2007**, 2069-2071.
(51) Hayashi, S.; Tanaka, M.; Hayashi, H.; Eu, S.; Umeyama, T.; Matano, Y.; Araki, Y.; Imahori, H. *J. Phys. Chem. C.* **2008**, *112*, 15576-15585.
(52) Eu, S.; Hayashi, S.; Umeyama, T.; Matano, Y.; Araki, Y.; Imahori, H. *J. Phys. Chem. C.* **2008**, *112*, 4396-4405.
(53) Kira, A.; Matsubara, Y.; Iijima, H.; Umeyama, T.; Matano, Y.; Ito, S.; Niemi, M.; Tkachenko, N. V.; Lemmetyinen, H.; Imahori, H. *J. Phys. Chem. C* **2010**, *114*, 11293-11304.
(54) Imahori, H.; Iijima, H.; Hayashi, H.; Toude, Y.; Umeyama, T.; Matano, Y.; Ito, S. *ChemSusChem* **2011**, *4*, 797-805.
(55) Hayashi, S.; Matsubara, Y.; Eu, S.; Hayashi, H.; Umeyama, T.; Matano, Y.; Imahori, H. *Chem. Lett.* **2008**, *37*, 846-847.
(56) Mai, C. L.; Huang, W. K.; Lu, H. P.; Lee, C. W.; Chiu, C. L.; Liang, Y. R.; Diau, E. W. G.; Yeh, C. Y. *Chem. Commun.* **2010**, *46*, 809-811.
(57) Mozer, A. J.; Griffith, M. J.; Tsekouras, G.; Wagner, P.; Wallace, G. G.; Mori, S.; Sunahara, K.; Miyashita, M.; Earles, J. C.; Gordon, K. C.; Du, L.; Katoh, R.; Furube, A.; Officer, D. L. *J. Am. Chem. Soc.* **2009**, *131*, 15621-15623.
(58) Park, J. K.; Chen, J.; Lee, H. R.; Park, S. W.; Shinokubo, H.; Osuka, A.; Kim, D. *J. Phys. Chem. C* **2009**, *113*, 21956-21963.
(59) Altobello, S.; Argazzi, R.; Caramori, S.; Contado, C.; Da Fré, S.; Rubino, P.; Choné, C.; Larramona, G.; Bignozzi, C. A. *J. Am. Chem. Soc.* **2005**, *127*, 15342-15343.
(60) Jiao, C.; Zu, N.; Huang, K. W.; Wang, P.; Wu, J. *Org. Lett.* **2011**, *13*, 3652-3655.
(61) Mishra, A.; Fischer, M. K. R.; Bäuerle, P. *Angew. Chem. Int. Ed.* **2009**, *48*, 2474-2499.
(62) Wang, Q.; Campbell, W. M.; Bonfantani, E. E.; Jolley, K. W.; Officer, D. L.; Walsh, P. J.; Gordon, K.; Humphry-Baker, R.; Nazeeruddin, M. K.; Grätzel, M. *J. Phys. Chem. B* **2005**, *109*, 15397-15409.
(63) Kay, A.; Grätzel, M. *J. Phys. Chem.* **1993**, *97*, 6272-6277.
(64) Lo, C. F.; Luo, L.; Diau, E. W. G.; Chang, I. J.; Lin, C. Y. *Chem. Commun.* **2006**, 1430-1432.
(65) Dos Santos, T.; Morandeira, A.; Koops, S.; Mozer, A. J.; Tsekouras, G.; Dong, Y.; Wagner, P.; Wallace, G.; Earles, J. C.; Gordon, K. C.; Officer, D.; Durrant, J. R. *J. Phys. Chem. C* **2010**, *114*, 3276-3279.
(66) Cid, J. J.; García-Iglesias, M.; Yum, J. H.; Forneli, A.; Albero, J.; Martínez-Ferrero, E.; Vázquez, P.; Grätzel, M.; Nazeeruddin, M. K.; Palomares, E.; Torres, T. *Chem. Eur. J.* **2009**, *15*, 5130-5137.
(67) Campbell, W. M.; Burrell, A. K.; Officer, D. L.; Jolley, K. W. *Coord. Chem. Rev.* **2004**, *248*, 1363-1379.
(68) Anderson, H. L. *Chem. Commun.* **1999**, 2323-2330.
(69) Lin, V. S. Y.; DiMagno, S. G.; Therien, M. J. *Science* **1994**, *264*, 1105-1111.

(70) Taylor, P. N.; Wylie, A. P.; Huuskonen, J.; Anderson, H. L. *Angew. Chem. Int. Ed.* **1998**, *37*, 986-989.
(71) Falaras, P. *Sol. Energy Mater. Sol. Cells* **1998**, *53*, 163-175.
(72) Duffy, N. W.; Dobson, K. D.; Gordon, K. C.; Robinson, B. H.; McQuillan, A. J. *Chem. Phys. Lett.* **1997**, *266*, 451-455.
(73) Weng, Y. X.; Li, L.; Liu, Y.; Wang, L.; Yang, G. Z. *J. Phys. Chem. B* **2003**, *107*, 4356-4363.
(74) Ma, T.; Inoue, K.; Yao, K.; Noma, H.; Shuji, T.; Abe, E.; Yu, J.; Wang, X.; Zhang, B. *J. Electroanal. Chem.* **2002**, *537*, 31-38.
(75) Shao, M.; Zhao, Y. *Tetrahedron Lett.* **2010**, *51*, 2892-2895.
(76) Veyrat, M.; Ramasseul, R.; Turowska-Tyrk, I.; Scheidt, W. R.; Autret, M.; Kadish, K. M.; Marchon, J. C. *Inorg. Chem.* **1999**, *38*, 1772-1779.
(77) Hagberg, D. P.; Yum, J. H.; Lee, H.; De Angelis, F.; Marinado, T.; Karlsson, K. M.; Humphry-Baker, R.; Sun, L.; Hagfeldt, A.; Grätzel, M.; Nazeeruddin, M. K. *J. Am. Chem. Soc.* **2008**, *130*, 6259-6266.
(78) Zhang, F.; Bai, S.; Yap, G. P. A.; Tarwade, V.; Fox, J. M. *J. Am. Chem. Soc.* **2005**, *127*, 10590-10599.
(79) Connelly, N. G.; Geiger, W. E. *Chem. Rev.* **1996**, *96*, 877-910.
(80) D'Andrade, B. W.; Datta, S.; Forrest, S. R.; Djurovich, P.; Polikarpov, E.; Thompson, M. E. *Org. Electron.* **2005**, *6*, 11-20.
(81) Tiwana, P.; Docampo, P.; Johnston, M. B.; Snaith, H. J.; Herz, L. M. *ACS Nano* **2011**, *5*, 5158-5166.
(82) Horiuchi, T.; Miura, H.; Uchida, S. *Chem. Commun.* **2003**, 3036-3037.
(83) O'Regan, B. C.; López-Duarte, I.; Victoria Martínez-Díaz, M.; Forneli, A.; Albero, J.; Morandeira, A.; Palomares, E.; Torres, T.; Durrant, J. R. *J. Am. Chem. Soc.* **2008**, *130*, 2906-2907.
(84) Mozer, A. J.; Wagner, P.; Officer, D. L.; Wallace, G. G.; Campbell, W. M.; Miyashita, M.; Sunahara, K.; Mori, S. *Chem. Commun.* **2008**, 4741-4743.
(85) Becke, A. D. *J. Chem. Phys.* **1993**, *98*, 5648-5652.
(86) Rassolov, V. A.; Ratner, M. A.; Pople, J. A.; Redfern, P. C.; Curtiss, L. A. *J. Comput. Chem.* **2001**, *22*, 976-984.
(87) Stevens, W. J.; Krauss, M.; Basch, H.; Jasien, P. G. *Can. J. Chem.-Rev. Can. Chim.* **1992**, *70*, 612-630.
(88) Snaith, H. J.; Ducati, C. *Nano Lett.* **2010**, *10*, 1259-1265.
(89) Kay, A.; Grätzel, M. *Chem. Mater.* **2002**, *14*, 2930-2935.

Chapter 6: Experimental Section

6.1 General Procedures

The handling of all air or water sensitive materials was carried out using standard high vacuum techniques. Freeze-thaw degassing was affected by freezing under nitrogen, pumping under vacuum, and then saturating with nitrogen. This process was repeated at least three times. Dry DCM, toluene and THF were obtained by passing through alumina under nitrogen pressure and stored over activated molecular sieves (3 Å, 8-12 mesh); triethylamine, diisopropylamine, *m*-xylene and DMF were freshly distilled from CaH_2 before use. Et_2O was freshly distilled from sodium/benzophenone before use. Unless specified otherwise, all other solvents were used as commercially supplied. Where mentioned, 'PET' refers to 40:60 petroleum ether. Where mixtures of solvents were used, ratios are reported by volume.

Flash chromatography was carried out on silica gel 60 under positive pressure. Size exclusion chromatography (SEC) was carried out under gravity using cross-linked polystyrene Bio-Beads® SX-1 (200–400 mesh). Analytical thin layer chromatography (TLC) was carried out on aluminum backed silica gel 60 F254 plates. Visualization was achieved using UV light when necessary.

UV-vis spectra were recorded in solution using a Perkin-Elmer Lambda 20 spectrometer (1 cm path length quartz cell). UV-vis-NIR spectra were recorded using a Perkin-Elmer Lambda 9 photospectrometer. NMR spectra were recorded at 298 K using Bruker DPX400 (400/100 MHz) or Bruker AVII500 (500/125 MHz) instruments. ^{1}H and ^{13}C NMR spectra are reported in parts per million (ppm) relative to tetramethylsilane (δ_H 0.00) with residual $CHCl_3$ at δH = 7.27 ppm and δC = 77.16 ppm; coupling constants (J) are given in Hertz and are accurate to ±0.4 Hz. Melting points were measured using a Leica Galen III melting point apparatus. IR spectra were recorded using a Bruker Tensor 27 FT-IR spectrometer by either attenuated total reflectance (ATR) or using KBr discs. Mass spectra were measured by electrospray ionisation (ESI) using a Bruker micOTOF, or by the matrix assisted laser desorption ionisation time of flight (MALDI-TOF) technique using a

Micromass MALDI micro MX spectrometer with dithranol matrix. Only the peak of the molecular ion is reported.

6.2 Synthesis of Known Compounds

Dipyrromethane[1]

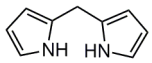

Formaldehyde (33% w/w solution in water, 8.10 mL, 90.0 mmol) was added to pyrrole (**143**) (150 mL, 2.16 mol) and the solution was degassed three times. With vigorous stirring, trifluoroacetic acid (TFA) (0.810 mL, 10.6 mmol) was added by syringe and the mixture was stirred for 5 min. DCM (150 mL) was added and the reaction was quenched with saturated $NaHCO_3$ (aq) (100 mL). The organic layer was separated and washed with saturated $NaHCO_3$ (aq) (2 × 50 mL) and then with water (3 × 100 mL). The organic layer was separated and the solvent was removed. The oily residue was distilled using a Kugelrohr (160 °C, 0.04 bar) to yield white crystals of dipyrromethane (5.40 g, 41%). ^{1}H NMR (400 MHz, $CDCl_3$) δH 7.77 (br. s, 2H, N*H*), 6.65 (m, 2H, pyrrole H_α), 6.17 (m, 2H, pyrrole H_β), 6.06 (m, 2H, pyrrole H_β), 3.97 (s, 2H, *meso*-CH_2). *As Lit.*

Free-base 5,15-bis-(3,5-di-*tert*-butylphenyl)porphyrin[2]

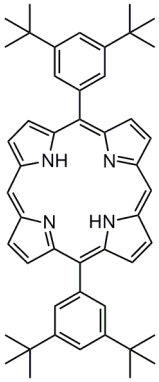

Dipyrromethane (1.00 g, 6.84 mmol) and 3,5-di-*tert*-butylbenzaldehyde (1.50 g, 6.88 mmol) were dissolved in dry DCM (2.0 L). The reaction mixture was degassed three times and TFA (352 μL, 4.59 mmol) was added by syringe. After stirring for 3 h in the dark, DDQ (2.52 g, 11.1 mmol) was added and the mixture was stirred for a further 20 min before triethylamine

(4.5 mL) was added to quench the acid. The mixture was then passed through a short silica plug (DCM) to remove tarry side products. The solvent was removed and the residue recrystallised from DCM/methanol to yield a purple powder of the title compound (1.01 g, 43%). ^{1}H NMR (400 MHz, $CDCl_3$) δH 10.33 (s, 2H, H_{meso}), 9.42 (d, 4H, J = 4.8 Hz, H_β), 9.16 (d, 4H, J = 4.8 Hz, H_β), 8.17 (d, 4H, J = 1.9 Hz, Ar-H_{ortho}), 7.86 (t, 2H, J = 1.9 Hz, Ar-H_{para}), 1.60 (s, 36H, *t*-Butyl-H), -2.99 (br. s, 2H, N*H). As Lit*.

[5,15-Bis-(3,5-di-*tert*-butylphenyl)porphyrinato]zinc(II)[2]

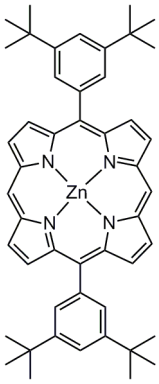

5,15-Bis-(3,5-di-*tert*-butylphenyl)porphyrin (1.01 g, 1.47 mmol) was dissolved in DCM (200 mL). Zinc (II) acetate dihydrate (1.88 g, 8.56 mmol) was dissolved in methanol (20 mL) and added to the solution of 5,15-bis-(3,5-di-*tert*-butylphenyl)porphyrin. The reaction mixture was stirred for 1 h at room temperature before being concentrated and passed through a short silica plug (DCM). The solvent was removed and the title compound was recrystallised from DCM/methanol to give the title compound as a pink powder (1.07 g, 97%). ^{1}H NMR (400 MHz, $CDCl_3$) δH 10.33 (s, 2H, H_{meso}), 9.46 (d, 4H, J = 4.45 Hz, H_β), 9.22 Hz (d, 4H, J = 4.45 Hz, H_β), 8.17 (d, 4H, J = 1.91 Hz, Ar-H_{ortho}), 7.86 (t, 2H, J = 1.91 Hz, Ar-H_{para}), 1.59 Hz (s, 36H, $H_{t\text{-}butyl}$). *As Lit*.

[5, 15-Dibromo-10,20-bis-(3,5-di-*tert*-butylphenyl)porphyrinato]zinc(II)[2]

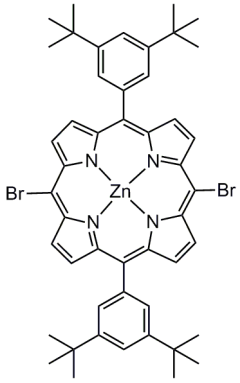

[5,15-Bis-(3,5-di-*tert*-butylphenyl)porphinato]-zinc(II) (0.150 g, 0.200 mmol) was dissolved in chloroform (30 mL) and pyridine (0.2 mL). To this stirred solution, *N*-bromosuccinimide (0.071 g, 0.399 mmol) in chloroform (10 mL) and pyridine (0.2 mL) was added dropwise at room temperature. The extent of the reaction was monitored by TLC and, at completion, acetone (30 mL) was added to quench the reaction. The solvents were removed and the product was precipitated from DCM/methanol to give the title compound as a purple solid (0.176 g, 97%). 1H NMR (400 MHz, $CDCl_3$) δH 9.65 (d, 4H, J = 4.6 Hz, H_{β}), 8.90 (4H, J = 4.6 Hz, H_{β}), 7.98 (d, 4H, J = 1.9 Hz, Ar-H_{ortho}), 7.79 (t, 2H, J = 1.7 Hz, Ar-H_{para}), 1.54 (s, 36 H, $H_{t\text{-}butyl}$). *As Lit*.

[5, 15-Dibromo-10,20-bis-(3,5-bis(octyloxy)phenyl)porphyrinato]zinc(II)[3] **(108)**

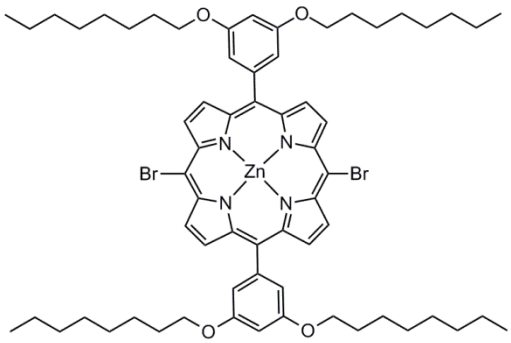

This known compound was prepared by modification of a literature procedure.[2] [5,15-Bis-(3,5-bis(octyloxy)phenyl)porphinato]-zinc(II) **(107)** (0.100 g, 0.096 mmol) was dissolved in chloroform (40 mL) and pyridine (0.2 mL). To this stirred solution, *N*-bromosuccinimide (0.036 g, 0.202 mmol) in chloroform (10 mL) and pyridine (0.2 mL) was added dropwise at room temperature. The extent of the reaction was monitored by TLC and, at completion,

acetone (20 mL) was added to quench the reaction. The solvents were removed and the product was precipitated from DCM/methanol to give the title compound as a purple solid (0.095 g, 83%). 1H NMR (400 MHz, $CDCl_3$) δH 9.62 (d, 4H, J = 4.7 Hz, H_{β}), 8.97 (4H, J = 4.7 Hz, H_{β}), 7.30 (d, 4H, J = 2.2 Hz, Ar-H_{ortho}), 6.88 (t, 2H, J = 2.2 Hz, Ar-H_{para}), 4.12 (t, 8H, J = 6.7 Hz, H_{oct}), 1.91-1.82 (m, 8H, H_{oct}), 1.55-1.46 (m, 8H, H_{oct}), 1.41-1.24 (m, 32H, H_{oct}), 0.89-0.83 (m, 12H, H_{oct}).

[5, 15-(4,4,5,5-Tetramethyl-[1,3,2]dioxaborolan-2-yl)-10,20-bis-(3,5-di-*tert*-butylphenyl)porphyrinato]zinc(II)[4,5] (109)

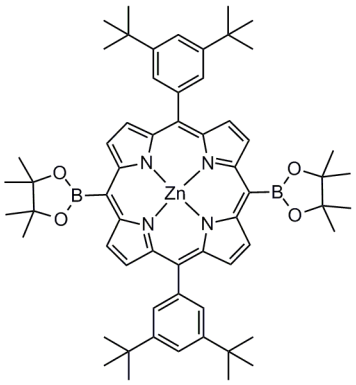

A two necked flask was dried under vacuum and charged with [5,15-dibromo-10,20-bis-(3,5-di-*tert*-butylphenyl)porphyrinato]zinc(II) (0.200 g, 0.220 mmol) and $Pd_2Cl_2(PPh_3)_2$ (0.031 g, 0.044 mmol). The flask was purged with argon and to this THF (20 mL), toluene (20 mL) and triethylamine (4.5 mL) were added by cannula. The reaction mixture was freeze-thaw degassed and the pinacolborane (1.12 mL, 7.72 mmol) was added by syringe. The reaction mixture was heated to 60 °C and stirred overnight. At completion the reaction mixture was allowed to cool to room temperature and water (10 mL) was added very slowly by syringe. The organic layer was separated and washed with water (3 × 10 mL). The organic layers were collected, dried over Na_2SO_4, filtered and the solvents removed. The residue was purified by silica gel chromatography where the side products were removed with an eluent of 2:1 DCM:PET and the product was eluted with ethyl acetate. The solvents were removed and the solid recovered was precipitate from DCM/methanol to give the title compound as a purple solid (0.162 g, 74%).[1]H NMR (400 MHz, $CDCl_3$) δH 9.93 (d, 4H, J = 4.7 Hz, H_{β}), 9.14

(d, 4H, J = 4.7 Hz, H_{β}), 8.09 (d, 4H, J = 1.8 Hz, Ar-H_{ortho}), 7.82 (t, 2H, J = 1.8 Hz, Ar-H_{para}), 1.86 (s, 24H, H_{methyl}), 1.56 (s, 36H, $H_{t\text{-}butyl}$).

Free-base 5,10,15,20-Tetraanthracene porphyrin[6] (67)

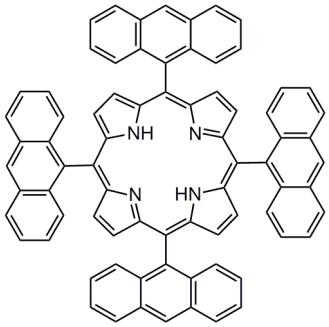

To a solution of 9-bromoanthracene **(70)** (2.00 g, 7.78 mmol) in freshly distilled diethyl ether (25 mL) was added butyllithium (1.6 M solution in hexanes, 4.9 mL, 7.84 mmol) and the mixture was stirred at room temperature for 1 h. After this, a solution of pyrrole-2-carboxaldehyde (0.350 g, 3.68 mmol) in diethyl ether (5 mL) was added and the solution was stirred for 1 h after which time the mixture was poured into a beaker containing ammonium chloride an ice (3 g:10 g). The precipitated anthracene was filtered off and the organic phase of the remaining mixture was extracted with diethyl ether and then washed with water (3 × 10 mL). The organic layer was collected and the solvent removed. The crude product was then dissolved in toluene (20 mL) and added to a boiling mixture of propionic acid (10 mL) and toluene (20 mL). A reflux condenser was attached to the flask and the reaction mixture was stirred for 3 h at 100 °C in the presence of air. The reaction mixture was then allowed to cool overnight where upon the porphyrin product precipitated. The porphyrin was collected by filtration and was washed with 1:1 $CHCl_3$: methanol (20 mL) and then with methanol (20 mL). The crude product was then passed through a short silica plug ($CHCl_3$). The solvents were then removed to give the title compound as a dark purple solid (0.061 g, 6.5% w.r.t pyrrole-2-carboxaldehyde). ^{1}H NMR (400MHz, $CDCl_3$) δH 8.86 (s, 4H, H_{anth}), 8.23 (d, 8H, J = 8.6 Hz, H_{anth}), 8.11 (s, 8H, H_{β}), 7.43 (ddd, 8H, J_1 = 1.1 Hz, J_2 = 6.5 Hz, J_3 = 8.4 Hz, H_{anth}), 7.19 (d, 8H, J = 8.7 Hz, H_{anth}), 7.04 (ddd, 8H, J_1 = 1.1 Hz, J_2 = 6.5 Hz, J_3 = 8.7 Hz, H_{anth}). m/z (MALDI TOF MS+) 1014.74, ($C_{76}H_{46}N_4$; [M]+, requires 1014.37). *As Lit*.

1, 8-Diacetoxyanthraquinone[7,8] **(83)**

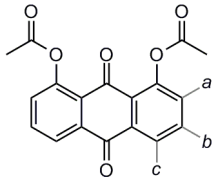

To a mixture of 1,8-dihydroxyanthraquinone **(82)** (2.00 g, 8.33 mmol) and acetic anhydride (23.6 mL, 250.1 mmol) was added dropwise concentrated sulphuric acid (0.44 mL, 8.25 mmol) and the reaction mixture was stirred at reflux for 30 min. The resulting yellow solution was added to water (50 mL) and the yellow precipitate formed was removed by filtration and washed with water (3 × 10 mL) then dried under reduced pressure to give the title compound as a yellow powder (2.50 g, 93%). ^{1}H NMR (400MHz, $CDCl_3$) δH 8.24 (dd, 2H, J_1 = 1.3 Hz, J_2 = 7.6 Hz, H_c), 7.80 (m, 2H, H_b), 7.42 (dd, 2H, J_1 = 1.3 Hz, J_2 = 8.2 Hz, H_a), 2.46 (s, 6H, H_{acetyl}). *As Lit*.

1, 8-Diacteoxyanthracene[9,10] **(84)**

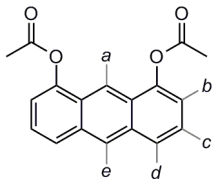

To 1,8–diacetoxyanthraquinone **(83)** (1.30 g, 4.01 mmol) was added acetic acid (14.0 mL) and acetic anhydride (35.2 mL). To this mixture, zinc dust (2.50 g, 38.2 mmol) and anhydrous sodium acetate (0.510 g, 6.22 mmol) were added and the mixture was stirred and heated to reflux for 30 min under nitrogen. The reaction mixture was then filtered to remove the zinc and the remaining solution was concentrated and then purified by silica gel chromatography (DCM) to yield a pale yellow solid of 1,8-diacetoxyanthracene **(84)** (0.790 g, 67%). ^{1}H NMR (400MHz, $CDCl_3$) δH 8.52 (s, 1H, H_e), 8.47 (s, 1H, H_a), 7.92 (d, 2H, J = 8.6 Hz, H_d), 7.49 (dd, 2H, J_1 = 7.3 Hz, J_2 = 8.6 Hz, H_c), 7.30 (dd, 2H, J_1 = 0.1 Hz, J_2 = 7.3 Hz, H_b), 2.54 (s, 6H, H_{acetyl}). *As Lit*.

10-Bromo-1,8-diacetoxyanthracene[11] **(85)**

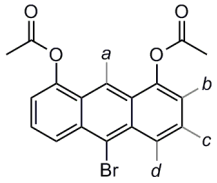

To a solution of 1,8-diacetoxyanthracene **(84)** (0.350 g, 1.19 mmol) in acetic acid (500 mL), bromine (0.068 mL, 1.32 mmol) was added dropwise and stirred at room temperature for 16 h after which formation of a green precipitate was observed. The reaction mixture was poured into water (1.5 L) to favour further precipitation of the product. The water was then filtered to isolate a green solid which was purified by silica gel chromatography (DCM) to give 10-bromo-1,8-diacetoxyanthracene **(85)** as a pale green solid (0.198 g, 45%). ^{1}H NMR (400 MHz, $CDCl_3$) δH 8.55 (s, 1H, H_a), 8.44 (d, 2H, J = 9.2 Hz, H_d), 7.62 (dd, 2H, J_1 = 7.3 Hz, J_2 = 8.9 Hz, H_c), 7.36 (dd, 2H, J_1 = 0.6 Hz, J_2 = 7.3 Hz, H_b), 2.54 (s, 6H, H_{acetyl}). m/z (ESI $[M+Na]^+$) 394.9887 ($[M+Na]^+$ 100%, $C_{18}H_{13}Br_1Na_1O_4$, requires 394.9889). *As Lit*.

10-Bromo-1,8-dihydroxyanthracene[11] **(86)**

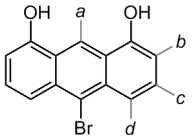

A solution of 10-bromo-1,8-diacetoxyanthracene **(85)** (0.100 g, 0.268 mmol) in THF (35 mL) was degassed and purged with N_2. To this an aqueous solution of sodium hydroxide (1.0 M, 1.73 mL, 1.73 mmol) was added dropwise and stirred under nitrogen. The solution turned deep yellow then bright red and then back to yellow. The reaction was monitored by TLC. At completion the reaction mixture was quenched with an aqueous solution of HCl (1.0 M, 1.73 mL, 1.73 mmol) and its pH monitored by Universal Indicator Paper. The mixture was then filtered and the solvents removed to give 10-bromo-1,8-dihydroxyanthracene **(86)** as a green solid (0.074 g, 96%). ^{1}H NMR (400 MHz, MeOD) δH 9.32 (s, 1H, H_a), 7.92 (d, 2H, J = 8.9 Hz, H_d), 7.42 (dd, 2H, J_1 = 7.3 Hz, J_2 = 8.9 Hz, H_c), 6.82 (d, 2H, J = 7.3 Hz, H_b). *As Lit*.

10-Bromo-1,8-bis(octyloxy)anthracene[11] **(72)**

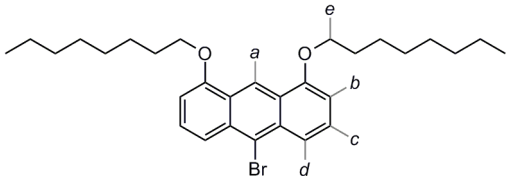

10-bromo-1,8-dihydroxyanthracene **(86)** (0.100 g, 0.346 mmol) was dissolved in acetone (30 mL) and to this 1-bromooctane (0.179 mL, 1.04 mmol), potassium carbonate (0.143 g, 1.04 mmol) and 18-crown-6 (0.018 g, 0.068 mmol) were added. The reaction mixture was refluxed under nitrogen for 60 h whilst being stirred. The reaction mixture was then allowed to cool before being filtered. The acetone was removed and the residue was purified by silica gel chromatography (3:1 PET: DCM) to give 10-bromo-1,8-dioctyloxyanthracene **(72)** as a yellow solid (0.072 g, 41%). ^{1}H NMR (400 MHz, $CDCl_3$) δH 9.41 (s, 1H, H_a), 8.03 (d, 2H, J = 8.9 Hz, H_d), 7.49 (dd, 2H, J_1 = 7.3 Hz, J_2 = 8.9 Hz, H_c), 6.76 (d, 2H, J = 7.3 Hz, H_b), 4.22 (t, 4H, J = 6.56 Hz, H_e), 2.06-1.97 (m, 4H, H_{oct}), 1.70-1.61 (m, 4H, H_{oct}), 1.49-1.29 (m, 16H, H_{oct}), 0.92-0.88 (m, 6H, H_{oct}), ^{13}C NMR (125 MHz, $CDCl_3$) δC 155.3, 131.8, 127.5, 125.0, 121.2, 119.4, 116.5, 102.5, 68.3, 31.9, 29.5, 29.4, 29.3, 26.3, 22.7, 14.1. m/z (MALDI TOF MS+) 512.25, ($C_{30}H_{41}BrO_2$; [M]+, requires 512.23). *As Lit*.

Methyl-4-iodobenzoate[12] **(202)**

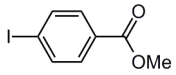

To a 100 mL round bottom flask was added 4-iodobenzoic acid **(201)** (1.00 g, 4.03 mmol). To this was added methanol (50 mL) and concentrated sulphuric acid (0.50 mL, 9.38 mmol). This reaction mixture was then heated under reflux and stirred. The extent of the reaction was monitored by TLC. At completion (3.5 h), the solvent was removed and the residue was dissolved in ethyl acetate and washed with water (3 × 10 mL) and brine (2 × 10 mL). The organic layer was separated and the solvent evaporated. The residue was then passed over a silica gel plug (1:1 ethyl acetate: PET) to give the title compound as a white solid (0.92 g, 87%). 1H NMR (400 MHz, $CDCl_3$) δH 7.81 (d, J = 8.6 Hz, 2H, Ar-H), 7.74 (d, J = 8.6 Hz, 2H, Ar-H), 3.91 (s, 3H, H_{methyl}). *As Lit.*

6.3 Synthesis of Novel Compounds

1,8-Bis(2,6-diisopropylphenoxy)anthraquinone (121)

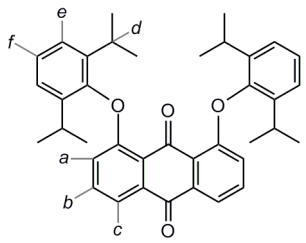

This novel compound was prepared by modification of a literature procedure.[13] A flask containing 1,8-dichloroanthraquinone **(124)** (0.050 g, 0.180 mmol) and potassium carbonate (0.132 g, 0.955 mmol) was dried overnight under vacuum and then purged with nitrogen. To this mixture 2,6-diisopropylphenol (0.074 mL, 0.400 mmol) and dry DMF (5 mL) were added by syringe. The reaction mixture was heated to 136 °C and stirred for 3 days. The extent of the reaction was monitored by TLC. At completion the reaction mixture was allowed to cool to room temperature and was quenched with water (20 mL) and extracted with ethyl acetate. The organic layers were collected, washed with water, dried over $MgSO_4$ and filtered. The solvent was removed and the solid was purified by chromatography on silica gel (2:1 PET : DCM). The solvents were then removed and the product was precipitated from DCM/methanol to give the title compound as a yellow solid (0.053 g, 53%). ^{1}H NMR (400 MHz, $CDCl_3$) δH 7.91 (dd, 2H, J_1 = 0.6 Hz, J_2 = 7.6 Hz, H_c), 7.48 (dd, 2H, J_1 = 8.0 Hz, J_2 = 8.3 Hz, H_b), 7.26-7.20 (m, 6H, H_{e+f}), 6.83 (dd, 2H, J_1 = 8.6 Hz, J_2 = 0.8 Hz, H_a), 3.10 (sep, 4H, J = 7.0 Hz, H_d), 1.23 (d, 12H, J = 7.0 Hz, H_{methyl}), 1.08 (d, 12H, J = 7.0 Hz, H_{methyl}). ^{13}C NMR (125 MHz, $CDCl_3$) δC 184.0, 181.4, 158.9, 148.4, 141.3, 135.2, 133.5, 126.2, 124.7, 123.2, 120.4, 119.9, 27.1, 24.0, 22.9. λ_{max} / nm ($CHCl_3$) 383, 274. m/z (MALDI TOF MS+) 561.60, ($C_{38}H_{40}O_4$; [M]+, requires 561.30). IR (ATR): ν / cm^{-1} 2964 (s), 1677 (s), 1584 (s), 1438 (s), 1384 (s), 1305 (s), 1258 (s), 1239 (s), 1176 (s), 1098 (m), 1033 (m), 979 (m), 937 (w), 861 (s), 842 (m), 779 (s), 762 (s), 741 (s). m.p.: 181— 184 °C.

1,8-Bis-(2,4,6-trimethylphenoxy)anthraquinone (125)

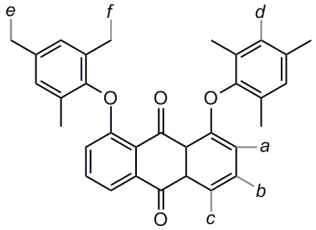

This novel compound was prepared by modification of a literature procedure.[13] A flask containing 1,8-dichloroanthraquinone **(124)** (0.500 g, 1.80 mmol), potassium carbonate (1.25 g, 9.04 mmol) and 2,4,6-trimethyphenol **(126)** (0.983 g, 7.22 mmol) was dried under vacuum and then purged with nitrogen. To this mixture, dry DMF (5.0 mL) was added by syringe. The reaction mixture was heated to 136 °C and stirred for 3 days. The extent of the reaction was monitored by TLC. At completion, the reaction mixture was allowed to cool to room temperature and water (10 mL) was added. The organic products were extracted with DCM and washed with water (3 × 30 mL). The organic layers were collected and the solvent removed. The solid residue was purified by chromatography on silica gel (2:1 PET:DCM) and then precipitated from DCM/methanol to give the title compound as a yellow solid (0.438 g, 51%). ^{1}H NMR (400 MHz, $CDCl_3$) δH 7.89 (d, 2H, J = 7.6 Hz, H_c), 7.47 (t, 2H, J = 8.1 Hz, H_b), 6.91 (s, 4H, H_d), 6.82 (d, 2H, J = 8.3 Hz, H_a), 2.31 (s, 6H, H_e), 2.14 (s, 12H, H_f). ^{13}C NMR (125 MHz, $CDCl_3$) δC 183.8, 181.9, 157.8, 148.7, 135.1, 134.8, 133.7, 130.5, 129.7, 123.4, 120.0, 119.7, 20.8, 16.3. m/z (MALDI TOF MS+), 477.21 ($C_{32}H_{28}O_4$; [M]+, requires 477.09). λ_{max} / nm ($CHCl_3$) (log ε) 258 (4.55), 384 (3.98). IR (KBr): ν / cm^{-1} 2919 (m), 1674 (s), 1585 (s), 1482 (s), 1439 (s), 1314 (s), 1242 (s), 1200 (s), 1143 (s), 1035 (m), 979 (m), 846 (s), 791 (m), 743 (s). m.p.: 218 — 220 °C.

4,5-Bis-(2,4,6-trimethylphenoxy)anthracen-9(10H)-one (127)

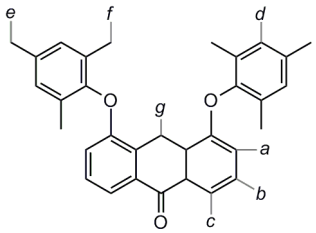

This novel compound was prepared by modifying a literature procedure.[14] To a suspension of 1,8-bis-(2,4,6-trimethylphenoxy)anthraquinone **(125)** (0.150 g, 0.315 mmol) in methanol (10

mL) was added sodium borohydride (1.19 g, 31.5 mmol). The reaction mixture stirred at room temperature for 3 days. When the colour of the suspension changed from deep yellow to off-white, the suspension was poured into a beaker containing ice (25 g). The mixture was filtered and the solid residue was washed with hot 1:1 AcOH/HCl (20 mL) then, when cool, was washed with a saturated solution of $NaHCO_3$ (aq) (3 × 10 mL) followed by water (3× 10 mL) then dried under vacuum. The pale yellow solid collected was found to be the title compound (0.124 g, 85%). ^{1}H NMR (500 MHz, $CDCl_3$) δH 8.04 (d, 2H, J = 8.0 Hz, H_c), 7.29 (t, 2H, J = 8.0 Hz, H_b), 6.95 (s, 4H, H_d), 6.65 (d, 2H, J = 8.0 Hz, H_a), 4.56 (s, 2H, H_g), 2.33 (s, 6H, H_e), 2.13 (s, 12H, H_f). ^{13}C NMR (125 MHz, $CDCl_3$) δC 184.2, 155.1, 148.7, 134.8, 133.1, 130.6, 129.7, 128.9, 127.4, 120.0, 115.4, 22.9, 20.8, 16.1. m/z (MALDI TOF MS+), 463.01 ($C_{32}H_{30}O_3$; [M]+, requires 463.23). λ_{max} / nm ($CHCl_3$) (log ε) 247 (4.27), 268 (4.01), 280 (3.91), 318 (3.42). IR (KBr): ν / cm^{-1} 2919 (m), 1665 (s), 1591 (s), 1458 (s), 1305 (s), 1246 (s), 1216 (s), 1145 (m), 980 (m), 865 (m). m.p.: 193 — 195 °C.

4,5-Bis-(2,4,6-trimethylphenoxy)anthracen-9-yl trifluoromethanesulfonate (128)

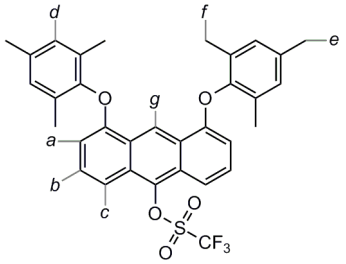

This novel compound was prepared by modifying a literature procedure.[15] A two-necked flask was dried under vacuum, purged with nitrogen and charged with 4,5-bis-(2,4,6-trimethylphenoxy)anthracen-9(10H)-one (**127**) (0.900 g, 1.95 mmol). To this, dry DCM (3.0 mL) was added and the solution was cooled to -78 °C and stirred. To this, LiHMDS (1.0 M solution in THF, 9.70 mL, 9.70 mmol) was added by syringe and the reaction mixture was stirred for 90 min. After this time, triflic anhydride (1.96 mL, 11.65 mmol) was added by syringe and the reaction mixture was stirred for a further 2 h at -78 °C. The reaction mixture was then warmed to room temperature, quenched with water (5 mL) and extracted with DCM. The organic layers were collected and the solvent removed. The solid residue was purified by silica chromatography (2:1 PET: DCM) to afford the title compound as a yellow

solid (0.635 g, 55%). ^{1}H NMR (400 MHz, $CDCl_3$) δH 9.88 (s, 1H, H_g), 7.85 (d, 2H, J = 8.9 Hz, H_c), 7.43 (d, 2H, J = 8.4 Hz, H_b), 6.98 (s, 4H, H_d), 6.40 (d, 2H, J = 7.8 Hz, H_a), 2.36 (s, 6H, H_e), 2.16 (s, 12H, H_f). ^{13}C NMR (125 MHz, $CDCl_3$) δC 154.0, 148.7, 139.7, 134.9, 130.8, 129.7, 128.3, 126.3, 124.3, 118.9 (q, J = 320.4 Hz, CF_3), 117.4, 113.7, 104.8, 20.8, 16.1. m/z (ESI [M+Na]+) 617.1579 ([M+Na]$^+$ 100%, $C_{33}H_{29}F_3NaO_5S$, requires 617.1580). λ_{max} / nm ($CHCl_3$) (log ε) 267 (5.05), 367 (3.76), 378 (3.81), 397 (3.89), 419 (3.73). IR (KBr): ν / cm^{-1} 2921 (m), 1626 (m), 1561 (m), 1481 (s), 1453 (m), 1404 (m), 1366 (m), 1337 (m), 1243 (s), 1207 (s), 1139 (s), 940 (s), 855 (m), 804 (s), 763 (m). m.p.: 158 — 160 °C.

4,5-Bis(octyloxy)anthracene-9-carbaldehyde (149)

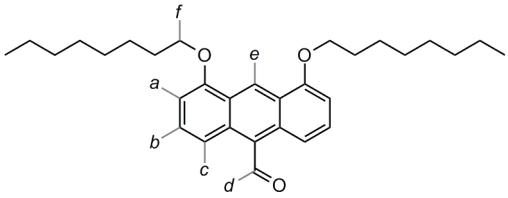

To a solution of 10-bromo-1,8-bis(octyloxy)anthracene **(72)** (0.100 g, 0.195 mmol) in dry THF (5.5 mL) at -78 °C was added butyllithium (1.6 M in THF, 0.488 mL, 0.781 mmol) under argon. The reaction mixture was stirred for 30 min then allowed to warm to 0 °C and stirred for 30 min before being allowed to warm to room temperature. The reaction mixture was stirred at room temperature for 1 h and then cooled to 0 °C, after which DMF (0.100 mL, 1.29 mmol) was added. The mixture was stirred at 0 °C for 30 min and then allowed to reach room temperature. After stirring for an hour, HCl (aq) (1 M solution, 0.200 mL, 0.200 mmol) was added and the mixture was washed with water and separated with $CHCl_3$. The organic layers were collected, the solvent was removed and the crude product was purified by silica gel chromatography (toluene) where the product was observed as an orange band. The solvent was removed to give the product as an orange solid (0.054 g, 60%). ^{1}H NMR (400 MHz, $CDCl_3$) δH 11.46 (s, 1H, H_d), 9.75 (s, 1H, H_e), 8.51 (d, 2H, J = 9.1 Hz, H_c), 7.58 (dd, 2H, J_1 = 7.6 Hz, J_2 = 9.1 Hz, H_b), 6.80 (d, 2H, J = 7.6 Hz, H_a), 4.23 (t, 4H, J = 6.4 Hz, H_f), 2.06-1.98 (m, 4H, H_{oct}), 1.70-1.61 (m, 4H, H_{oct}), 1.49-1.29 (m, 16H, H_{oct}), 0.92-0.88 (m, 6H, H_{oct}). ^{13}C NMR (125 MHz, $CDCl_3$) δC 193.5, 155.9, 133.4, 129.8, 124.8, 124.0, 123.5, 115.1, 102.6, 68.3,

31.9, 29.4 (× 2), 29.2, 26.3, 22.7, 14.1. *m*/*z* (MALDI TOF MS+) 462.83, ($C_{31}H_{42}O_3$; [M]+, requires 462.31).

4,5-Bis-(2,4,6-trimethylphenoxy)-9-bromoanthracene (156)

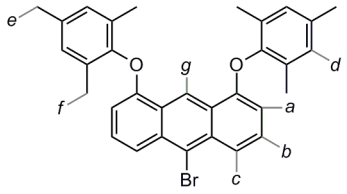

A two-necked flask was dried under vacuum, purged with nitrogen and charged with 4,5-bis-(2,4,6-trimethylphenoxy)anthracen-9(10H)-one **(127)** (0.343 g, 0.741 mmol). PBr_3 (3.0 mL, 31.61 mmol) was added and the reaction mixture was heated to 110 °C and stirred for 1 h. The mixture was allowed to cool to room temperature before being poured into water (50 mL). The yellow precipitate was collected by filtration and washed with saturated $NaHCO_3$ (aq) (40 mL) and water (20 mL) then dried. The solid was purified by silica chromatography (toluene). The first yellow band was collected and the solvents removed to yield the title compound as a yellow solid (0.308 g, 79%). ^{1}H NMR (400 MHz, $CDCl_3$) δ_H 9.87 (s, 1H, H_g), 8.13 (d, 2H, J = 8.9 Hz, H_c), 7.38 (dd, 2H, J_1 = 7.3 Hz, J_2 = 8.9, H_b), 6.97 (s, 4H, H_d), 6.38 (d, 2H, J = 7.31 Hz, H_a), 2.35 (s, 6H, H_e), 2.15 (s, 12H, H_f). ^{13}C NMR (125 MHz, $CDCl_3$) δ_C 154.0, 149.1, 134.7, 132.1, 130.9, 129.6, 127.5, 124.5, 121.8, 120.5, 116.3, 104.5, 20.8, 16.1. λ_{max} / nm ($CHCl_3$) (log ε) 267 (4.94), 418 (3.80), 396 (3.92), 374 (3.85). *m*/*z* (MALDI TOF MS+) 526.89, ($C_{32}H_{29}O_2Br$; $[M]^+$, requires 527.14). m.p. 237— 239 °C.

1,8-Bis-(octadecyloxy)anthraquinone (172)

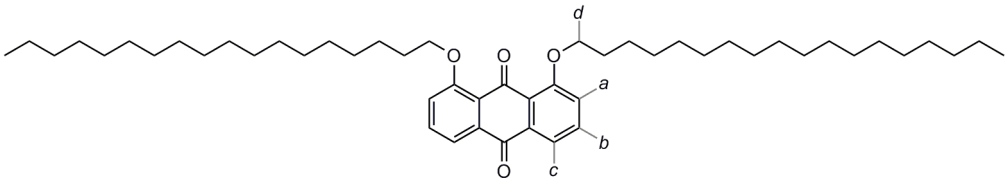

This novel compound was prepared by modification of a literature procedure.[16] A two-necked flask was charged with 1,8-dihydroxyanthraquinone **(82)** (0.584 g, 2.43 mmol), 1-iodooctadecane (3.73 g, 9.81 mmol), tetrabutylammonium chloride (0.067 g, 0.241 mmol) and potassium hydroxide (0.25 g, 4.46 mmol). To this was added chlorobenzene (5 mL) and water

(5 mL) and the mixture was heated to reflux and stirred. The reaction mixture changed colour from red-purple to yellow over the course of the reaction. After heating overnight, the mixture was cooled to room temperature and the organic layer was separated and washed with water (3 × 15 mL). The solvents were removed and the residue was dissolved in DCM and passed through a silica plug (DCM). The solvent was removed and the residue was precipitated from DCM/pentane to give the title compound as a yellow solid (0.72 g, 40%). ^{1}H NMR (400 MHz, $CDCl_3$) δH 7.81 (dd, 2H, J_1 = 1.0 Hz, J_2 = 7.6 Hz, H_c), 7.59 (dd, 2H, J_1 = 7.6 Hz, J_2 = 8.3 Hz, H_b), 7.28 (m, 2H, H_a), 4.13 (t, 4H, J = 6.7 Hz, H_d), 1.97-1.86 (m, 4H, H_{alkyl}), 1.60-1.51(m, 4H, H_{alkyl}), 1.44-1.22 (m, 56H, H_{alkyl}), 0.92-0.85 (m, 6H, H_{alkyl}). ^{13}C NMR (125 MHz, $CDCl_3$) δC 184.3, 182.2, 158.9, 134.8, 133.4, 124.7, 119.6, 118.8, 69.8, 31.9, 29.7 (very broad, 8 carbon signals overlapping by integration), 29.6 (× 2), 29.4 (× 2), 29.1, 25.9, 22.7,14.1. λ_{max} / nm ($CHCl_3$) (log ε) 388 (3.81), 274 (4.04). m/z (MALDI TOF MS+) 744.57 ($C_{50}H_{80}O_4$; [M]+, requires 744.61). IR (ATR): ν / cm^{-1} 2917 (s), 2850 (s), 1673 (s), 1587 (s), 1467 (m), 1436 (m), 1314 (s), 1284 (s), 1218 (s), 1072 (m), 962 (m), 944(m), 895 (m), 841 (m), 792 (m), 741 (s), 722 (m), 663 (m). m.p. 106 — 108 °C. Anal. calc. for $C_{50}H_{80}O_4$: C 80.59, H 10.82. Found: C 80.68, H 10.94.

1,8-Bis-(3-pentadecylphenoxy)anthraquinone (175)

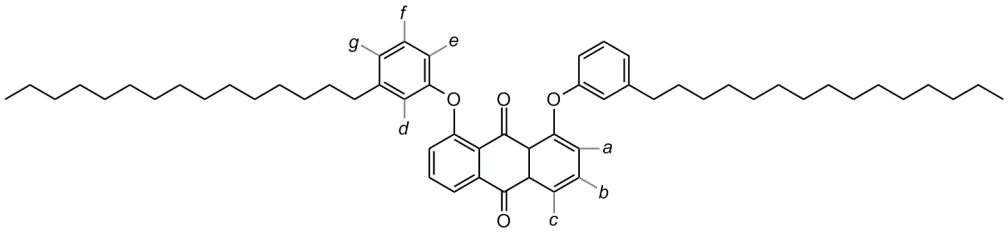

This novel compound was prepared by modification of a literature procedure.[13] A flask containing 1,8-dichloroanthraquinone **(124)** (1.00 g, 3.61 mmol), potassium carbonate (1.83 g, 13.2 mmol) and 3-pentadecylphenol **(176)** (4.02 g, 13.2 mmol) was dried under vacuum and then purged with nitrogen. To this mixture, DMF (15 mL) was added by syringe. The reaction mixture was heated to 130 °C and stirred. The extent of the reaction was monitored by TLC. At completion (16 h), the reaction mixture was allowed to cool to room temperature and water (20 mL) was added. The organic products were extracted with DCM and washed with water (3 × 30 mL). The organic layers were collected and the solvent removed. The solid

residue was purified by chromatography on silica gel (2:1 PET:DCM) and then precipitated from DCM/methanol to give the title compound as an orange solid (1.23 g, 42%). ^{1}H NMR (500 MHz, $CDCl_3$) δH 8.02 (dd, 2H, J_1 = 1.1 Hz, J_2 = 7.8 Hz, H_c), 7.59 (dd, 2H, J_1 = 7.8 Hz, J_2 = 8.3 Hz, H_b), 7.24 (dd, 2H, J_1 = 8.0 Hz, J_2 = 8.2 Hz, H_f), 7.21 (dd, 2H, J_1 = 1.1 Hz, J_2 = 8.3 Hz, H_a), 6.96 (d, 2H, 7.6 Hz, H_g), 6.91 (t, 2H, J = 1.9 Hz, H_d), 6.86 (ddd, 2H, J_1 = 0.8 Hz, J_2 = 2.5 Hz, J_3 = 8.0 Hz, H_e), 2.62-2.53 (m, 4H, H_{alkyl}), 1.65-1.53 (m, 4H, H_{alkyl}), 1.36-1.18 (m, 48H, H_{alkyl}), 0.91-0.86 (m, 6H, H_{alkyl}). ^{13}C NMR (125 MHz, $CDCl_3$) 183.3, 181.1, 157.8, 156.2, 145.3, 134.8, 133.8, 129.5, 125.4, 125.2, 124.3, 121.5, 119.9, 116.9, 35.8, 31.9, 31.2, 29.7 (× 2, both broad – 3 carbon signals overlapping for each peak by integration), 29.6, 29.5, 29.4, 29.3, 22.7, 14.11. λ_{max} / nm ($CHCl_3$) (log ε) 380 (3.82), 275 (4.18). m/z (MALDI TOF MS+) 814.59 ($C_{56}H_{78}O_4$; [M]+, requires 814.39). IR (ATR): ν / cm^{-1} 2917 (s), 2850 (s), 1677 (s), 1612 (s), 1585 (s), 1486 (m), 1439 (m), 1317 (s), 1239 (s), 1146 (s), 989 (m), 937 (m), 853 (m), 829 (m), 764 (m), 739 (m), 720 (m), 693 (m). m.p. 55 — 57 °C.

[5,15-(4,4,5,5-Tetramethyl-[1,3,2]dioxaborolan-2-yl)-10,20-bis-(3,5-bis(octyloxy)phenyl) porphyrinato]zinc(II) (104)

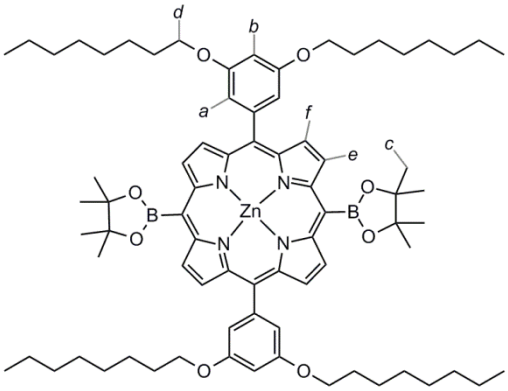

This novel compound was prepared by modification of a literature procedure.[4,5] A flask containing [5,15-dibromo-10,20-bis(octyloxy)porphyrinato]zinc (II) **(108)** (0.150 g, 0.125 mmol), and $PdCl_2(PPh_3)_2$ (0.018 g, 0.026 mmol) was dried under vacuum and purged with argon. To this DCE (25 mL) was added by cannula before freshly distilled triethylamine (2.5 mL) was added by syringe. The mixture was freeze-thaw degassed and the pinacolborane (0.64 mL, 4.41 mmol) was added by syringe. The reaction mixture was heated to 80 °C and stirred over night under argon. The extent of the reaction was monitored by TLC and, at

completion, the reaction mixture was allowed to cool to room temperature and was very slowly quenched with water (10 mL). The organic layers were collected, washed with water and the solvents removed. The crude product was purified by silica gel chromatography where the side products were removed in a mixture of 2:1 DCM:PET and the product was eluted with ethylacetate. The solvents were removed to give the product as a purple solid (0.128 g, 79%). ^{1}H NMR (400 MHz, $CDCl_3$) δH 10.02 (d, 4H, J = 4.8 Hz, H_f), 9.31 (d, 4H, J = 4.8 Hz, H_e), 7.50 (d, 4H, J = 2.2 Hz, H_a), 6.99 (t, 2H, J = 2.2 Hz, H_b), 4.22 (t, 8H, J = 6.6 Hz, H_d), 2.04-1.88 (m, 32H, H_{c+oct}), 1.67-1.54 (m, 8H, H_{oct}), 1.49-1.33 (m, 32H, H_{oct}), 1.01-0.93 (m, 12H, H_{oct}). ^{13}C NMR (125 MHz, $CDCl_3$) δC 158.2, 153.4, 149.9, 144.9, 132.8, 132.5, 114.6, 101.1, 85.3 (× 2), 68.6, 53.5, 32.0, 29.5 (× 2), 29.3, 26.2, 25.4, 22.7, 14.2. λ_{max} / nm ($CHCl_3$) 417, 547, 583. m/z (MALDI TOF MS+) 1288.70, ($C_{76}H_{106}N_4O_8B_2Zn$; [M]+, requires 1288.75).

[5,15-[10-(1,8-Bis(octyloxy)anthracene)]-10,20-bis-(3,5-di-octyloxyphenyl)-porphyrinato]zinc(II) (105) and [5-[10-(1,8-bis(octyloxy)anthracene)]-10,20-bis-(3,5-dioctyloxyphenyl)-porphyrinato]zinc(II) (106)

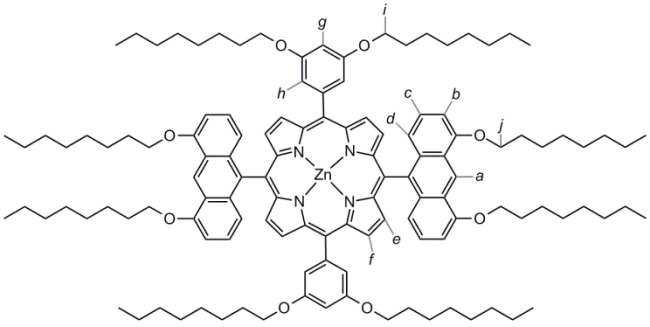

105

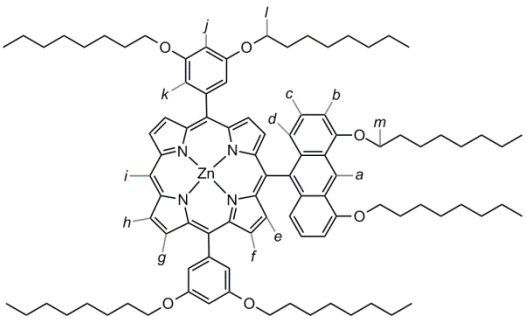

106

These novel compounds were prepared by modification of a literature Suzuki coupling reaction.[11] A two necked pear shaped flask was charged with [5,15-(4,4,5,5-tetramethyl-[1,3,2]dioxaborolan-2-yl)-10,20-bis-(3,5-bis(octyloxy)phenyl)porphyrinato]zinc(II) **(104)** (0.100 g, 0.078 mmol), 10-bromo-1,8-bis(octyloxy)anthracene **(72)** (0.091 g, 0.177 mmol), potassium hydroxide (0.800 g, 14.3 mmol), 2-dicyclohexylphosphino-2',6'-dimethoxybiphenyl (SPhos) (0.025 g, 0.061 mmol) and $Pd_2(dba)_3$ (0.014 g, 0.015 mmol) and dried for 6 h under vacuum. Dry *m*-xylene (2 mL) was added by syringe and the reaction mixture was freeze-thaw degassed. The reaction mixture was purged with nitrogen, heated to 90 °C and stirred overnight. The progress of the reaction was monitored by TLC and at completion the

reaction mixture was allowed to cool to room temperature. Water (5 mL) was added to the reaction mixture and the organic layers were separated and washed with water (3 × 10 mL) and then collected and dried over anhydrous $MgSO_4$ before being filtered. The solvents were removed and the solid was dissolved in DCM and passed through a short silica plug (DCM). The solvent was again removed and the solid was dissolved in THF and passed through a size exclusion column to separate the bis-anthracene porphyrin product, the mono-anthracene porphyrin product, and the diaryl side product. After separation the solvent was removed and the solids were precipitated from DCM and methanol to give the title compounds as purple-red oily solids of bis-anthracene porphyrin **(105)** (0.023 g, 16%) and mono-anthracene porphyrin **(106)** (0.024 g, 21%).

Bis-anthracene porphyrin **(105)**: ^{1}H NMR (500 MHz, $CDCl_3$) δH 9.87 (s, 2H, H_a), 8.82 (d, 4H, J = 4.8 Hz, H_f), 8.30 (d, 4H, J = 4.8 Hz, H_e), 7.33 (d, 4H, J = 2.1 Hz, H_h), 6.85 (m, 4H, H_c), 6.77 (t, 2H, J = 2.2 Hz, H_g), 6.70 (d, 4H, J = 7.6 Hz, H_b), 6.50 (d, 4H, J = 8.9 Hz, H_d), 4.43 (t, 8H, J = 6.2, H_j), 4.04 (t, 8H, J = 6.5 Hz, H_i), 2.20-2.11 (m, 8H, H_{oct}), 1.85-1.74 (m, 16H, H_{oct}), 1.51-1.36 (m, 36H, H_{oct}), 1.33-1.21 (m, 36H, H_{oct}), 0.98-0.93 (m, 12H, H_{oct}), 0.86-0.80 (m, 12H, H_{oct}). ^{13}C NMR (125 MHz, $CDCl_3$) δC 158.1, 155.3, 151.4, 149.9, 144.7, 136.4, 135.9, 132.4, 131.7, 125.6, 124.0, 121.0, 120.5, 117.0, 116.9, 114.3, 101.6, 100.8, 68.3 (× 2), 32.1, 31.8, 29.7, 29.6, 29.5, 29.4 (× 2), 29.2, 26.6, 26.1, 22.8, 22.7, 14.2, 14.1. m/z (MALDI TOF MS+) 1903.20, ($C_{124}H_{164}N_4O_8Zn$; [M]+, requires 1903.70).

Mono-anthracene porphyrin **(106)**: ^{1}H NMR (500 MHz, $CDCl_3$) δH 10.29 (s, 1H, H_i), 9.88 (s, 1H, H_a), 9.42 (d, 2H, J = 4.7 Hz, H_h), 9.22 (d, 2H, J = 4.7 Hz, H_g), 8.91 (d, 2H, J = 4.7 Hz, H_f), 8.37 (d, 2H, J = 4.7 Hz, H_e), 7.39 (d, 4H, J = 2.2 Hz, H_k), 6.87-6.83 (m, 4H, H_{c+j}), 6.69 (d, 2H, J = 7.3 Hz, H_b), 6.47 (d, 2H, J = 9.1 Hz, H_d), 4.34 (t, 4H, J = 6.3 Hz, H_m), 4.09 (t, 8H, J = 6.6 Hz, H_l), 2.19-2.12 (m, 4H, H_{oct}), 1.87-1.76 (m, 8H, H_{oct}), 1.50-1.44 (m, 12H, H_{oct}), 1.41-1.23 (m, 48H, H_{oct}), 0.97-0.93 (m, 6H, H_{oct}), 0.90-0.83 (m, 12H, H_{oct}). ^{13}C NMR (125 MHz, $CDCl_3$) δC 158.3, 155.3, 151.3, 150.1, 149.9 (× 2), 144.4, 136.4, 135.5, 132.6 (× 2), 131.9, 131.6, 125.7, 124.0, 120.9, 120.4, 117.4, 117.2, 114.3, 106.3, 101.7, 101.0, 68.4, 50.9, 32.0, 31.8, 29.6 (×2),

29.5, 29.4, 29.3 (× 2), 26.6, 26.1, 22.8, 22.7, 14.2, 14.1. *m*/*z* (MALDI TOF MS+) 1471.7, ($C_{94}H_{124}N_4O_6Zn$; [M]+, requires 1470.9).

[5,15-Di-[10-(1,8-dioctyloxyanthracene)]-10,20-bis-(3,5-di-*tert*-butylphenyl)-porphyrinato]zinc(II) (110) and [5-[10-(1,8-dioctyloxyanthracene)]-10,20-bis-(3,5-di-*tert*-butylphenyl)-porphyrinato] zinc(II) (111)

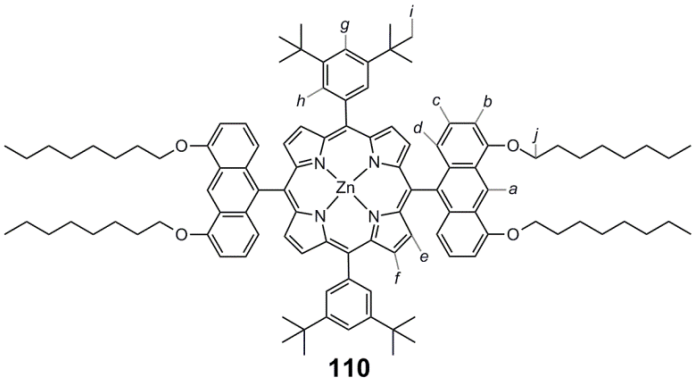

110

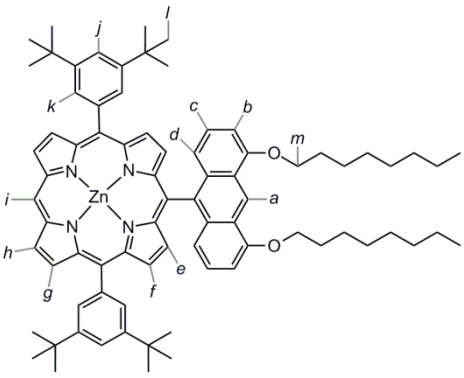

111

These novel compounds were prepared by modification of a literature Suzuki coupling procedure.[11] A two-necked pear shaped flask was charged with [5,15-di-(4,4,5,5-tetramethyl-[1,3,2]dioxaborolan-2-yl)-10,20-bis-(3,5-di-*tert*-butylphenyl)-porphyrinato]zinc(II) **(109)** (0.160 g, 0.160 mmol), 10-bromo-1,8-bis(octyloxy)-anthracene **(72)** (0.180 g, 0.351 mmol), potassium hydroxide (0.800 g, 14.3 mmol), 2-dicyclohexylphosphino-2',6'-dimethoxybiphenyl (SPhos) (0.105 g, 0.256 mmol) and $Pd_2(dba)_3$ (0.029 g, 0.032 mmol) and dried for 6 h under vacuum. Dry *m*-xylene (2.0 mL) was added by syringe and the reaction mixture was freeze-thaw degassed. The reaction mixture was purged with nitrogen, heated to 90 °C and stirred overnight. The progress of the reaction was monitored by TLC and at completion the reaction mixture was allowed to cool to room temperature. Water (5 mL) was added to the reaction mixture and the organic layers were separated and washed with water (3 × 10 mL) and then collected. The solvents were removed and the solid was dissolved in DCM and passed through a short silica plug (DCM). The solvent was again removed and the solid was dissolved in THF and passed through a size exclusion column to separate the bis-anthracene porphyrin, the mono-anthracene porphyrin, and the diaryl side product. After separation the solvent was removed and the solids were precipitated from DCM/methanol to give the title

compounds as purple-red solids of bis-anthracene porphyrin **(110)** (0.121 g, 47%) and mono-anthracene porphyrin **(111)** (0.038 g, 20%).

Bis-anthracene porphyrin **(110)**: ^{1}H NMR (500 MHz, $CDCl_3$) δH 9.86 (s, 2H, H_a), 8.75 (d, 4H, J = 4.4 Hz, H_f), 8.32 (d, 4H, J = 4.7 Hz, H_e), 8.03 (d, 4H, J = 1.8 Hz, H_h), 7.69 (t, 2H, J = 1.9 Hz, H_g), 6.87 (dd, 4H, J_1 = 7.3 Hz, J_2 = 8.9 Hz, H_c), 6.70 (d, 4H, J = 7.3 Hz, H_b), 6.55 (d, 4H, J = 8.9 Hz, H_d), 4.34 (t, 8H, J = 6.3 Hz, H_j), 2.19-2.11 (m, 8H, H_{oct}), 1.84-1.76 (m, 8H, H_{oct}), 1.60-1.36 (m, 68H, H_{oct+i}), 0.94-0.99 (m, 12H ,H_{oct}). ^{13}C NMR (125 MHz, $CDCl_3$) δC 155.3, 151.3, 150.5, 148.4, 141.6, 136.3, 135.6, 132.8, 131.7, 129.6, 125.7, 124.0, 122.1, 120.9, 120.7, 117.2, 117.0, 101.6, 68.3, 35.0, 32.0, 31.7, 29.7, 29.6, 29.5, 26.6, 22.8, 14.2. λ_{max} / nm ($CHCl_3$) 429, 552, 589. m/z (MALDI TOF MS+) 1615.11, ($C_{108}H_{132}O_4N_4Zn$; $[M]^+$, requires 1614.96). m.p: > 300 °C.

Mono-anthracene porphyrin **(111)**: ^{1}H NMR (500 MHz, $CDCl_3$) δH 10.32 (s, 1H, H_i), 9.87 (s, 1H, H_a), 9.45 (d, 2H, J = 4.4 Hz, H_h), 9.16 (d, 2H, J = 4.4 Hz, H_g), 8.86 (d, 2H, J = 4.4 Hz, H_f), 8.40 (d, 2H, J = 4.7 Hz, H_e), 8.11 (d, 4H, J = 1.9 Hz, H_k), 7.79 (t, 2H, J = 1.8 Hz, H_j), 6.86 (dd, 2H, J_1 = 7.3 Hz, J_2 = 9.1 Hz, H_c), 6.68 (d, 2H, J = 7.3 Hz, H_b), 6.51 (d, 2H, J = 9.1 Hz, H_d), 4.33 (t, 4H, J = 6.3 Hz, H_m), 2.19-2.11 (m, 4H, H_{oct}), 1.83-1.76 (m, 4H, H_{oct}), 1.53 (s, 36H, H_l) 1.51-1.35 (m, 16H, H_{oct}), 0.99-0.94 (m, 6H, H_{oct}). ^{13}C NMR (125 MHz, $CDCl_3$) δC 155.3, 151.1, 150.6, 150.3, 149.7, 148.6, 141.5, 136.3, 135.6, 132.8 (× 2), 131.8, 131.5, 129.8, 125.7, 124.0, 121.8, 120.9, 120.7, 117.2, 117.1, 106.2, 101.6, 68.3, 35.0, 32.0, 31.7, 29.6, 29.5 (× 2), 26.5, 22.7, 14.2. λ_{max} / nm ($CHCl_3$) 419, 545, 579. m/z (MALDI TOF MS+) 1180.48, ($C_{78}H_{92}O_2N_4Zn$; $[M]^+$, requires 1180.65). m.p: > 300 °C.

[5,15-Bis-[10-(1,8-dioctyloxyanthracene)]-10,20-bis-(3,5-di-*tert*-butylphenyl)-porphyrinato]nickel(II) (115)

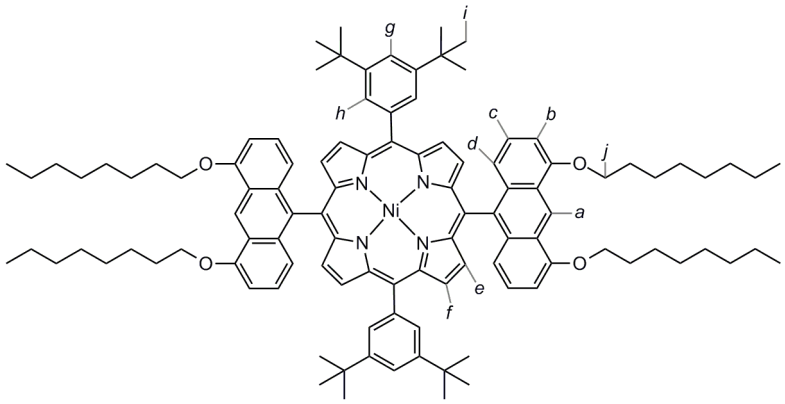

To a solution of [5,15-bis-[10-(1,8-dioctyloxyanthracene)]-10,20-bis-(3,5-di-*tert*-butylphenyl)-porphyrinato]zinc(II) **(110)** (0.025 g, 0.0155 mmol) in DCM (10 mL) was added dropwise TFA (0.119 mL, 1.55 mmol). The reaction was monitored by TLC and, at completion, the reaction was quenched with saturated $NaHCO_3$ (aq) (20 mL). The organic phase was collected, washed with water (3 × 10 mL) and then passed through a short silica plug (DCM). The solvents were removed and the solid was placed in a two-necked flask and dissolved in *m*-xylene (10 mL). To this nickel(II) acetylacetonate (0.088 g, 0.343 mmol) was added and the mixture was refluxed at 136 °C under nitrogen. The progress of the reaction was monitored by TLC and, at completion, the mixture was allowed to cool and was then passed through a short silica plug (DCM). The solvents were removed and the solid was precipitated from DCM/methanol to yield the title compound as a bright pink solid (0.023 g, 92%). ^{1}H NMR (400 MHz, $CDCl_3$) δH 9.80 (s, 2H, H_a), 8.63 (d, 4H, J = 4.7 Hz, H_f), 8.24 (d, 4H, J = 4.8 Hz, H_e), 7.87 (d, 4H, J = 1.7 Hz, H_h), 7.64 (t, 2H, J = 1.7 Hz, H_g), 6.97 (dd, 4H, J_1 = 7.5 Hz, J_2 = 8.7 Hz, H_c), 6.70 (d, 4H, J = 7.6 Hz, H_b), 6.59 (d, 4H, J = 8.8 Hz, H_d), 4.32 (t, 8H, J = 6.2 Hz, H_j), 2.19-2.08 (m, 8H, H_{oct}), 1.83-1.72 (m, 8H, H_{oct}), 1.60-1.36 (m, 68H, H_{oct+i}), 0.97-0.92 (m, 12H ,H_{oct}). ^{13}C NMR (125 MHz, $CDCl_3$) δC 155.3, 148.8, 143.9, 143.0, 140.0, 135.7, 133.7, 132.9, 132.2, 128.8, 125.9, 124.1, 121.0, 120.6, 120.4, 117.3, 115.4, 101.8, 68.4, 35.0, 32.0, 31.7 (× 2), 29.6, 29.5, 26.5, 22.8, 14.1. λ_{max} / nm ($CHCl_3$) 426, 532. m/z (MALDI TOF MS+) 1607.61, ($C_{108}H_{132}O_4N_4Ni$; $[M]^+$, requires 1607.96). m.p: > 300 °C.

[3,5,7-[4,5,10-(1,8-Dioctyloxyanthracene)]-10,20-bis-(3,5-di-*tert*-butylphenyl)-15-[10-(1,8-dioctyloxyanthracene)]porphyrinato] nickel(II) (116)

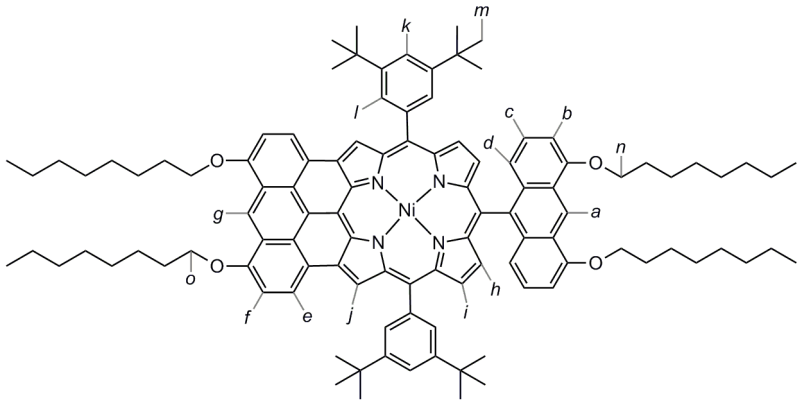

This novel compound was prepared by modification of literature fusion procedures.[17,18] A two-necked flask was charged with $FeCl_3$ (0.010 g, 0.062 mmol) and dried under vacuum overnight after which nitromethane (2.0 mL) was added under argon. The $FeCl_3$ solution was added by syringe to a solution of [5,15-bis-[10-(1,8-dioctyloxyanthracene)]-10,20-bis-(3,5-di-*tert*-butylphenyl)-porphyrinato]nickel(II) **(115)** (0.010 g, 0.006 mmol) in dry DCM (5.0 mL) under argon and stirred at room temperature. The reaction mixture was monitored by TLC and at completion (after 30 min) the reaction was quenched by addition of saturated $NaHCO_3$ (aq) (10 mL). The organic phase was collected and washed with water (3 × 10 mL). The organic layer was collected and passed through a short silica plug (DCM). The solvents were then removed and the solid was precipitated from DCM/methanol to give the title compound as a dark red-brown solid (0.008 g, 81%). ^{1}H NMR (500 MHz, $CDCl_3$) δH 9.76 (s, 1H, H_a), 9.75 (s, 1H, H_g), 9.18 (s, 2H, H_j), 8.86 (d, 2H, J = 7.6 Hz, H_e), 8.47 (d, 2H, J = 5.0 Hz, H_i), 8.01 (d, 4H, J = 1.9 Hz, H_l), 7.96 (d, 2H, J = 5.0 Hz, H_h), 7.76 (t, 2H, J = 1.9 Hz, H_k), 7.18 (d, 2H, J = 8.2 Hz, H_f), 6.95 (dd, 2H, J_1 = 7.3 Hz, J_2 = 8.8 Hz, H_c), 6.71-6.65 (m, 4H, H_{b+d}), 4.41 (t, 4H, J = 6.3 Hz, H_o), 4.29 (t, 4H, J = 6.3 Hz, H_n), 2.18-2.08 (m, 8H, H_{oct}), 1.80-1.71 (m, 8H, H_{oct}), 1.51 (s, 36H, H_m), 1.48-1.32 (m, 32H, H_{oct}), 0.96-0.89 (m, 12H, H_{oct}). ^{13}C NMR (125 MHz, $CDCl_3$) δC 158.3, 155.3, 148.9, 145.8, 143.2, 143.1, 140.7, 138.6, 135.5, 134.6, 134.3, 132.7, 130.7, 128.7, 128.6, 125.7, 125.0, 124.4, 124.0, 123.9, 122.1, 121.3, 120.9, 120.5, 120.4 119.0, 116.9, 113.7, 110.5, 105.4, 101.8, 68.7, 68.2, 35.1, 32.0, 31.9, 31.7, 31.6, 29.6, 29.5, 29.4 (× 2), 29.3, 26.4, 26.3, 22.7 (× 2), 14.1 (× 2). m/z (MALDI TOF MS+), 1604.02, ($C_{108}H_{128}O_4N_4Ni$; $[M]^+$, requires 1604.94). m.p: > 300 °C.

[5,15-[10-(1,8-Bis(2,4,6-trimethylphenoxy)anthracene)]-10,20-bis-(3,5-di-*tert*-butylphenyl)-porphyrinato]zinc(II) (129) and [5-[10-(1,8-bis(2,4,6-trimethylphenoxy)anthracene)]-10,20-bis-(3,5-di-*tert*-butylphenyl)-porphyrinato]zinc(II) (130)

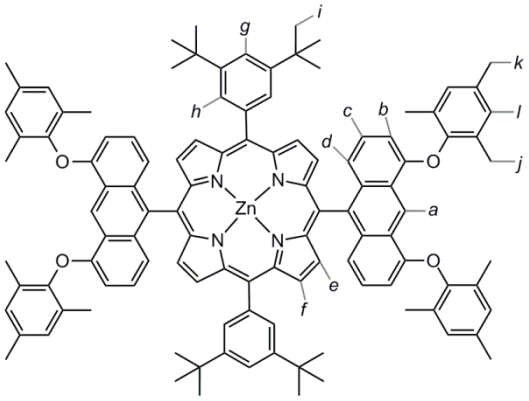

129

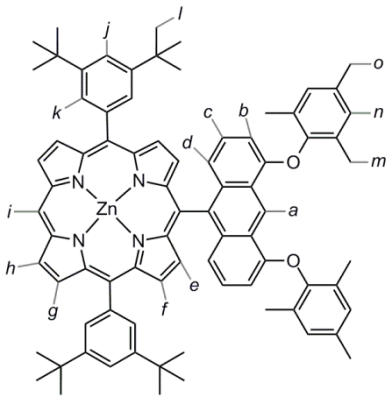

130

These novel compounds were prepared by modification of a literature Suzuki coupling procedure.[11] A two-necked pear shaped flask was charged with [5,15-bis-(4,4,5,5-tetramethyl-[1,3,2]dioxaborolan-2-yl)-10,20-bis-(3,5-di-*tert*-butylphenyl)-porphyrinato]zinc(II) **(109)** (0.050 g, 0.050 mmol), 4,5-bis-(2,4,6-trimethylphenoxy)anthracen-9-yl trifluoromethanesulfonate **(128)** (0.065 g, 0.112 mmol), potassium hydroxide (0.800 g, 14.3 mmol), 2-dicyclohexylphosphino-2',6'-dimethoxybiphenyl (SPhos) (0.033 g, 0.080 mmol) and $Pd_2(dba)_3$ (0.009 g, 0.010 mmol) and dried for 6 h under vacuum. Dry *m*-xylene (3.0 mL) was added by syringe and the reaction mixture was freeze-thaw degassed. The reaction mixture was purged with nitrogen, heated to 90 °C and stirred overnight. The progress of the reaction was monitored by TLC and, at completion, the reaction mixture was allowed to cool to room temperature. Water (10 mL) was added to the reaction mixture and the organic layers were separated, washed with water (3 × 10 mL) and then collected. The solvents were removed and the solid was dissolved in DCM and passed through a short silica plug (DCM). The solvent was again removed and the solid was dissolved in toluene and passed through a size exclusion column to separate the bis-anthracene porphyrin, the mono-anthracene porphyrin, and the diaryl side product. After separation the solvent was removed and the solids were precipitated from DCM/methanol to give the title compounds as purple-red solids of bis-anthracene porphyrin **(129)** (0.012 g, 15%) and mono-anthracene porphyrin **(130)** (0.026 g, 44%).

Bis-anthracene porphyrin **(129)**: ^{1}H NMR (400 MHz, $CDCl_3$) δH 10.29 (s, 2H, H_a), 8.84 (d, 4H, J = 4.6 Hz, H_f), 8.52 (d, 4H, J = 4.6, H_e), 8.06 (d, 4H, J = 1.8 Hz, H_h), 7.72 (t, 2H, J = 1.6 Hz, H_g), 7.02 (s, 8H, H_l), 6.78 (dd, 4H, J_1 = 7.3 Hz, J_2 = 8.8 Hz, H_c), 6.67 (d, 4H, J = 8.8 Hz, H_d), 6.31 (d, 4H, J = 7.3 Hz, H_b), 2.37 (s, 12H, H_k), 2.35 (s, 24H, H_j), 1.46 (s, 36H, H_i). ^{13}C NMR (125 MHz, $CDCl_3$) δC 154.0, 151.3, 150.5, 149.3, 148.4, 141.5, 136.6, 136.1, 134.5, 132.8, 131.9, 131.1, 129.6, 129.5, 125.6, 123.5, 122.2, 121.8, 120.7, 117.0, 116.8, 103.6, 35.0, 31.7, 20.9, 16.4. λ_{max} / nm ($CHCl_3$) (log ε) 430 (5.34), 551 (4.26), 589 (3.35). m/z (MALDI TOF MS+), 1638.77 ($C_{112}H_{108}O_4N_4Zn$; $[M]^+$, requires 1638.95). m.p.: > 300 °C. Anal. calc. for $C_{112}H_{108}N_4O_4Zn$: C 82.05, H 6.64, N 3.42. Found: C 81.86, H 6.65, N 3.37.

Mono-anthracene porphyrin **(130)**: ^{1}H NMR (400 MHz, $CDCl_3$) δH 10.31 (s, 1H, H_i), 10.29 (s, 1H, H_a), 9.44 (d, 2H, J = 4.6 Hz, H_h), 9.16 (d, 2H, J = 4.5 Hz, H_g), 8.90 (d, 2H, J = 4.6 Hz, H_f), 8.53 (d, 2H, J = 4.6 Hz, H_e), 8.12 (d, 4H, J = 1.8 Hz, H_k), 7.79 (t, 2H, J = 1.8 Hz, H_j), 7.01 (s, 4H, H_n), 6.73 (dd, 2H, J_1 = 7.5 Hz, J_2 = 8.9 Hz, H_c), 6.59 (d, 2H, J = 8.9 Hz, H_d), 6.29 (d, 2H, J = 7.4 Hz, H_b), 2.36 (s, 6H, H_o), 2.34 (s, 12H, H_m), 1.53 (s, 36H, H_l). ^{13}C NMR (125 MHz, $CDCl_3$) δC 154.0, 151.1, 150.6, 150.2, 149.7, 149.3, 148.5, 141.6, 136.7, 136.3, 134.5, 132.8 (× 2), 131.9, 131.5, 131.1, 129.8, 129.6, 125.5, 123.5, 121.9, 121.8, 120.7, 116.8 (× 2), 106.2, 103.6, 35.0, 31.7, 20.9, 16.4. λ_{max} / nm ($CHCl_3$/1% pyridine) (log ε) 429 (5.57), 558 (4.25), 597 (3.68). m/z (MALDI TOF MS+), 1193.45 ($C_{80}H_{80}O_2N_4Zn$; $[M]^+$, requires 1193.57). m.p.: > 300 °C. Anal. calc. for $C_{80}H_{80}N_4O_2Zn$: C 80.41, H 6.75, N 4.69. Found: C 80.52, H 6.70, N 4.58.

[5,15-[10-(1,8-Bis(2,4,6-trimethylphenoxy)anthracene)]-10,20-bis-(3,5-di-*tert*-butylphenyl)-porphyrinato]nickel(II) (131)

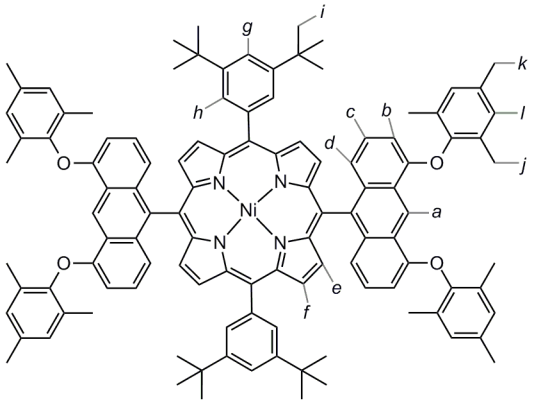

To a solution of [5,15-bis-[10-(1,8-bis(2,4,6-trimethylphenoxy)anthracene)]-10,20-bis-(3,5-di-*tert*-butylphenyl)-porphyrinato]zinc(II) **(129)** (0.025 g, 0.015 mmol) in DCM (10 mL) was added dropwise TFA (0.116 mL, 1.51 mmol). The reaction was monitored by TLC and, at completion, the reaction was quenched with saturated $NaHCO_3$ (aq) (10 mL). The organic phase was collected, washed with water (3 × 10 mL) and then passed through a short silica plug (DCM). The solvents were removed and the solid was then placed in a two-necked flask and dissolved in *m*-xylene (10 mL). To this nickel(II) acetylacetonate (0.089 g, 0.346 mmol) was added and the mixture was refluxed at 136 °C under nitrogen. The progress of the reaction was monitored by TLC and, at completion, the mixture was allowed to cool and was then passed through a short silica plug (DCM). The solvents were removed and the solid was precipitated from DCM/methanol to yield the title compound as a bright pink-orange solid (0.023 g, 92%). ^{1}H NMR (400 MHz, $CDCl_3$) δH 10.22 (s, 2H, H_a), 8.68 (d, 4H, J = 4.9 Hz, H_f), 8.38 (d, 4H, J = 4.9 Hz, H_e), 7.87 (d, 4H, J = 1.8 Hz, H_h), 7.65 (t, 2H, J = 1.8 Hz, H_g), 7.00 (s, 8H, H_l), 6.83 (dd, 4H, J_1 =7.4 Hz, J_2 = 8.8 Hz, H_c), 6.68 (d, 4H, J = 8.8 Hz, H_d), 6.30 (d, 4H, J = 7.3 Hz, H_b), 2.36 (s, 12H, H_k), 2.31 (s, 24H, H_j), 1.41 (s, 36H, H_i). ^{13}C NMR (125 MHz, $CDCl_3$) δC 153.9, 149.3, 148.7, 143.8, 143.0, 139.9, 136.0, 134.5, 134.2, 132.9, 132.3, 131.1, 129.6, 128.6, 125.8, 123.5, 121.4, 121.0, 120.3, 117.0, 115.2, 103.8, 34.9, 31.6, 20.9, 16.3. λ_{max} / nm ($CHCl_3$/1% pyridine) (log ε) 427 (5.40), 531 (4.40). m/z (MALDI TOF MS+), 1633.15 ($C_{112}H_{108}O_4N_4Ni$; $[M]^+$, requires 1632.78). m.p.: > 300 °C.

[3,5,7-[4,5,10-(1,8-Bis(2,4,6-trimethylphenoxy)anthracene)]-10,20-bis-(3,5-di-*tert*-butylphenyl)-15-[10-(1,8-bis(2,4,6-trimethylphenoxy)anthracence)]-porphyrinato]nickel(II) (132)

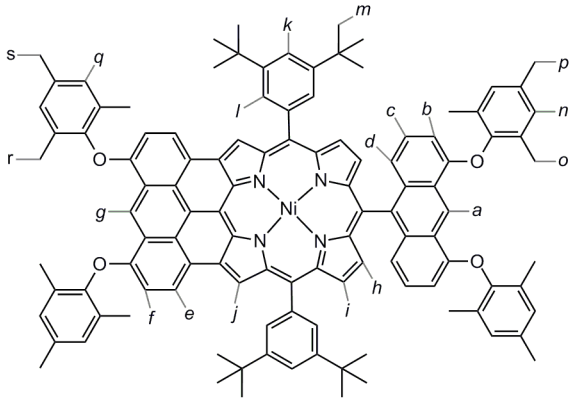

This novel compound was prepared by modification of literature fusion procedures.[17,18] A two-necked flask was charged with $FeCl_3$ (0.020 g, 0.123 mmol) and dried under vacuum overnight after which nitromethane (1.0 mL) was added under argon. The $FeCl_3$ solution was added by syringe to a solution of [5,15-bis-[10-(1,8-bis(2,4,6-trimethylphenoxy)anthracene)]-10,20-bis-(3,5-di-*tert*-butylphenyl)-porphyrinato]nickel(II) **(131)** (0.020 g, 0.012 mmol) in dry DCM (5.0 mL) under argon and stirred at room temperature. The reaction was monitored by TLC and at completion (after 10 min) the reaction was quenched by addition of saturated $NaHCO_3$ (aq) (10 mL). The organic phase was collected and washed with water (3 × 10 mL). The organic layers were collected, the solvent evaporated and the product dissolved in DCM and passed through a short silica plug (DCM). The product was precipitated from DCM/methanol and then DCM/pentane to give the title compound as a dark red-brown solid (0.014 g, 72%). ^{1}H NMR (400 MHz, $CDCl_3$) δH 10.24 (s, 1H, H_a), 10.18 (s, 1H, H_g), 9.15 (s, 2H, H_j), 8.70 (d, 2H, J = 7.9 Hz, H_e), 8.51 (d, 2H, J = 4.8 Hz, H_i), 8.09 (d, 2H, J = 4.9 Hz, H_h), 7.99 (d, 4H, J = 1.8 Hz, H_l), 7.74 (t, 2H, J = 1.8 Hz, H_k), 7.07 (s, 4H, H_q), 7.00 (d, 4H, H_n), 6.84 (dd, 2H, J_1 = 7.3 Hz, J_2 = 8.9 Hz, H_c), 6.79 (d, 2H, J = 8.07 Hz, H_f), 6.76 (d, 2H, 8.97, J = 9.0 Hz, H_d), 6.29 (d, 2H, J = 7.3 Hz, H_b), 2.42 (s, 6H, H_s), 2.35 (s, 6H, H_p), 2.33 (s, 12H, H_r), 2.30 (s, 12H, H_o), 1.50 (s, 36H, H_m). ^{13}C NMR (125 MHz, $CDCl_3$) δC 157.0, 153.9, 149.3, 149.0, 148.9, 145.8, 143.4, 143.1, 140.5, 138.7, 135.8, 135.0, 134.8, 134.6, 134.4, 132.8, 131.1, 131.0, 130.9, 129.8, 129.6, 128.7, 128.4, 125.9, 125.7, 124.8, 123.6, 123.5, 122.4 (× 2), 121.4, 121.0, 119.9, 119.6, 116.8, 113.9, 110.2, 107.3, 103.8,

35.0, 31.7, 20.9, 20.8, 16.3 (× 2). λ_{max} / nm ($CHCl_3$/1% pyridine) (log ε) 374 (4.35), 419 (4.43), 498 (4.54), 535 (4.48), 583 (4.30), 749 (4.33), 828 (4.55). m/z (MALDI TOF MS+), 1628.87 ($C_{112}H_{104}O_4N_4Ni$; $[M]^+$, requires 1628.75). m.p.: > 300 °C.

[3,5,7,12,15,17-[4,5,10-(1,8-Bis(2,4,6-trimethylphenoxy)anthracene)]-10,20-bis-(3,5-di-*tert*-butylphenyl)-porphyrinato]nickel(II) (133)

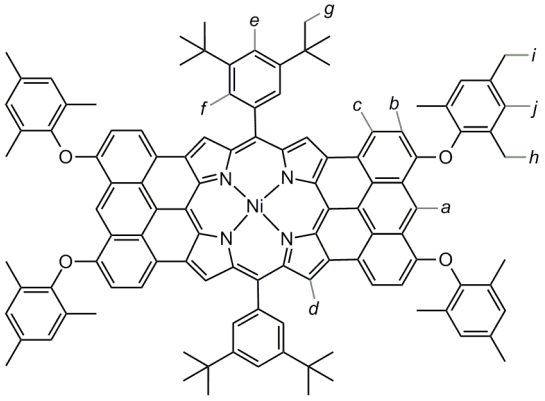

This novel compound was prepared by modification of literature fusion procedures.[17,18] A flask containing [3,5,7-[4,5,10-(1,8-bis(2,4,6-trimethylphenoxy)anthracene)]-10,20-bis-(3,5-di-*tert*-butylphenyl)-15-[10-(1,8-bis(2,4,6-trimethylphenoxy)anthracence)]-porphyrinato]nickel(II) **(132)** (0.017 g, 0.010 mmol) was dried under vacuum. In a dessicator, $FeCl_3$ (0.017 g, 0.105 mmol) and AgOTf (0.081 g, 0.315 mmol) were dried in separated vials under high vacuum. To the porphyrin was added toluene (2.0 mL) under nitrogen. To the $FeCl_3$ was added nitromethane (1.0 mL) — this yellow solution was then added to the AgOTf and this mixture was added by syringe to the porphyrin solution. The reaction was stirred for 10 min and was then quenched by addition of a saturated $NaHCO_3$ (aq) (10 mL). The mixture was filtered then the organic layer was washed with water (3 × 10 mL), separated and the solvents removed. The solid residue was purified by silica chromatography (1:1 DCM/PET then toluene) and the product was eluted with toluene. The solvents were removed and the solid was precipitated from DCM/pentane to give the title compound as a dark purple-black solid (0.0025 g, 15%). ^{1}H NMR (400 MHz, $CDCl_3$) δH 10.08 (s, 2H, H_a), 8.97 (s, 4H, H_d), 8.56 (d, 4H, J = 8.2 Hz, H_c), 8.09 (d, 4H, J = 1.8 Hz, H_f), 7.82 (m, 2H, H_e), 7.05 (s, 8H, H_j), 6.73 (d, 4H, J = 8.2 Hz, H_b), 2.41 (s, 12H, H_i), 2.31 (s, 24H, H_h), 1.57 (s, 36H,

H_g). λ_{max} / nm ($CHCl_3$/1% pyridine) (log ε) 557 (4.98), 650 (4.37), 865 (4.52), 973 (5.14). m/z (MALDI TOF MS+), 1624.91 ($C_{112}H_{100}O_4N_4Ni$; $[M]^+$, requires 1624.72). m.p.: > 300 °C.

[3,3',5,5',7,7',12,12',-[4,5,10-(1,8-Bis(2,4,6-trimethylphenoxy)anthracene)]-10,10',20,20'-bis-(3,5-di-*tert*-butylphenyl)-13,13',15,15',17,17'-dicyclo-biporphyrinato]zinc(II) (134)

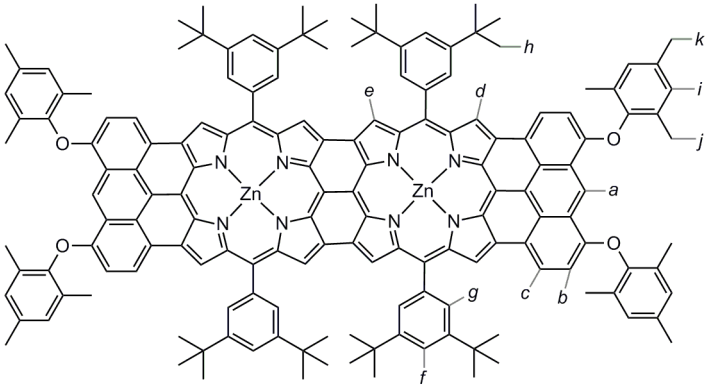

This novel compound was prepared by modification of literature procedures.[11,19] A two-necked flask was charged with [5-[10-(1,8-bis(2,4,6-trimethylphenoxy)anthracene)]-10,20-bis-(3,5-di-*tert*-butylphenyl)-porphyrinato]zinc(II) **(130)** (0.050 g, 0.042 mmol), DDQ (0.142 g, 0.628 mmol) and $Sc(OTf)_3$ (0.309 g, 0.628 mmol) and dried overnight under vacuum. The flask was purged with nitrogen and to this was added dry DCM (5.0 mL). The reaction mixture was stirred at room temperature for 25 min before being loaded onto a silica plug (5% pyridine in DCM). The eluate was collected and the solvent was then removed. The solid residue was purified by silica chromatography (2:1 THF/PET). The product was found to elute as the first blue-green band. The solvents were then removed and the product was precipitated from DCM/methanol to give the title compound as a dark blue-black solid (0.006 g, 13%). ^{1}H-DOSY NMR (500 MHz, pyridine-d_5) δH 10.34 (s, 2H, H_a), 8.46 (s, 4H, H_d), 8.34 (d, 4H, J = 8.0 Hz, H_c), 8.12 (d, 8H, J = 1.5 Hz, H_g), 7.92 (t, 4H, J = 1.6 Hz, H_f), 7.67 (s, 4H, H_e), 7.00 (s, 8H, H_i), 6.76 (d, 4H, J = 8.0 Hz, H_b), 2.31 (s, 12H, H_k), 2.27 (s, 24H, H_j), 1.54 (s, 72H, H_h). λ_{max} / nm ($CHCl_3$/1% pyridine) (log ε) 438 (4.76), 466 (4.73), 633 (5.21), 665 (5.26), 1260 (4.59), 1495 (5.16). m/z (MALDI TOF MS+) 2375.09, ($C_{160}H_{146}O_4N_8Zn_2$; $[M]^+$, requires 2375.01). m.p.: > 300 °C.

5,10,15,20-[4,5-Bis-(2,4,6-trimethylphenoxy)anthracene]porphyrin (161)

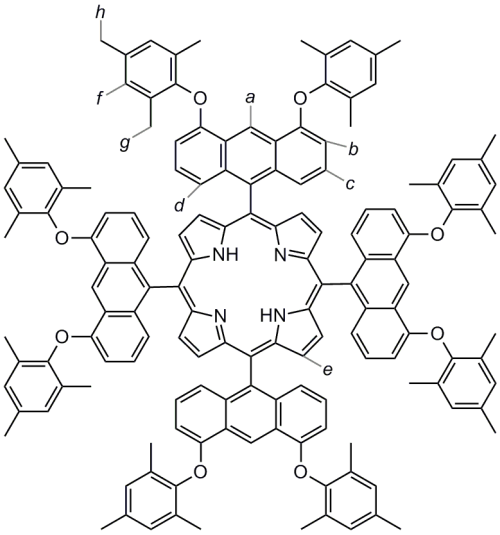

This novel compound was prepared by modification of a literature procedure.[6] To a solution of 4,5-bis-(2,4,6-trimethylphenoxy)-9-bromoanthracene **(156)** (1.28 g, 2.44 mmol) in freshly distilled diethyl ether (5 mL) was added butyllithium (1.6 M solution in hexanes, 1.6 mL, 2.56 mmol) and the mixture was stirred at room temperature for 25 min. After this, a solution of pyrrole-2-carboxaldehyde (0.114 g, 1.20 mmol) in diethyl ether (3 mL) was added and the solution was stirred for 1 h then poured into a beaker containing ammonium chloride (3 g) and ice (10 g). The organic phase was separated, washed with water (3 × 10 mL) and the solvent was removed. This crude product was then dissolved in toluene (6.5 mL) and added to a boiling mixture of propionic acid (3.2 mL) and toluene (4.9 mL). The reaction mixture was stirred for 3 h at 100 °C. The mixture was then allowed to cool overnight. Triethylamine (6 mL) was added to the mixture and the solvents were removed. The crude mixture was then dissolved in $CHCl_3$ and passed through a silica plug ($CHCl_3$). The first red-brown fraction was collected and the solvents removed. The porphyrin was further purified by size exclusion chromatography (THF). The red band was collected and the solvents removed. The product was precipitate from DCM/methanol to give the title porphyrin as a red-brown solid (0.061 g, 9.6% with respect to pyrrole-2-carboxaldehyde). ^{1}H NMR (400 MHz, $CDCl_3$) δH 10.22 (s, 4H, H_a), 8.28 (s, 8H, H_e), 6.89 (s, 16H, H_f), 6.80-6.70 (m, 16H, H_{c+d}), 6.26 (dd, 8H, J_1 = 1.0 Hz, J_2 = 7.3 Hz, H_b), 2.34 (s, 24H, H_h), 2.27 (s, 48H, H_g), -1.73 (s, 2H, H_{NH}). ^{13}C NMR (125 MHz, $CDCl_3$) δC 153.9, 149.2, 136.6, 134.8, 134.5, 131.1, 129.6, 129.1, 125.9, 123.4, 121.7, 117.1, 116.4, 103.6, 20.8, 16.3 (one aromatic peak missing, likely to be the

alpha carbon due to broadening of the signal as a result of proton exchange). λ_{max} / nm (toluene) (log ε) 430 (5.37), 520 (4.48), 553 (3.88), 593 (3.96), 648 (3.54). m/z (MALDI TOF MS+) 2088.6, ($C_{148}H_{126}O_8N_4$; $[M]^+$, requires 2088.0). m.p. > 300 °C. Anal. calc. for $C_{148}H_{126}O_8N_4$: C 85.11, H 6.08, N 2.68. Found: C 85.31, H 6.05, N 2.57.

[5,10,15,20-[4,5-Bis-(2,4,6-trimethylphenoxy)anthracene]porphyrinato]zinc(II) (163)

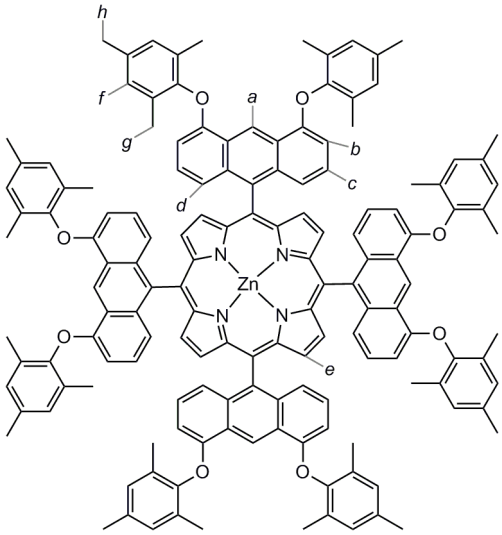

To a solution of 5,10,15,20-[4,5-bis-(2,4,6-trimethylphenoxy)anthracene]porphyrin **(161)** (0.025 g, 0.012 mmol) in DCM (10 mL) was added $Zn(OAc)_2{\cdot}2H_2O$ (0.042 g, 0.191 mmol). The mixture was heated to 35 °C and stirred for 4 h. The extent of the reaction was monitored by TLC. At completion, the mixture was allowed to cool and loaded onto a silica plug (DCM). The red-purple product was collected and the solvents removed. The product was precipitated from DCM/methanol to give the title compound as a red solid (0.023 g, 89%). ^{1}H NMR (400 MHz, $CDCl_3$) δH 10.20 (s, 4H, H_a), 8.30 (s, 8H, H_e), 6.99 (s, 16H, H_f), 6.73 (dd, 8H, J_1 = 7.3 Hz, J_2 = 8.8 Hz, H_c), 6.68 (d, 8H, J = 8.8 Hz, H_d), 6.24 (d, 8H, J = 7.3 Hz, H_b), 2.34 (s, 24H, H_h), 2.28 (s, 48H, H_g). ^{13}C NMR (125 MHz, $CDCl_3$) δC 153.9, 151.4, 149.3, 136.7, 136.3, 134.5, 132.3, 131.1, 129.7, 125.6, 123.4, 122.0, 116.9, 116.6, 103.6, 20.9, 16.4. λ_{max} / nm (toluene) (log ε) 432 (5.47), 553 (4.46). m/z (MALDI TOF MS+) 2151.53, ($C_{148}H_{124}O_8N_4Zn$; $[M]^+$, requires 2151.88). m.p. > 300 °C.

[5,10,15,20-[4,5-Bis-(2,4,6-trimethylphenoxy)anthracene]porphyrinato]nickel(II) (164)

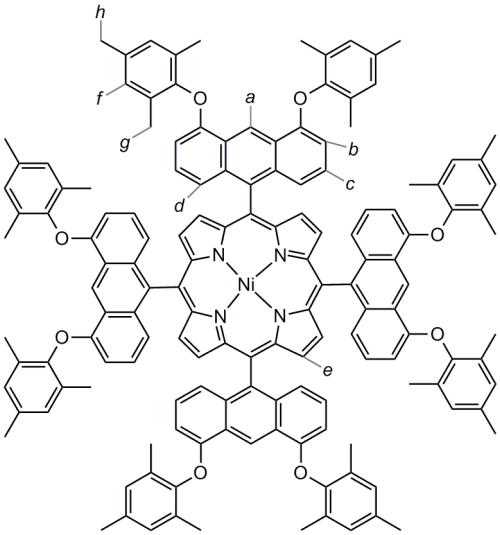

To a solution of 5,10,15,20-[4,5-bis-(2,4,6-trimethylphenoxy)anthracene]porphyrin **(161)** (0.060 g, 0.029 mmol) in *m*-xylene (10 mL) was added $Ni(acac)_2$ (0.112 g, 0.436 mmol). The mixture was heated to reflux and stirred under nitrogen. The extent of the reaction was monitored by TLC. After 3 h the reaction reached completion. The mixture was allowed to cool, then the crude mixture was loaded onto a silica plug (DCM). The orange-red product was collected and the solvents removed. The product was precipitated from DCM/methanol to give the title compound (0.052 g, 84%). ^{1}H NMR (400 MHz, $CDCl_3$) δH 10.16 (s, 4H, H_a), 8.24 (s, 8H, H_e), 6.97 (s, 16H, H_f), 6.83 (dd, 8H, J_1 = 7.3 Hz, J_2 = 8.9 Hz, H_c), 6.71 (d, 8H, J = 8.9 Hz, H_d), 6.25 (d, 8H, J = 7.3 Hz, H_b), 2.34 (s, 24H, H_h), 2.25 (s, 48H, H_g). ^{13}C NMR (125 MHz, $CDCl_3$) δC 153.85, 149.22, 144.21, 135.97, 134.46, 134.08, 132.80, 131.05, 129.60, 125.85, 123.40, 121.47, 117.00, 115.73, 103.69, 20.83, 16.26. λ_{max} / nm (toluene) (log ε) 427 (5.36), 533 (4.41), 564 (3.97). m/z (MALDI TOF MS+) 2145.79, ($C_{148}H_{124}O_8N_4Ni$; $[M]^+$, requires 2145.89). m.p. > 300 °C.

[3,5,7,8,10,12,13,15,17,18,20,2-(1,8-Bis(2,4,6-trimethylphenoxy)anthracene)]-porphyrinato]nickel(II) (165)

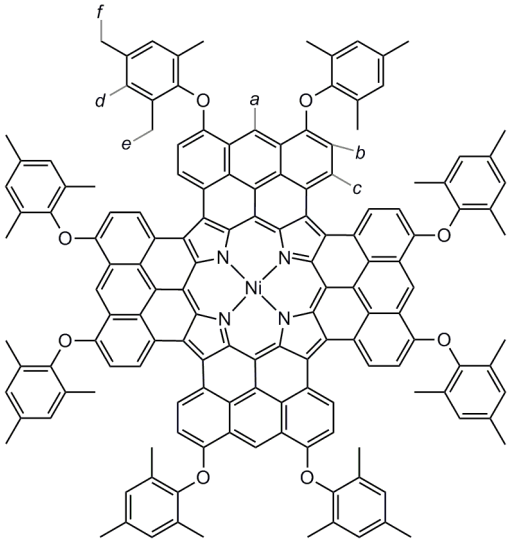

This novel compound was prepared by modification of a literature procedure.[17,18] A two-necked flask was charged with $FeCl_3$ (0.090 g, 0.555 mmol) and dried under vacuum overnight, then nitromethane (1.0 mL) was added under argon. The $FeCl_3$ solution was added by syringe to a solution of [5,10,15,20-[4,5-bis-(2,4,6-trimethylphenoxy)anthracene]porphyrinato]nickel(II) **(164)** (0.027 g, 0.013 mmol) in dry DCM (5 mL) under nitrogen and stirred at room temperature. The reaction was monitored by TLC and at completion (after 30 min) it was quenched by addition of saturated $NaHCO_3$ (aq) (10 mL). The organic phase was extracted with DCM (10 mL), collected and washed with water (3 × 10 mL). The organic layers were collected and the solvent evaporated. The solid residue was purified by silica chromatography (1:1 PET:DCM with 5% NEt_3) and the dark blue-green band was collected. The solvents were removed and the residue was purified further by size exclusion chromatography (toluene). The blue-green band was collected, the solvents were removed, and the product was precipitated from DCM/methanol and then DCM/pentane to give the title compound as a green-black solid (0.013 g, 49%). ^{1}H NMR (500 MHz, C_6D_6) δH 10.68 (s, 4H, H_a), 10.44 (d, 8H, J = 7.9 Hz, H_c), 6.98 (s, 16 H, H_d), 6.64 (d, 8H, J = 7.9 Hz, H_b), 2.40 (s, 48 H, H_e), 2.37 (s, 24 H, H_f). λ_{max} / nm (toluene) (log ε) 313 (5.08), 466 (4.43), 504 (4.35), 681 (4.52), 767 (4.60), 847 (4.85), 1198 (4.56), 1417 (5.07). m/z (MALDI TOF MS+) 2129.39, ($C_{148}H_{108}O_8N_4Ni$; $[M]^+$, requires 2129.76). m.p. > 300 °C.

[5-Bromo-15-[10-(1,8-bis(2,4,6-trimethylphenyoxy)anthracene)]-10,20-bis-(3,5-di-*tert*-butylphenyl)-porphyrinato]zinc(II) (194)

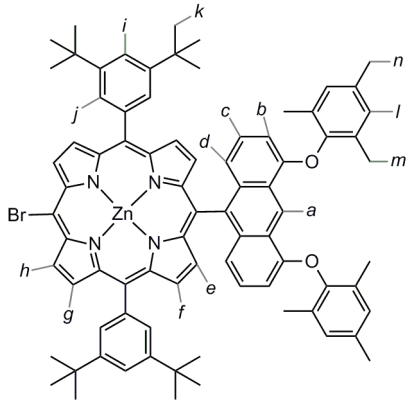

To a solution of [5-[10-(1,8-bis(2,4,6-trimethylphenyoxy)anthracene)]-10,20-bis-(3,5-di-*tert*-butylphenyl)-porphyrinato]zinc(II) **(130)** (0.200 g, 0.167 mmol) in $CHCl_3$/1% pyridine (150 mL) was added dropwise whilst stirring, a solution of NBS (0.033 g, 0.185 mmol) in $CHCl_3$/1% pyridine (50 mL). The extent of the reaction was monitored by TLC. At completion (30 min), acetone (100 mL) was added and the reaction mixture was stirred for a further 10 min. The solvents were then removed and the product was precipitated from DCM/methanol to give the title compound (0.203 g, 95%). ^{1}H NMR (400 MHz, $CDCl_3$/1% pyridine-d_5) δH 10.23 (s, 1H, H_a), 9.72 (d, 2H, J = 4.7 Hz, H_h), 8.95 (d, 2H, J = 4.7 Hz, H_g), 8.71 (d, 2H, J = 4.7 Hz, H_f), 8.33 (d, 2H, J = 4.7 Hz, H_e), 8.00 (d, 4H, J = 1.9 Hz, H_j), 7.74 (t, 2H, J = 1.9 Hz, H_i), 6.99 (s, 4H, H_l), 6.62 (dd, 2H, J_1 = 7.3 Hz, J_2 = 9.1 Hz, H_c), 6.45 (d, 2H, J = 9.1 Hz, H_d), 6.24 (d, 2H, J = 7.3 Hz, H_b), 2.34 (s, 6H, H_n), 2.30 (s, 12H, H_m), 1.49 (s, 36H, H_k). ^{13}C NMR (125 MHz, $CDCl_3$/1% d_5 pyridine) 153.9, 151.6, 151.0, 150.4, 149.3 (x 2), 148.3, 142.0, 136.7, 136.6, 134.5, 133.1, 132.9, 132.2, 131.9, 131.1, 129.8, 129.6, 125.3, 123.3, 122.5, 121.8, 120.6, 116.6, 116.5, 104.2, 103.5, 35.0, 31.7, 20.9, 16.3. λ_{max} / nm ($CHCl_3$/ 1% pyridine) (log ε) 416 (4.73) shoulder, 436 (5.69), 570 (4.28), 610 (4.07). m/z (MALDI TOF MS+) 1273.26 ($C_{80}H_{79}O_2N_4ZnBr$; [M]+, requires 1273.48). m.p. > 300 °C. Anal. calc. for $C_{80}H_{79}O_2N_4ZnBr$: C 75.43, H 6.25, N 4.40. Found: C 75.39, H 6.15, N 4.37.

[5-(Trihexylsilylacetylene)-15-[10-(1,8-bis(2,4,6-trimethylphenyoxy)anthracene)]-10,20-bis-(3,5-di-*tert*-butylphenyl)-porphyrinato]zinc(II) (195)

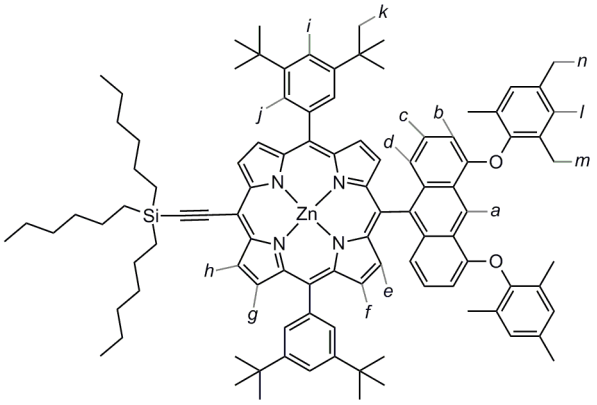

A 2-necked flask was dried under vacuum and charged with [5-bromo-15-[10-(1,8-bis(2,4,6-trimethylphenyoxy)anthracene)]-10,20-bis-(3,5-di-*tert*-butylphenyl)-porphyrinato]zinc(II) **(194)** (0.030 g, 0.024 mmol), CuI (0.001 g, 0.005 mmol), PPh_3 (0.005 g, 0.019 mmol) and $Pd_2(dba)_3$ (0.004 g, 0.005 mmol). These compounds were dried for a further 3 h under vacuum then purged with nitrogen. To this was added toluene (1.5 mL) and freshly distilled diisopropylamine (1.5 mL). The reaction mixture was freeze-thaw degassed and the THS acetylene (0.01 mL, 0.026 mmol) was added by syringe. The reaction mixture was heated to 80 °C and the extent of the reaction was monitored by TLC. At completion (3 h), the reaction mixture was allowed to cool and the solvents were removed. The residue was purified by silica gel chromatography and the solvents were removed to give the product as a green oily solid (0.020 g, 56%). ^{1}H NMR (400 MHz, $CDCl_3$) δH 10.27 (s, 1H, H_a), 9.81 (d, 2H, J = 4.8 Hz, H_h), 9.04 (d, 2H, J = 4.8 Hz, H_g), 8.78 (d, 2H, J = 4.8 Hz, H_f), 8.44 (d, 2H, 4.5, H_e), 8.06 (d, 4H, J = 1.4 Hz, H_j), 7.77 (t, 2H, J = 1.91, H_i), 7.01 (s, 4H, H_l), 6.75 (dd, 2H, J_1= 7.3 Hz J_2 = 8.9 Hz, H_c), 6.61 (d, 2H, J = 8.9 Hz, H_d), 6.28 (d, 2H, J = 7.3, H_b), 2.36 (s, 6H, H_n), 2.32 (s, 12H, H_m), 1.85-1.75 (m, 6H, H_{hexyl}), 1.62-1.49 (m, 42H, $H_{hexyl+k}$), 1.47-1.32 (m, 12H, H_{hexyl}), 1.07-1.01 (m, 6H, H_{hexyl}), 0.94-0.89 (m, 9H, H_{hexyl}). ^{13}C NMR (125 MHz, $CDCl_3$) 154.0, 152.5, 151.2, 150.6, 150.4, 149.2, 148.6, 141.3, 136.5, 135.8, 134.5, 133.0, 132.8, 132.1, 131.1, 131.0, 129.7, 129.6, 125.7, 123.5, 123.2, 121.7, 120.9, 118.4, 116.9, 108.8, 103.6, 100.4, 99.7, 35.0, 33.4, 31.7 (× 2), 24.4, 22.7, 20.9, 16.4, 14.2, 13.9. λ_{max} / nm ($CHCl_3$) 415 (shoulder), 436, 564, 604. m/z (MALDI TOF MS+) 1500.90 ($C_{100}H_{118}O_2N_4ZnSi$; [M]+, requires 1500.83). m.p. > 300 °C.

[5-(Triisopropylsilylacetylene)-15-[10-(1,8-bis(2,4,6-trimethylphenyoxy)anthracene)]-10,20-bis-(3,5-di-*tert*-butylphenyl)-porphyrinato] zinc(II) (199)

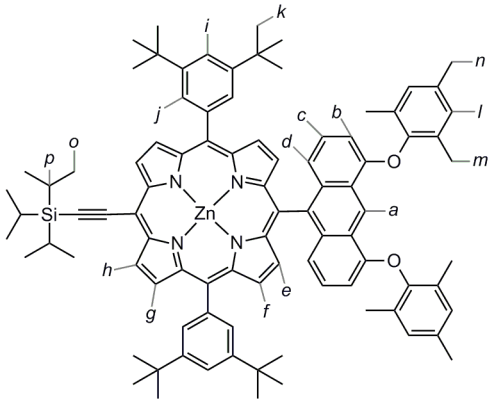

A 2-necked flask was dried under vacuum and charged with [5-bromo-15-[10-(1,8-bis(2,4,6-trimethylphenyoxy)anthracene)]-10,20-bis-(3,5-di-*tert*-butylphenyl)-porphyrinato]zinc(II) **(194)** (0.200 g, 0.157 mmol), CuI (0.006 g, 0.032 mmol), PPh_3 (0.033 g, 0.126 mmol) and $Pd_2(dba)_3$ (0.029 g, 0.032 mmol). These compounds were dried for a further 3 h under vacuum then purged with nitrogen. To this was added dry toluene (9.0 mL) and freshly distilled diisopropylamine (3.0 mL). The reaction mixture was freeze-thaw degassed and the TIPS acetylene (0.88 mL, 3.92 mmol) was added by syringe. The reaction mixture was heated to 80 °C and the extent of the reaction was monitored by TLC. At completion (3 h), the reaction mixture was allowed to cool and the solvents were removed. The residue was purified by silica gel chromatography (1:1 DCM:PET) and precipitated (DCM/MeOH) to give the product as a purple powder (0.177 g, 82%). ^{1}H NMR (400 MHz, $CDCl_3$) δH 10.28 (s, 1H, H_a), 9.85 (d, 2H, J = 4.5 Hz, H_h), 9.05 (d, 2H, J = 4.5 Hz, H_g), 8.78 (d, 2H, J = 4.5 Hz, H_f), 8.45 (d, 2H, J = 4.5 Hz, H_e), 8.05 (d, 4H, J = 1.9 Hz, H_j). 7.76 (t, 2H, J = 1.9 Hz, H_i), 7.01 (s, 4H, H_l), 6.75 (dd, 2H, J_1 = 7.3 Hz, J_2 = 8.9 Hz, H_c), 6.63 (d, 2H, J = 8.9 Hz, H_d), 6.29 (d, 2H, J = 7.3 Hz, H_b), 2.36 (s, 6H, H_n), 2.34 (s, 12H, H_m), 1.51 (s, 36H, H_k), 1.49-1.46 (m, 21H, H_{o+p}) ^{13}C NMR (125 MHz, $CDCl_3$) 154.0, 152.5, 151.2, 150.6, 150.4, 149.3, 148.6, 141.3, 136.6, 135.8, 134.5, 133.2, 132.8, 132.1, 131.1, 130.9, 129.6, 129.4, 125.7, 123.5, 123.2, 121.8, 120.9, 118.4, 116.9, 109.5, 103.7, 100.5, 97.6, 35.0, 31.7, 20.9, 19.2, 16.4, 11.9. λ_{max} / nm ($CHCl_3$) (log ε) 416 (4.71) shoulder, 435 (5.66), 564 (4.26), 604 (4.16). m/z (MALDI TOF MS+) 1375.73

($C_{91}H_{100}O_2N_4ZnSi$; [M]+, requires 1375.70). m.p. > 300 °C. Anal. calc. for $C_{91}H_{100}O_2N_4ZnSi$: C 79.47, H 7.33, N 4.07. Found: C 79.57, H 7.45, N 3.98.

[5-(Methyl-4-ethynylbenzoate)-15-[10-(1,8-bis(2,4,6-trimethylphenyoxy)anthracene)]-10,20-bis-(3,5-di-*tert*-butylphenyl)-porphyrinato]zinc(II) (204)

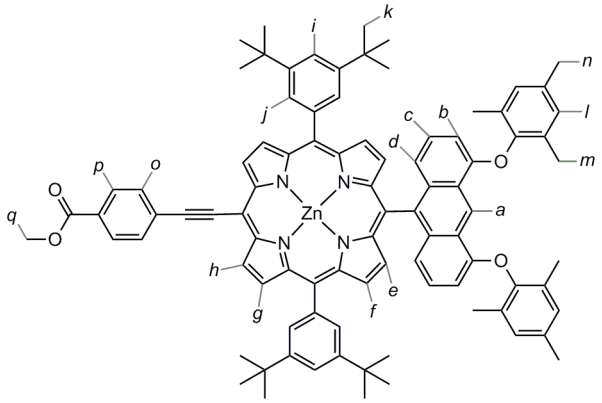

A 2-necked flask was dried under vacuum and charged with [5-(triisopropylsilylacetylene)-15-[10-(1,8-bis(2,4,6-trimethylphenyoxy)anthracene)]-10,20-bis-(3,5-di-*tert*-butylphenyl)-porphyrinato]zinc(II) **(199)** (0.050 g, 0.036 mmol), 4-iodobenzoic ester **(202)** (0.048 g, 0.183 mmol), CuI (0.001 g, 0.007 mmol), PPh_3 (0.008 g, 0.029 mmol) and $Pd_2(dba)_3$ (0.007 g, 0.007 mmol). These compounds were dried for a further 3 h under vacuum then purged with nitrogen. To this was added dry THF (3.0 mL) and freshly distilled diisopropylamine (2.0 mL). The reaction mixture was freeze-thaw degassed three times and purged with nitrogen. To this was added TBAF (1.0 M in THF, 0.037 mL, 0.037 mmol) by syringe and the reaction mixture was warmed to 50 °C and stirred. The extent of the reaction was monitored by TLC. At completion (3 h) the mixture was allowed to cool and the solvents were removed. The solid residue was dissolved in DCM and passed over a short silica plug (DCM). The solvents were again removed and the solid residue was dissolved in toluene/ 1% pyridine and passed through a short size exclusion column to remove excess iodo-benzoic ester. The solvents were removed and the residue was precipitated from DCM/methanol to give the title compound as a green powder (0.036 g, 74%). ^{1}H NMR (500 MHz, $CDCl_3$/1% pyridine-d_5) δH 10.22 (s, 1H, H_a), 9.78 (d, 2H, J = 4.6 Hz, H_h), 8.98 (d, 2H, J = 4.6 Hz, H_g), 8.68 (d, 2H, J = 4.6 Hz, H_f), 8.31 (d, 2H, J = 4.6 Hz, H_e), 8.22 (d, 2H, J = 8.5 Hz, H_p), 8.08 (d, 2H, J = 8.5 Hz, H_o), 8.01 (d, 4H, J

= 1.8 Hz, H_j), 7.74 (t, 2H, J = 1.8 Hz, H_i), 6.98 (s, 4H, H_l), 6.63 (dd, 2H, J_1 = 7.3 Hz J_2 = 9.0 Hz, H_c), 6.47 (d, 2H, J = 9.0 Hz, H_d), 6.24 (d, 2H, J = 7.3 Hz, H_b), 3.99 (s, 3H, H_q), 2.33 (s, 6H, H_n), 2.30 (s, 12H, H_m), 1.49 (s, 36H, H_k). ^{13}C NMR (125 MHz, $CDCl_3$/1% pyridine-d_5) 166.7, 154.0, 152.1, 151.3, 150.8, 150.4, 149.3, 148.7, 141.2, 136.5, 135.7, 134.5, 133.3, 132.9, 132.3, 131.3, 131.1, 130.5, 129.8, 129.7 (x2), 129.2, 129.1, 125.7, 123.6, 123.5, 121.7, 121.0, 118.9, 117.0, 103.7, 99.4, 96.1, 95.5, 52.2, 35.0, 31.7, 20.9, 16.4. λ_{max} / nm ($CHCl_3$) (log ε) 445 (5.89), 568 (4.53), 615 (4.74). m/z (MALDI TOF MS+) 1353.46 ($C_{90}H_{86}O_4N_4Zn$; [M]+, requires 1353.60). m.p. > 300 °C. Anal. calc. for $C_{90}H_{86}N_4O_4Zn$: C 79.89, H 6.41, N 4.14. Found: C 79.95, H 6.48, N 4.21.

[5-(4-Ethynylbenzoic acid)-15-[10-(1,8-bis(2,4,6-trimethylphenyoxy)anthracene)]-10,20-bis-(3,5-di-*tert*-butylphenyl)-porphyrinato]zinc(II) (192)

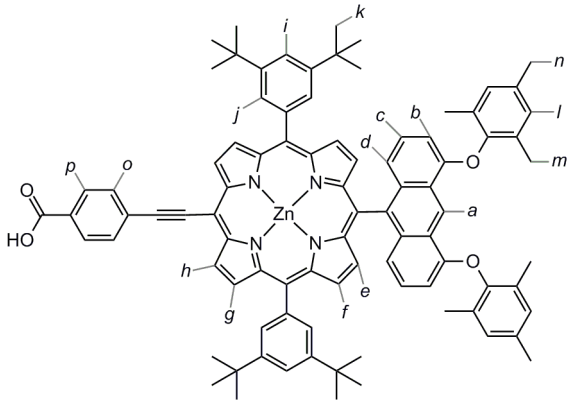

To a solution of [5-(methyl-4-ethynylbenzoate)-15-[10-(1,8-bis(2,4,6-trimethylphenyoxy)anthracene)]-10,20-bis-(3,5-di-*tert*-butylphenyl)-porphyrinato]zinc(II) (0.020 g, 0.015 mmol) **(204)** in THF (5.0 mL) was added methanol (3.0 mL) and sodium hydroxide (aq) (8.0 M, 1.0 mL, 8.00 mmol). The reaction mixture was stirred at room temperature and the extent of the reaction was monitored by TLC. At completion (5 h) water (10.0 mL) was added to the mixture together with acetic acid (1.0 mL). The organic layer was extracted with DCM and washed with water (3 × 10 mL). The solvent was then removed and solid residue was dissolved in DCM and precipitated from DCM/pentane to give the title compound as a green solid (0.016 g, 81%). ^{1}H NMR (400 MHz, $CDCl_3$/ 5% MeOD) δH 10.25 (s, 1H, H_a), 9.81 (d, 2H, J = 4.6 Hz, H_h), 9.02 (d, 2H, J = 4.6 Hz, H_g), 8.71 (d, 2H, J = 4.6 Hz, H_f), 8.37 (d, 2H, J = 4.6 Hz, H_e), 8.25 (d, 2H, J = 8.2 Hz, H_p), 8.11 (d, 2H, J = 8.2 Hz, H_o), 8.05 (d,

4H, J = 1.8 Hz, H_j), 7.75 (t, 2H, J = 1.8 Hz, H_i), 6.99 (s, 4H, H_l), 6.73 (dd, 2H, J_1 = 7.3 Hz, J_2 = 8.9 Hz, H_c), 6.63 (d, 2H, J = 8.9 Hz, H_d), 6.27 (d, 2H, J = 7.3 Hz, H_b), 2.34 (s, 6H, H_n), 2.32 (s, 12H, H_m), 1.50 (s, 36H, H_k). ^{13}C NMR (125 MHz, $CDCl_3$/ 5% MeOD) 168.5, 157.2, 153.7, 150.0, 149.9, 148.9 (x 2), 145.2, 141.7, 135.1, 134.7, 133.3, 131.0, 130.9, 130.1, 129.9, 129.6 (x 2), 129.5, 129.4, 128.9, 127.7, 125.6, 124.9, 123.7, 122.8, 120.8, 120.3, 118.9, 111.6, 107.6, 97.4, 96.7, 94.8, 35.1, 31.8, 20.9, 16.4. λ_{max} / nm ($CHCl_3$/1% pyridine) (log ε) 453 (5.69), 584 (4.18), 639 (4.67). m/z (MALDI TOF MS+) 1339.58 ($C_{89}H_{84}O_4N_4Zn$; [M]+, requires 1339.59). m.p. > 300 °C.

[5-(Triisopropylsilylacetylene)-13,15,17-[4,5,10-(1,8-bis(2,4,6-trimethylphenyoxy)anthracene)]-10,20-bis-(3,5-di-*tert*-butylphenyl)-porphyrinato]zinc(II) (200)

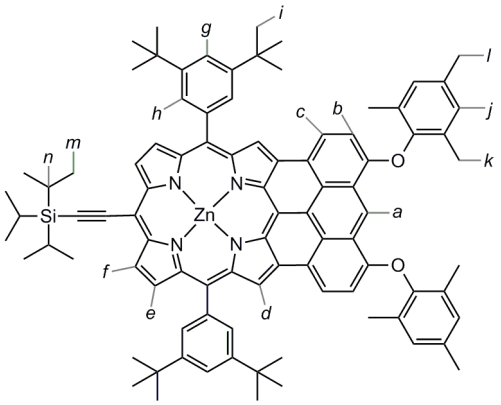

This novel compound was prepared by modification of literature fusion conditions.[17,18] To a solution of [5-(triisopropylsilylacetylene)-15-[10-(1,8-bis(2,4,6-trimethylphenyoxy)anthracene)]-10,20-bis-(3,5-di-*tert*-butylphenyl)-porphyrinato]zinc(II) **(199)** (0.010 g, 0.007 mmol) and zinc(II) chloride (0.050 g, 0.370 mmol) in dry DCM (3.0 mL) was added $FeCl_3$ (0.012 g, 0.074 mmol) in dry nitromethane (1.0 mL) and the reaction mixture was stirred under nitrogen. After 30 min 1,8-bis(dimethylamino)naphthalene (proton sponge) was added (0.016 g, 0.074 mmol) and the mixture was stirred for another 30 min. After this time $FeCl_3$ (0.012 g, 0.074 mmol) in nitromethane (1.0 mL) was added and the mixture was stirred for a further 30 min after which time 1,8-bis(dimethylamino)naphthalene (0.016 g, 0.074 mmol) was again added. This $FeCl_3$/1,8-bis(dimethylamino)naphthalene cycle was repeated for a third time, with a 30 min interval

between addition of the two different reagents. Saturated $NaHCO_3$ (aq) (10 mL) was then added to quench the reaction. The organic layer was separated and washed with water (3 × 10 mL). The organic layer was collected and the solvents removed. The solid residue was purified by silica gel chromatography (2:1 PET:DCM) and precipitated from DCM/methanol to give the title compound as a dark solid (0.006 g, 63%). ^{1}H NMR (400 MHz, $CDCl_3$/5% pyridine-d_5) δH 10.27 (s, 1H, H_a), 9.43 (d, 2H, J = 4.5 Hz, H_f), 9.13 (s, 2H, H_d), 8.77 (d, 2H, J = 8.0 Hz, H_c), 8.71 (d, 2H, J = 4.8 Hz, H_e), 8.08 (d, 4H, J = 1.9 Hz, H_h), 7.80 (t, 2H, J = 1.9 Hz, H_g), 7.06 (s, 4H, H_j), 6.80 (d, 2H, J = 8.0 Hz, H_b), 2.41 (s, 6H, H_l), 2.32 (s, 12H, H_k), 1.57 (s, 36H, H_i), 1.41-1.45 (m, 21H, H_{m+n}). ^{13}C NMR (125 MHz, $CDCl_3$/5% d_5 pyridine) 156.9, 154.0, 150.1, 149.9, 149.0, 148.6, 145.3, 142.1, 135.0, 134.6, 133.0, 131.0, 129.8, 129.7, 129.4, 128.9, 128.3, 125.2, 124.9, 123.8, 123.1, 120.7, 119.4, 119.0, 111.0, 110.9, 107.5, 98.1, 95.6, 35.0, 31.8, 20.9, 19.1, 16.4, 12.0. λ_{max} / nm ($CHCl_3$) (log ε) 886 (4.99), 798 (4.76), 598 (4.87), 548 (4.90), 508 (4.73), 473 (5.06), 448 (4.92), 414 (4.77), 395 (4.79), 343 (4.98), 330 (4.88). m/z (MALDI TOF MS+) 1371.69 ($C_{91}H_{96}O_2N_4ZnSi$; [M]+, requires 1371.67). m.p. > 300 °C.

[5-(Methyl-4-ethynylbenzoate)-13,15,17-[4,5,10-(1,8-bis(2,4,6-trimethylphenyoxy)anthracene)]-10,20-bis-(3,5-di-*tert*-butylphenyl)-porphyrinato]zinc(II) (203)

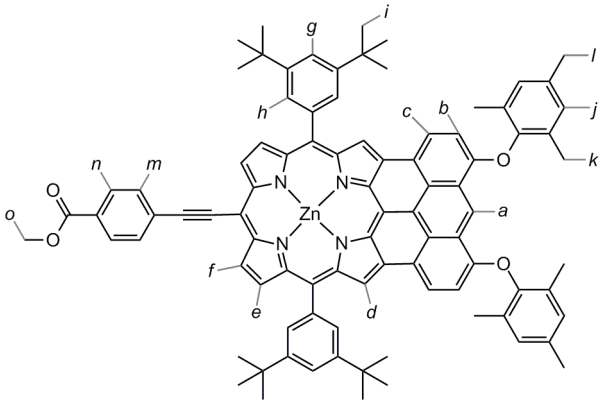

A 2-necked flask was dried under vacuum and charged with [5-(triisopropylsilylacetylene)-13,15,17-[4,5,10-(1,8-bis(2,4,6-trimethylphenyoxy)anthracene)]-10,20-bis-(3,5-di-*tert*-butylphenyl)-porphyrinato]zinc(II) **(200)** (0.032 g, 0.023 mmol), 4-iodobenzoic ester **(202)** (0.033 g, 0.125 mmol), CuI (0.001 g, 0.005 mmol), PPh_3 (0.005 g, 0.019 mmol) and $Pd_2(dba)_3$ (0.005 g, 0.005 mmol). These compounds were dried for a further 3 h under vacuum then

purged with nitrogen. To this was added dry THF (3.0 mL) and freshly distilled diisopropylamine (1.5 mL). The reaction mixture was freeze-thaw degassed three times and purged with nitrogen. To this was added TBAF (1.0 M in THF, 0.026 mL, 0.026 mmol) by syringe and the reaction mixture was warmed to 50 °C and stirred. The extent of the reaction was monitored by TLC. At completion (3 h) the mixture was allowed to cool and the solvents were removed. The solid residue was dissolved in DCM and passed over a short silica plug (DCM). The solvents were again removed and the solid residue was dissolved in toluene/ 1% pyridine and passed through a short size exclusion column (toluene/1% pyridine) to remove excess benzoic ester. The solvents were removed and the residue was precipitated from DCM/methanol to give the title compound as a black powder (0.026 g, 83%).^{1}H NMR (400 MHz, $CDCl_3$) δH 10.33 (s, 1H, H_a), 9.48 (d, 2H, J = 4.5 Hz, H_f), 9.19 (s, 2H, H_d), 8.82 (d, 2H, J = 8.1 Hz, H_c), 8.79 (d, 2H, J = 4.5 Hz, H_e), 8.20 (d, 2H, J = 8.6 Hz, H_n), 8.13 (d, 4H, J = 1.7 Hz, H_h), 8.03 (d, 2H, J = 8.6 Hz, H_m), 7.83 (t, 2H, J = 1.7 Hz, H_g), 7.07 (s, 4H, H_j), 6.83 (d, 2H, J = 8.1 Hz, H_b), 4.00 (s, 3H, H_o), 2.42 (s, 6H, H_l), 2.33 (s, 12H, H_k), 1.60 (s, 36H, H_i). ^{13}C NMR (125 MHz, $CDCl_3$) 166.8, 157.1, 153.7, 150.1, 150.0, 149.0, 148.8, 145.3, 142.0, 135.1, 134.7, 133.2, 131.0, 129.9, 129.8, 129.7 (x 2), 129.3, 129.2, 128.6, 128.1, 125.7, 124.9, 123.8, 123.2, 123.0, 120.7, 119.9, 119.0, 111.5, 107.6, 98.0, 96.5, 94.7, 52.2, 35.1, 31.8, 20.9, 16.4. λ_{max} / nm ($CHCl_3$) (log ε) 418 (4.55), 490 (5.00), 565 (4.60), 609 (4.63), 755 (4.16), 829 (4.56), 925 (4.80). m/z (MALDI TOF MS+) 1349.55 ($C_{90}H_{82}O_4N_4Zn$; [M]+, requires 1349.57). m.p. > 300 °C. Anal. calc. for $C_{90}H_{82}N_4O_4Zn$: C 80.13, H 6.13, N 4.15. Found: C 80.22, H 6.06, N 4.06.

[5-(4-Ethynylbenzoic acid)-13,15,17-[4,5,10-(1,8-bis(2,4,6-trimethylphenyoxy)anthracene)]-10,20-bis-(3,5-di-*tert*-butylphenyl)-porphyrinato]zinc(II) (193)

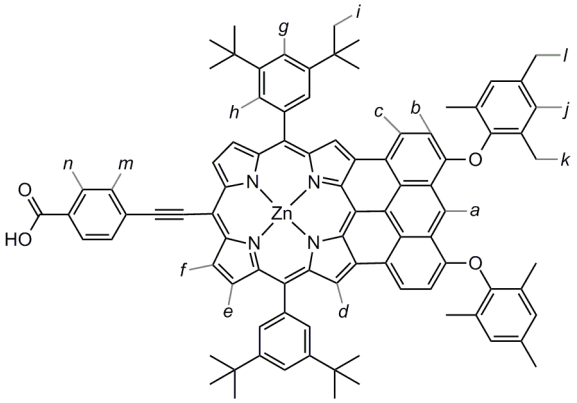

To a solution of [5-(methyl-4-ethynylbenzoate)-13,15,17-[4,5,10-(1,8-bis(2,4,6-trimethylphenyoxy)anthracene)]-10,20-bis-(3,5-di-*tert*-butylphenyl)-porphyrinato]zinc(II) **(203)** (0.018 g, 0.013 mmol) in THF (5.0 mL) was added methanol (3.0 mL) and sodium hydroxide (aq) (8 M, 1.0 mL, 8.00 mmol). The reaction mixture was stirred at room temperature and the extent of the reaction was monitored by TLC. At completion (5 h) water (10 mL) was added to the mixture together with acetic acid (1.0 mL). The organic layer was extracted with DCM and washed with water (3 × 10 mL). The solvent was then removed and solid residue was dissolved in DCM and precipitated from pentane to give the title compound as a black solid (0.015 g, 86%). ^{1}H NMR (400 MHz, $CDCl_3$/MeOD) δH 10.36 (s, 1H, H_a), 9.49 (d, 2H, J = 4.6 Hz, H_f), 9.21 (s, 2H, H_d), 8.85 (d, 2H, J = 8.0 Hz, H_c), 8.80 (d, 2H, J = 4.6 Hz, H_e), 8.21 (d, 2H, J = 8.3 Hz, H_n), 8.15 (d, 4H, J = 1.8 Hz, H_h), 8.03 (d, 2H, J = 8.3 Hz, H_m), 7.84 (t, 2H, J = 1.8 Hz, H_g), 7.06 (s, 4H, H_j), 6.85 (d, 2H, J = 8.0 Hz, H_b), 2.41 (s, 6H, H_l), 2.33 (s, 12H, H_k), 1.59 (s, 36 H, H_i).^{13}C NMR (125 MHz, $CDCl_3$/MeOD) 168.5, 157.2, 153.7, 150.0, 149.8, 148.9 (× 2), 145.1, 141.7, 135.1, 134.6, 133.3, 131.0, 130.9, 130.1, 129.8, 129.6, 129.5, 129.4, 129.0, 127.7, 125.6, 124.8, 123.7, 122.7, 120.8, 120.3, 118.9, 111.5, 107.6, 97.3, 96.6, 94.8, 35.0, 31.7, 20.9, 16.3 (1 aromatic signal missing- probably overlapping with other signals, unidentifiable by HSQC/DEPT). λ_{max}/ nm ($CHCl_3$/1% pyridine) (log ε) 418 (4.55), 488 (5.00), 565 (4.60), 609 (4.63), 757 (4.16), 829 (4.56), 924 (4.80). m/z (MALDI TOF MS+) 1335.57 ($C_{89}H_{80}O_4N_4Zn$; [M]+, requires 1335.56).

6.4 References

(1) Littler, B. J.; Miller, M. A.; Hung, C. H.; Wagner, R. W.; O'Shea, D. F.; Boyle, P. D.; Lindsey, J. S. *J. Org. Chem.* **1999**, *64*, 1391-1396.
(2) Plater, M. J.; Aiken, S.; Bourhill, G. *Tetrahedron* **2002**, *58*, 2405-2413.
(3) Liu, Y. L.; Liu, Z. B.; Tian, J. G.; Zhu, Y.; Zheng, J. Y. *Optics Communications* **2008**, *281*, 776-781.
(4) Baba, H.; Chen, J.; Shinokubo, H.; Osuka, A. *Chem. Eur. J.* **2008**, *14*, 4256-4262.
(5) Hyslop, A. G.; Kellett, M. A.; Iovine, P. M.; Therien, M. J. *J. Am. Chem. Soc.* **1998**, *120*, 12676-12677.
(6) Volz, H.; Schäffer, H. *Chem. Ztg.* **1985**, *109*, 308-309.
(7) Andreani, A.; Rambaldi, M.; Bonazzi, D.; Lelli, G.; Greci, L.; Bossa, R.; Galatulas, I. *Arch. Pharm.* **1985**, *318*, 400-405.
(8) Fonge, H.; Jin, L.; Wang, H.; Ni, Y.; Bormans, G.; Verbruggen, A. *Bioorg. Med. Chem. Lett.* **2007**, *17*, 4001-4005.
(9) Liebermann, C. *Chem. Ber.* **1879**, *1*, 182-188.
(10) Brockmann, H.; Budde, G. *Chem. Ber.* **1952**, *86*, 432-433.
(11) Davis, N. K. S.; Pawlicki, M.; Anderson, H. L. *Org. Lett.* **2008**, *10*, 3945-3947.
(12) Shao, M.; Zhao, Y. *Tetrahedron Lett.* **2010**, *51*, 2892-2895.
(13) Brewis, M.; Clarkson, G. J.; Humberstone, P.; Makhseed, S.; McKeown, N. B. *Chem. Eur. J.* **1998**, *4*, 1633-1640.
(14) Prinz, H.; Burgemeister, T.; Wiegrebe, W.; Müller, K. *J. Org. Chem.* **1996**, *61*, 2857-2860.
(15) Toyota, S.; Makino, T. *Tetrahedron Lett.* **2003**, *44*, 7775-7778.
(16) Robello, D. R.; Eldridge, T. D.; Urankar, E. J. *Org. Prep. Proced. Int.* **1999**, *31*, 433-439.
(17) Kurotobi, K.; Kim, K. S.; Noh, S. B.; Kim, D.; Osuka, A. *Angew. Chem. Int. Ed.* **2006**, *45*, 3944-3947.
(18) Tanaka, M.; Hayashi, S.; Eu, S.; Umeyama, T.; Matano, Y.; Imahori, H. *Chem. Commun.* **2007**, 2069-2071.
(19) Tsuda, A.; Osuka, A. *Science* **2001**, *293*, 79-82.

Appendix: X-ray Crystal Data

For crystal structure data for fully fused bis-anthracene porphyrin **133** and fully fused tetra-anthracene porphyrin **165** please see the references 1 and 2 (below) respectively:

(1) Davis, N. K. S.; Thompson, A. L.; Anderson, H. L. *Org. Lett.*, **2010**, *12*, 2124 — 2127

(2) Davis, N. K. S.; Thompson, A. L.; Anderson, H. L. *J. Am. Chem. Soc.* **2011**, *133*, 30—31

1,8-Bis(2,6-diisopropylphenoxy)anthraquinone (121)

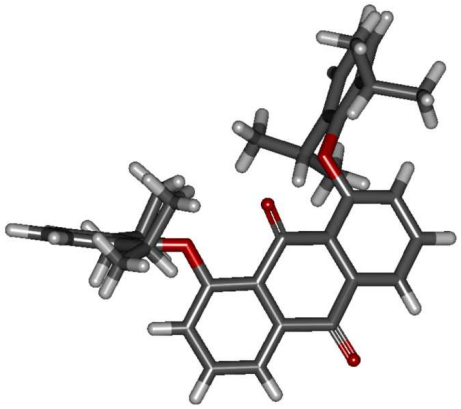

Figure 1: Three different views of the molecular structure of anthraquinone **121** in the crystal.

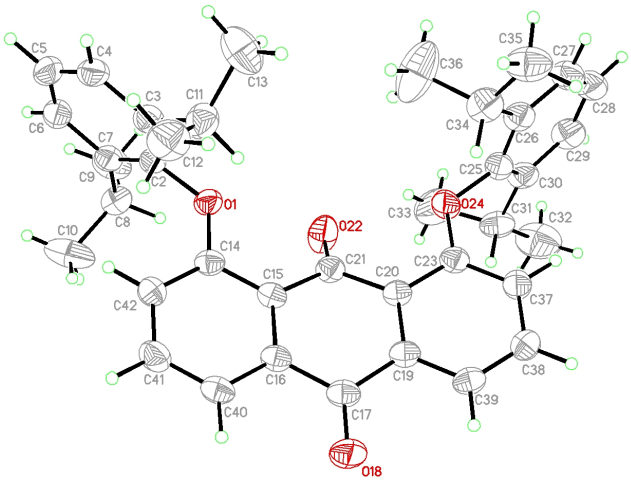

Figure 2: Molecular structure of **121** in the crystal showing the numbering system employed.

Table 1: Crystal data and structure refinement for **121**

Empirical formula	C38 H40 O4	
Formula weight	560.73	
Temperature	150 K	
Wavelength	0.71073 Å	
Crystal system	Monoclinic	
Space group	P 1 21/n 1	
Unit cell dimensions	a = 8.4636(1) Å	α= 90°.
	b = 13.2438(2) Å	β= 97.8810(7)°.
	c = 28.2717(5) Å	γ = 90°.
Volume	3139.05(8) $Å^3$	
Z	4	
Density (calculated)	1.186 Mg/m^3	
Absorption coefficient	0.075 mm^{-1}	
F(000)	1200	
Crystal size	0.370 x 0.300 x 0.260 mm^3	
Theta range for data collection	5.102 to 27.496°.	
Index ranges	-10<=h<=10, 0<=k<=17, 0<=l<=36	
Reflections collected	30307	
Independent reflections	7098 [R(int) = 0.056]	
Completeness to theta = 25.000°	98.9 %	
Absorption correction	Semi-empirical from equivalents	
Max. and min. transmission	0.98 and 0.90	
Refinement method	Full-matrix least-squares on F^2	
Data / restraints / parameters	4375 / 0 / 379	
Goodness-of-fit on F^2	0.9364	
Final R indices [I>2sigma(I)]	R1 = 0.0419, wR2 = 0.0976	
R indices (all data)	R1 = 0.0659, wR2 = 0.1206	
Largest diff. peak and hole	0.32 and -0.28 $e.Å^{-3}$	

Table 2: Atomic coordinates (x 10^4) and equivalent isotropic displacement parameters ($Å^2$x 10^3) for **121**. U(eq) is defined as one third of the trace of the orthogonalized U^{ij} tensor.

	x	y	z	U(eq)
O(1)	4040(2)	1666(1)	3883(1)	36
C(2)	3126(3)	778(2)	3877(1)	35
C(3)	1747(3)	792(2)	4095(1)	38
C(4)	800(3)	-75(2)	4047(1)	42
C(5)	1214(3)	-903(2)	3795(1)	44
C(6)	2593(3)	-885(2)	3581(1)	41
C(7)	3588(3)	-42(2)	3617(1)	37
C(8)	5091(3)	-15(2)	3378(1)	43
C(9)	4779(3)	-367(3)	2862(1)	59
C(10)	6416(3)	-638(3)	3655(1)	77
C(11)	1260(3)	1696(2)	4369(1)	48
C(12)	1164(4)	1439(2)	4891(1)	60
C(13)	-333(4)	2130(3)	4135(1)	68
C(14)	5071(3)	1883(2)	4289(1)	33
C(15)	5646(2)	2877(2)	4345(1)	30
C(16)	6638(3)	3120(2)	4770(1)	32
C(17)	7171(3)	4180(2)	4865(1)	37
O(18)	8153(2)	4388(1)	5208(1)	57
C(19)	6414(3)	4985(2)	4544(1)	32
C(20)	5491(2)	4730(2)	4107(1)	30
C(21)	5316(3)	3650(2)	3960(1)	34
O(22)	4997(2)	3403(1)	3544(1)	53
C(23)	4790(3)	5518(2)	3819(1)	34
O(24)	3891(2)	5261(1)	3398(1)	42
C(25)	2992(3)	6006(2)	3124(1)	38
C(26)	1459(3)	6199(2)	3223(1)	39
C(27)	542(3)	6865(2)	2915(1)	47
C(28)	1139(3)	7286(2)	2529(1)	51
C(29)	2668(3)	7073(2)	2444(1)	49
C(30)	3656(3)	6424(2)	2743(1)	41
C(31)	5324(3)	6130(2)	2651(1)	49
C(32)	6086(4)	6879(3)	2345(1)	86

C(33)	5324(4)	5063(3)	2447(1)	84
C(34)	809(3)	5658(2)	3627(1)	48
C(35)	-563(3)	6197(3)	3814(1)	61
C(36)	344(6)	4584(3)	3482(1)	100
C(37)	5019(3)	6513(2)	3964(1)	39
C(38)	5958(3)	6742(2)	4391(1)	40
C(39)	6655(3)	5982(2)	4681(1)	37
C(40)	7099(3)	2393(2)	5115(1)	38
C(41)	6543(3)	1422(2)	5047(1)	42
C(42)	5513(3)	1167(2)	4640(1)	39

Table 3: Bond lengths [Å] and angles [°] for **121**.

O(1)-C(2)	1.407(3)	C(15)-C(21)	1.492(3)
O(1)-C(14)	1.372(3)	C(16)-C(17)	1.488(3)
C(2)-C(3)	1.393(3)	C(16)-C(40)	1.389(3)
C(2)-C(7)	1.396(3)	C(17)-O(18)	1.218(3)
C(3)-C(4)	1.396(3)	C(17)-C(19)	1.488(3)
C(3)-C(11)	1.513(3)	C(19)-C(20)	1.408(3)
C(4)-C(5)	1.380(4)	C(19)-C(39)	1.383(3)
C(4)-H(41)	0.955	C(20)-C(21)	1.491(3)
C(5)-C(6)	1.386(4)	C(20)-C(23)	1.405(3)
C(5)-H(51)	0.965	C(21)-O(22)	1.215(3)
C(6)-C(7)	1.393(3)	C(23)-O(24)	1.365(3)
C(6)-H(61)	0.971	C(23)-C(37)	1.385(3)
C(7)-C(8)	1.521(3)	O(24)-C(25)	1.412(3)
C(8)-C(9)	1.519(3)	C(25)-C(26)	1.388(3)
C(8)-C(10)	1.519(4)	C(25)-C(30)	1.395(3)
C(8)-H(81)	0.999	C(26)-C(27)	1.397(3)
C(9)-H(91)	0.976	C(26)-C(34)	1.514(3)
C(9)-H(92)	0.980	C(27)-C(28)	1.383(4)
C(9)-H(93)	0.986	C(27)-H(271)	0.964
C(10)-H(103)	0.974	C(28)-C(29)	1.377(4)
C(10)-H(102)	0.976	C(28)-H(281)	0.956
C(10)-H(101)	0.980	C(29)-C(30)	1.399(4)
C(11)-C(12)	1.527(4)	C(29)-H(291)	0.961
C(11)-C(13)	1.530(4)	C(30)-C(31)	1.521(4)
C(11)-H(111)	0.996	C(31)-C(32)	1.519(4)
C(12)-H(123)	0.973	C(31)-C(33)	1.526(4)
C(12)-H(122)	0.976	C(31)-H(311)	0.992
C(12)-H(121)	0.982	C(32)-H(323)	0.982
C(13)-H(131)	0.983	C(32)-H(322)	0.979
C(13)-H(132)	0.983	C(32)-H(321)	0.975
C(13)-H(133)	0.984	C(33)-H(331)	0.972
C(14)-C(15)	1.406(3)	C(33)-H(332)	0.974
C(14)-C(42)	1.386(3)	C(33)-H(333)	0.965
C(15)-C(16)	1.405(3)	C(34)-C(35)	1.518(4)

C(34)-C(36)	1.518(4)	C(2)-C(7)-C(8)	121.8(2)
C(34)-H(341)	1.008	C(6)-C(7)-C(8)	121.3(2)
C(35)-H(351)	0.979	C(7)-C(8)-C(9)	111.9(2)
C(35)-H(352)	0.988	C(7)-C(8)-C(10)	111.2(2)
C(35)-H(353)	0.966	C(9)-C(8)-C(10)	110.3(2)
C(36)-H(363)	0.970	C(7)-C(8)-H(81)	107.4
C(36)-H(362)	0.980	C(9)-C(8)-H(81)	106.8
C(36)-H(361)	0.977	C(10)-C(8)-H(81)	109.1
C(37)-C(38)	1.385(3)	C(8)-C(9)-H(91)	108.9
C(37)-H(371)	0.966	C(8)-C(9)-H(92)	107.4
C(38)-C(39)	1.379(3)	H(91)-C(9)-H(92)	109.9
C(38)-H(381)	0.971	C(8)-C(9)-H(93)	110.6
C(39)-H(391)	0.954	H(91)-C(9)-H(93)	110.2
C(40)-C(41)	1.374(3)	H(92)-C(9)-H(93)	109.9
C(40)-H(401)	0.966	C(8)-C(10)-H(103)	109.5
C(41)-C(42)	1.387(3)	C(8)-C(10)-H(102)	108.4
C(41)-H(411)	0.967	H(103)-C(10)-H(102)	110.7
C(42)-H(421)	0.977	C(8)-C(10)-H(101)	107.8
		H(103)-C(10)-H(101)	110.1
C(2)-O(1)-C(14)	118.13(16)	H(102)-C(10)-H(101)	110.3
O(1)-C(2)-C(3)	118.4(2)	C(3)-C(11)-C(12)	111.8(2)
O(1)-C(2)-C(7)	117.65(19)	C(3)-C(11)-C(13)	111.2(2)
C(3)-C(2)-C(7)	123.7(2)	C(12)-C(11)-C(13)	110.0(2)
C(2)-C(3)-C(4)	116.8(2)	C(3)-C(11)-H(111)	108.3
C(2)-C(3)-C(11)	122.7(2)	C(12)-C(11)-H(111)	108.0
C(4)-C(3)-C(11)	120.5(2)	C(13)-C(11)-H(111)	107.3
C(3)-C(4)-C(5)	121.4(2)	C(11)-C(12)-H(123)	108.9
C(3)-C(4)-H(41)	119.0	C(11)-C(12)-H(122)	108.5
C(5)-C(4)-H(41)	119.6	H(123)-C(12)-H(122)	110.5
C(4)-C(5)-C(6)	120.0(2)	C(11)-C(12)-H(121)	107.4
C(4)-C(5)-H(51)	120.7	H(123)-C(12)-H(121)	110.4
C(6)-C(5)-H(51)	119.3	H(122)-C(12)-H(121)	111.0
C(5)-C(6)-C(7)	121.2(2)	C(11)-C(13)-H(131)	108.6
C(5)-C(6)-H(61)	120.0	C(11)-C(13)-H(132)	109.1
C(7)-C(6)-H(61)	118.7	H(131)-C(13)-H(132)	110.0
C(2)-C(7)-C(6)	116.9(2)	C(11)-C(13)-H(133)	108.8

H(131)-C(13)-H(133)	110.0	C(27)-C(28)-C(29)	120.5(2)
H(132)-C(13)-H(133)	110.3	C(27)-C(28)-H(281)	118.7
O(1)-C(14)-C(15)	117.44(18)	C(29)-C(28)-H(281)	120.8
O(1)-C(14)-C(42)	122.2(2)	C(28)-C(29)-C(30)	121.3(2)
C(15)-C(14)-C(42)	120.3(2)	C(28)-C(29)-H(291)	119.9
C(14)-C(15)-C(16)	117.89(19)	C(30)-C(29)-H(291)	118.8
C(14)-C(15)-C(21)	122.24(19)	C(29)-C(30)-C(25)	116.1(2)
C(16)-C(15)-C(21)	119.77(19)	C(29)-C(30)-C(31)	123.1(2)
C(15)-C(16)-C(17)	120.13(19)	C(25)-C(30)-C(31)	120.7(2)
C(15)-C(16)-C(40)	121.3(2)	C(30)-C(31)-C(32)	114.0(2)
C(17)-C(16)-C(40)	118.51(19)	C(30)-C(31)-C(33)	110.4(2)
C(16)-C(17)-O(18)	121.0(2)	C(32)-C(31)-C(33)	111.5(3)
C(16)-C(17)-C(19)	118.07(18)	C(30)-C(31)-H(311)	107.3
O(18)-C(17)-C(19)	120.9(2)	C(32)-C(31)-H(311)	106.9
C(17)-C(19)-C(20)	120.3(2)	C(33)-C(31)-H(311)	106.2
C(17)-C(19)-C(39)	118.53(19)	C(31)-C(32)-H(323)	107.7
C(20)-C(19)-C(39)	121.2(2)	C(31)-C(32)-H(322)	109.5
C(19)-C(20)-C(21)	119.79(19)	H(323)-C(32)-H(322)	111.1
C(19)-C(20)-C(23)	118.0(2)	C(31)-C(32)-H(321)	106.8
C(21)-C(20)-C(23)	122.24(18)	H(323)-C(32)-H(321)	110.5
C(15)-C(21)-C(20)	116.96(18)	H(322)-C(32)-H(321)	111.0
C(15)-C(21)-O(22)	121.1(2)	C(31)-C(33)-H(331)	109.4
C(20)-C(21)-O(22)	121.9(2)	C(31)-C(33)-H(332)	110.5
C(20)-C(23)-O(24)	117.42(19)	H(331)-C(33)-H(332)	111.1
C(20)-C(23)-C(37)	120.3(2)	C(31)-C(33)-H(333)	105.7
O(24)-C(23)-C(37)	122.3(2)	H(331)-C(33)-H(333)	109.9
C(23)-O(24)-C(25)	119.91(17)	H(332)-C(33)-H(333)	110.2
O(24)-C(25)-C(26)	117.8(2)	C(26)-C(34)-C(35)	114.5(2)
O(24)-C(25)-C(30)	117.2(2)	C(26)-C(34)-C(36)	110.3(2)
C(26)-C(25)-C(30)	124.7(2)	C(35)-C(34)-C(36)	110.6(3)
C(25)-C(26)-C(27)	116.4(2)	C(26)-C(34)-H(341)	107.0
C(25)-C(26)-C(34)	120.8(2)	C(35)-C(34)-H(341)	106.3
C(27)-C(26)-C(34)	122.7(2)	C(36)-C(34)-H(341)	107.7
C(26)-C(27)-C(28)	121.0(2)	C(34)-C(35)-H(351)	107.9
C(26)-C(27)-H(271)	119.8	C(34)-C(35)-H(352)	108.5
C(28)-C(27)-H(271)	119.2	H(351)-C(35)-H(352)	112.0

C(34)-C(35)-H(353)	107.4	C(39)-C(38)-H(381)	120.0
H(351)-C(35)-H(353)	110.3	C(19)-C(39)-C(38)	119.7(2)
H(352)-C(35)-H(353)	110.5	C(19)-C(39)-H(391)	119.4
C(34)-C(36)-H(363)	108.4	C(38)-C(39)-H(391)	120.9
C(34)-C(36)-H(362)	110.0	C(16)-C(40)-C(41)	119.5(2)
H(363)-C(36)-H(362)	110.6	C(16)-C(40)-H(401)	119.0
C(34)-C(36)-H(361)	107.3	C(41)-C(40)-H(401)	121.5
H(363)-C(36)-H(361)	108.9	C(40)-C(41)-C(42)	120.6(2)
H(362)-C(36)-H(361)	111.4	C(40)-C(41)-H(411)	120.2
C(23)-C(37)-C(38)	120.4(2)	C(42)-C(41)-H(411)	119.3
C(23)-C(37)-H(371)	119.3	C(41)-C(42)-C(14)	120.3(2)
C(38)-C(37)-H(371)	120.3	C(41)-C(42)-H(421)	120.9
C(37)-C(38)-C(39)	120.4(2)	C(14)-C(42)-H(421)	118.8
C(37)-C(38)-H(381)	119.6		

Symmetry transformations used to generate
equivalent atoms:

Table 4: Anisotropic displacement parameters ($Å^2 x\ 10^3$) for **121**. The anisotropic displacement factor exponent takes the form: $-2\pi^2[\ h^2\ a^{*2}U^{11} + ... + 2\ h\ k\ a^*\ b^*\ U^{12}\ ]$

	U_{11}	U_{22}	U_{33}	U_{23}	U_{13}	U_{12}
O(1)	37(1)	36(1)	32(1)	5(1)	-4(1)	-8(1)
C(2)	33(1)	35(1)	33(1)	8(1)	-5(1)	-5(1)
C(3)	35(1)	41(1)	37(1)	7(1)	0(1)	-2(1)
C(4)	33(1)	49(2)	41(1)	11(1)	-2(1)	-5(1)
C(5)	45(2)	40(1)	43(1)	6(1)	-7(1)	-10(1)
C(6)	46(2)	38(1)	35(1)	2(1)	-5(1)	-3(1)
C(7)	38(1)	39(1)	31(1)	4(1)	-4(1)	-2(1)
C(8)	42(1)	45(2)	43(1)	-2(1)	5(1)	-6(1)
C(9)	52(2)	84(2)	40(1)	-1(1)	5(1)	11(2)
C(10)	40(2)	135(3)	53(2)	7(2)	-1(1)	11(2)
C(11)	44(2)	42(2)	60(2)	1(1)	15(1)	-3(1)
C(12)	65(2)	64(2)	48(2)	-9(1)	2(1)	0(2)
C(13)	75(2)	75(2)	57(2)	11(2)	20(2)	30(2)
C(14)	30(1)	40(1)	28(1)	0(1)	2(1)	-2(1)
C(15)	28(1)	38(1)	24(1)	1(1)	5(1)	3(1)
C(16)	31(1)	40(1)	24(1)	1(1)	3(1)	1(1)
C(17)	37(1)	48(1)	26(1)	-1(1)	-1(1)	-1(1)
O(18)	67(1)	56(1)	40(1)	1(1)	-23(1)	-8(1)
C(19)	32(1)	40(1)	24(1)	-2(1)	4(1)	-1(1)
C(20)	32(1)	36(1)	22(1)	-1(1)	4(1)	-1(1)
C(21)	38(1)	38(1)	25(1)	-2(1)	0(1)	-2(1)
O(22)	90(1)	39(1)	25(1)	-2(1)	-5(1)	-7(1)
C(23)	36(1)	39(1)	26(1)	-1(1)	-1(1)	0(1)
O(24)	53(1)	38(1)	30(1)	0(1)	-13(1)	3(1)
C(25)	45(1)	37(1)	27(1)	2(1)	-8(1)	0(1)
C(26)	45(1)	43(1)	28(1)	0(1)	-4(1)	-4(1)
C(27)	44(1)	53(2)	40(1)	3(1)	-5(1)	3(1)
C(28)	50(2)	55(2)	43(2)	13(1)	-9(1)	0(1)
C(29)	56(2)	56(2)	32(1)	10(1)	-2(1)	-8(1)
C(30)	43(1)	47(1)	31(1)	1(1)	-5(1)	-6(1)
C(31)	44(1)	65(2)	36(1)	-5(1)	-3(1)	-6(1)
C(32)	58(2)	117(3)	84(2)	21(2)	20(2)	-7(2)
C(33)	68(2)	94(3)	94(3)	-40(2)	21(2)	-9(2)

C(34)	56(2)	56(2)	32(1)	5(1)	2(1)	-7(1)
C(35)	47(2)	87(2)	50(2)	9(2)	6(1)	-9(2)
C(36)	168(4)	67(2)	73(2)	0(2)	47(2)	-43(2)
C(37)	45(1)	36(1)	35(1)	-1(1)	-2(1)	2(1)
C(38)	44(1)	36(1)	40(1)	-7(1)	2(1)	-1(1)
C(39)	38(1)	43(1)	28(1)	-6(1)	1(1)	-4(1)
C(40)	35(1)	48(2)	29(1)	3(1)	-2(1)	3(1)
C(41)	43(1)	45(2)	36(1)	10(1)	0(1)	3(1)
C(42)	41(1)	37(1)	37(1)	6(1)	-2(1)	-2(1)

Table 5: Hydrogen coordinates (x 10^4) and isotropic displacement parameters (Å^{2}x 10^3) for **121**.

	x	y	z	U(eq)
H(41)	-144	-96	4197	53
H(51)	548	-1497	3762	54
H(61)	2883	-1466	3403	50
H(81)	5442	705	3372	55
H(91)	5751	-280	2717	92
H(92)	4495	-1084	2866	92
H(93)	3897	20	2684	93
H(103)	7391	-559	3511	113
H(102)	6573	-406	3985	113
H(101)	6077	-1347	3639	113
H(111)	2081	2233	4361	60
H(123)	912	2049	5056	93
H(122)	2193	1168	5033	93
H(121)	315	936	4895	93
H(131)	-564	2744	4308	102
H(132)	-1176	1626	4151	102
H(133)	-246	2296	3800	102
H(271)	-527	7031	2970	59
H(281)	468	7726	2321	63
H(291)	3072	7369	2174	59
H(311)	6008	6106	2965	63
H(323)	7177	6647	2325	128
H(322)	6086	7552	2488	128
H(321)	5450	6870	2030	128
H(331)	6416	4856	2428	130
H(332)	4805	4596	2643	131
H(333)	4732	5104	2131	130
H(341)	1701	5624	3902	60
H(351)	-802	5834	4097	93
H(352)	-244	6903	3887	93
H(353)	-1467	6172	3565	93
H(363)	81	4228	3761	148
H(362)	1226	4249	3353	148
H(361)	-607	4621	3244	148

H(371)	4512	7045	3764	48
H(381)	6124	7443	4485	51
H(391)	7318	6134	4973	45
H(401)	7819	2582	5397	48
H(411)	6862	909	5284	53
H(421)	5088	483	4594	49

Table 6: Hydrogen bonds for **121** [Å and °].

D-H...A	d(D-H)	d(H...A)	d(D...A)	<(DHA)
C(28)-H(281)...O(22)#1	0.96	2.58	3.392(4)	142
C(34)-H(341)...O(18)#2	1.01	2.50	3.291(4)	135

Symmetry transformations used to generate equivalent atoms: #1 -x+1/2,y+1/2,-z+1/2 #2 -x+1,-y+1,-z+1